# APPLICATION OF COMPUTER SIMULATION METHODS TO THE STUDY OF PLATINUM GROUP MINERALS

By

PETROS SENAUOA NTOAHAE

Submitted in fulfillment of the requirement for the degree of
Doctor of Philosophy in the Department of Physics
School of Physical and Mineral Sciences,
in the Faculty of Science, Health and Agriculture
University of Limpopo (formerly University of the North),
Turfloop, South Africa.

**Supervisor: Professor P.E. Ngoepe**
**Co-Supervisor: Professor D.G. Pettifor**

04 August 2005

# DECLARATION

I declare that the thesis hereby submitted to the University of Limpopo for the degree of Doctor of Philosophy has not previously been submitted by me for a degree at this or any other university, that is my own work in design and in execution, and that all material contained herein has been duly acknowledged.

_____

Petros Senauoa Ntoahae

# ACKNOWLEDGEMENTS

I am indebted to a small number of people who helped me during the research and preparation of this thesis. First thanks must go to my supervisor Professor P. E. Ngoepe (University of Limpopo, A Fellow of the Council of Scientific and Industrial Research (CSIR)) for his choice of subject and his encouragement throughout the course of this work.

Secondly, I wish to thank my co-supervisor Professor D. G. Pettifor (Oxford University, A Fellow of the Royal Society (FRS), and Commander of British Empire (CBE)) for his help in assembling this thesis and throughout provoking discussions.

I wish also thank Professor D. Vaughan (Manchester University) and Dr K. Wright (Curtin University of Technology) for their help during the first stage of the project. Their encouragement and interest were of great value.

It would also be inappropriate not to acknowledge Professor S.C. Parker (University of Bath) whose contribution expanded this work to its present level. In addition, Dr Duc Nguyen-Mahn, and Dr D. Cooke for many useful and wide ranging discussions, and for making me think harder about computing issues than I ever thought possible.

I extend particular gratitude to the researchers and lecturing staff in Material Modelling Laboratory (Oxford University), Computational Chemistry Group (University of Bath), Physics Department and Material Modelling Centre (University of Limpopo) for providing a good working environment. I am also grateful to my colleagues in the department of Physics for taking some of my load during the execution of this work.

I am grateful to National Research Foundation (NRF), Royal Society (RS) and University of Limpopo (Turfloop campus) for financial support and provision of computer time. Many thanks to Professors Phuti Ngoepe and Richard Catlow for coordinating the NRF-RS initiative.

The contributions of my friends and colleagues are numerous and gratefully acknowledged. Of my colleagues, past and present, particular thanks must go those in Materials Modelling Centre (MMC), Materials Modelling Laboratory (MML) and Computational Chemistry (Parkers' Group). I have learnt from their scientific prowess and have greatly enjoyed their social company and informed comments.

Finally, I would like to thank my own family, particularly my mother (Moseekane), brother (Molotsi), sisters (Keneuoe, Masenooe, Nthabiseng), and my nieces (Tshepiso, Nozipho, Karabo and Mosa), for their continued

support. Ke ya leboha bahlakoana! Ke leboha Modimo, ha a ile a mpoloka ho fihlela ke phetha morero ona. PULA, NALA MA-AFRICA.

**DEDICATION TO:**

MY PARENTS

MY LATE FATHER SENOOE SAFERI
MY MOTHER MAPHATUDI MOSEEKANE

AND

THE LATE MIKE PHAMBANE, THULANE MTSHALI AND REUBEN RAMALI, WHO LOST THEIR LIVES ON THE WAY TO AN ANNUAL PHYSICS CONFERENCE ON THE 2nd OF JULY 1995.

# ABSTRACT

Computer simulation studies of a few representative Platinum-Group-Minerals (PGM), which are of industrial importance to the mining industry in South Africa were carried out. The electronic, structural and optical properties of PGM (PtS, $PdPt_3S_4$, $PtAs_2$ and $Pt_4As_4S_4$) were calculated within the framework of the density functional theory. We have used both the pseudopotential planewave and the Tight Binding Linear Muffin-Tin Orbital (TB-LMTO) methods to complement each other, since there is not much experimental data available for these systems. In the TB-LMTO method, the radii of overlapping Muffin Tin (MT) spheres were chosen to provide an efficient packing of space while ensuring that the overlap between the spheres remains small. The ground state structural properties were obtained by self-consistent energy minimization with respect to the atomic volume. The predicted equilibrium volume is within less than 15% of experiment. We have also found non-metallic semi-conducting behaviour for the three systems, PtS, $PdPt_3S_4$ and $PtAs_2$ using both ab initio techniques. On the other hand, $Pt_4As_4S_4$ was predicted to be metallic. We argue that the strong bonding between the Pt 5d and the S(As) 3p(4p) states plays a crucial role in the formation of the band gap in the semiconducting. The optical properties of PtS, $PdPt_3S_4$ and $PtAs_2$ were calculated, and their reflectance spectra were found to be in good agreement with the experimental measurements. Full relaxation of both the volume and the internal parameters was carried out using the plane-wave pseudopotential method. It was found that the internal parameters as well as the bond lengths decrease with hydrostatic compression particularly for the cubic $PtAs_2$, $Pt_4As_4S_4$ and tetragonal $PdPt_3S_4$, and PtS has no internal parameters. The bulk moduli were calculated for these representatives of PGM and there are currently no experimental results available. We have derived a new set of potential models for PtS, $PdPt_3S_4$, $PtAs_2$ and $Pt_4As_4S_4$ structures. The models were used to study the pressure dependence of lattice constant for all the four systems and agree well with our electronic structure methods. However, PtS display anomaly under hydrostatic pressure, by expanding along c-lattice constant with increased pressure, for which there are no experimental evidence. We then modelled the structure and stabilities of $PtAs_2$ and $Pt_4As_4S_4$ of the dry and hydrated surfaces for low and high index surfaces, and predicted the $\{100\}$ surface to be the most stable in both cases. It is further shown that molecular absorption of water has a stabilising effect on all the surfaces of the two structures. Stepped surfaces were

created for {510} and {610} for both $PtAs_2$ and $Pt_4As_4S_4$ in order to model more realistic surfaces under dry condition with one dimensional defects, and then acute stepped were found to be the most stable compared to the obtuse steps. The three surfaces expressed in the equilibrium morphology of $PtAs_2$, {100}, {210} and {102}, are in good agreement with experiment.

# Contents

# List of Tables

# List of Figures

# Chapter 1

# Introduction

Compounds such as cooperite, braggite, sperrylite and platarsite are important sources of platinum and palladium in many of the world's largest deposits of platinum group minerals (PGM) [1]. They also contain the sulfides of other transition metals such as Os, Ir, Ru, Pd, Fe, Ni and Cu [2]. Platinum and Palladium play important roles as catalysts in the petroleum refining industry. They represent the only known class of stable catalytically active phases for strongly sulpho-reductive hydroprocessing conditions [3]. Palladium and platinum are usually active ingredients in automotive catalysts [4]. It has been known for some time that many intermetallic compounds containing platinum-group metals have reflection coefficients that are strongly dependent on wavelength in the visible region of the spectrum, and are therefore coloured. Apart from inherently interesting properties of these materials, they have attracted interest because they have potential applications as opto-electronic components, as selective solar absorbers, and in jewellery and other decorative arts [5]. In the last few years, interest in the development of polymer electrolyte fuel cell (PEFC) has considerably increased due to its many advantages: high power density, compactness, high performance by cost, quick and stable operation at low temperature, nanoelectrolyte leakage, and so on, for applications such as transportation, portable power generators for on-site use compared with other fuel cell system. The electrodes usually contain a platinum catalyst in the form of Pt black or Pt-supported on carbon [6]. During the last few years, there has been a great deal of interest, especially in the mining industry, in understanding the electronic, magnetic, optical, structural and thermodynamic properties of platinum group minerals, since these affect ore formation and environmental

mineralogy. The mining industry is the main contributor to export earning for South Africa, and research and development in this field is essential. The major producers of platinum group metals are South Africa and Russia, with less production from USA, Canada, and Zimbabwe [7]. The industry is, however, under threat because of the decline in commodity prices in real terms over the past few years. It is, therefore, focussing on efficiency in the extraction and production of these commodities. Research and development is, therefore, essential for the economic and social developments needed to lift the South African and indeed the African populations from their existing state of poverty as compared with first world countries, and also profitability and survival of the mining industry. The use of platinum as jewellery has an interesting historical perspective. The great draw back was the high melting point of platinum. The Equadorian Indians, nevertheless, devised a way of alloying platinum with gold, by using gold as a cement to bind the particles of platinum. By heating a mixture of platinum and gold particles together to the melting point of gold, the still solid platinum particles were permanently bound together. This application provides one of the earliest examples of powder metallurgy technology. In the jewellery industry, where platinum and gold play an important role, by virtue of their high price and densities, it is necessary to harden these metals in order to minimise scratches. Mixture of platinum and other metals do play an important role in the jewellery industry, although the colour does not look any different from other white metals, but it can be restored by addition of other metals, like copper [8]. In spite of these metals being widely used in the jewellery industry, it is surprising how much less well developed knowledge of the physical properties of these precious metals compared to iron and steels.

The next section of this chapter describes the structures of a few representative PGM and the impact of the local environment on these minerals. The last two sections present literature review and outline the objectives of this study.

## 1.1 Structure of platinum group minerals

In general terms, a mineral is an element or chemical compound that is normally crystalline and which has been formed as a result of geological processes [9]. Many minerals were formed under conditions of high temperature or pressure and are metastable under ambient conditions; others

may tend to hydrate or dehydrate when removed from their place of origin. Platinum group element (PGE) bearing deposits display a large spectrum of platinum group minerals (PGM) which are produced during the different stages of the ore forming processes [10]. An important observation is that the morphology of the PGM in each of the textural types is strongly controlled by the local mineralogical environment. Studies of fluid inclusions in silicates from the PGE mineralisation zone of the Merensky Reef in South Africa show that fluids participated in the formation of PGM [11]. Merenskyite is usually present at the contact between sulphides and hydrosilicates. The platinum group minerals occur in three distinct textural environments; (a) at the boundary of sulphides and silicates/hydrosilicates, (b) entirely enclosed within sulphides and (c) entirely enclosed within silicates or hydrosilicate minerals. Platinum is the most abundant element constituting the PGM, especially in the sulphide and arsenide groups. Palladium is the next most dominant PGE; the other elements make a negligible contribution to the platinum group mineralogy as a whole [12]. PGE occurs as sulphides and arsenides included in chromite crystals, but in many cases Pt and Pd minerals are in close association with the base metal sulphides interstitial to the chromite.

### 1.1.1 Platinum group minerals with tetragonal symmetry

Braggite and cooperite are two PGE sulphide minerals found in the Pt-Pd-S system. The members of both the cooperite and braggite series belong to the most abundant platinum group minerals in many PGE deposits; such as the Merensky reef; UG-2 chromitite layer, Bushveld complex [13]. The sulphide group of PGM (cooperite and braggite) occurs dominantly at the silicates-sulphide boundary. Cooperite(PtS) adopts a tetragonal structure (fig. 1.1), space group P42/mmc, in which each Pt atom forms four coplanar bonds to bridging sulphur atoms. The position of the atoms are generated by Pt(2c): $(0, \frac{1}{2}, 0)$, $(\frac{1}{2}, 0, \frac{1}{2})$ , S(2e): $(0, 0, \frac{1}{4}), (0, 0, \frac{3}{4})$. It has four atoms per unit cell and it is a tetragonal structure with lattice constant a = 3.47 Å and c = 6.1 Å. The structure of cooperite(PtS) is a compromise between the "square-planar" stereochemical requirements of $Pt^{2+}$ and the " tetrahedral" requirements of $S^{2-}$, and hence, represents a distorted derivative of the sphalerite structure. In the PtS lattice the S atoms occupy the corners of

a tetragonally distorted simple cubic lattice, while the Pt atoms occupy the centres of two opposite faces of the cell, alternately in the (100) and (010) planes. The S-Pt-S bond angles of 82.7° and 97.3° represent a distortion of a perfectly square planar platinum coordination; the sulfur environment( bond angles Pt-S-Pt 97.3° and 115.9° ) is a distortion of the regular tetrahedron (bond angle 109.5° ) [1]. Braggite is also tetragonal and crystallised with P42/m space group. Braggite ($PdPt_3S_4$) has 16 atoms per unit cell as shown in figure 1-1. The metal atoms are located at the special positions Pd (2d): $(0,\frac{1}{2},\frac{1}{2})$ ,$(\frac{1}{2},0,0)$; $(Pt)_1$(2e): $(0,0,\frac{1}{4})$,$(0,0,\frac{3}{4})$ , $(Pt)_2$(4j): $(u,v,0)$, $(-u,-v,0),(-v,u,\frac{1}{2}),(v,-u,\frac{1}{2})$ , and the sulphur atoms at the general position S(8k): $\pm(u,v,w),\pm(u,v,-w)$, $\pm(-v,u,w+\frac{1}{2}),\pm(v,-u,w+\frac{1}{2})$.The Pt content is greater than that of Pd. The structure of braggite (fig. 1.2), is essentially a superlattice of cooperite. It is a tetragonal structure with lattice constant a = 6.38 Å and c = 6.57 Å, with the combined coordination of square-planar coordinated metals and tetrahedrally coordinated sulphur [14].

### 1.1.2 Platinum Group Mineral with Cubic symmetry

The presence of anion pairs ($S_2^{2-}$ , $AsS^{2-\ 1}$) is the unifying feature of this group of structures. Sperrylite ($PtAs_2$) takes cubic pyrite structure with octahedrally coordinated metal atoms at the corners and face centers of the cube unit cell as shown in fig. 1.3. " Dump-bell" shaped disulphide atoms $As_2^{2-1}$ lie at the center of the cube and mid-points of the cube edges. The mid-point of the S2 group occupies the Cl sites of NaCl structure, while the As atoms occupy the Na positions. The $S_2^{2-}$ pairs are oriented such that their axes are parallel to four non-intersecting body diagonals of the cubic space lattice. Each As atom is coordinated to three Pt and one As in a distorted tetrahedral configuration. Sperrylite has the lattice parameters, a = 5.9861 Å and the internal parameter $u = 0.38345$. Its space group is Pa-3 and the positions of the atoms are generated by Pt (4a): $(0,0,0),(0,\frac{1}{2},\frac{1}{2}),(\frac{1}{2},0,\frac{1}{2}),(\frac{1}{2},\frac{1}{2},0)$; S(8c): $\pm(u,u,u),\pm(u+\frac{1}{2},\frac{1}{2}-u,-u),\pm(-u,u+\frac{1}{2},\frac{1}{2}-u),\pm(\frac{1}{2}-u,-u,u+\frac{1}{2})$; and the additional symmetry positions (24d): $(x,y,z)$ with x = 0.31681, y = 0.09448 and z = 0.21363. A large number of synthetic analogs, including mixed-cation

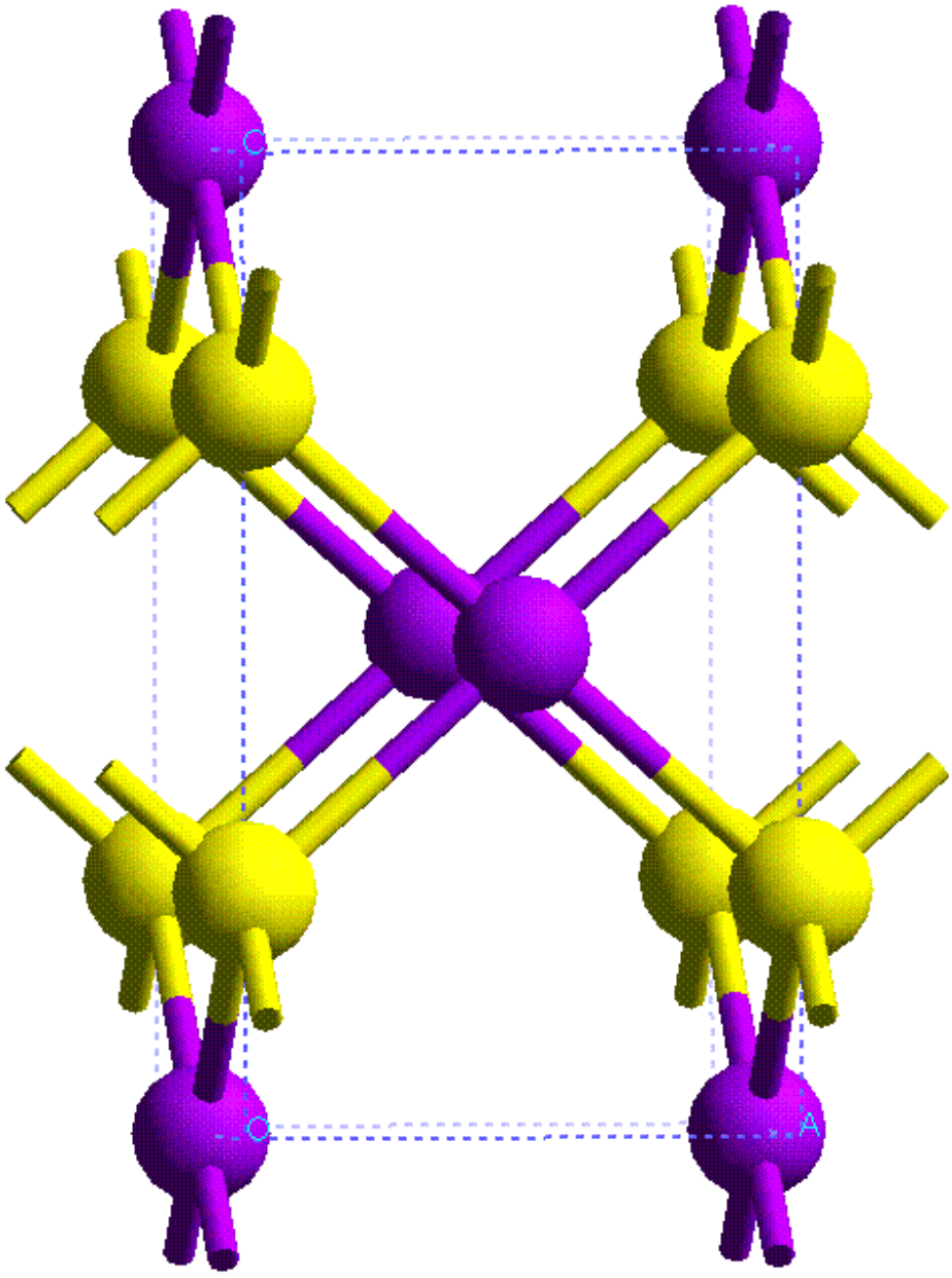


Figure 1.1: Crystal structure of cooperite (PtS). Pt atoms are represented by purple balls and S atoms by yellow balls [1].

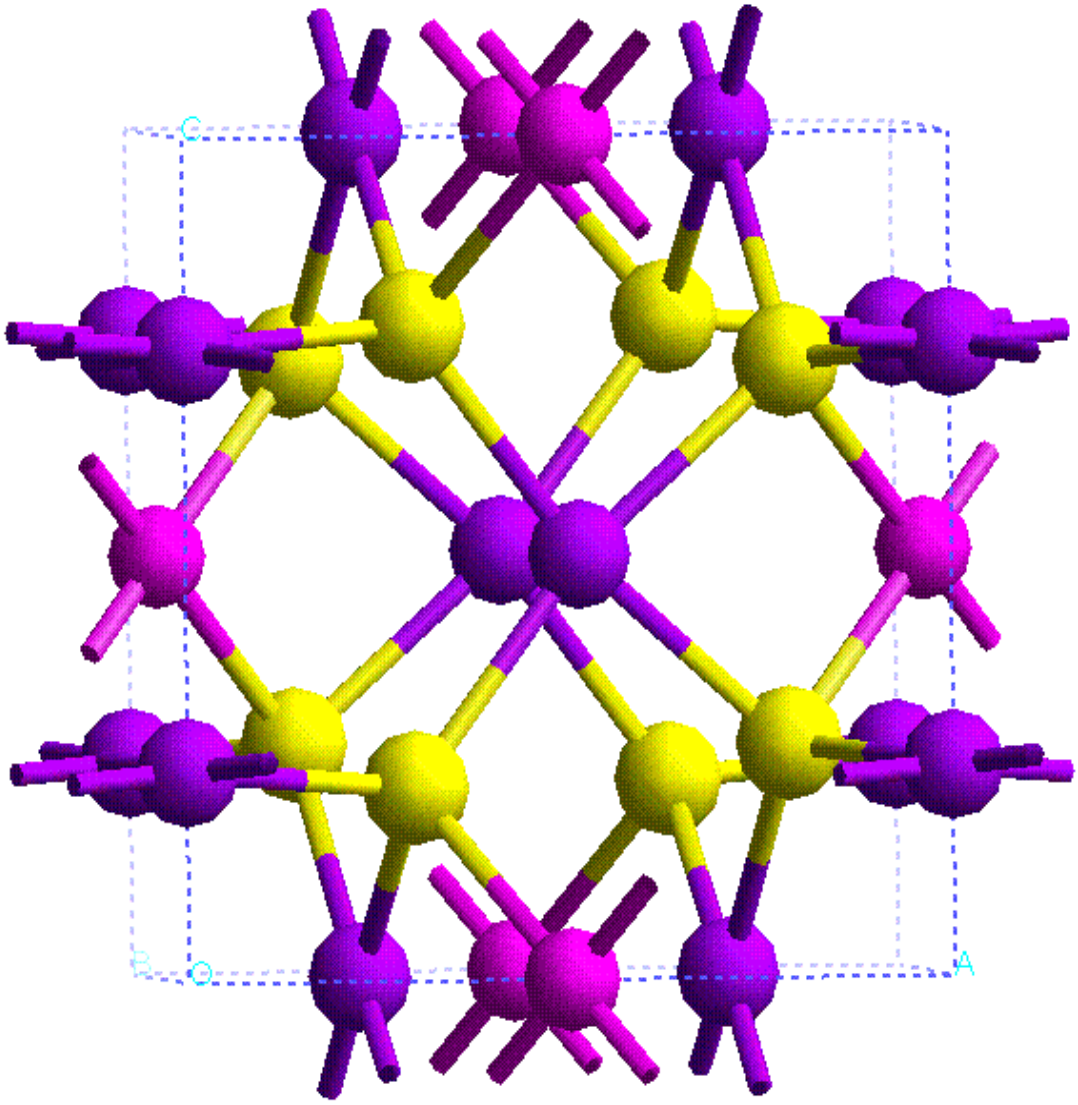


Figure 1.2: Crystal structure of braggite ($PdPt_3S_4$). Pt atoms are represented by purple, Pd atoms by magenta and S atoms by yellow colour [52].

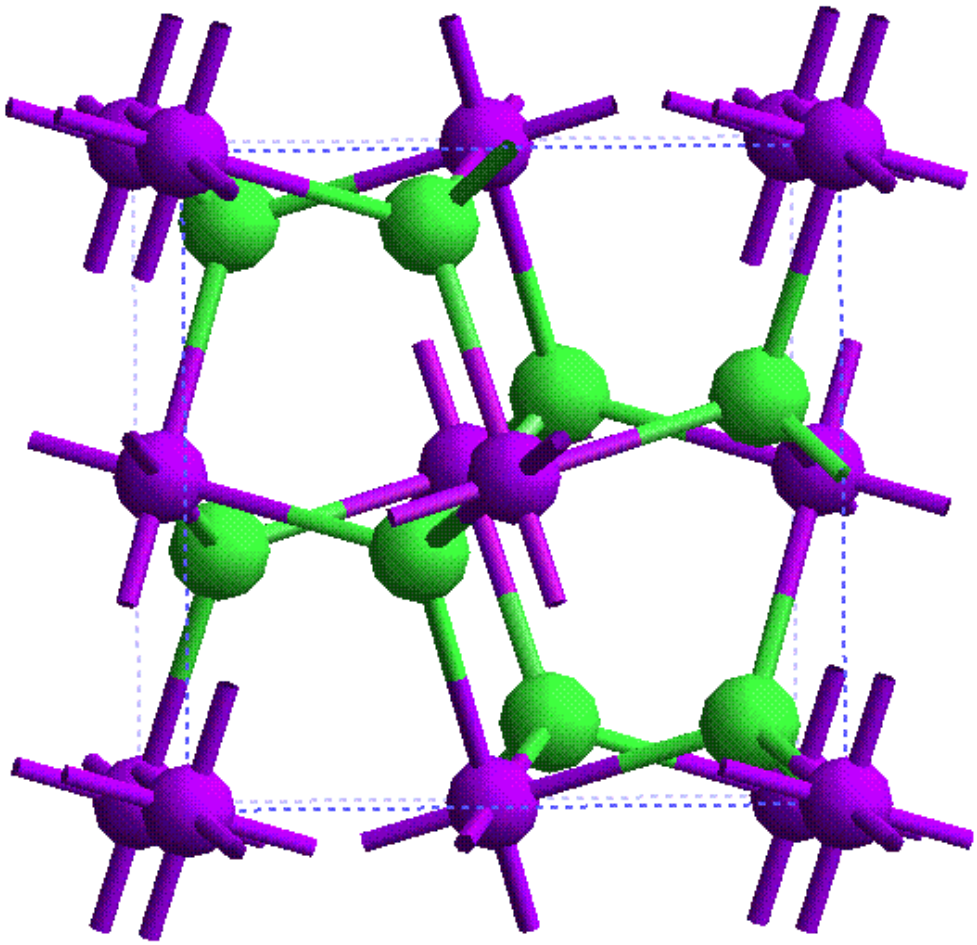

Figure 1.3: The crystal structure of sperrylite($PtAs_2$). Pt atoms are represented by purple while light green represent As atoms [1].

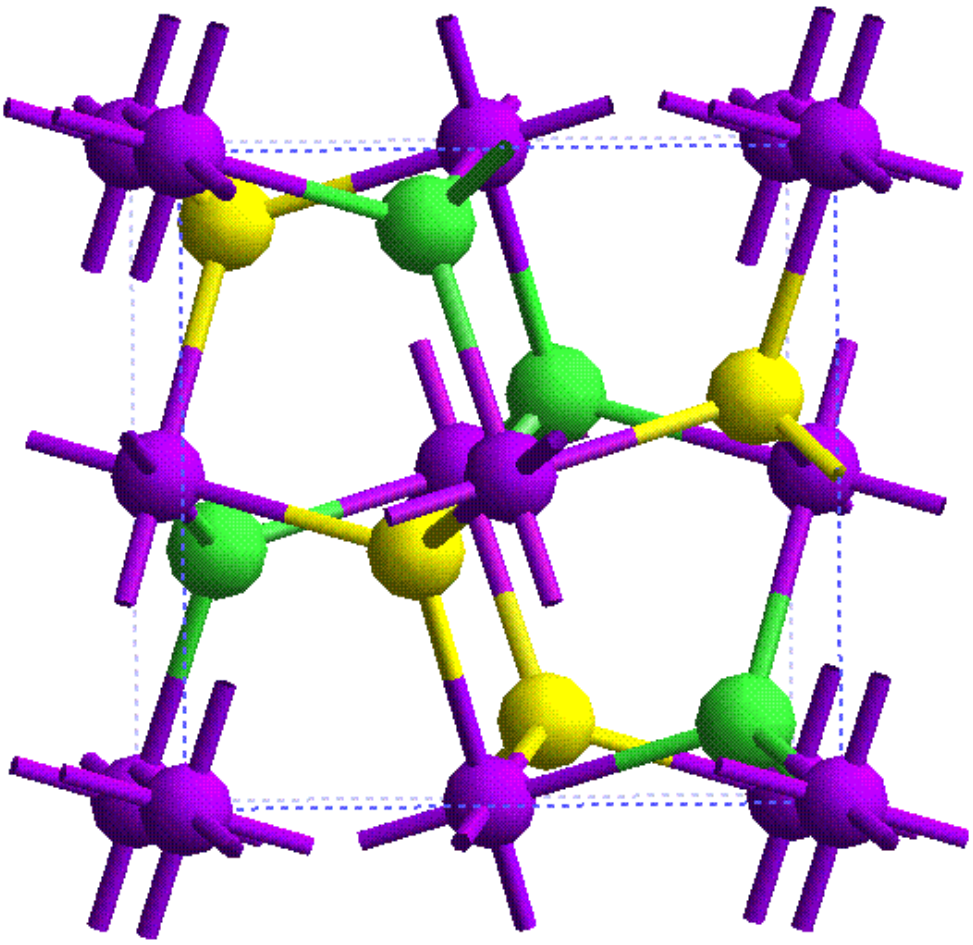

Figure 1.4: The cubic crystal structure of $Pt_4As_4S_4$. Pt atoms are represented by purple, As by light green and S atoms by yellow balls.

phases, have been prepared [1]. Many of these phases, such as the compounds $CuS_2$, $ZnS_2$ and $CdS_2$, require high pressure for their synthesis. In minerals such as gersdorffite (( Ni, Co, Fe)AsS) and cobatite((Co, Fe)AsS), ordering of the As and S atoms at lower temperatures can produce distortion of the pyrite structure and reduce the symmetry of the crystals. Whereas in pyrite the $MX_6$ octahedra share corners, in marcasite ($FeS_2$), platarsite ($Pt_4As_4S_4$) and loellingite ($FeAs_2$), they share edges and form chains of linked octahedra. In all three cases, the octahedra share edges lying in the (001) plane, thereby reducing the intermetallic distance across the shared edge in the direction parallel to the c-axis [1]. Platarsite (fig. 1.4 ) is another cubic mineral that has a structure very similar to that of sperrylite. The bonding geometry in the two minerals is almost identical, but the bond lengths in platarsite are significantly shorter than those of sperrylite. It has been confirmed that the As and S atoms are randomly distributed about the the octahedra surrounding the central platinum atoms. Platarsite contains metals atoms which are displaced along the c-axis so that short metal-metal distances alternate with longer ones. The space group of platarsite is Pa-3 where the four metal atoms are generated by Pt (4a):$(0,0,0),(0,\frac{1}{2},\frac{1}{2}),\ (\frac{1}{2},0,\frac{1}{2}),(\frac{1}{2},\frac{1}{2},0)$, and As (8c): $\pm(u,u,u),\pm(u+\frac{1}{2},\frac{1}{2}-u,-u)$ , $\pm(-u,u+\frac{1}{2},\frac{1}{2}-u)$, $\pm(\frac{1}{2}-u,-u,u+\frac{1}{2})$;S (8c): $\pm(u,u,u),\pm(u+\frac{1}{2},\frac{1}{2}-u,-u)$ , $\pm(-u,u+\frac{1}{2},\frac{1}{2}-u)$, $\pm(\frac{1}{2}-u,-u,u+\frac{1}{2})$; each have 50% occupancy and the additional symmetry positions (24d) $(x,y,z)$ with x = 0.31681, y = 0.09448 and z = 0.21363 , with lattice parameters a = 5.788Å [1].

## 1.2 Literature Review

Research on the sulphide minerals has long been undertaken to determine and better understand their properties, to clarify phase relations and hence the conditions under which these minerals form [15]. However, research on sulphides minerals has reached a particularly interesting point; even though over two decade ago processes whereby large scale concentration of sulphides actually form in nature were never directly observed, the discovery of active hydrothermal systems on ocean ridges now provide present day examples of large scale sulphide deposition [15].

Minerals of the platinum-group elements are notoriously difficult to identify due to the small size of the crystallites and the similarities of their optical properties . However, the confusion that has surrounded the qualitative

descriptions of these minerals has been resolved experimentally by X-ray diffraction(XRD) [16, 17] , transmission electron microscopy (TEM) [18] and Raman Spectroscopy [19]. Reflectance spectra and color values demonstrate the false-hood of the long-standing belief that cooperite resembles pyrrhotite, and originally braggite was described as cooperite. Where the PGM grains are only a few micrometers in size, the electron microprobe generally provides only semiquantitative data owing to possible problems with interference from surrounding sulfides. Similarly, analysis by other structurally sensitive techniques, such as X-ray diffraction, transmission electron microscopy, are quite difficult owing to problems with minerals separation and sample manipulation. Use of the proton microprobe for the analysis of sulfide minerals is now widely accepted [18, 20, 21, 22], and it has recently been applied to the analysis of PGMs . It is thus surprising that their optical characteristics, particularly those of cooperite and braggite, have remained ill-defined since their discovery. At present their identification with the microscope is uncertain, owing to erroneous and conflicting descriptive and quantitative data in the literature [19]. However, the reflectance spectra for cooperite PtS and braggite (Pt,Pd)S from the type locality at Potgietersrus, South Africa, were measured between 400 and 700nm [18]. The absorption curve from the x-ray diffraction indicate that PtS has a band gap 0.8 eV and the second one 1.4eV was also deduced [16]. In recent years, density-functional theory has provided a good or convenient first-principles framework for studying the properties of a wide range of transition metal sulphides including the (Pt, Pd, F, Ni, Fe) sulfides [3]. In particular, the equations of state (EOS), electronic structure, optical and bonding properties of $FeS_2$, have been studied using both TB-LMTO and planewave pseudopotential methods [23]. A new interatomic potential model derived recently [24], has also been used to study the structural and dynamic properties of $FeS_2$. In addition, the surface stability and reactivity of $FeS_2$ were successfully studied. These results compare very well with the experiment. The theoretical work done (plane wave) to date predicts the band gap of 0.06eV for PtS [3], which is quite different from 0.8eV obtained experimentally by Hulliger [16].

## 1.3 Objectives

During the last few years, there has been a great deal of interest especially in the mining industry in trying to understand the properties of PGMs

since they contain precious and base metals (eg platinum, palladium, nickel, chromium etc). As today's world of high technology advances, it is recognized that scientific explanation and understanding needs to precede commercial applications, and that intuition and the art of application will recede further. Today our understanding of technological application relies heavily on known scientific facts, and modelling is based on such facts. In the field of mineral exploration, knowledge of physics is widely applied, particularly as economic mineral deposits become increasingly difficult to discover. Flotation relies on the surface properties of minerals which render them amenable to extraction when bubbles are introduced into the pulp, thereby causing selected minerals to attach themselves to the bubble surface. By so-doing, the valuable minerals are removed from the gangue. Collectors are added to promote flotation by rendering the surface of minerals more amenable to separation.

The goal of our research has been spurred by the enormous technological relevance of mineral surfaces. Since surface properties are related to the electronic structure, our attention has focused on applying well-known theoretical methods to calculate bulk properties of PGMs with the intention that we will treat surfaces in the near future. The dissertation is, therefore, concerned with the study of bulk properties of a few representative platinum group minerals, viz. cooperite, braggite, sperrylite and platarsite in order to understand their structural, electronic and optical properties. We shall calculate the bulk properties of these minerals using ab initio density functional theory. In particular, we will adopt the plane wave pseudopotential approach [25] and the Tight Binding Linear Muffin Tin Orbitals (TB-LMTO) [26, 27, 28] and atomistic approach.

New sets of interatomic potentials that will best describe the bulk properties of PtS, $PdPt_3S_4$, $PtAs_2$ and $Pt_4As_4S_4$ will be derived from our ab initio results . These new sets of potential models will be used to study the bulk properties, temperature and pressure depedence of these four systems and the predicted values of the lattice constants, elastic constants and bulk moduli, will be compared with those of our ab initio method to validate the potential models. The bulk derived potential models, will then be used to study surface energies and stabilities of both the dry and hydrated surfaces of $PtAs_2$ and $Pt_4As_4S_4$ and subsequently to calculate the crystal morphologies and compare them with experiment.

## 1.4 Outline of the Study

The presentation in the dissertation has been arranged in the following manner:

Chapter 1 contains, a general introduction to the platinum group minerals followed by a literature survey.

In chapter 2 we describe in detail the electronic structure techniques and well as atomistic simulation approaches, in particular, the ab initio plane wave pseudopotential, the TB-LMTO, and atomistic methods.

In chapter 3 we present and discuss results for the structural parameters such as the equilibrium lattice constants and the bulk modulli.

In chapter 4, we discuss the results on the effect of pressure on the electronic and optical properties of these materials.

In chapter 5 the potentials models used in this study are presented. In addition, discussions of how the forces acting on the systems are calculated and methods by which potential models can be derived, are also included.

Chapter 6 contains, a detailed report of the results obtained from our simulations of surfaces of $PtAs_2$ and $Pt_4As_4S_4$, including hydration of the surafces and the calculations of the crystal morphologies.

Finally, chapter 7 summarises the main conclusions and sets out recommendations for future prospects.

# Chapter 2

# COMPUTATIONAL METHODS

## 2.1 Introduction

This chapter outlines the theory underlying the calculations on which the remainder of this thesis is based. We briefly review the fundamental aspects of two ab initio methods, the Planewave Pseudopotential method, which is used to calculate the internal coordinates of our PGM and the Tight-Binding Linear Muffin Tin Orbirtal (TB-LMTO) method, which is well suited for approximate but reliable studies of the electronic structures. Ab initio techniques, such as the methods described herein, attempt to solve the quantum mechanical equations governing the behaviour of the system studied. In the selection of methodologies we focus our attention exclusively on ab initio methods which are based on density functional theory, so that we are required to solve self-consistent field problem. In practice, the exact solution is intractable, hence a number of approximations must be made.

## 2.2 The Many- Body Schroedinger Equation

The aim of an ab initio method is to find the solution to the many-body Schroedinger equation for the system being studied. The first simplification that we make is the Born Oppenheimer approximation [29], whereby the electronic and nuclear degrees of freedom are separated. The justification for this is that the electrons are much less massive than the nuclei but experience

similar forces and therefore the electrons will respond almost instantaneously to the movement of the nuclei. Thus, the energy for a given nuclear configuration will be that of the ground state of the electrons in that configuration. The equation we must solve is, therefore,

$$H\Psi = E\Psi \tag{2.1}$$

where $\Psi$ is the many body wavefunction for the N electronic eigenstates, being an anti-symmetric function of the electronic coordinates $\{ \mathrm{r}_i\colon\ \iota = 1...\mathrm{N}\}$, and E is the total energy. The Hamiltonian H operator is given by

$$H = \sum_i -\frac{\hbar^2}{2m_e}\nabla^2_{r_i} + V_{ext}(\{R_I\}) + V_{e-e}(\{r_i\}), \tag{2.2}$$

where $\mathrm{V}_{ext}$ is the external potential imposed by the nuclear configuration $\{\mathrm{R}_I\}$ and $\mathrm{V}_{e-e}$ is the electron-electron coulombic interaction.

In principle, this equation may solved to arbitrary accuracy by representing $\Psi$ as a direct product wavefunction and diagonalising the Hamiltonian. The total energy E can then be written as

$$E[\Psi] = \frac{\langle \Psi \mid H \mid \Psi \rangle}{\langle \Psi \mid \Psi \rangle} \tag{2.3}$$

where the variational principle states that the ground state is that given by minimisation of E over all possible $\Psi(\{\mathrm{r}_i\})$. Quantum Monte Carlo techniques may then be used to evaluate $\mathrm{E}[\Psi]$ [30] for a given wavenfunction and perform the minimisation over all possible wavefunction configurations [31, 32, 33]but these increase the computational cost still further. The following sections of this chapter describe approximations which allow $H$ and $\Psi$ to be written in a simpler form, allowing the ground state energy of a system to be obtained with far less computational effort, and thus making feasible the calculations presented in later chapters of this dissertation.

## 2.3 Density Functional Theory

Density Functional Theory (DFT) has proved to be hugely successful in predicting and explaining the properties of materials from first principles.

This elegant method relies on the fact that the ground state energy of a system is a functional of the ground state charge density only . The Kohn-Sham formalism expresses the density in terms of a fictitious set of non-interacting orbitals, allowing the ground state density and energy to be found as long as there is a reasonable ( practical) approximation for the so-called exchange and correlation energy.

The idea of using the electron density as the fundamental entity of a quantum mechanical theory was first suggested by Thomas and Fermi [34, 35], in the early days of quantum mechanics. However, in the subsequent decades, the Hartee-Fock approach was developed and first applied to small molecular systems rather than the Thomas-Fermi approach. Calculations on realistic solid state systems were then out of reach. It was not until the 1960s that an exact theoretical framework called Density Functional Theory (DFT) was formulated by Hohenberg, Kohn and Sham [36, 37], providing the foundation for accurate calculations. Ealier Slater [38] had already taken ideas from the theory of a homogeneous electron gas to simplify Hartee-Fock theory to a point where electronic structure calculations, on solids became feasible. Slater's work, which led to the so-called X$\alpha$ method [39], has contributed tremendously to the development of electronic structure calculations. Today, Slater's X$\alpha$ method can be seen as an early, simplified form of DFT. In contrast to the Hartree-Fock picture, which begins conceptually with a description of individual electrons interacting with nuclei and all other electrons in the system, DFT starts with a consideration of the entire electrons system. The total energy of a system is expressed as a functional of the total electron density, which in turn depends on the positions of the atoms

$$E = E[\rho(\mathbf{r}), \mathbf{R}_\alpha]. \tag{2.4}$$

$\mathrm{R}_\alpha$ denotes the position of all atoms $\alpha$ in the system under consideration. A critical aspect of the Kohn-Sham formulation of DFT is the decomposition of the total energy into three terms, as given below in equation (2.5)

$$E[\rho] = T_0[\rho] \ + \ U[\rho] \ + \ E_{xc}[\rho\,]. \tag{2.5}$$

The first term of eq. (2.5) corresponds to the kinetic energy

$$T_0[\rho\,] \ = \sum_i n_i \int \psi_i^*(r)[-\frac{\hbar^2}{2m}\nabla^2]\psi_i(\mathbf{r})d\mathbf{r} \tag{2.6}$$

of non-interacting, electrons which are defined such that their corresponding one-particle wave functions generate the exact density of the interacting many-electron system,

$$\rho(\mathbf{r}) = \sum_i n_i \left|\psi(\mathbf{r})\right|^2 . \tag{2.7}$$

The second term on the right hand side of equation (2.5) represents the Coulombic energy. This term is purely classical and contains the electrostatic energy arising from the Coulombic attraction between the electrons and nuclei, the repulsion between all electronic charge and the repulsion between the nuclei i.e.

$$U[\rho] = U_{en} \; + \; U_{ee} \; + \; U_{nn}$$

$$= \sum_\alpha Z_\alpha \int \frac{\rho(\mathbf{r})}{|\mathbf{r} \; - \; \mathbf{R}_\alpha)|} d\mathbf{r} \; + \; \int\int \frac{\rho(\mathbf{r})\rho(\mathbf{r}')}{|\mathbf{r} \; - \; \mathbf{r}'|} d\mathbf{r} d\mathbf{r}' + \sum_{\alpha\alpha'} \frac{Z_\alpha Z_{\alpha'}}{|\mathbf{R}_\alpha \; - \; \mathbf{R}_{\alpha'}|}, \tag{2.8}$$

where $Z_\alpha$ is the atomic number of atom $\alpha$ at position $R_\alpha$. The summations extend over all atoms, and the integrations over all space. The third term of equation (2.5), includes all remaining complicated electronic contributions to the total energy and is called the exchange-correlation energy, $E_{xc}$. The more important of these two contributions is the exchange term. The exchange-correlation energy reduces the interaction between two electrons with same spin, such that electrons behave like they are surrounded by a positive" exchange hole". This decomposition is formally exact, but the actual expressions for the many-body exchange and correlation interactions are unknown. As an approximation, the exchange correlation energy is taken from known results of an interacting electron system of constant density, the "homogeneous electron gas", and it is assumed that the exchange and correlation effects are not dependent on the inhomogeneities of the electron density away from a reference point, $\mathbf{r}$. Thus the local electron density can be used to evaluate the exchange and correlation effects of a volume element around $\mathbf{r}$.

$$E_{xc}[\rho(\mathbf{r})] = \int \rho(\mathbf{r}) \mu_{xc}[\rho(\mathbf{r})] d\mathbf{r} \tag{2.9}$$

$$\mu(\mathbf{r}) = \frac{\delta E_{xc}[\rho]}{\delta \rho(\mathbf{r})}$$

### 2.3.1 The Local Density Approximation

The Kohn-Sham theorem, which is the central part of DFT, states that the total energy is at its minimum for the ground state density so that the total energy is stationary with respect to first-order variations in the density i.e $\partial E[\rho]/\partial \rho$

As a consequence of the Kohn-Sham theorem, the exchange-correlations energy depends only on the electron density. As a simple but, as it turns out, suprisingly good approximation, the exchange-correlation energy is assumed to depend only on the local electron density around each volume element d$\mathbf{r}$. This is called the local density approximation (LDA), namely

$$E_{xc}[\rho\,] = \int \rho(\mathbf{r}) \epsilon_{xc}[\rho(\mathbf{r})] d\mathbf{r}\ , \tag{2.10}$$

where $\epsilon_{xc}[\rho(\mathbf{r})]$ is the exchange-correlation energy density for a homogeneous electron gas of density $\rho(\mathbf{r})$. For practical calculations, $\epsilon_{xc}[\rho]$ is expressed as an analytical function of the electron density. There are different analytical forms with different coefficients in their representation of the exchange-correlation terms. These coefficients are not adjustable parameters, but rather they are determined through first-principles theory. Hence, the LDA is a first principles approach in the sense that the quantum mechanical problem is solved without any adjustable, system-dependent parameters.

### 2.3.2 Solution of the Kohn-Sham Equation

The Kohn-Sham equation's has the form of a one-particle eigenvalue equations:

$$H\Psi_i(\mathbf{r}) \ = \varepsilon_i\, \Psi_i(\mathbf{r}), \tag{2.11}$$

$\epsilon_i$ and $\Psi_i$ are the eigenvalues and eigenstates for the i-the state, with the effective one-particle Hamiltonian operator

$$H = -\frac{\hbar^2}{2\,\nabla^2} \ + \ V_c(\mathbf{r}) \ + \ \mu_{xc}(\mathbf{r})\ . \tag{2.12}$$

Following standard mathematical techniques for solving eigenvalue problems, one can expand the unknown solutions $\Psi_i(\mathbf{r})$ in a set of known functions, $\Phi_j(\mathbf{r})$, with unknown linear coefficients, $c_{ij}$ ,

$$\Psi_i(\mathbf{r}) \;=\; \sum_j c_{ij}\Phi_j(\mathbf{r}). \tag{2.13}$$

These coefficients are determined through the variation of the following matrix

$$(H \;-\; \varepsilon S)C \;=\; 0\;. \tag{2.14}$$

H and S are the so-called Hamiltonian and overlap matrices with the following matrix elements

$$H_{ij} \;=\; \int \Phi_i^*(\mathbf{r})[-\frac{\hbar^2}{2m\,\nabla^2} \;+\; V_c(\mathbf{r}) \;+\; \mu_{xc}(\mathbf{r})]\Phi_j(\mathbf{r})d\mathbf{r} \tag{2.15}$$

$$S_{ij} \;=\; \int \Phi_i^*(\mathbf{r})\Phi_j(\mathbf{r})d\mathbf{r} \qquad . \tag{2.16}$$

In standard density functional calculations one diagonalises the matrix (H - $\varepsilon$S) to find the eigenvalues and coefficients (eigenvectors). The dimension of the matrices is determined by the number of basis functions in the expansion (2.13). Both the Coulombic potential and the exchange-correlation potential in the Kohn-Sham equations (2.11), depends on the charge density, which is constructed from the one-particle wave functions. This problem is, therefore, solved by an iterative, self-consistent procedure as shown in figure 2-1.

### 2.3.3 Periodic Boundary Conditions and Bloch's Theorem

Periodic boundary conditions allow an infinite crystal to be studied at a calculational cost that is determined by the number of atoms in the unit cell. Defect structures, surfaces, and even molecules can also be studied with periodic boundary conditions by generating supercells that contain the object of interest.

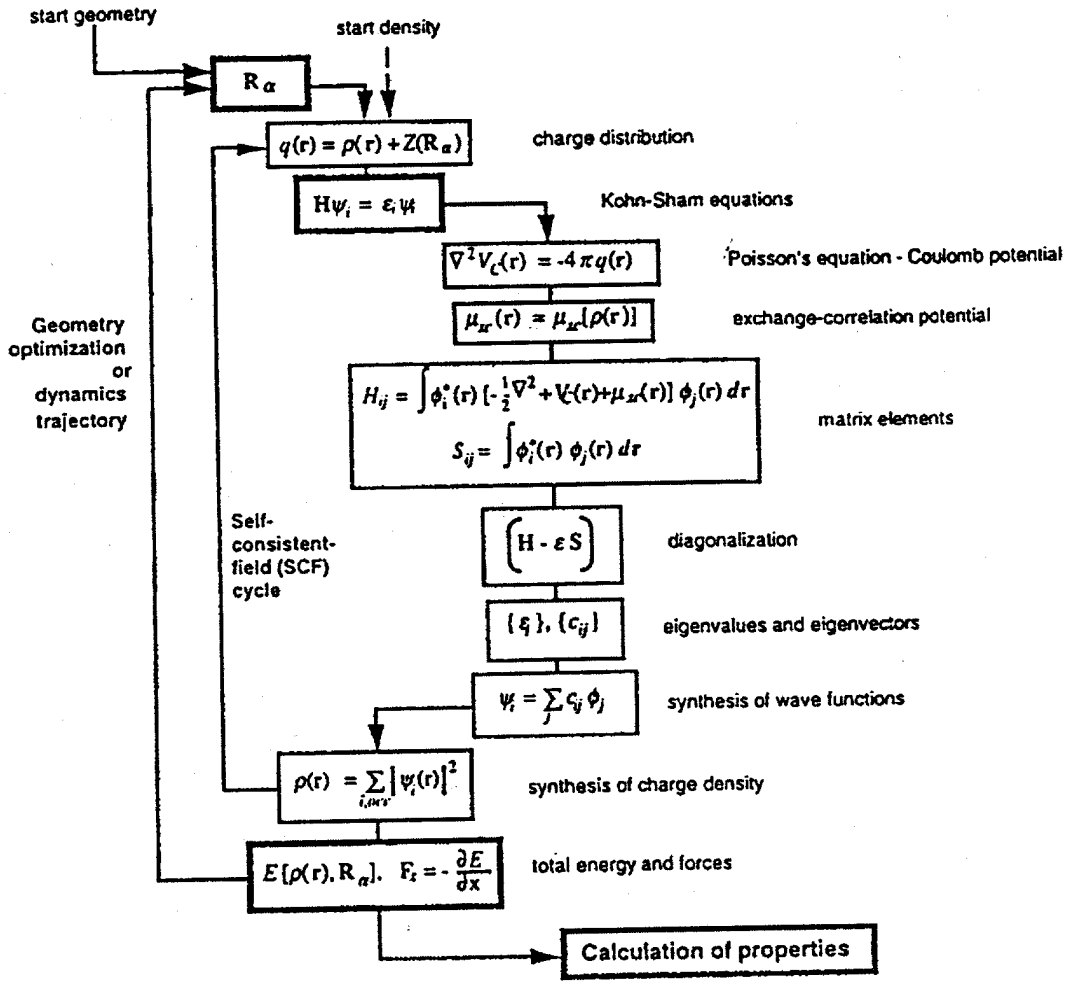


Figure 2.1: calculations. The outer cycle represents the geometry optimization or other manipulation of the geometry such as energy minimization procedure. The inner cycle is the self-consistency procedure to solve procedure to solve the Kohn-Sham equation. E. Wimmer [57]

In the study of periodic systems, extensive use is made of the concept of the reciprocal lattice. The unit cell for the calculation can be defined in terms of three real-space primitive translation vectors $\mathrm{R}_{\mathbf{1}}$, $\mathrm{R}_{\mathbf{2}}$, and $\mathrm{R}_{\mathbf{3}}$. A general vector in the Bravais lattice can be written as:

$$R = n_1 R_1 + n_2 R_2 + n_3 R_3 \tag{2.17}$$

where $\mathrm{n}_1$, $\mathrm{n}_2$, and $\mathrm{n}_3$ are arbitrary integers. A set of primitive reciprocal-space translation vectors can be defined, which obey:

$$R_i . G_j = 2\pi \delta_{ij}, \tag{2.18}$$

for i and j in the range 1 to 3. $\mathrm{G}_1$ is given explicitly by:

$$G_1 = 2\pi \frac{R_1 X R_3}{R_1 . (R_2 X R_3)}. \tag{2.19}$$

Similar expressions hold for $\mathrm{G}_2$ and $\mathrm{G}_3$, which can be obtained by cyclic permutation of the subscripts. A general point in the reciprocal-space lattice is given by:

$$G = n_1 G_1 + n_2 G_2 + n_3 G_3, \tag{2.20}$$

where again $\mathrm{n}_1$, $\mathrm{n}_2$, and $\mathrm{n}_3$ are arbitrary integers.

Solutions of the Schroedinger equation for a periodic structure are known to obey Bloch's theorem which states that all such solutions can be expressed in the form

$$\psi_k(\mathbf{r} - \mathbf{R}_v) = e^{ik.R_v} \psi_{\mathbf{k}}(\mathbf{r}), \tag{2.21}$$

where $\mathbf{R}_v$ is a Bravais lattice vector and k an abitrary point in k-space. On invoking Bloch's theorem and writing the allowed wavefunctions as Bloch functions, the Schroedinger equation can be regarded as restricted to a single unit cell, with the extended nature of the orbitals described by a boundry condition at the edges of the cell. Bloch functions are characterized by a discrete label, called the 'band-index', plus a continuous label, the Bloch wavevector k (ordinarily restricted to the first Brillouin zone).

### 2.3.4 k-space sampling

Electronic states are allowed only at the set of k points which are determined by the boundary conditions that apply to the bulk solid. The density of allowed k points is proportional to the volume of the solid. The infinite number of electrons in the solid are accounted for by an infinite number of k points, and only a finite number of electronic states are occupied at each k point. The Bloch theorem changes the problem of calculating at an infinte number of electronic wave functions to one of calculating a finite number of electronic wave functions at an infinte number of k points. The occupied states at each k point contribute to the electronic potential in the bulk solid so that, in principle, an infinte number of calculations are needed to compute this potential . However, the electronic wave functions at k points that are very close together will be almost identical. Hence it is possible to represent the electronic wave functions over a region of k space by the wave functions at a single k point. In this case the electronic states at only a finite number of k points are required to calculate the electronic potential and hence determine the total energy of the solid. Methods have been devised for obtaining very accurate approximations to the electronic potential and the contribution to the total energy from a filled electronic band by calculating the electronic states at special sets of k points in the Brillioun zone [40, 41, 42, 43]. Using these methods, one can obtain an accurate approximation for the electronic potential and the total energy of an insulator or a semi-conductor by calculating the electronic states at a very small number of k points. The electronic potential and total energy are more difficult to calculate if the system is metallic because a dense set of k points is required to define the Fermi surface precisely.

The magnitude of any error in the total energy due to an inadequacy of k-point sampling can always be reduced by using a denser set of k points. The computed total energy will converge as the density of k points increases, and the error due to the k-point sampling then approaches zero. In principle, a converged electronic potential and total energy can always be obtained provided that the computational time is available to calculate the electronic wave functions at a sufficiently dense set of k points.

## 2.4 The Plane-Wave Pseudopotential Method

This method uses a plane wave expansion for the wavefunctions and a pseudopotential representation of the ions. The convergence of this expansion is controlled by a single parameter, namely the highest frequency at which the series is terminated. The solution of the Kohn-Sham equation for a periodic system has thus been expanded in plane waves, which amounts essentially to a three-dimensional Fourier series. The control of the basis set convergence by a single parameter is a very appealing feature, particularly when compared with the tedious task of basis set improvements with Gaussians or other localised functions. Mathematically, a plane wave expansion can be written as

$$\Psi_k^i(\mathbf{r}) = \sum_{j=()}^{\max} x_j(k) e^{i(k+G_j).\mathbf{r}}. \tag{2.22}$$

The vector G is a reciprocal lattice vector. It defines the "frequency", i.e. the ability to describe spatial variations of a wave function. A large value for the cutoff $G_{max}$ in plane wave basis means the ability to resolve rapid variations of the wave functions and charge density. The plane wave basis set can be truncated to include only plane waves that have kinetic energies less than some particular cutoff energy. The sharp structures of wave functions near atomic nuclei are obviously a problem for a plane wave expansion. A radical way to eliminate this difficulty is the use of pseudopotentials, since plane waves are intimately linked to pseudopotentials. In a plane wave expansion, each basis function is no longer associated with a particular atom, but is defined over the entire unit cell. The number of plane waves required to reach a certain accuracy depends primarily on the size of the unit cell and not directly on the number of atoms. Periodic systems with a fairly uniform distribution of atoms are particularly well suited for a pseudopotential plane wave approach.

### 2.4.1 The Pseudopotential Approximation

It is often convenient to use a pseudopotential [44, 45, 46] to represent the core electrons, so reducing the number of electrons to be dealt with explicitly. The core electrons on different atoms will not overlap significantly, so their properties will be fairly independent of environment. Most properties of solids are governed by the valence orbitals, as demonstrated by the similarity

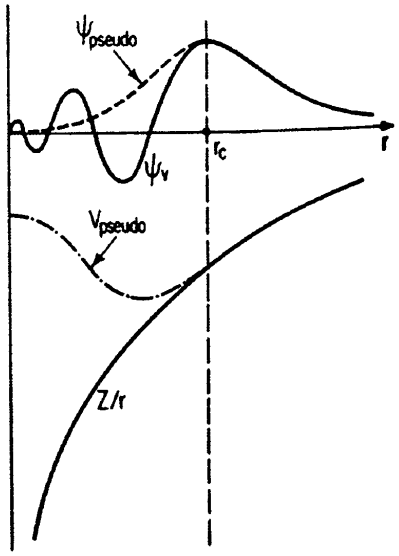


Figure 2.2: Schematic illustration of how the true potential and wavefunction are modified in the pseudopotential approach [66].

of atoms in the same group of periodic table. Thus a good representation of the valence electrons is vital for an accurate description of chemical and physical processes in solids. A problem arises from the fact that the valence wavefunctions usually have rapid oscillations near the ion core so that a large number of plane waves are required to accurately represent the true valence wavefunction.

In the pseudopotential approach only the valence electrons are explicitly considered. They move in a modified potential which includes the Pauli repulsion of the core electrons as well as the strongly attractive nuclear potential. This modified potential is termed the pseudopotential. The pseudopotential is constructed so that the modified electron wavefunctions to match the true potential wavefunction and outside the ion core. As the valence electrons are not now forced to be orthogonal to the core states, the rapid oscillations are removed, hence reducing the number of plane waves needed to expand these wavefunctions. This is schematically illustrated in fig. 2.2.

A pseudopotential is constructed to reproduce the atomic properties of the element, including phase shifts on scattering across the core. These phase

shifts will be different for different angular momentum components and so in general, a pseudopotential must be non-local, with projectors for different angular components. The pseudopotential is often represented using the form

$$V_{NL} = \sum |lm\rangle V_l \langle lm| \tag{2.23}$$

where $| \ lm\rangle$ are spherical harmonics and $V_l$ is the pseudopotential for angular momentum $l$. The majority of the pseudopotentials currently used in electronic-structure are generated from all electron atomic calculations. However, a pseudopotential that uses the same potential for all the angular momentum components of the wave function is called a local pseudopotential. The norm-conserving pseudopotential, are an example of the non-local pseudopotential, and uses a different potential for each angular momentum components of the wave function.

### 2.4.2 Norm conserving pseudopotential

In total-energy calculations, the exchange-correlation energy of the electronic system is a function of the electron density. If the exchange-correlation energy is to be desired accurately, it is necessary that outside the core regions the pseudo wave functions and real wave functions be identical, not just in their spatial dependences but also in their absolute magnitudes, so that two wave functions generate identical charge densities. Adjustment of the pseudopotential to ensure that the integrals of the squared amplitudes of the real and pseudo wave functions inside the core region. One of the first attempts to construct pseudopotentials of this type was by Starkloff and Joannopoulos [47, 48]. They introduced class of local pseudopotentials that described the valence energies and wave functions of many heavy atoms accurately.

In general, the scattering from the ion core is best described by nonlocal pseudopotential that uses a different potential for angular momentum component of the wave function. A match of the pseudo and real wave functions outside the core region also assures that the first-order energy dependence of the scattering is accurately described over a wide range of energy. A method for the construction of pseudoptentials that corrects even the higher-order energy dependence of the scattering has recently been introduced by Shirley et al. [49]. Local and nonlocal pseupotentials of these types are correctly termed ab initio or norm conserving and are capable of describing the scat-

tering due to the ion in a variety of atomic environments, a property referred to as transferability.

### 2.4.3 Ultrasoft pseudopotentials

The idea of ultrasoft pseudopotentials as put by Vanderbilt [50] is that the relaxation of the norm-conserving condition can be used to generate much softer potentials. In this scheme the pseudo-wave-functions are allowed to be soft as possible within the core region, so that the cutoff energy can be reduced dramatically. Technically, this is achieved by introducing a generalized orthonormality condition. The electron density given by the squared moduli of the wave functions has to be augmented in the core region in order to recover the full electronic charge. The electron density is thus subdivided into (i) a smooth part that extends throughout the unit cell, and (ii) a hard part localized in the core regions. The augmented part appears in the density approach is applied to wavefunctions. Ultrasoft potentials is much softer than the norm conserving potential. The ultrasoft potentials generation algorithm guarantees good scattering properties over a pre-specified energy range, which results in much better transferability and accuracy of pseudopotentials. It usually also "shallow" core states as valence by including multiple sets of occupied states in each angular momentum channel. This also adds to high accuracy and transferability of the potentials, although at a price of computational efficiency.

### 2.4.4 The Linear Combination of Atomic Orbital (LCAO ) Approximation

The LMTO method is similar to LCAO which will be discussed. A first general approach to solving the crystal-Schroedinger equation is based on the Linear Combination of Atomic (LCAO) method. In this method, the Bloch orbitals of the crystal are expanded in fixed orbitals, each of which is associated with a specific atom or ion of the crystal. Given such orbitals, $\chi_j(\mathbf{r} - R_v)$, a Bloch function is written as

$$\boldsymbol{\chi}_{j\mathbf{k}}(\mathbf{r}) = \sum_{\nu} e^{i\mathbf{k}.\mathbf{R}_\nu} \boldsymbol{\chi}_j(\mathbf{r} - \mathbf{R}_{\boldsymbol{\nu}}), \tag{2.24}$$

where the summation extends over the Bravais lattice vectors $\{R_\nu\}$ and j is a combination of quantum numbers characterizing the orbital $\chi$ i.e the angular momentum, principal quantum number and magnetic quantum number. The Bloch functions defined above form a basis set to calculate the eigenfunctions of the crystal-Schroedinger equation. To obtain these eigenfunctions, we use the expansion

$$\Psi_{\mathbf{k}}(\mathbf{r}) = \sum_j \alpha_j(\mathbf{k})\chi_{j\mathbf{k}}(\mathbf{r}), \tag{2.25}$$

and determine the coefficients variationally. This leads to the following secular equation for the coefficients,

$$\sum_j \{\int d\mathbf{r}\chi^*_{i\mathbf{k}} H_{ij}\chi_{j\mathbf{k}} - \varepsilon_{\mathbf{k}} \int d\mathbf{r}\chi^*_{i\mathbf{k}}\chi_{j\mathbf{k}}\}\alpha_j(\mathbf{k}) = 0 \tag{2.26}$$

which must hold for all i. The eigenvalues $\varepsilon$ and the eigenvectors $\alpha_j(k)$ can now be obtained by solving the generalized eigenvalue (2.23).

The convergence properties of (2.23) with respect to the orbital index j depends strongly on the choice of the set of orbitals. Ordinarily, quite large LCAO expansions are necessary to attain accuracy.

The tight-binding linear muffin-tin orbital (TB-LMTO) methods was originally formulated by transforming the basis of the conventional linear muffin-tin orbitals into a new basis of the tight-binding linear muffin-tin orbital [51]. The physical motivation for this transformation came from the idea of screened electrostatic multipole fields. In the screened LMTO theory, real constants $\alpha_{RL}$ are introduced, defined for each RL-index, traditionally called screened constants. The screening matrix $\alpha_{RL,R'L'} = \alpha_{RL}\delta_{RR'LL'}$ characterizes the corresponding LMTO representation. Most of the calculations using the LMTO method have been performed within the so-called atomic sphere approximation (ASA) [27]. This approximation is as follows: (i) spherically symmetry potentials inside slightly overlapping, space-filling atomic (Wigner-Seitz) spheres centered at the individual nuclei are used, and (ii) the electronic kinetic energy outside the Wigner-Seitz spheres is neglected. Therefore, ASA removes the inconvenient interstitial region and replaces integrals over the whole space by a sum over Wigner-Seitz spheres which may be considered as approximation to the true Wigner-Seitz cells. The overlap of the atomic sphere is neglected. The details are discussed in the next paragraphs.

### 2.4.5 The Tight-Binding (TB) Approximation

If we can consider the energy levels in the isolated atom and then bring the atoms together and modifying the energy levels is known as the 'tight-binding approximation' because we have started from tightly bound electrons in the atoms.

The application of the TB method to bulk systems is easily introduced by first considering a lattice of atoms with overlapping s orbitals, $\psi_s$, and corresponding free atomic energy levels, $E_s$. Generalizing the LCAO method for the diatomic molecule to a periodic lattice of $N$ atoms, we look for a crystal wave function, $\psi_k$, that is a linear combination of the atomic orbitals, namely

$$\psi_k(\mathbf{r}) = N^{-1/2} \sum_R e^{ik\cdot R} \psi_s(\mathbf{r} - R) \tag{2.27}$$

The phase factor automatically guarantees that $\psi_k(\mathbf{r})$ satisfies Bloch's theorem

$$\psi_k(\mathbf{r} + R) = e^{ik\cdot R} \psi_k(\mathbf{r}) \tag{2.28}$$

since

$$\psi_k(\mathbf{r} + S) = e^{ik\cdot S} N^{-1/2} \sum_{R'=R-S} e^{ik\cdot R'} \psi_s(\mathbf{r} - R') = e^{ik\cdot S} \psi_k(\mathbf{r}) \tag{2.29}$$

The Schroedinger equation

$$H\psi_k = E_k \psi_k \tag{2.30}$$

then has the solution

$$E_k = \frac{\int \psi_k^* H \psi_k dr}{\int \psi_k^* \psi_k dr} \tag{2.31}$$

Making the usual assumption that the crystalline potential, V, is given by the sum of overlapping atomic potentials, $v$, we have

$$\int \psi_k^* H \psi_k dr = N^{-1} \sum_{R,S} e^{ik\cdot(R-S)} X \int \psi_s(\mathbf{r}-S) \left[ \frac{-\mathrm{h}^2}{2m} \nabla^2 + \sum_T v(\mathbf{r} - T) \right] \psi_s(\mathbf{r}-R) d\mathbf{r} \tag{2.32}$$

and

$$\int \psi_k^* \psi_k d\mathbf{r} = N^{-1} \sum_{R,S} e^{ik\cdot(R-S)} \int \psi_s(\mathbf{r}-S)\psi_s(\mathbf{r}-R)d\mathbf{r} \tag{2.33}$$

since $\psi_s^* = \psi_s(\mathbf{r})$ as $\psi_s$ is real. Neglecting the three centre integrals corresponding to $R \neq S \neq T$ in eq (2.32 ) and the overlap integrals, $R \neq S$, in eq. (2.33 ), we find the TB expression for the eigenvalues $E_k$, namely

$$E_k = E_s + \int \psi_s(\mathbf{r}) \left[\sum_R v(\mathbf{r}-R)\right] \psi_s(\mathbf{r})d\mathbf{r} + \sum_R e^{ik\cdot R} \int \psi_s(\mathbf{r}) v(\mathbf{r}) \psi_s(\mathbf{r}-R)d\mathbf{r} \tag{2.34}$$

### 2.4.6 Muffin-Tin (MT) Orbitals.

The convergence of the LCAO method, which is based on free-atom orbitals, is usually slow for bulk materials. This led Anderson [52] to introduce atomic-like obitals that are more appropriate for close-packed systems, the so-called MTOs. These are derived from the MT approximation to the potential in close-packed systems which is essentially spherically symmetric (fig. 2.3) inside the inscribed spheres about the atoms. The MTA takes only the spherically symmetric part $\nu(\mathbf{r})$ for the potential inside atom-centered muffin-tin spheres and a flat potential outside the MT spheres, of which the value is the so-called muffin-tin zero $V_{MTZ}$.

The MT potential $v_{MT}(r)$ is shown in fig. 2.4. The electrons in the interstitial region ($r \geqslant S_{MT}$) behave as free electrons with kinetic energy $\kappa^2 \equiv \epsilon - v_{MTZ}$.

The Schroedinger equation for an electron moving in the potential from an isolated $MT$ well embedded in the flat potential $v_{MTZ}$, is given by:

$$[-\nabla^2 + v_{MT}(r) - \kappa^2]\psi_L(r,\epsilon) = 0 \tag{2.35}$$

where $L = lm$ represent the angular character. The MTOs are related to the solutions of this equation, for $\kappa^2 = 0$ namely

$$[-\nabla^2 + v_{MT}(\mathbf{r})]\psi_L(\mathbf{r}) = 0 \tag{2.36}$$

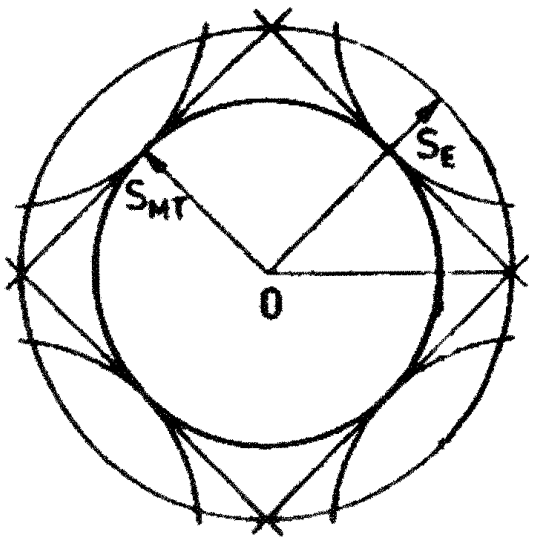


Figure 2.3: The Muffin-tin sphere of radius,$s_{MT,}$and the inscribed sphere of radius $s_E$ in the MTA.

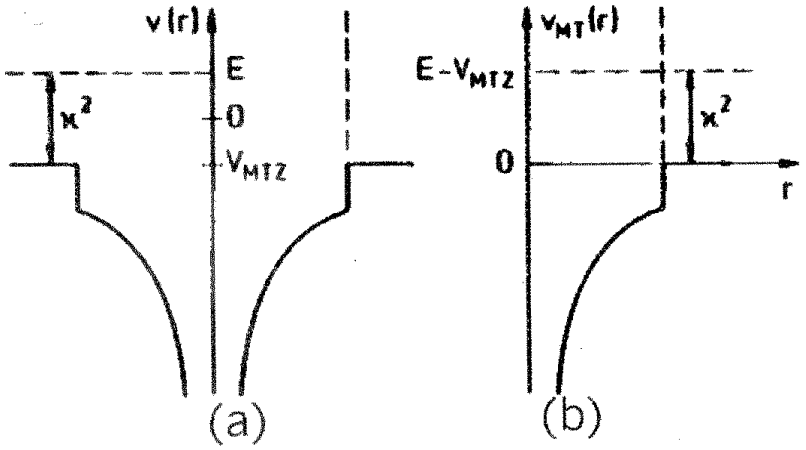


Figure 2.4: (a) The muffin-tin part of the crystal potential $v(r)$ and (b) the muffin-tin potential $v_{MT}(r)$.

Writing

$$\psi_L(\mathbf{r}) = \psi_l(\mathbf{r})Y_L(\widetilde{r}) \tag{2.37}$$

where $\mathrm{Y}(\widetilde{r})$ is spherical harmonic, the radial function $\psi_L(\mathbf{r})$ inside the MT may be obtained by numerical integration of the radial Schroedinger equation

$$[-\frac{d^2}{dr^2} + \frac{l(l+1)}{r^2} + v_{MT}(r)]r\psi_l(r) = 0. \tag{2.38}$$

outside the MT well the resultant Laplace equation (2.39) in the interstitial region of a regular solution at $r = 0, J(r) = \frac{1(r/w)^l}{2l(2l+1)}$, and $K_l(r) = \left(\frac{w}{r}\right)^{l+1}$ ,which are regular at infinity. The scaling constant, $w$, makes the solutions dimensionless, and is normally equal to the Wigner-Seitz radius.

$$\left[\frac{d^2}{dr^2} + \frac{l(l+1)}{r^2}\right] r\psi_l(\epsilon, r) = 0. \tag{2.39}$$

The solution for the radial Schroedinger equation inside the MT potential, $\psi_l$, must be connected smoothly onto this linear combination of $J_l$ and $K_l$ as illustrated by fig. 2.5, essentially matching the logarithmic derivative of solutions inside and outside the MT spheres at the sphere boundary ($r = s_{MT}$).

Because the MTOs are the 'natural' basis for solving the Muffin tin potential, a linear combination of MTOs leads to a much more rapid convergence than using AOs. In practice, the MTOs depend on the energy, as shown in (2.35). However, this energy dependence can be removed through linearizing the equation with respect to energy. The resultant linear MTO method (LMTO) has an equation that is similar to that of the LCAO methods, equation (2.24). However, in addition to faster convergence, the matrix elements of LMTO theory also have appealing canonical form. They can be shown to factorise into a contribution that depends on the chemistry (i.e. the nature of the individual MT potential and the structure) through the famous canonical structure constants [27].

For the case $k^2 \neq 0$, the solutions are given by,

$$\left[\frac{d^2}{dr^2} + \frac{l(l+1)}{r^2} - k^2\right] r\psi_l(\epsilon, r) = 0 \tag{2.40}$$

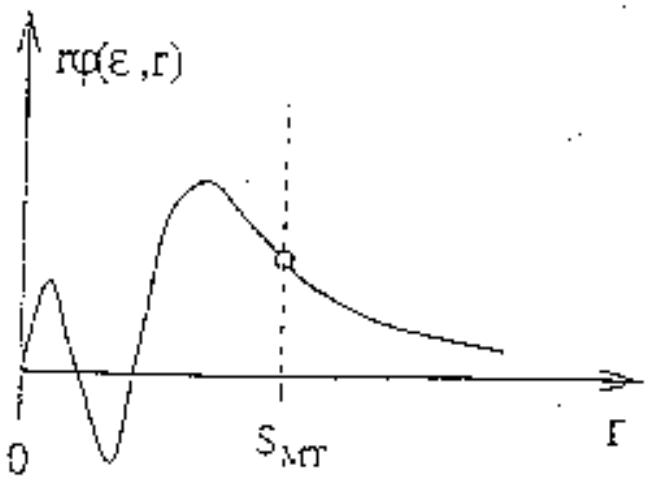


Figure 2.5: Matching of the radial wavefunction at the sphere boundary [191].

which is the Helmholtz equation being a linear combination of the spherical Bessel funcion $j_l(kr)$,which is regular at $r = 0$, and the spherical Neuman function $n_l(kr)$, given by

$$j_l(kr) \rightarrow \frac{(kr)^l}{(2l+1)!!} \tag{2.41}$$

$$n_l(kr) \rightarrow -\frac{(2l-1)!!}{(kr)^{l+1}} \tag{2.42}$$

when $kr \rightarrow 0$, where !!=1.2.3... and -1!!=1.

The next step is to find the solution of the one-electron Schrodinger for a crystal potential consisting of an array of MT potential at site R, which is a superposition of the muffin-tin orbitals(MTOs)

$$\psi(r) = \sum_{R,L} a_{R,L} \Psi_{R,L}(\epsilon, r) \tag{2.43}$$

where the MTO $\Psi_{R,L}(\epsilon, r)$ are defined by

$$\Psi_{R,L}(\epsilon,r)=\left\{\begin{array}{c} N_{Rl}(\epsilon)\varphi_l(\epsilon,r-R)+P_{Rl}(\epsilon)J_L(r-R) \text{ for } |r-R|\leq s_R \\ K(r-R) \text{ for } |r-R|\geq s_R \end{array}\right\} \tag{2.44}$$

The MTOs are regular, continuous and differentiable in the whole space, and the parts of the MTO inside and outside the MT spheres at R are often referred to as head and tail of the MTO, respectively. The function $K_L(r)$ is called the envelope function and defined in the whole space. Tail of the orbital is chosen to have zero kinetic energy and satisfies the Laplace equation . The tail of the MTO at site R may be expanded inside the other MT sphere at R$'$ by the function $J_L(r-R')$, given

$$\Psi_{R,L}(\epsilon,r)=\left\{\begin{array}{c} {\scriptstyle N_{RL}(\epsilon)\varphi_l(\epsilon,r-R)+P_{RL}(\epsilon)J_L(r-R) \text{ for } |r-R|\leq S_R} \\ -\sum_{L'} S_{RLR'L'}J_L(r-R') \text{ for } |r-R'|\leq s_R(R\neq R') \\ K_L(r-R) \text{ for } r\epsilon I \end{array}\right\} \tag{2.45}$$

where I represents the interstitial region outside the sphere. The expansion coefficients $S_{RlR'L'}$ are called the canonical structure constants. Since the term $N_{RL}(\epsilon)\varphi_l(\epsilon,r-R)$ is the exact solution inside the MT sphere at site R, the additional terms $P_{Rl}(\epsilon)J_L(r-R)$ must be cancelled out by the sum of the tail of the MTOs from the other MT sphere, that is,

$$\sum_L a_{Rl}[P_{RL}(\epsilon)\delta_{RR'}\delta_{LL'}-S_{RLR'L'}]=0 \tag{2.46}$$

where we have defined the on site canonical structure constants as zero, i.e $S_{RLR'L'}=0$

Non-trivial solutions of the set of linear equations for the eigenvectors $a_{RL}$ exist when a secular determinant vanishes, namely

$$\det[P(\epsilon)\delta_{RR'}\delta_{LL'}-S_{RLR'L'}]=0 \tag{2.47}$$

This is called the Koringa-Kohn-Rostoker(KKR) equation. With the use of the MTOs, the eigenvalue problem is separated into two parts, namely, the potential functions $P_{Rl}(\epsilon)$ have the non-linear energy dependence, which is undesirable from computational point of view. This unfavourable point is removed by the linearization of the MTOs, which leads to LMTO method.

### 2.4.7 The Atomic Sphere Approximation

In order to simplify the LMTO expression for the matrix elements, Anderson [51] introduce an approximation where MT spheres are assumed to expand and take the atomic volume, so that they overlap with each other. This is called the atomic sphere approximation(ASA). There is no interestial region in the ASA. Thus, $\kappa^2$ is essentially arbitrary because there is no interstial region. Hence, the atomic sphere approximation [52, 53, 54] makes the following two approximations . Firstly, the kinetic energy of the partial wave, $k^2 \equiv \epsilon - v_{MTZ}$, is treated as a parameter independent of $\epsilon$ where $v_{MTZ}$ is the constant potential in the interstitial region. Secondly, the atomic polyhedron or the Weigner-Seitz cell is replaced by an atomic sphere with the same volume as the atomic polyhedron so that the interstitial region vanishes. This second approximation allows the atomic spheres to overlap with each other, and the relative amount of sphere overlap is defined by

$$\omega_{\mathbf{R}\mathbf{R}'} = \frac{s_{\mathbf{R}} + s_{R'}}{|\mathbf{R} - \mathbf{R}^{'}|} - 1 \tag{2.48}$$

In the ASA the one electron potential entering the Schroedinger equation is, therefore, a superposition of overlapping spherical potential wells with positions R and radii $s_R$, which leads to a kinetic-energy error that is proportional to the fourth power of the relative sphere overlap [51].

In many mineral structure-types such as the cooperite, braggite, sperrylite and platarsite, the use of only atom-centred spheres within ASA would cause substantial errors, either due to large overlap and misrepresentation of the potential, or due to neglect of charge in the van der Waals gap. Therefore, it is necesary to pack the van der Waals gap with interstitial spheres. In general, the requirement for choosing the sphere positions is that the super-position of the spherical potentials approximate the full three-dimensional potential as well as possible [55]. Here the full potential is modelled by the superposition of the neutral atom potentials, and for simplicity, only the Hartree part is retained. The atomic centered spheres are then determined by tracing the potentials along the line connecting nearest-neighbour atoms and finding the saddle-points. For a given atom with position R, the distance to the closest saddle-point is taken as the radius of a sphere which usually touches the spheres constructed in the same way about other atoms. The ASA radii are then obtained by inflating these atom-centered non-overlapping spheres until they either fill space or until their overlap reaches a maximum value of

16%. In the latter case, the potential between the atomic potentials must be represented by additional interstitial spheres, which are usually repulsive. The positions of these interstitial spheres are first chosen among the non-occupied symmetry positions of the space group. Then their radii are chosen in such way that the maximum overlap between an atomic and interstitial sphere is 18% and maximum overlap between two interstitial spheres is 20%.

In LMTO, the Hamiltonian matrix has a two center form

$$H_{RLR'L'} \approx \epsilon_{iRl}\delta_{RR'}\delta_{LL'} + h_{RLR'L'} \tag{2.49}$$

$$\approx c_{Rl}\delta_{RR'}\delta_{LL'} + \sqrt{d_{Rl}}S_{RLR'L'}\sqrt{d_{R'L'}}$$

where S is the structure constant matrix, c and d are potential parameters. The overlap matrix is given by

$$O_{RLR'L'} \approx \langle\varphi_{RL}|\varphi_{R'L'}\rangle \tag{2.50}$$

The ASA is a reasonable approximation provided that there are few electrons in the interstitial region, or rather, that the touching MT spheres can be substituted by overlapping Weigner-Seitz spheres which fill the electron-containing regions but do not overlap more than 30% into one sphere, i.e

$$s_R + s_{R'} - |R' - R| \leq 0.3s_R \text{ for all } R \tag{2.51}$$

In the ASA the integral $\langle\varphi| - \nabla^2 + v_{ns}|\varphi\rangle$, where $v_{ns}$ is the non-spherical part of the potential, vanish. A combined correction (CC) for the neglect of the interstitial region and the higher partial waves is usually included.

### 2.4.8 Combined Correction

The ASA works well near the Fermi energy when the system is closely packed and the sphere-overlapping region is small. Once the overlapping region is not negligible or the interesting energy is rather high, we introduced the combined correction which compensates for the error introduced by the ASA. Then the overlap matrix and the corresponding matrix of the Hamiltonian are not simply quantity integrated over the interstitial region, but should be quantity compensating-introduced errors.

Here the LMTO $k^2 = 0$ basis set is transformed exactly into a basis set $\{|\varphi^\alpha\rangle\}$ of the form

$$|\varphi^\alpha\rangle = |\varphi^0\rangle(1 + \alpha S^\alpha) \tag{2.52}$$

where $S^\alpha = S^0(1 - \alpha S^0)^{-1}$ are the screened structure constants. The screened structure constant fall off in real space much faster than the screened canonical structure constants, which gives the formalism a similar form to that of the semi-empirical TB approximation. Hence, the name TB-LMTO. The $S^\alpha$ can be generated in real space for each site R by inverting the positive matrix $\alpha_{Rl}^{-1}\delta_{RR'}\delta_{LL'} - S^0_{RLR'L'}$ for a cluster with 20-40 nearest neighbours $R'$. The Hamiltonian in the orthonormal representation may be expressed as a power in the following two center tight-binding Hamiltonian:

$$h^\alpha_{RL,R'L'} \equiv (c^\alpha_{RL} - E_{RL})\delta_{RR'}\delta_{LL'} + \sqrt{d^\alpha_{RL}}S^\alpha_{RL,R'L'}\sqrt{d^\alpha_{R'L'}} \tag{2.53}$$

with c and d being potential parameters which may be derived from the slope and amplitude of the corresponding radial wave functions $\varphi$ at the sphere. The more terms that are included in this power series in $h^\alpha$, the wider is the energy range around E in which the eigenvalues equal the one-electron energies, $E_{j.}$

## 2.5 Atomic Simulations

Although first principles methods are extremely precise, they are restricted to investigate zero-temperature properties of systems with relatively few number of atoms due to limited computer resources. Atomistic simulation methods on the other hand, are well known to treat large and complex structures, such as surfaces, point defects, dislocations, grain boundaries, and fracture cracks. The effectiveness of atomistic methods obviously depends upon the quality of the model potentials employed. Recent studies [56, 57, 58, 59, 60] have shown that the incorporation of ab initio data during the fitting of interatomic potentials can significantly enhance their ability to mimic interatomic interactions. For example, Baskes et al. [61] examined the range interatomic forces in aluminum using model potentials and ab initio methods. They found that potentials that included ab initio data during the fitting procedure could reproduce ab initio forces much more accurately than the potential fits to experiment data only.

Atomistic simulation technique use simple, parameterised, analytic functions to described the interaction between all species in the crystal. This enables the lattice energy of the system to be calculated. This is defined as the energy released when the component ions at infinity are brought together on the lattice sites. The interactions in a crystal is made up of the short range attractions and repulsions, which are modelled using adjustable parameters and long range electrostatic interactions, which contribute approximately 80% of the total interaction energy.

### 2.5.1 Static Lattice Energy Minimization

On calculating a crystal structure (pure or defect) it must be brought to its mechanical equilibrium (minimised). A crystal structure is minimised when the ions are in their minimum energy position, i.e. there is zero net force on the ions. There are two procedures to minimize the latice energy : either at constant volume or constant pressure. **Constant volume minimzatio**n determines the minimum energy via ionic coordinates, where only the strains on individual ions are considered. For **constant pressure techniques**, it is necessary to determine the minimum energy not only through the adjustment of ionic coordinates, but also unit cell dimensions, accounting for the strains both on individual ions as well as the unit cell.

Under constant volume conditions the lattice energy $U_L$ can be expanded to the second order about a point $r$, and for the new set of coordinates $r'$ can be express as:

$$U_L(r) = U_L(r) + g^T \bullet \delta + \frac{1}{2}\left(\delta^T \bullet W \bullet \delta\right) \tag{2.54}$$

In equation 2.54, g is the first derivative of the lattice energy with respect to ionic positions:

$$g = \frac{\partial U_L}{\partial r} \tag{2.55}$$

$\delta$ is the displacement (or strain ) of a given ion
and W is the second derivative of the lattice energy with respect to $r$ :

$$W = \frac{\partial^2 U_L}{\partial r^2} \tag{2.56}$$

At equilibrium, the change in energy with respect to strain is zero. Therefore:

$$\frac{\partial U_L(r')}{\partial \delta} = 0 = g + W \bullet \delta \tag{2.57}$$

The optimum ion displacement to give rise to the minimum lattice energy is:

$$\delta = -W^{-1} \bullet g \tag{2.58}$$

or:

$$\delta = -H \bullet g \tag{2.59}$$

where $H$ is the Hessian matrix is the inverse of the second derivative of the lattice energy with respect to ionic displacement.

The energy of the systems considered in this work are not harmonic, thus the energy minimum can not be arrived at in a single step. Rather, subsequent displacements, in general, result in lower energy configurations. Thus, the ionic coordinates are adjusted iteratively until the forces on the atoms are zero. There are two methods of energy minimization employed in this work: Newton-Raphson and Conjugate Gradient.

All Newton-Raphson type formulae (e.g. the Borgden, Fletcher, Goldfard, Shanno formula [62]) serve to iteratively update the Hessian matrix, H, from equation **2.59**

$$r_{n+1} = r_n - H_i \bullet g_i \tag{2.60}$$

This however requires the storage of the Hessian matrix of second derivatives, which is computationally intensive. Furthermore, solving for the second derivative matrix at each step would result in a less than expenditious overall calculation. For this reason, Conjugate Gradient type minimizations are also employed. These only require the calculations of the first derivatives of the lattice energy:

$$\beta = \frac{g_{i-1}^T \bullet g_{i-1}}{g_{i-2}^T \bullet g_{i-2}} \tag{2.61}$$

Conjugate Gradient calculations are computationally less expensive than those of the Newton-Raphson variety and converge quickly when far from the lattice energy minimum. However, when near the minimum, the Conjugate Gradient technique becomes less efficient due to the small gradient. Thus, a

combination of these two techniques is used during the minimization process, beginning with Conjugate Gradient as a coarse refinement until a certain small gradient is met and then switching to Newton-Raphson type methods in order to finalize the minimization.

**Constant Pressure Minimization**

In contrast, in pressure minimization both unit cell dimensions and ion coordinates are allowed to vary. The minimizations are carried out simultaneously using the same approach as for constant volume minimization, with the lattice vectors treated as additional variables. As in constant volume minimizations, the ions are at equilibrium in their minimised positions when the strain on the lattice vector is zero.

The strain on the unit cell is defined by

$$r^{'} = (I + \varepsilon) \cdot r \tag{2.62}$$

where $I$ is the identity matrix, $\varepsilon$ is the strain on the lattice vectors, $r$ and $r'$ are the transformed lattice vectors. Using the Voigt notation equation 2.62 can be written in a matrix form:

$$\begin{bmatrix} x' \\ y' \\ z' \end{bmatrix} = \begin{bmatrix} 1+\varepsilon_1 & \frac{1}{2}\varepsilon_6 & \frac{1}{2}\varepsilon_5 \\ \frac{1}{2}\varepsilon_6 & 1+\varepsilon_2 & \frac{1}{2}\varepsilon_4 \\ \frac{1}{2}\varepsilon_5 & \frac{1}{2}\varepsilon_4 & 1+\varepsilon_3 \end{bmatrix} \begin{bmatrix} x \\ y \\ z \end{bmatrix}$$

where $x', y', z'$ and $x, y, z$ are components of $r'$ and $r$ respectively.

The static pressure is given by the first derivative of the lattice energy with respect to the strain and can be determined using the chain rule:

$$P_{static} = \frac{\partial \Psi}{\partial \varepsilon_j} = \frac{\partial \Psi}{\partial r} \frac{\partial r}{\partial r^2} \frac{\partial r^2}{\partial \varepsilon_j} \tag{2.63}$$

The first term represents the first derivative, the second term equates to $\frac{1}{2r}$ and the solution of the third term can be found by squaring the equation defining the bulk strains and differentiating:

$$\frac{\partial r'^2}{\partial \varepsilon_j} = 2r^{\alpha} \cdot r^{\beta} + 2r^{\alpha} \cdot \varepsilon \cdot r^{\beta} \tag{2.64}$$

In the equilibrium condition, there is no strain, i.e. $\varepsilon = 0$, and equation (2.64 ) then becomes:

$$\frac{\partial r'^2}{\partial \varepsilon_j} = 2r^{\alpha} \cdot r^{\beta} \tag{2.65}$$

More information on these equations can be found from references [63] and [64].

The proportionality constant between the stress and strain can be calculated as well, which is the last compliances matrix, and the inverse of the second derivative of the energy with respect to strain. It is determined by expanding the lattice energy to second order:

$$\Psi(r') = \Psi(r) + g \cdot \delta' + \frac{1}{2}\delta'^{T} \cdot W \cdot \delta \tag{2.66}$$

now $\delta'$ is the $3N + 6$, strain matrix containing the components of the symmetric strain matrix $\varepsilon$, and $r'$ is the same as in equation ( **2.62**) ($r' = (I + \varepsilon) \cdot r$). $W$(equation(**2.66** )) now also includes mixed coordinates and strain derivatives and is of order $3N + 6$ by $3N + 6$.

$$W = \begin{bmatrix} \frac{\partial^2\Psi}{\partial r^2} & \frac{\partial^2\Psi}{\partial r \partial \varepsilon} \\ \frac{\partial^2\Psi}{\partial \epsilon \partial r} & \frac{\partial^2\Psi}{\partial \varepsilon^2} \end{bmatrix} = \begin{bmatrix} W_{rr} & W_{\varepsilon r} \\ W_{r\varepsilon} & W_{\varepsilon\varepsilon} \end{bmatrix}$$

$W_{rr}$ is the coordinate second derivative matrix of $3N$ by $3N$, $W_{r\varepsilon}$ and $W_{\varepsilon r}$ are the mixed coordinates and strain second derivative matrices of 6 by $3N$ and 3n by 6 and $W_{\varepsilon\varepsilon}$ is the strain second derivative matrix of 6 by 6. Again if we apply the equilibrium condition where the strain is zero and splitting $\delta'$ into components of $\delta'$ and $\varepsilon$, equation ( 2.66) can be written as:

$$\Psi(r') = \Psi(r) + \frac{1}{2}\delta \cdot W_{rr} \cdot \delta + \delta \cdot W_{re} \cdot \varepsilon + \frac{1}{2}\varepsilon \cdot W_{\varepsilon\varepsilon} \cdot \varepsilon \tag{2.67}$$

and differentiating with respect to $\delta$ and again applying the equilibrium condition, we have:

$$\frac{\partial\Psi}{\partial\delta} - 0 = \delta \cdot W_{rr} + W_{r\varepsilon} \tag{2.68}$$

thus

$$\delta = -W_{rr^{-1}} \cdot W_{r\varepsilon} \cdot \varepsilon \tag{2.69}$$

Hence equation (2.67 ) can be written as:

$$\Psi(r') = \Psi(r) + \frac{1}{2}\varepsilon \cdot [W_{\varepsilon\varepsilon} - (W_{\varepsilon r} \cdot W_{rr^{-1}} \cdot W_{r\varepsilon})] \cdot \varepsilon \tag{2.70}$$

The elastic constant $c$ is defined as the second derivative of the lattice energy with respect to lattice strain, normalised cell volume. Now if we differentiate equation ( 2.70) twice with respect to strain $\varepsilon$, we get the constant as

$$c = \frac{1}{V}\left[W_{\varepsilon\varepsilon} - (W_{\varepsilon r} \cdot W_{rr^{-1}} \cdot W_{r\varepsilon})\right] \tag{2.71}$$

and the strains are given by the stress divided by the elastic constant $c$. Assuming Hooke's law, the strain can be calculated as

$$\varepsilon = (P_{static} + P_{applied}) \cdot c^{-1} \tag{2.72}$$

and this can be used to evaluate the new coordinates after the strain. Because these expressions are approximations, this process continues iteratively until all the strains are removed.

### 2.5.2 Calculation of Surface Properties

The properties of the surfaces of materials are every bit as important as the bulk properties, since they control the interaction between the substance and the external environment. At the most obvious level, the very shape of the particles or crystallites formed is determined by the properties of the surface relative to the bulk, while catalysis and reactions of the material also predominantly occur at the surface.

The surface stability and reactivity are calculated using computer code METADISE (Minimum Energy Techniques Applied to Dislocation, Interfaces and Surface Energies) [65] , which emanated from the MIDAS code, developed by Tasker [66].

Here, the simulation cell is modelled as two blocks where each consists of two regions, I and II as shown in fig. **2.6**.The ions in regions II are held fixed at their equilibrium position, while the ions in region I are allowed to relax relative to region II. Both region I and II need to be sufficiently large for the energy to converge.

The energy of the crystal is therefore made up of two parts,

$$E_{total} = E_1 + E_2 \tag{2.73}$$

where $E_1$ and $E_2$ are the energies of the ions in region $I$ and $II$ respectively. The energy of region $I$ is given by Equation 2.74 below:

$$E_1 = \sum_{i\epsilon I, j\epsilon I} \sum_{l} \Psi_{ij}\left(|r_{ij} - r_l|\right) + \frac{1}{2} \sum_{i\epsilon I, j\epsilon II} \sum_{l} \Psi_{ij}\left(|r_{ij} - r_l|\right) \tag{2.74}$$

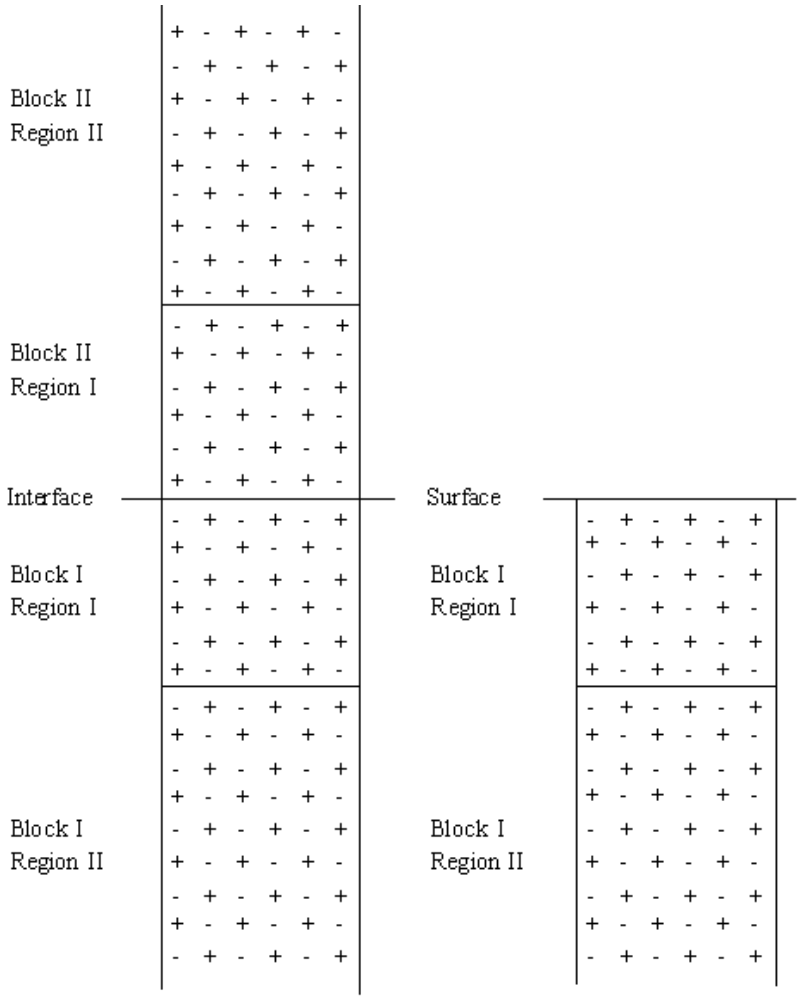


Figure 2.6: The two region approach used in METADISE, the left hand case for a complete crystal unit (BULK) and the right hand case a half crystal exposing a surface.

where the first term includes interactions between the ions in region I and the second term the interactions between the ions in region I and region II. The energy of region II consists of only the second term as the ions are kept fixed and hence the iterations between the ions in region II is unchanged. The energy contribution is therefore given by the equation 2.75

$$E_2 = \frac{1}{2} \sum_{i \epsilon I, j \epsilon II} \Psi ij \left( |r_{ij} - r_l| \right) \tag{2.75}$$

When calculating the surface enegy of a crystal face it is neccessary to perform two METADISE calculations, one using a surface block and one using a block, as seen in fig. 2.6. The surface energy is then derived using the following method.

If the energy of the surface bock is $E_s$ and the bulk block is $E_b$, then these energies can be broken down into the following components:

$$E_s = E^{'}_{I-II} + E^{'}_{I-I} + E^{'}_{II-I} + E^{'}_{II-II} \tag{2.76}$$

$$E_b = E^{''}_{I-II} + E^{''}_{I-I} + E^{''}_{II-I} + E^{''}_{II-II} \tag{2.77}$$

where $E_{I-I}$ is the interaction energy of ions in region I with other in region I, $E_{I-II}$ is the interaction energy of all the ions in region I with all the ions in region $II$, etc. The surface energy of a crystal face is defined as the excess in energy of a surface simulation over the energy of a bulk system containing the same number of atoms per unit area and is therefore described by the equation 2.78.

$$\gamma = \frac{(E_s - E_b)}{AREA} \tag{2.78}$$

Since the ions in Region II do not relax, the total interaction energy, $E_{II-II}$ , of all the ions in Region $II$ with all the other ions in Region II does not change, and will therefore cancel in the surface energy calculation.

### 2.5.3 Surface Types

There are two phases to any surface calculation, namely the creation of the surface from the bulk material and the subsequent calculation of its optimized structure and properties. Surfaces can be studied by considering the crystal as a stack of planes.

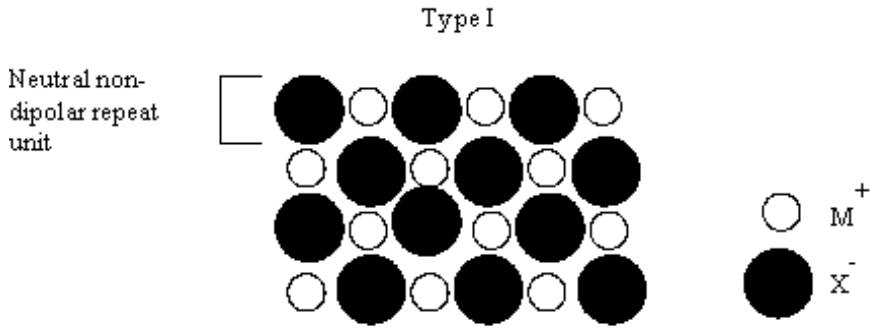


Figure 2.7: Type I Stacking Sequences

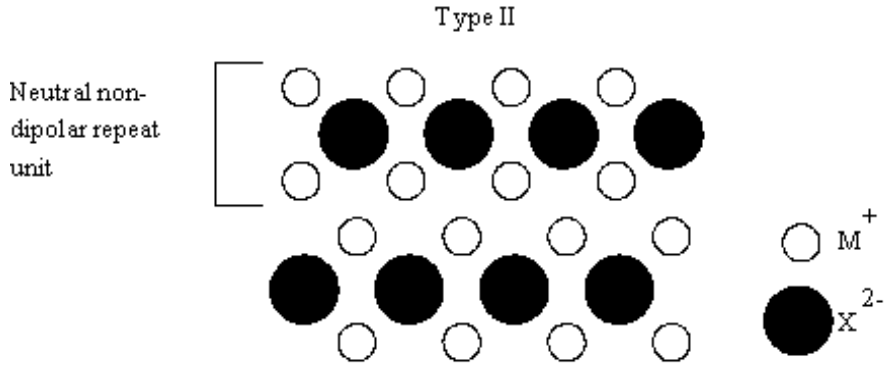


Figure 2.8: Type II Stacking Sequences

The stacking sequence of the ions making up the ionic solids has to be such that there is no dipole moment in the repeat unit cell perpendicular to the surface. This is to prevent the lattice sums from diverging, as the surface charge would generate an electric field throughout the bulk of the crystal and hence the surface energy for an infinite surface be defined [67]. Each surface is specified by at least two pieces of information. Firstly, there are miller indices (hkl) of the plane that define the orientation of the bulk cleavage. When cleaving surfaces there are also other important consideration to take into account, in particular the type of surface.There are three basic types of surfaces as suggested by Tasker [68], type $I, II$ and $III$.

In case of a type I surface the stacking plane is neutral and is composed of both cations and anions in a stoichiometric ratio and there is no dipole perpendicular to the surface (fig. **2.7**). Type II surfaces, as shown in fig. **2.8**, although charged, have no net dipole moment in the repeat units due to a symmetrical stacking sequence. As the bulk of the crystal is not affected in either of these surface types, lattice sums are convergent and therefore have small positive surface energies. The type III surafces are composed of alternately charged planes that produce a dipole perpendicular to the surface. In order to calculate an accurate surface energy, these surfaces must be reconstructed. This can be achieved by creating vacancies, addition of ions on opposite surfaces, or by having species adsorbed to the surface. The number of posible surfaces in the case of type $III$ stacking units are therefore limited and are only generally observed in ionic crystals if the material is non-stoicheometric. Fig. 2.9 shows the stacking sequence of type $III$ surfaces and a simple computational reconstruction, where 50% of the ions in the top surface are removed and added to the bottom surface, there by cancelling the dipole, enabling it to be simulated.

### 2.5.4 Crystal Morpholgy

The equilibrium crystal morphology of a material can be determined by applying Wulff's Theorem, although it was Gibbs [69] who first proposed that the equilibrium form of a crystal should posses minimial total surface energy for a given volume, i.e.

$$\gamma_{crystal} = \sum_i \gamma_i A_i = \min imum \text{ at constant volume} \tag{2.79}$$

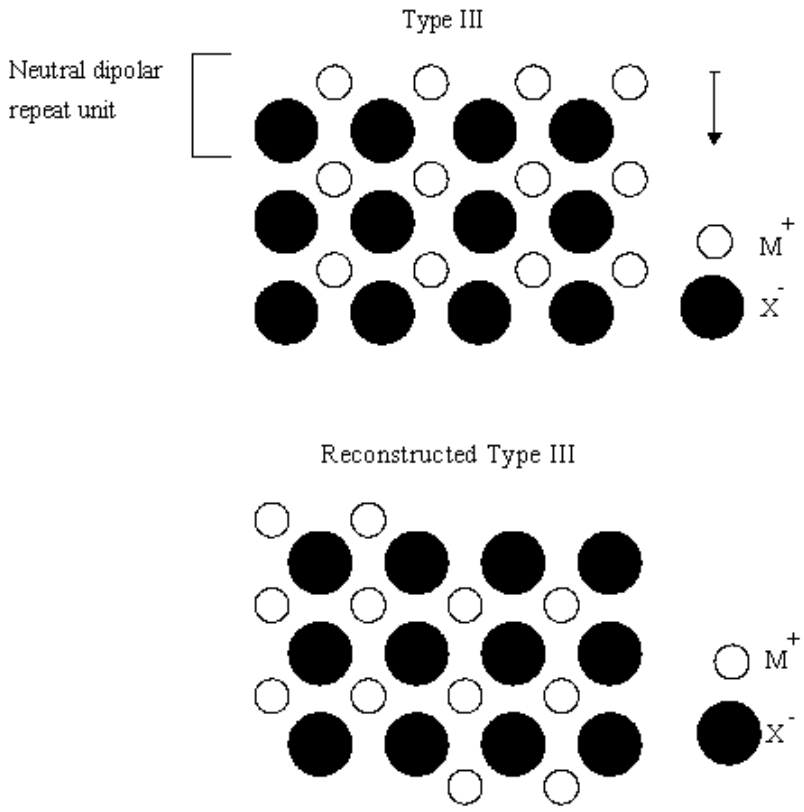


Figure 2.9: Type III and reconstructed Type III stacking sequences

where $\gamma_i$ and $A_i$ are the specific surface energy and specific area if the the $ith$ crystallographic face.

From this Wuff proposed that the shape thus defined would be such that $h_i$, the face normal vector from a point within the crystal would be proportional to $\gamma_i$ or

$$h_i = \lambda \gamma_i \tag{2.80}$$

where $\gamma$ is a constant depending on the absolute size of the crystal. Strictly the theorem is only true for crystal grown infintely slowly, but this is impossible practically. Therefore the theorem is said to be true for small crystals in which rearrangement of the crystal is possible at all stages of growth due to the short distances over which matter has to travel. This methodology has been implemented in in METADISE [65].

### 2.5.5 Lattice Dynamics

The interior of the earth is natural high-pressure, temperature environment, and composed of materials, such as minerals and metal alloys, with different structures and properties from those at the surface. Hence, understanding of materials in the earth's interior requires generation of high pressure-temperature that are difficult to simulate in the laboratory. Lattice dynamics is capable of predicting a crystal's structure at a wide range of temperatures and pressures. Thus unlike static lattice energy minimisation, it takes account the effect of temperature on the system. Application of lattice dynamics is limited to moderate temperatures and does not allow for a detailed study of dynamic nature of processes.

The theory behind the analytical free energy minimization method is developed by Kantorovich [70, 71].

The Helmholtz free energy can be written as he sum of the static internal energy, $U_{static}$, that would be calculated in a conventional energy minimzation, the vibrational energy, $U_{vib}$, and the term arising from the vibrational entropy, $S_{vib}$:

$$A = U_{static} + U_{vib} - TS_{vib} \tag{2.81}$$

This assumes that there is no contribution from configurational disorder that must be corrected separately. The sum of the vibrational energy and entropy can be expressed together, due to the cancellation of a common term, as

$$Uvib - TSvib = \sum_k \sum_m \left\{ \frac{1}{2} h\omega_m(k) + kT \ln \left[ 1 - \exp\left( -\frac{h\omega_m(k)}{kT} \right) \right] \right\} \tag{2.82}$$

where the sum over K points is used to approximate the integral over the Brillouin zone of the phonon density of states. The vibrational frequencies at ecah K point are given by the square root of the eigenvalues of the dynamical matrix, which in turn are related to the phased second-derivate matrix mulitiplied by vectors containing the inverse square root of the atomic masses:

$$\omega^2(k) = e^{-1}(k) D(k) e(k) \tag{2.83}$$

$$D^{ij}_{\alpha\beta}(k) = \frac{1}{\left(\sqrt{m_i m_j}\right)} \sum \left( \frac{\partial^2 U_{static}}{\partial\alpha\partial\beta} \right) \exp\left( ik \left( r_{ji} - r_{i0} \right) \right) \tag{2.84}$$

The derivatives of the free energy with respect to structural parameters can be related to the derivatives of the eigenvalues or frequencies squared:

$$\left( \frac{\partial A}{\partial \epsilon} \right) = \left( \frac{\partial U_{static}}{\partial \epsilon} \right) + \sum_k \sum_m \left\{ \frac{1}{2\omega_m(k)} \left( \frac{1}{2} + \frac{1}{\exp\left( h\omega_m(k) \right) / kT - 1} \right) \left( \frac{\partial \omega^2}{\partial \epsilon} \right) \right\} \tag{2.85}$$

Hence the key is obtain the derivatives of the eigenvalues. Through the application of peturbation theory these derivatives can be related to derivatives of the elements of the dynamical matrix projected onto the eigenvectors of each phonon mode:

$$\left( \frac{\partial \omega^2}{\partial \epsilon} \right) = e^*_m(k) \left( \frac{\partial D(k)}{\partial \epsilon} \right) e_m(k) \tag{2.86}$$

The derivatives of the dynamical matrix elements are just the third derivatives with respect to either three Cartesian coordinates, for internal degrees of freedom, or two Catersian and the external strain in the case of unit cell derivatives. Both must also be multiplied by the appropriate phase factor for the point in the Brillouin zone.

Although the determination of the first derivatives of the free energy in this way is in principle straightforward, the difficulty lies in making an

efficient implementation so that calculations are practical for moderately large systems. The first dilemma is that the second derivative terms are needed both to calculate the dynamical matrix and to generate the third derivatives. However, the derivative cannot be utilized until the eigenvectors are known, which is after the dynamical matrix has been completely built and diagonalized.

Taylor et al. [72] have implemented a scheme where a number of intermediate terms are stored between various stages of calculation as a compromise between computational efficiency and memory usage.

For large systems there are two parts of the calculation which scale as $N^3$ and therefore potentially dominate the computational expense. The first is diagonalization of the complex Hermitian dynamical matrix, for which there are already efficient libriaries of routines. The second is the projection of each phonon mode. This second part can potentially be a bottleneck for large systems, and therefore it is crucial to minimize the number of multiplication operation. By doing this carefully, the prefactor for this part can be reduced by more than an order of magnitude. As a result, the matrix diagonalization always becomes the dominant expense with increasing number of atoms, unless Hessian recalculation is required frequently, in which case matrix inversion becomes the limiting factor.

Having obtained the first derivatives of the free energy, we need to be able to efficiently optimize the geometry of the system with respect to this quantity. Here we follow the approach by Taylor et al. [72], which is to use a Newton-Raphson method based on approximate Hessian matrix which is calculated from the static second derivatives only. This matrix is update subsequently using the BFGS scheme, which will, in principle, tend to correct for missing vibration contributions over sufficient cycles. In practice, the static Hessian is already a good approximation, and so only a few cycles of minimzation are required when starting from the statically optimized structure.

The above scheme generates both internal and external derivatives with respect to the free energy. However, for comparison we would also like to be able to perform calculations within the zero static internal stress approximation (ZSISA) in the notation of Taylor et al. [72], as used previously in numerical formulation. In this case the internal variables must be minimized with respect to the internal energy while only the strain variables are minimized with respect to the free energy. To achieve this, we must first neglect the thermal contribution to the internal forces. However, there will also be a

correction term arising for the strain derivatives associated with the fact that the internal energy must remain at its minimum point as the cell is strained [73]. This is analogous to the internal second derivative contribution to the elastic constant tensor.

The strain correction can be derived simply as follows. The free energy can be expanded about the current structure with respect to strain as a Taylor series:

$$A(d\epsilon) = A(0) + \frac{dA}{d\epsilon}d\epsilon + \frac{d^2\epsilon}{d\epsilon d\alpha}d\alpha d\epsilon + \frac{d^2A}{d\epsilon^2}(d\epsilon)^2 + ... \tag{2.87}$$

If we collect together terms in $d\epsilon$, then the ZSISA strain derivative can be seen to be

$$\left(\frac{dA}{d\epsilon}\right)_{ZSISA} = \frac{dA}{d\epsilon} + \frac{d^2A}{d\epsilon d\alpha}d\alpha \tag{2.88}$$

Using the standard result for the estimate of the internal displacements required to reach the minimum energy coordinates that comes from Newton-Raphson minimzation, we now obtain the following results:

$$\left(\frac{dA}{d\epsilon}\right)_{ZSISA} = \frac{dA}{d\epsilon} - \frac{d^2A}{d\epsilon d\alpha}\left(\frac{d^2A}{d\alpha d\beta}\right)^{-1}\frac{dA}{d\beta} \tag{2.89}$$

As we wish to avoid calculating the second derivatives with respect to the free energy due to the complexity and computational cost, we can approximate the two second derivative matrices by the static only components. Since one matrix is multiplied by the inverse of the other, there will be significant cancellation of errors, and this turns out to be a good approximation. All calculations have been performed using program GULP.

.

# Chapter 3

# STRUCTURAL PROPERTIES

## 3.1 Introduction

The purpose of this chapter is to calculate the change in internal parameters and lattice constants under pressure. This requires the relaxation of all the atoms, in the unit cell and hence the forces, using the accurate planewave code [25]. The Atomic Sphere Approximation (ASA) within TB-LMTO method is unable to predict reliable forces and is, therefore, not used in this chapter. ASA is sufficient for calculating bulk moduli (where the symmetry of the structure considered does not change during deformation), but it fails when calculating shear elastic constants. The reason is an inaccurate evaluation of the Coulomb and exchange-correlation energies with the spheroidized charge density within the ASA [78].

## 3.2 Methodology

### 3.2.1 Cut-off Energy Convergence

The calculations were performed using CASTEP (Cambridge Serial Total Energy Package) code, whose details have been documented in details elsewhere [25]. Castep is a pseudopotential total energy code which employs special point integration over the Brillouin zone and a plane-wave basis for the expansion of the wavefunctions. Norm-conserving non-local pseudo-potentials

of the form suggested by Kleinmann and Bylander [79] and ultrasoft pseudopotentials [50] were used. Geometry optimization was performed using a Broyden-Fletcher-Goldfarb-Shanno (BFGS) based minimization technique. This optimization procedure incorporates symmetry constraints. For point of accuracy, some test convergence with respect to the basis set size were carried out for each system. We begin by examining the convergence of the total energy with respect to the cut-off energy corresponding to the reciprocal lattice vector chosen in the plane wave basis.

The total-energy versus plane wave cutoff energies curves for PtS, $PdPt_3S_4$, $PtA_2$ and $Pt_4As_4S_4$ pseudo wave funcion are shown in figure 3.1. Therefore it

was determined that the energy cut-off of 800eV(normconserving pseudopotentials ) will be used for cooperite, braggite and sperrylite and cut-off of 400 eV (ultrasoft pseudopotentials ) for platarsite. In addition, we have checked our results for $Pt_4As_4S_4$ with an accurate norm-conserving pseudopotential (which required a cutoff of about 800 eV) and obtained virtually the same results, but it takes longer than with ultrasoft pseudopotential. These energy cutoff are important to ensure that the pseudo wave functions have the fastest (rapid) convergence. They give a Fast Fourier Transform (FFT) grid of 30 x 30 x 50 for PtS, 54 x 54 x 54 for $PdPt_3S_4$, 40 x 40 x 40 for $PtAs_2$ and 45 x 45 x 45 for $Pt_4As_4S_4$. The Monkhorst-Pack scheme was employed to select an optimal set of special k-points of the first Brillouin zone such that the greatest possible accuracy is achieved from the number of points used. In the present calculations a 3 x 3 x 2 for PtS, 2 x 2 x 2 for $PdPt_3S_4$, 4 x 4 x 4 for $PtAs_2$, and 6 x 6 x 6 for $Pt_4As_4S_4$ were used and the finite basis set correction (Pullay correction) was included to compensate the cut-off energies. In optimizations, the total tolerance in the total energy and pressure change before self-consistency (convergence) was deemed to have been achieved was 2 x $10^{-5}$ eV/atom and 0.1GPa, respectively.

## 3.3 Results and Discussion

### 3.3.1 Cooperite (PtS)

In many cases, it is interesting to explore the behaviour of any crystalline system as a function of pressure. High pressures and temperatures are the key parameters for the deep interior of the earth. The subtle changes in the

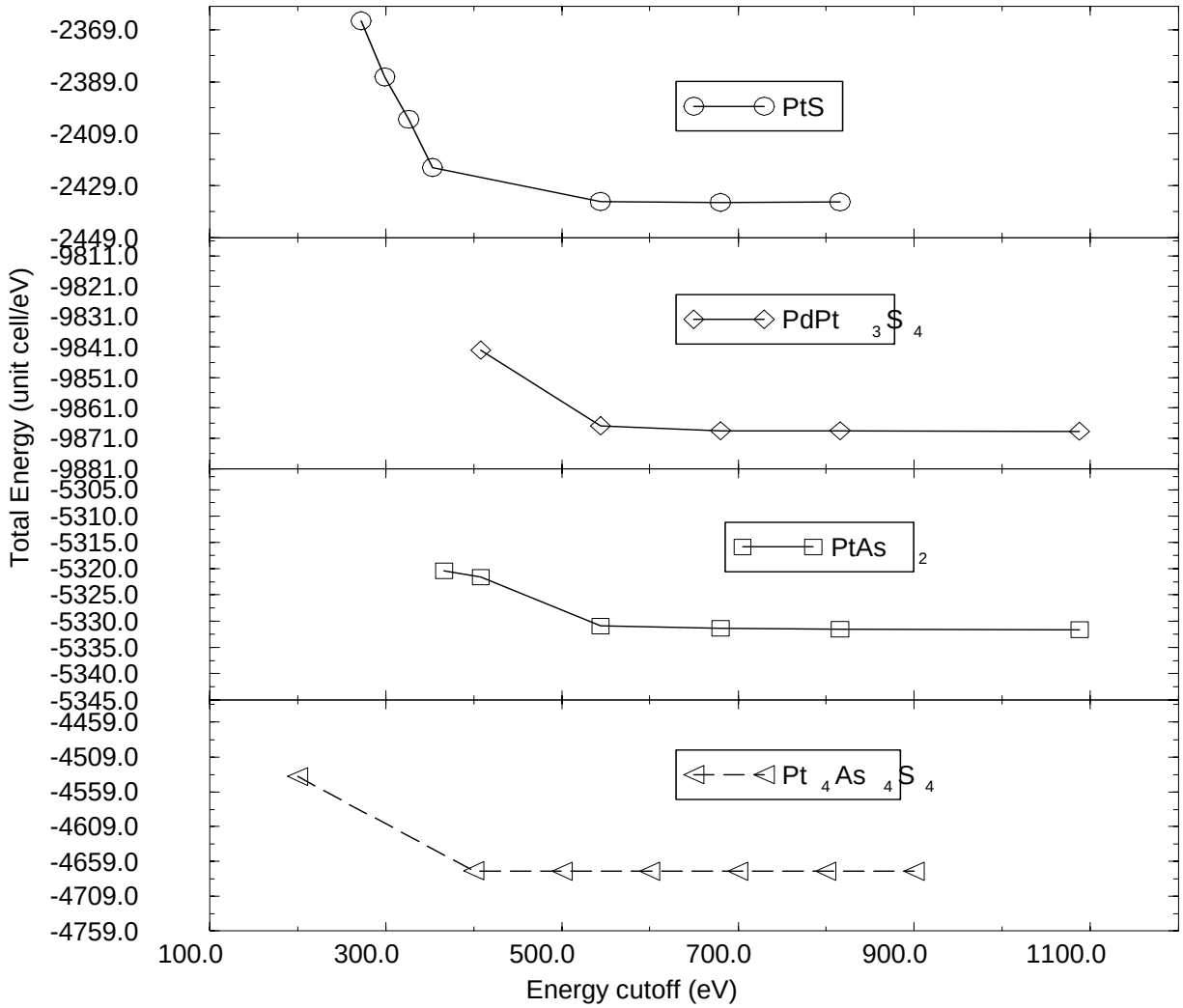


Figure 3.1: Total energy as a function of energy cutoff for PtS, $PdPt_3S_4$, $PtAs_2$ and $Pt_4As_4S_4$. The first three curves were calculated using norm conserving (full curve) and the fourth curve with ultrasoft pseudopotential (dotted curve).

crystal structure, which are induced by pressure and temperature can result in major changes in a mineral's properties and behaviour and, therefore are of considerable importance for understanding geophysical processes in the earth's inaccessible depth. PtS has two structural parameters: two lattice constants a and c, with no internal parameters. PtS was optimized at several pressures up to 50GPa enforcing its tetragonal symmetry throughout the simulations. The results of these calculations are displayed in (fig. 3.2, 3.3) and in (table 3.1). Fig. 3.2 shows the variation of lattice parameters a and c with respect to the applied pressure. Lattice parameter a decreases with increase in pressure while lattice parameter c increases with increase in pressure. The calculated zero pressure structural parameters are in excellent agreement with the experiment (table 3.1). The small underestimation (by less than 5%) of the lattice constants at zero pressure is attributed to the LDA and partly zero temperature (static) calculations. The LDA is expected to work better at higher pressures since the charge density becomes more uniform under compression. The calculated pressure-volume data were fit to the third-order Birch-Murnaghan equation [80] of state (fig. 3.3 ). The value of the deduced bulk modulus is presented in table 3.1. Presently, there are no experimental values for the bulk modulus of PtS.

Table 3.1: The structural parameters of PGM. The bulk moduli are calculated at the equilibrium volume.

| Structures | $a_{exp}$[1] | $a_{pseudo}$ | $V_{exp}$ | $V_{pseudo}$ | $B_{pseudo}$ |
|---|---|---|---|---|---|
| | Å | Å | Å$^3$ | Å$^3$ | GPa |
| PtS | a = 3.47, c = 6.11 | a = 3.439, c = 6.092 | 73.57 | 72.08 | 141.12 |
| $PdPt_3S_4$ | a = 6.37, c = 6.54 | a = 6.354, c = 6.554 | 265.37 | 264.67 | 184.22 |
| $PtAs_2$ | a = 5.97 | a = 5.933 | 213.85 | 214.50 | 184.59 |
| $Pt_4As_4S_4$ | a = 5.788 | a = 5.846 | 193.90 | 189.06 | 201.49 |

Table 3.2: First- and second-order axial compression coefficients of PtS calculated using Castep pseudopotential method. $B_0^{-1}$ is the linear compressibility at zero pressure and $B^{'}$ is the pressure derivative of B.

| $B_a$(a-axis)GPa | $B_c$(c-axis)GPa | $B_a^{'}$(a-axis) | $B_c^{'}$(c-axis) | $\kappa_a$ $10^{-3}$GPa$^{-1}$ | $\kappa_c$ $10^{-6}$GPa$^{-1}$ |
|---|---|---|---|---|---|
| 238.03 | 609876.3401 | 3.8 | 1340874.33 | 4.201 | 1.639 |

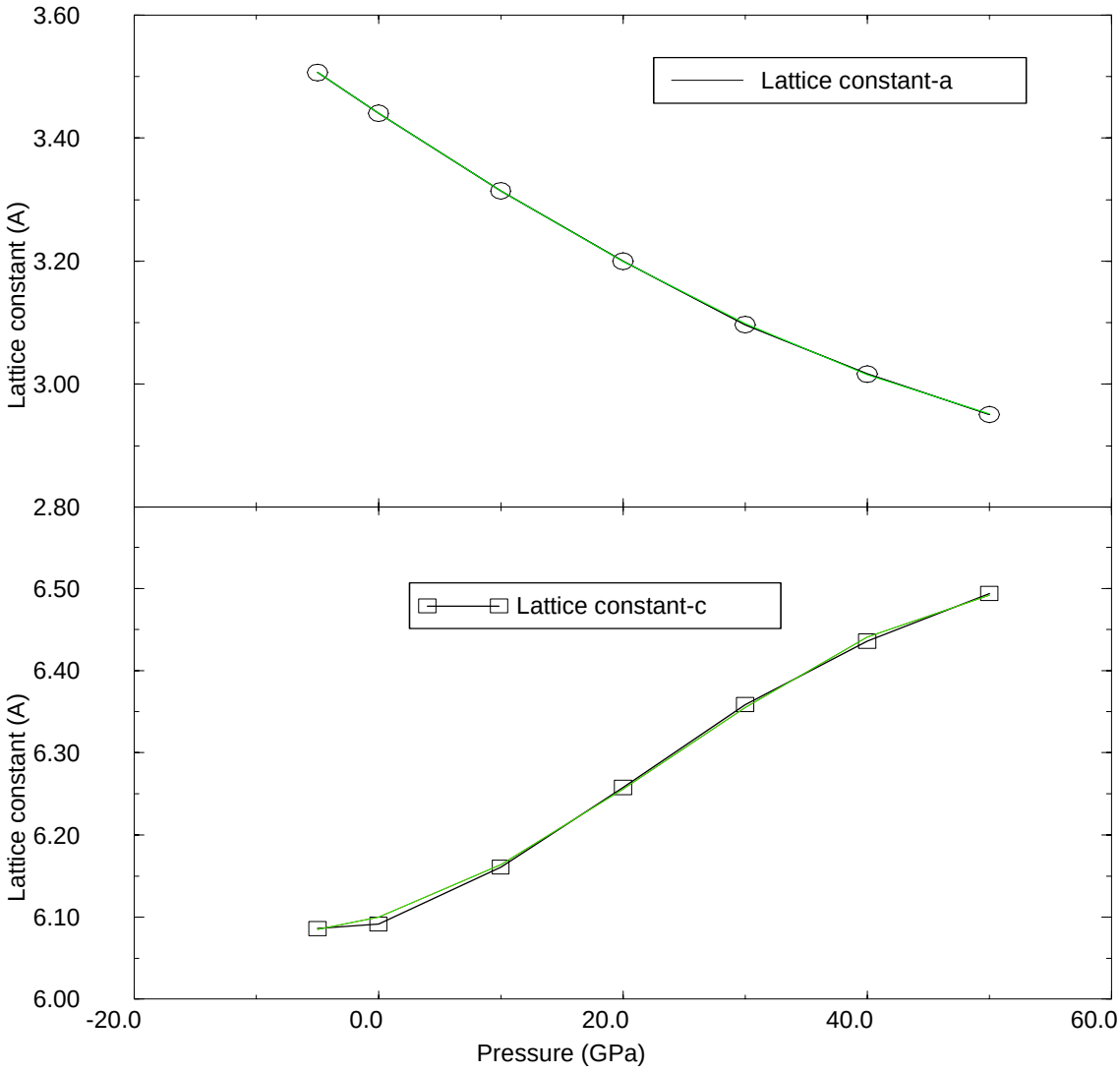


Figure 3.2: Lattice constant of PtS as a function of pressure: open circle represents the calculated values and solid green line curve fitting.

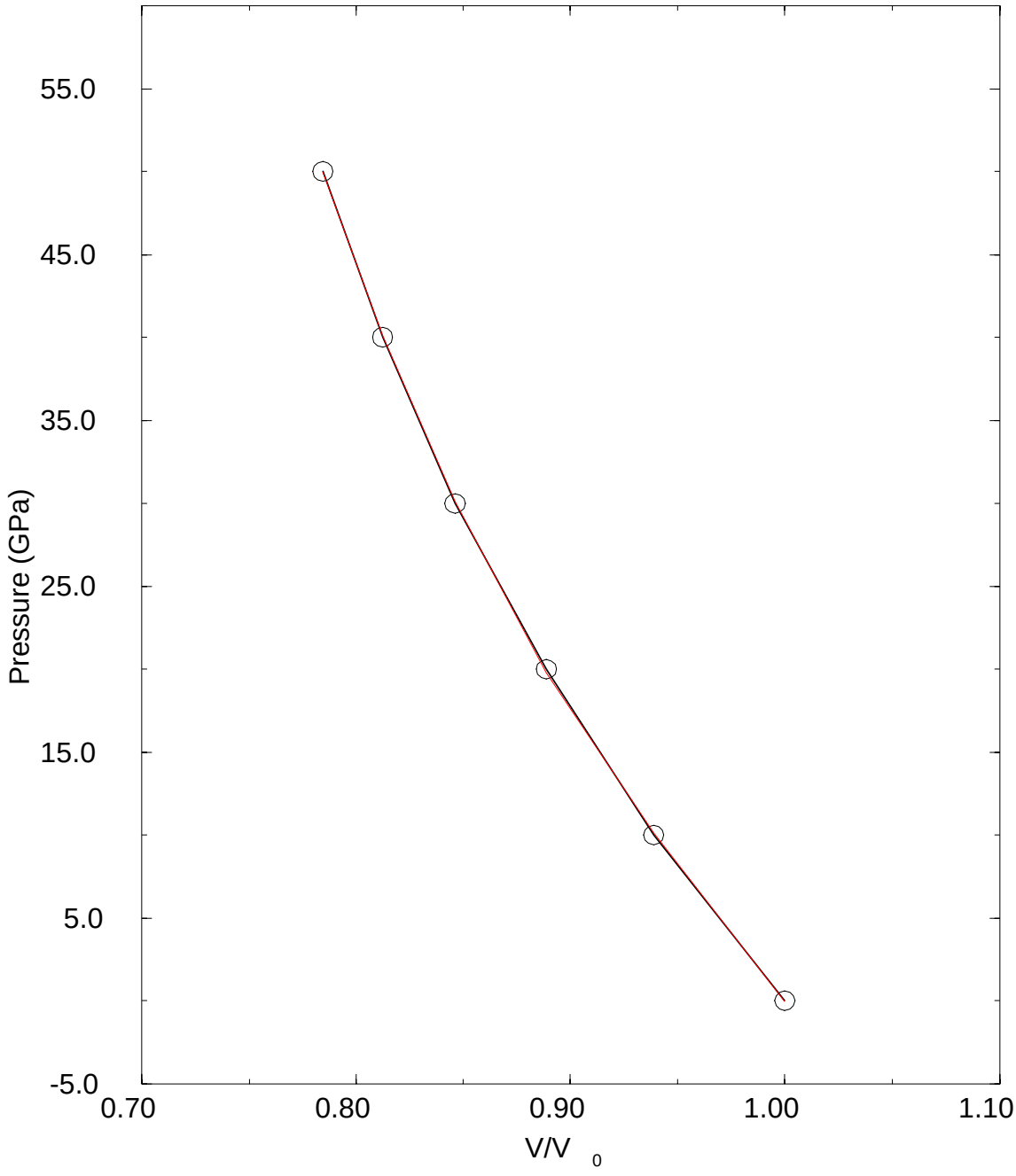


Figure 3.3: The calculated equation of states of PtS. The red solid line represents the curve fit and open circle calculated value.

The one dimensional analog of the Murnaghan equation [80] provides an approximation for describing the nonlinear relation between the normalized lattice parameters and pressure P, for the hexagonal and tetragonal structures,

$$r/r_{_0} = \left[\left(\frac{B'}{B_0}\right) P + 1\right]^{-\frac{1}{B'}} \tag{3.1}$$

Here, $r$ is the lattice constant along one of the crystal axes, $\kappa = B_0^{-1} = -\left(\frac{\partial \ln r}{\partial P}\right)_{P=0}$ is the linear compressibilty, and $B'$ is the pressure derivative of $B(i.e.\frac{\partial B}{\partial P})$, or the compressibilty of the a-axis or c-axis. The compressibility along c-axis is also defined as

$$\kappa_c = \frac{1}{c_0}\left(\frac{\partial c}{\partial P}\right)_{P=0} \tag{3.2}$$

where c is the c-axis lattice constant and $c_0$ is the c-axis lattice constant at the reference pressure $P_0$.

After a spread of calculations across a-c space, we were able to deduce the approximate position of the hydrostatic curve and concentrate further calculations along it. The gradient of the hydrostatic curve alone can be used to deduce the ratio of the linear expansion of coefficients. The plots of relative lattice constant $a/a_0$ ,$c/c_0$ and c/a as a function of pressure are fitted to a Murnaghan equation of state or equation 3.1 from which we obtain bulk moduli of $B_0$(a), $B_0$(c) and the derivative of the bulk moduli at zero pressure B′(a) and B′(c), and the compressility $\kappa_a$ and $\kappa_c$, respectively and the results are shown in table 3.2 and fig. 3.4. The gradient of the hydrostatic curve can be used to deduce the ratio of the linear expansion coefficients. The exact value can be determined from the equation (dc/cdP)/(da/adP), which is negative in the present calculations. The negative sign shows that the structure has a highly anisotropic response to the increase in pressure and the material expands along the c axis while contracting along a axis. The propensity of LDA to overbind is well known, as is its tendency to underestimate lattice parameters. Our calculations underestimate the a constant, but overestimate the c constant, at variance with the expected LDA discrepancy in lattice parameter. A plausible explanation for this could be that overbinding due to the LDA induces a spurious extra pressure on the system. Calculated and experimental bond lengths for PtS at equilibrium pressure are shown in table 3.3. Fig. 3.5 shows the variation of bond lengths with respect to the applied pressure. The Pt-Pt bond length decreases more rapidly than the Pt-S bond

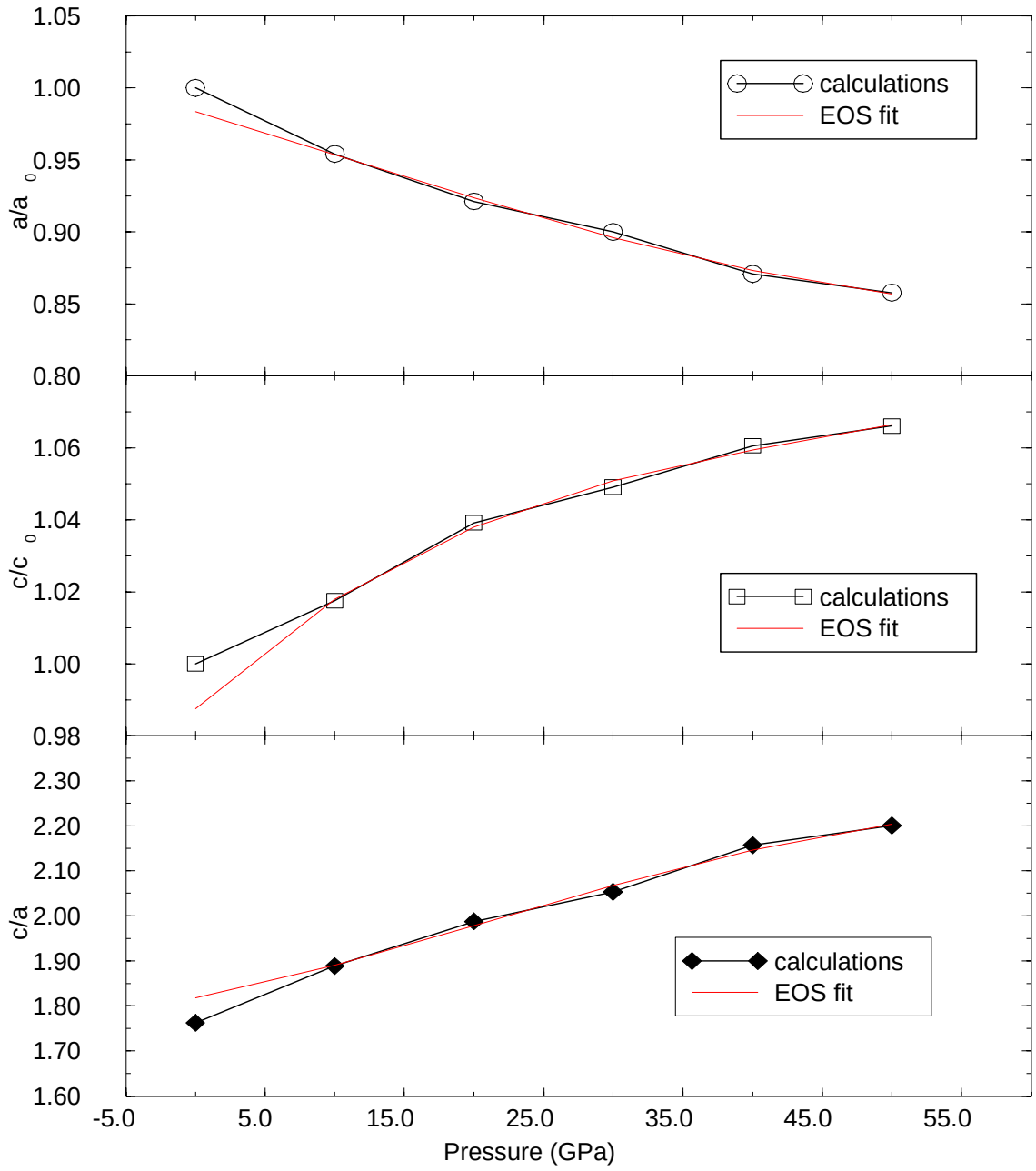


Figure 3.4: The relative lattice constant $a/a_0$, $c/c_0$ and c/a of PtS as a function of pressure.

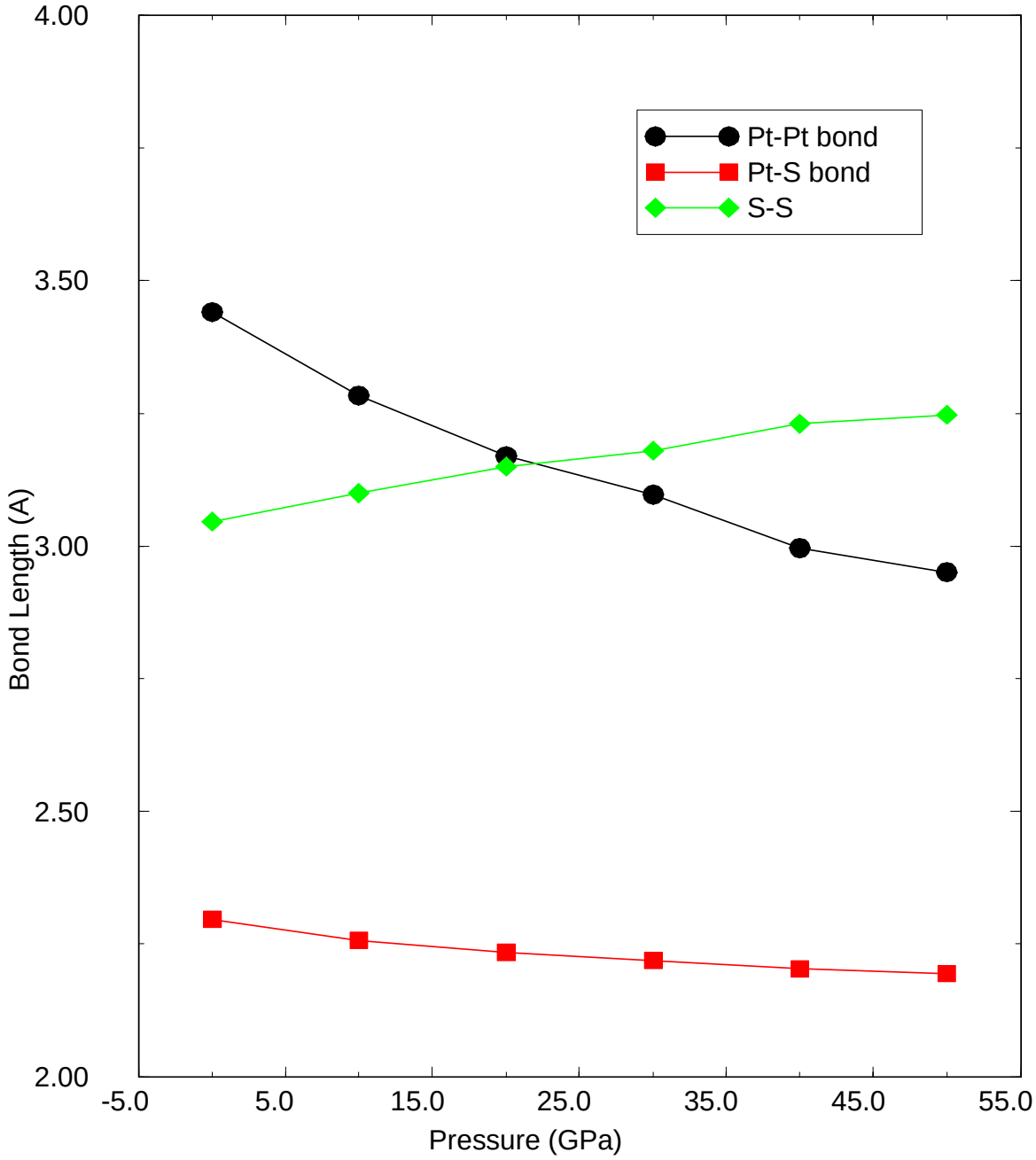


Figure 3.5: The calculated hydrostatic pressure response of the bond lengths for PtS.

length with increase in pressure, and the S-S bond length increases with the increase in the pressure. This gives a good account of the unusual behaviour of relative lattice constant c and $c/c_0$ as the pressure increases.

Table 3.3: Experimental and calculated bond lengths of PtS at equilbrium volume.

| Bond Lengths | Calculated | Experimental [1] |
|---|---|---|
| Pt-S (Å) | 2.297 | 2.31 |
| Pt-Pt (Å) | 3.46 | 3.47 |
| S-S (Å) | 3.44 | 3.47 |

### 3.3.2 Braggite $PdPt_3S_4$

In order to study qualitatively the electronic structure of braggite, we have replaced all (Pt, Ni) mixed experimental positions by platinum atoms. It is also important at this stage to mention that most of the minerals used for measurements are not absolutely pure. $PdPt_3S_4$ has five structural parameters: two lattice constants a and c , and internal parameters u = 0.3121, v = 0.1903 and w = 0.2267. $PdPt_3S_4$ was optimized at several pressures up to 50GPa enforcing its tetragonal symmetry throughout the simulations. Fig. 3.6 shows the decrease in the lattice parameters a and c with respect to the applied pressure. The calculated zero pressure structural parameters are in excellent agreement with the experiment (table 3.1 ). The theoretical values are slightly larger than the experimental values due probably to the different atomic sizes between platinum and nickel. The calculated pressure-volume data were fit to the third-order Birch-Murnaghan equation of state (fig. 3.7). The value of the deduced bulk modulus is presented in table 3.1. Presently, there is no experimental value for the bulk modulus of $PdPt_3S_4$. The normalized lattice parameters $a/c_0$ , $c/c_0$ and c/a as a function pressures were computed and the results are displayed in fig. 3.8. These normalized parameters are observed to decrease with an increase in pressure. The plots of relative lattice constant $a/a_0$ and $c/c_0$ as a function of pressure are fitted to a Murnaghan equation of state or equation 3.1, from which we obtain bulk moduli of $B_a$, $B_c$ and the derivative of the bulk moduli at zero pressure $B'_a$ and $B'_c$, and the compressility $\kappa_a$ and $\kappa_c$, respectively and the results are shown in table 3.4. There is no experimental value for the bulk modulus of $PdPt_3S_4$, presently.

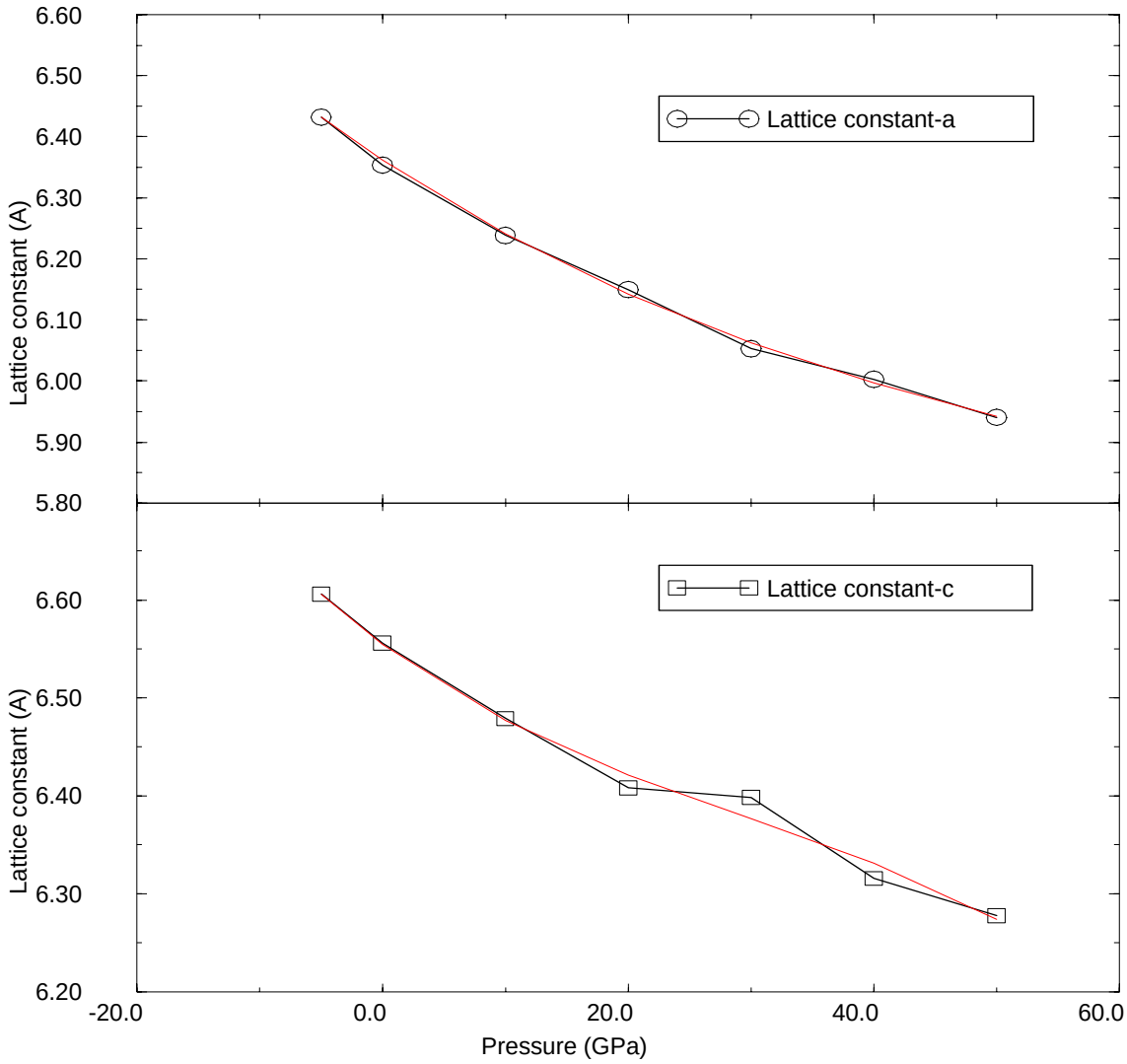


Figure 3.6: Lattice constant of $PdPt_3S_4$ as a function of pressure: open circle represents the calculated values and solid red line curve fitting.

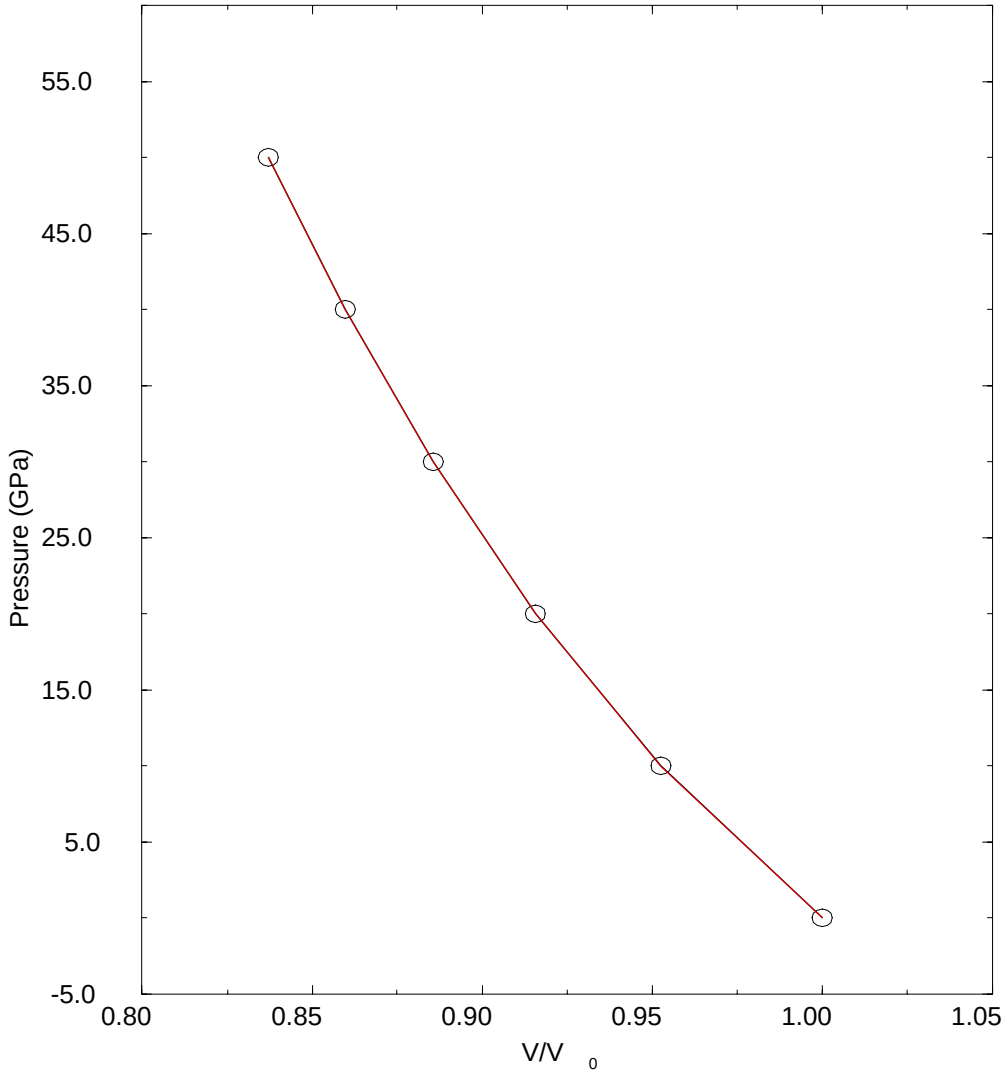


Figure 3.7: The calculated equation of states of $PdPt_3S_4$.The red solid line represents the curve fit and open circle calculated value.

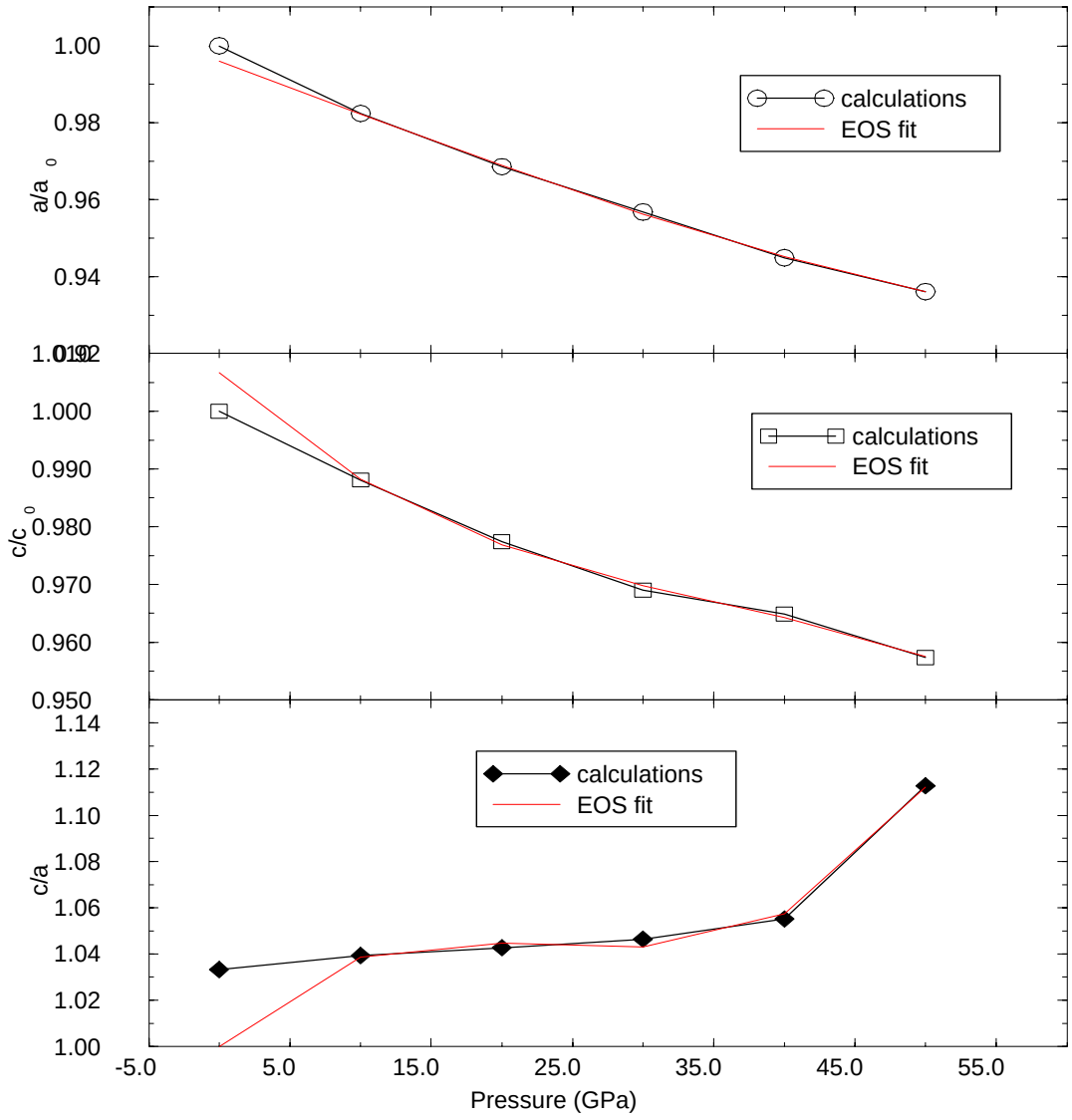


Figure 3.8: The relative lattice constant $a/a_0$, $c/c_0$ and c/a of $PdPt_3S_4$ as a function of pressure.

Table 3.4: First- and second-order axial compression coefficients of $PdPt_3S_4$ calculated using Castep pseudopotential method. $B_0^{-1}$ is the linear compressibility at zero pressure and $B^{'}$ is the pressure derivative of B.

| $B_a$(a-axis)GPa | $B_c$(c-axis)GPa | $B_a^{'}$(a-axis) | $B_c^{'}$(c-axis) | $\kappa_a$ $10^{-3}$GPa$^{-1}$ | $\kappa_c$ $10^{-3}$GPa$^{-1}$ |
|---|---|---|---|---|---|
| 370.3 | 874.77 | 16.2 | 12.8 | 2.7 | 1.14 |

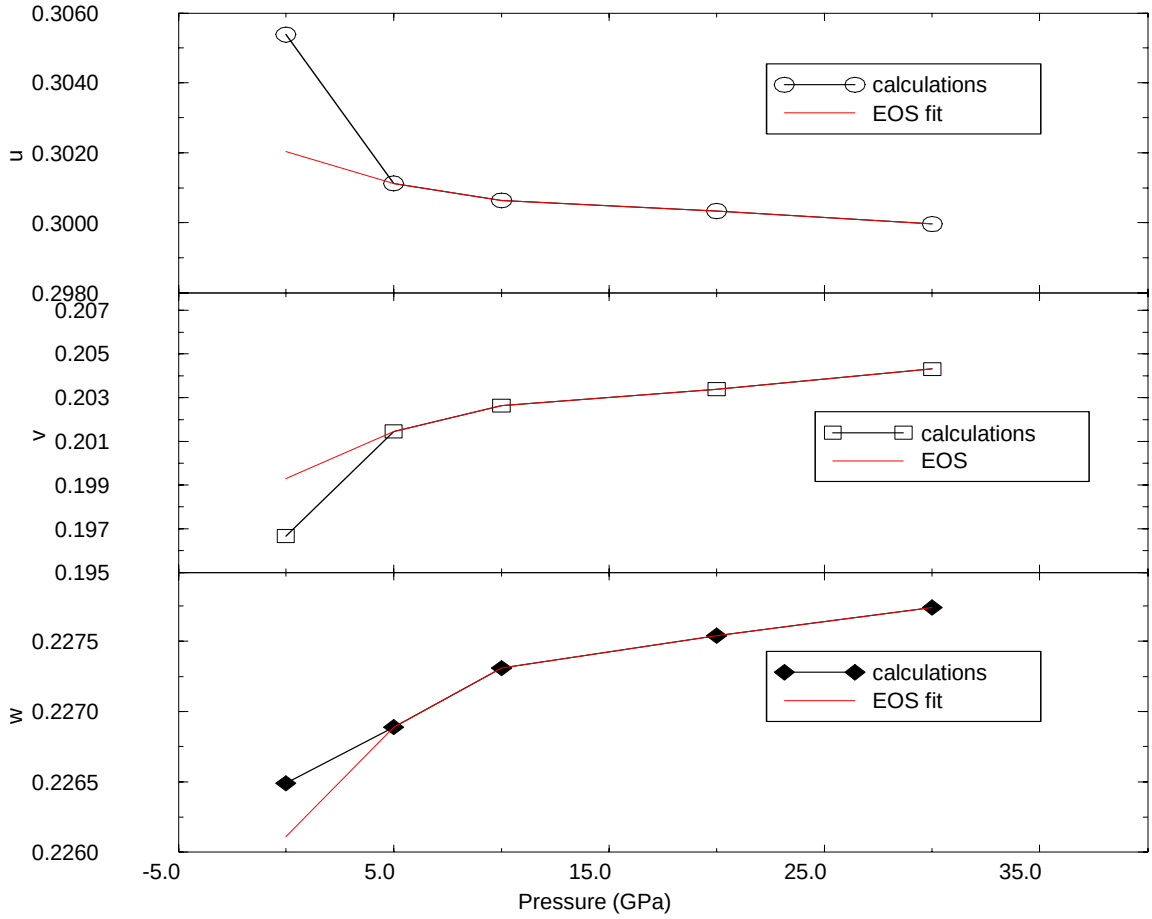


Figure 3.9: The pressure dependence of the internal parameter u, v and w of $PdPt_3S_4$.

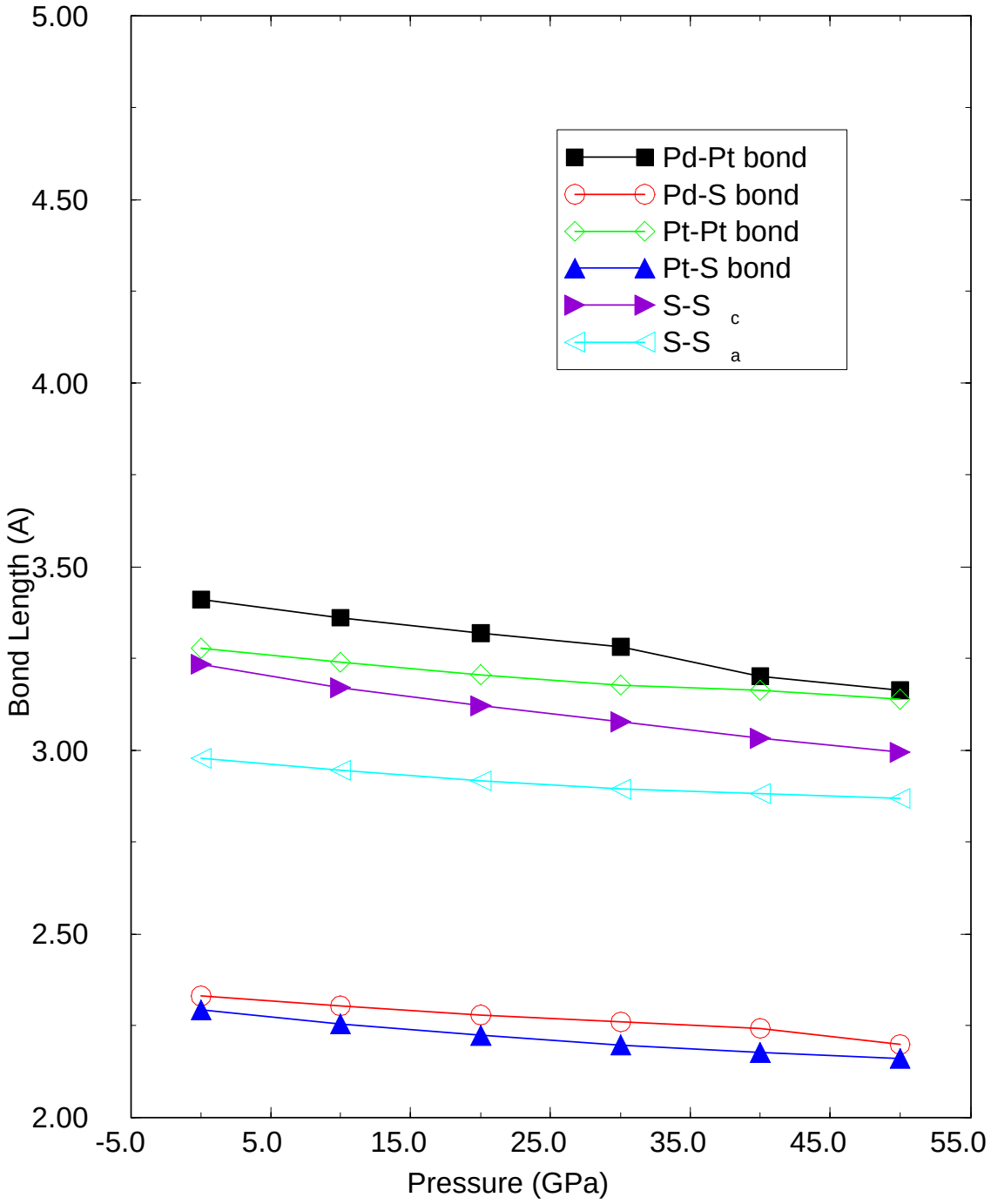


Figure 3.10: The calculated hydrostatic pressure response of the bond lengths for $PdPt_3S_4$ (where S-$S_a$ and S-$S_c$ are bond lengths along a- and c-axis).

The gradient of c/a vs hydrostatic pressure shows that the lattice constant, a, reduces faster than lattice constant c. We are unaware of previous calculations of these parameters in $PdPt_3S_4$. The pressure dependence of the atomic positional parameters have also been studied. We next consider the internal structural parameters at ambient pressure. The relaxed internal parameters of $PdPt_3S_4$ as predicted by our pseudopotential calculations at equilibrium geometry (0GPa), u = 0.3053, v = 0.1966, w = 0.2264 compare well to the experimental value of u = 0.3121, v = 0.1903 and w = 0.2267. As seen from fig. 3.9, the internal parameter u decreases with increase in pressure and both v and w increase with increase in pressure. The calculated and experimental bond lengths for $PdPt_3S_4$ (braggite) at equilibrium pressure are shown in table 3.5 and compare well. The Pt-S bond length in $PdPt_3S_4$ is longer than in PtS, whereas the Pt-Pt bond length in $PdPt_3S_4$ is shorter. Fig. 3.10 shows the variation of bond lengths with respect to the applied pressure. Again here, the bonds decrease with the increase in the pressure. The bond length Pd-Pt decreases faster than the Pt-Pt, Pt-S, S-$S_a$, S-$S_c$ and Pd-S bond lengths. At above 30GPa a small steep decrease in the bond Pd-Pt, Pd-S, and generally a reduced decrease in the bonds lengths Pt-S, Pt-Pt and S-Sa, were observed.

Table 3.5: Experimental and calculated bond lengths of $PdPt_3S_4$ at equilbrium volume.

| Bond Length | Calculated | Experimental [1] |
|---|---|---|
| Pt-S (Å) | 2.332 | 2.335 |
| Pd-S (Å) | 2.301 | 2.301 |
| Pt-Pt (Å) | 3.278 | 3.278 |

### 3.3.3 Sperrylite ($PtAs_2$)

The crystal structure of sperrylite ($PtAs_2$) is similar to that of iron pyrite ($FeS_2$). Moreover, since the total number of valence electrons per formula unit is the same for both compounds, we can expect the formation of a semiconductor gap in $PtAs_2$ as is observed in $FeS_2$.

The calculated zero pressure structural parameters are shown in table 3.1 and compare well with experimental results. Figure 3.11 gives the decrease of the lattice constant with pressure, and similar experimental results are

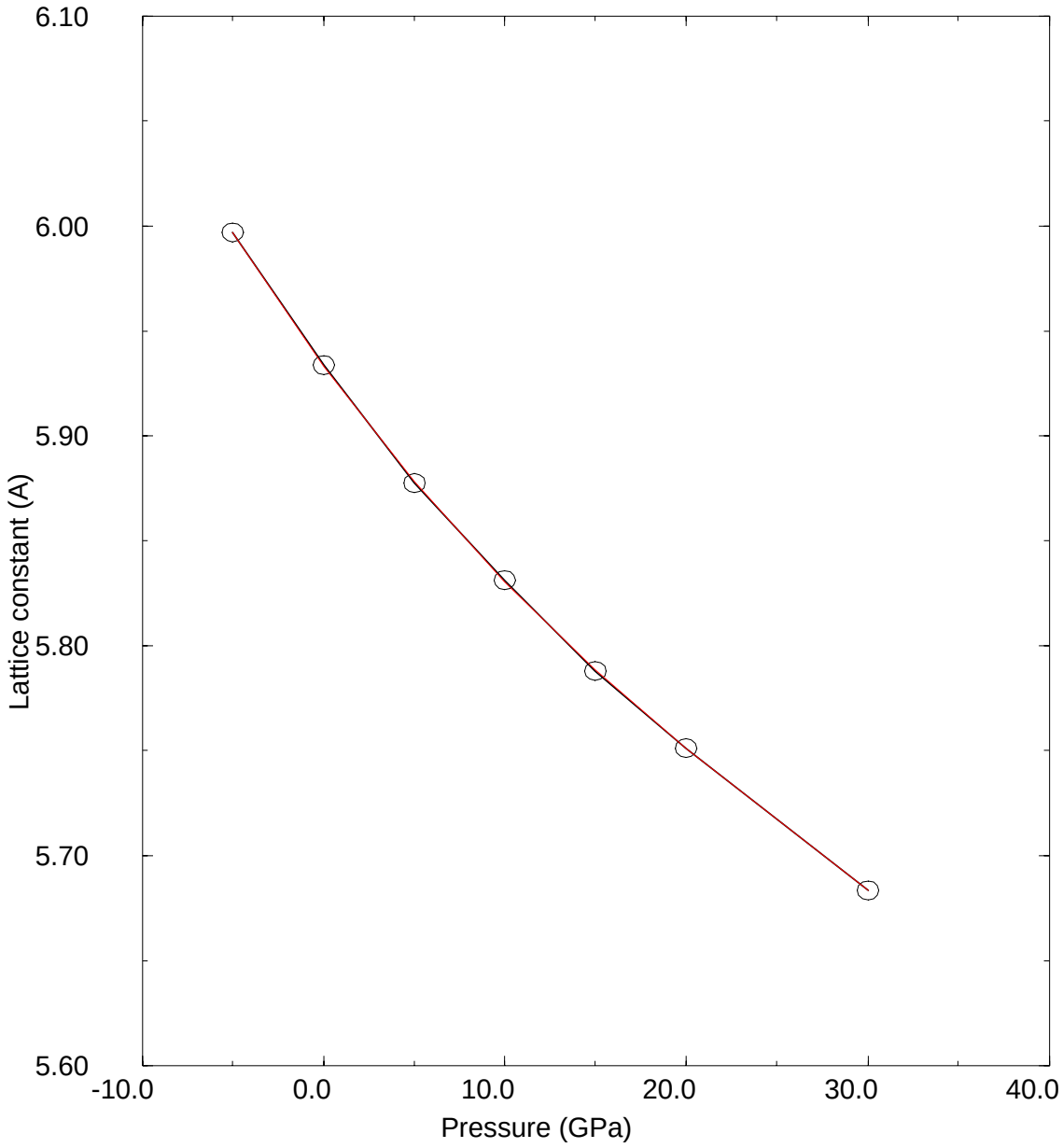


Figure 3.11: Lattice constant of $PtAs_2$ as a function of pressure: open circle represents the calculated values and solid red line curve fitting.

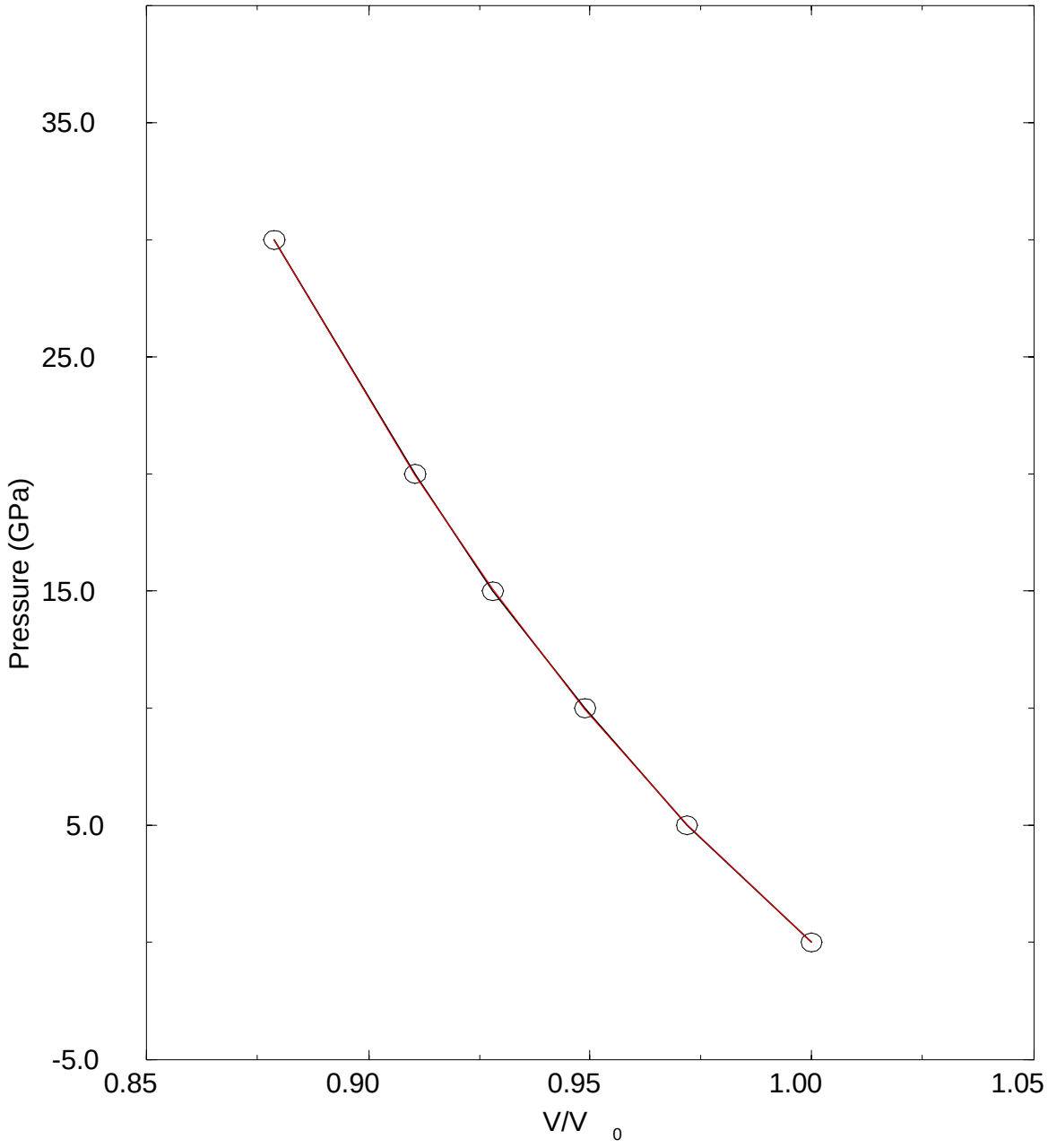


Figure 3.12: The calculated equation of states of $PtAs_2$. The red solid line represents the curve fit and open circle calculated value.

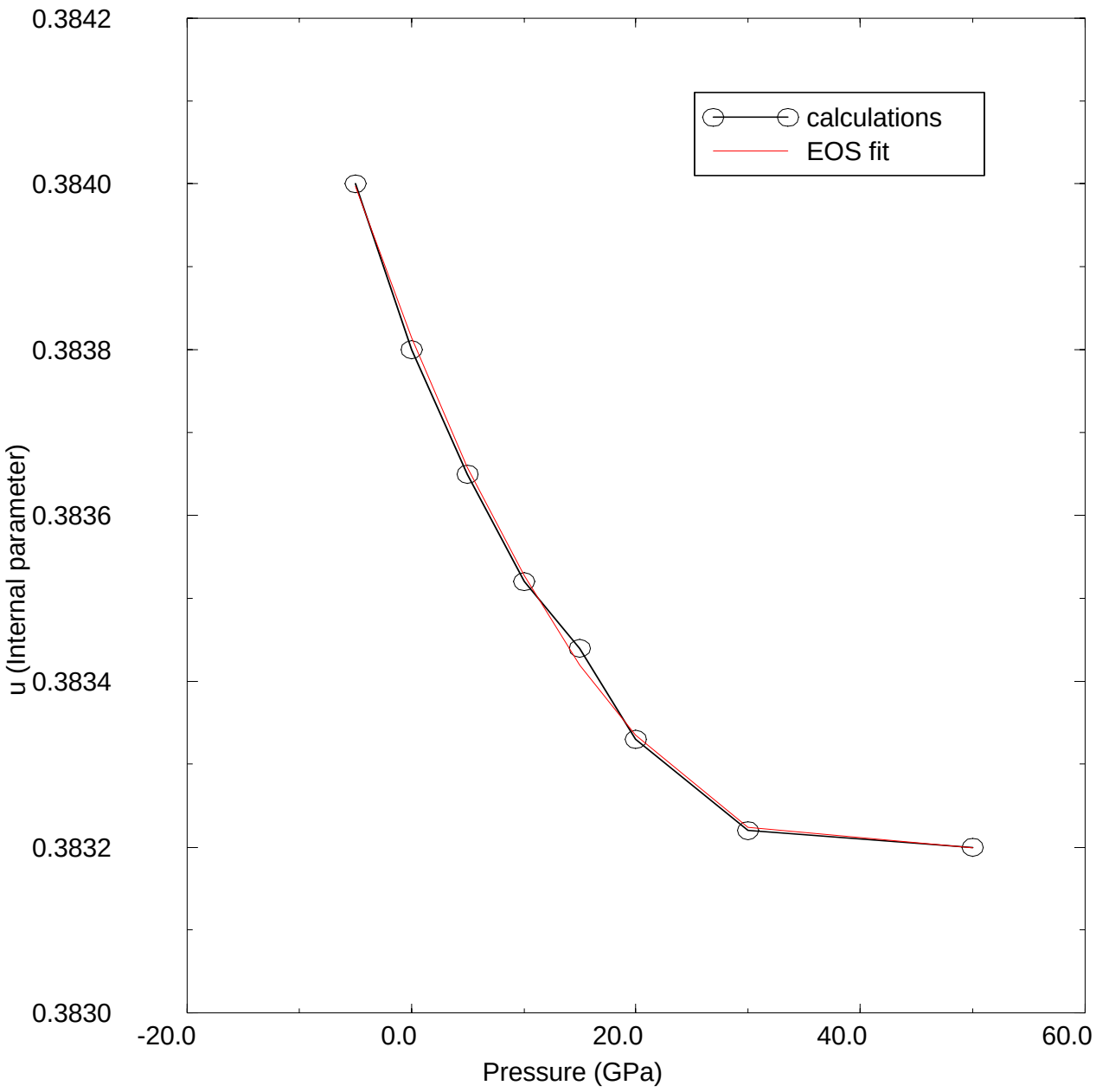


Figure 3.13: The pressure dependence of the internal parameter of $PtAs_2$.

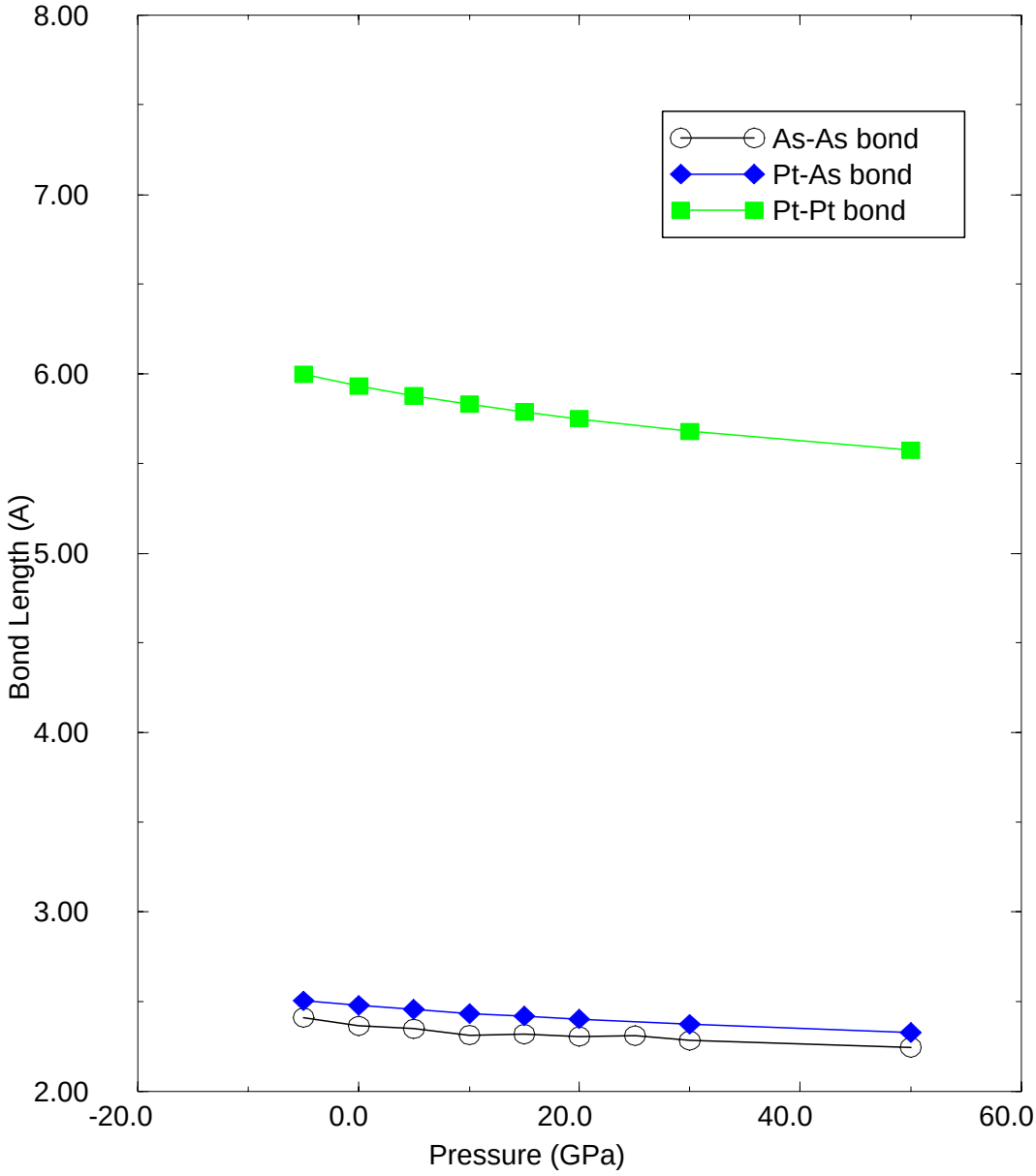


Figure 3.14: Bond lengths in sperrylite ($PtAs_2$) as a function of the applied hydrostatic pressure.

not yet available. EOS of $PtAs_2$ where pressure is plotted as a function of normalized volume is shown in fig. 3.12. At every unit cell volume the atomic positional parameters were relaxed and the unit cell parameters were also optimized to minimize enthalpy. Thus, the curve represents the hydrostatic pressure response of $PtAs_2$. The value of the deduced bulk modulus is shown in table 3.1, and again related experimental value has not yet been measured.

The relaxed internal $PtAs_2$ structure, as predicted by our calculations at equilibrium geometry (0GPa), corresponds to positional parameters given by the equilibrium value u = 0.383 and compares well to the experimental value of 0.384. Fig. 3.13 gives the decrease of the internal parameter with pressure, and a reduced change is noted above 30GPa.

Table 3.6: Experimental and calculated bond lengths of $PtAs_2$ at equilbrium volume.

| Bond Lengths | Calculated | Experimental [1] |
|---|---|---|
| Pt-As | 2.479 | 2.498 |
| Pt-Pt (Å) | 5.932 | 5.986 |
| As-As (Å) | 2.364 | 2.417 |

It is found that the optimized value of u decreases with increasing pressure due to the Pt-Pt bond length decreasing more rapidly than As-As and Pt-As bond lengths, as seen in fig. 3.14.

### 3.3.4 Platarsite ($Pt_4As_4S_4$)

The calculated zero pressure structural parameters are in excellent agreement with the experiment (table 3.1). Fig. 3.15 gives the decrease of the lattice constant with pressure, and similar experimental results are not yet available. The calculated cell parameter is roughly 1% larger than the corresponding room temperature value, since most of minerals used for measurement are not absolutely pure. The calculated pressure as a function of reduced volume is shown in fig. 3.16, and the curve represents an equation of state of $Pt_4As_4S_4$. The value of the deduced bulk modulus is shown in table 3.1, and again related experimental value is not yet available. The pressure dependence of the internal atomic positional parameters has also been studied. Fig. 3.17 shows the decrease of the internal parameter, u, of $Pt_4As_4S_4$ with the applied pressure. The calculated equilibrium value of the internal paramater u is

found to be 0.3826 and compares well to the experimental value of 0.3858. The optimised value of u decreases with increasing pressure due to the Pt-As and Pt-S bond length decreasing more rapidly than the As-S bond length as noted in the fig. 3.18.

The optimized bond lengths for both $PtAs_2$ and $Pt_4As_4S_4$ structure at equilibrium pressure are shown in table 3.6 and 3.7, respectively. The bond lengths Pt-As and Pt-Pt in $PtAs_2$ are longer than of $Pt_4As_4S_4$. Fig. 3.18 shows the variation of bond lengths of $Pt_4As_4S_4$ with respect to the applied pressure. Again here, the bonds decrease with the increase in the pressure. The bond length Pt-S decreases faster than Pt-As and As-S bond lengths.

Table 3.7: Experimental and calculated bond lengths of $Pt_4As_4S_4$ at equilbrium volume.

| Bond Length | Experimental | Calculated [1] |
|---|---|---|
| Pt-S(Å) | 2.483 | 2.498 |
| Pt-As(Å) | 2.451 | 2.498 |
| As-S(Å) | 2.266 | 2.417 |
| Pt-Pt(Å) | 5.882 | 5.986 |

## 3.4 Conclusion

We have performed highly precise calculations of the total energy of the major representatives of PGM as a function of the lattice constant, preserving their symmetries. The agreement of the calculated lattice constants with experiment are very good, and show that the Castep pseudopotential method, used under local density approximation, does not lead to larger than usual discrepancies for these systems. We also managed to carry out full total energy relaxations in order to predict the P-V equations of state, which have yielded bulk moduli of the studied systems. The variation of PtS bond lengths with respect to the applied pressure were computed. In PtS both Pt-Pt and Pt-S bond lengths decrease with increase in pressure, while S-S bond length increase with the increase in the pressure. This gives an account of the unusual behaviour of relative lattice constant c and $c/c_0$ which increase as the pressure increases. We have also shown the pressure response of the internal parameters for $PdPt_3S_4$, $PtAs_2$ and $Pt_4As_4S_4$. It is clear that the internal

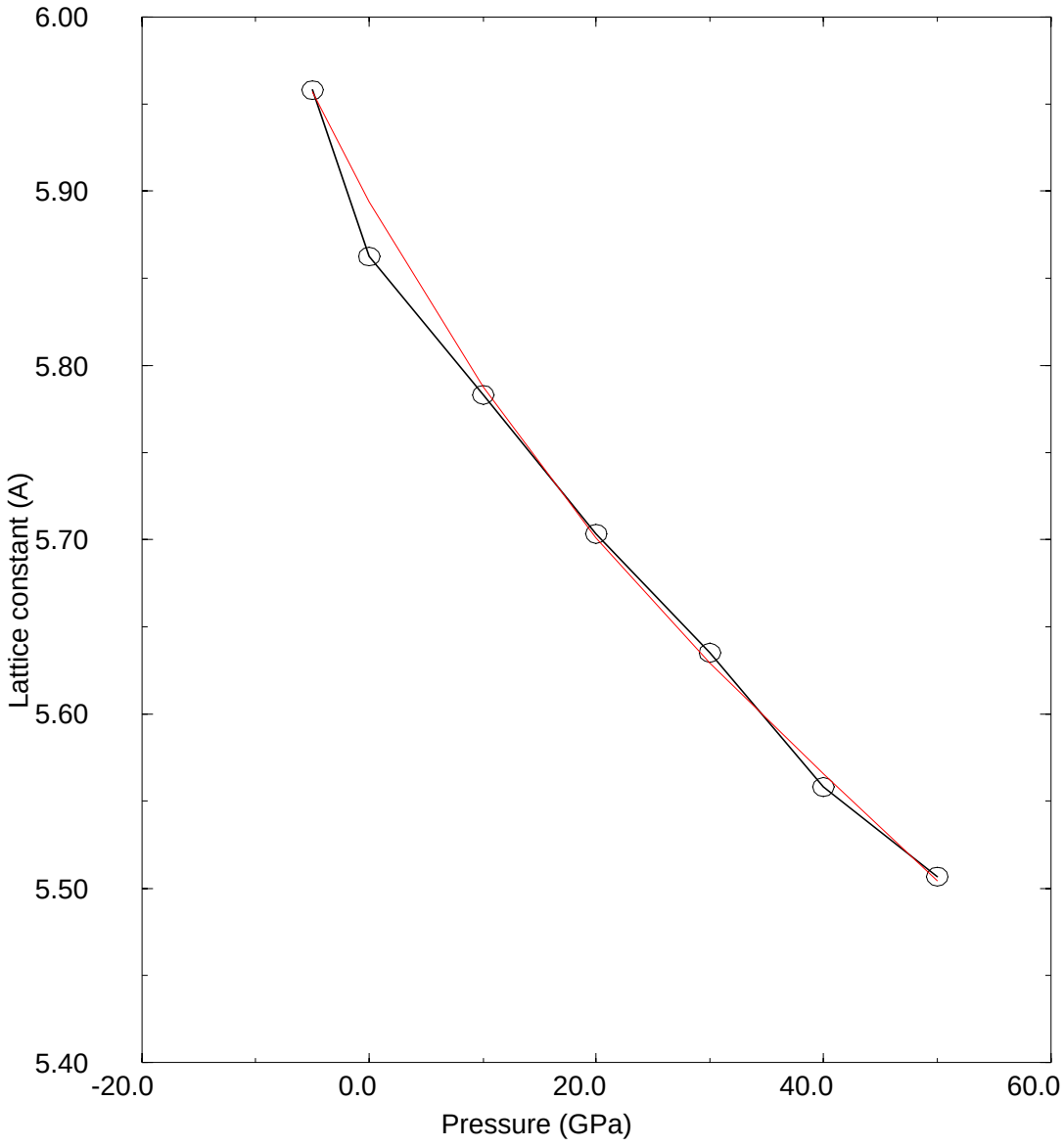


Figure 3.15: Lattice constant of $Pt_4As_4S_4$ as a function of pressure: open circle represents the calculated values and solid red line curve fitting.

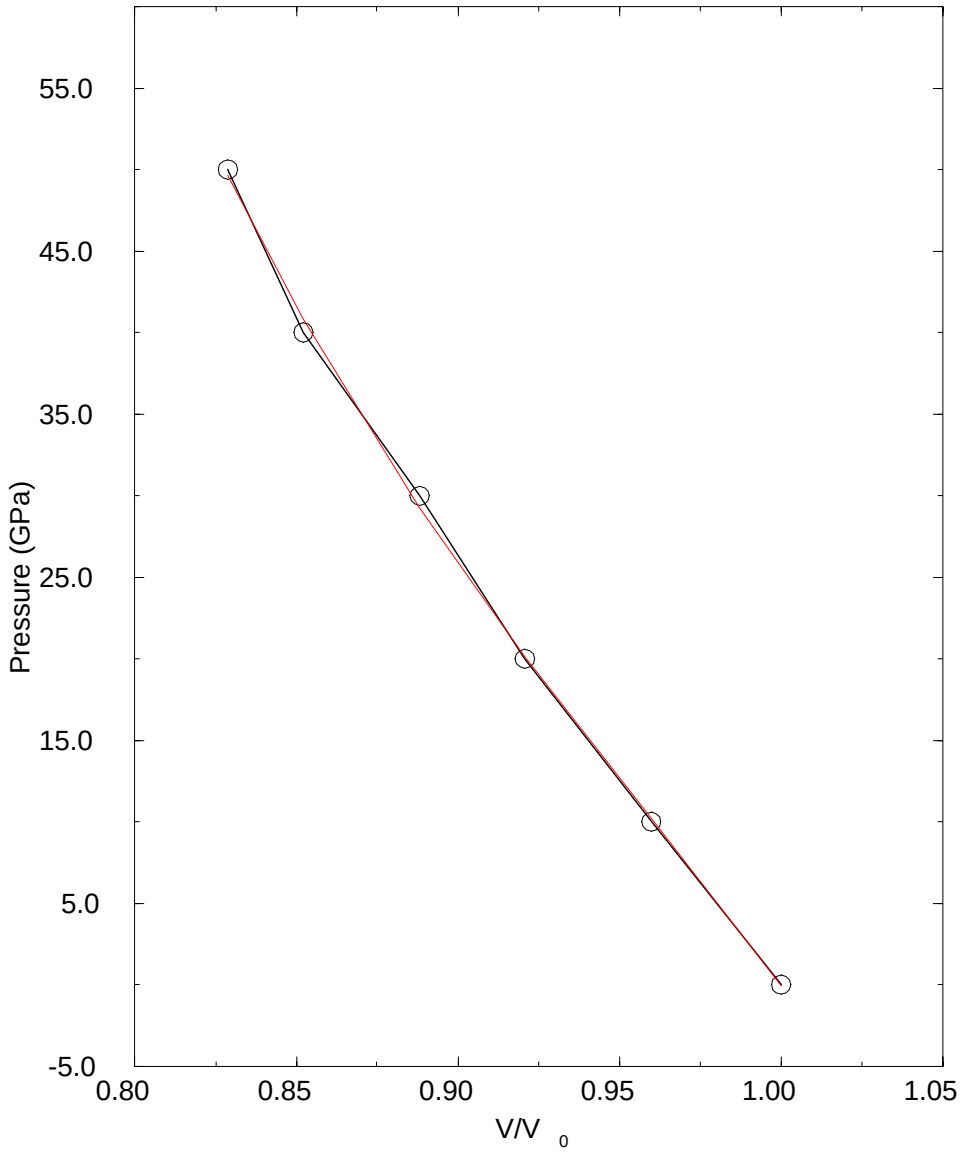


Figure 3.16: The calculated equation of states of $Pt_4As_4S_4$.The red solid line represents the curve fit and open circle calculated value.

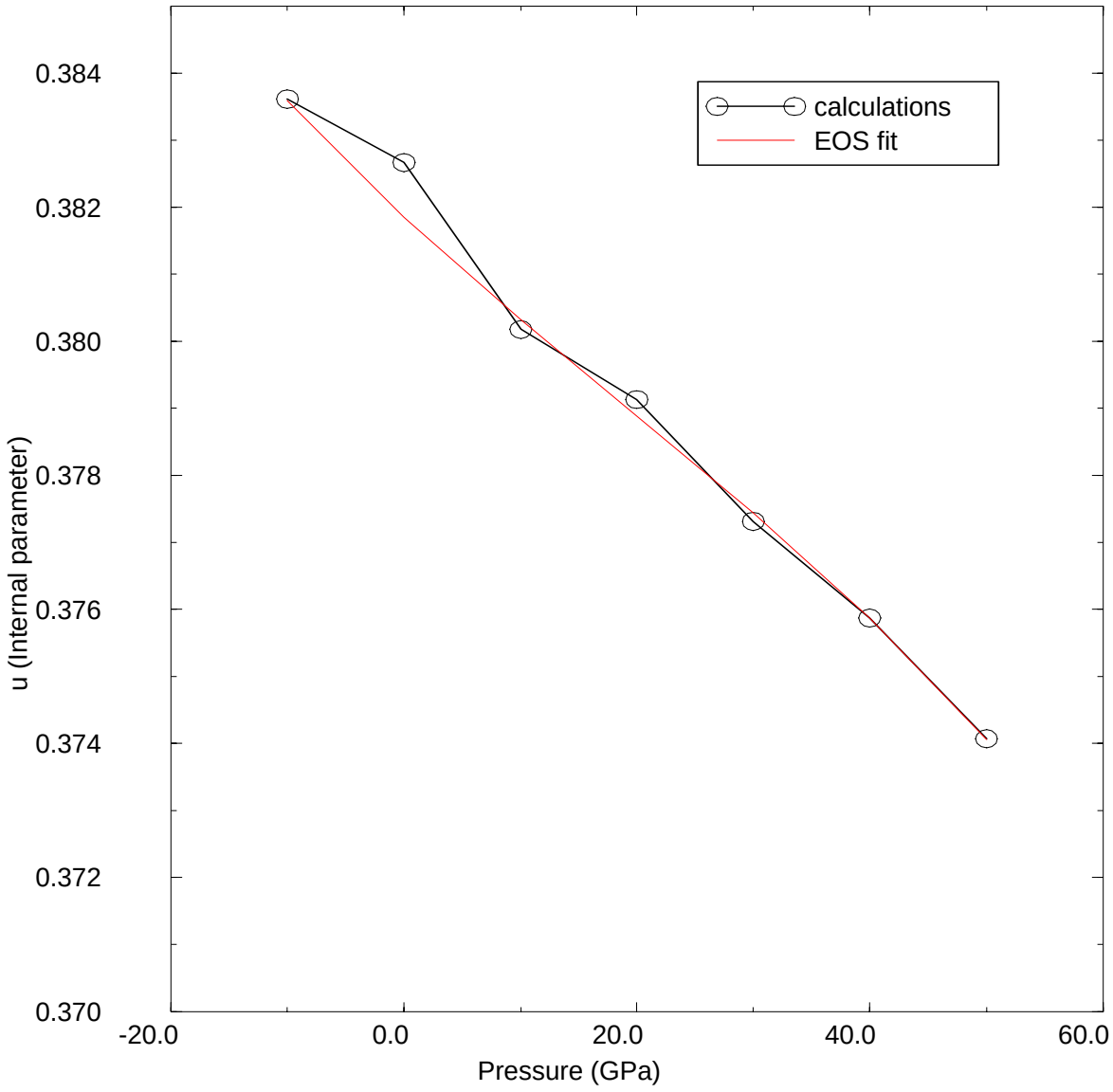


Figure 3.17: The pressure dependence of the internal parameter of $Pt_4As_4S_4$.

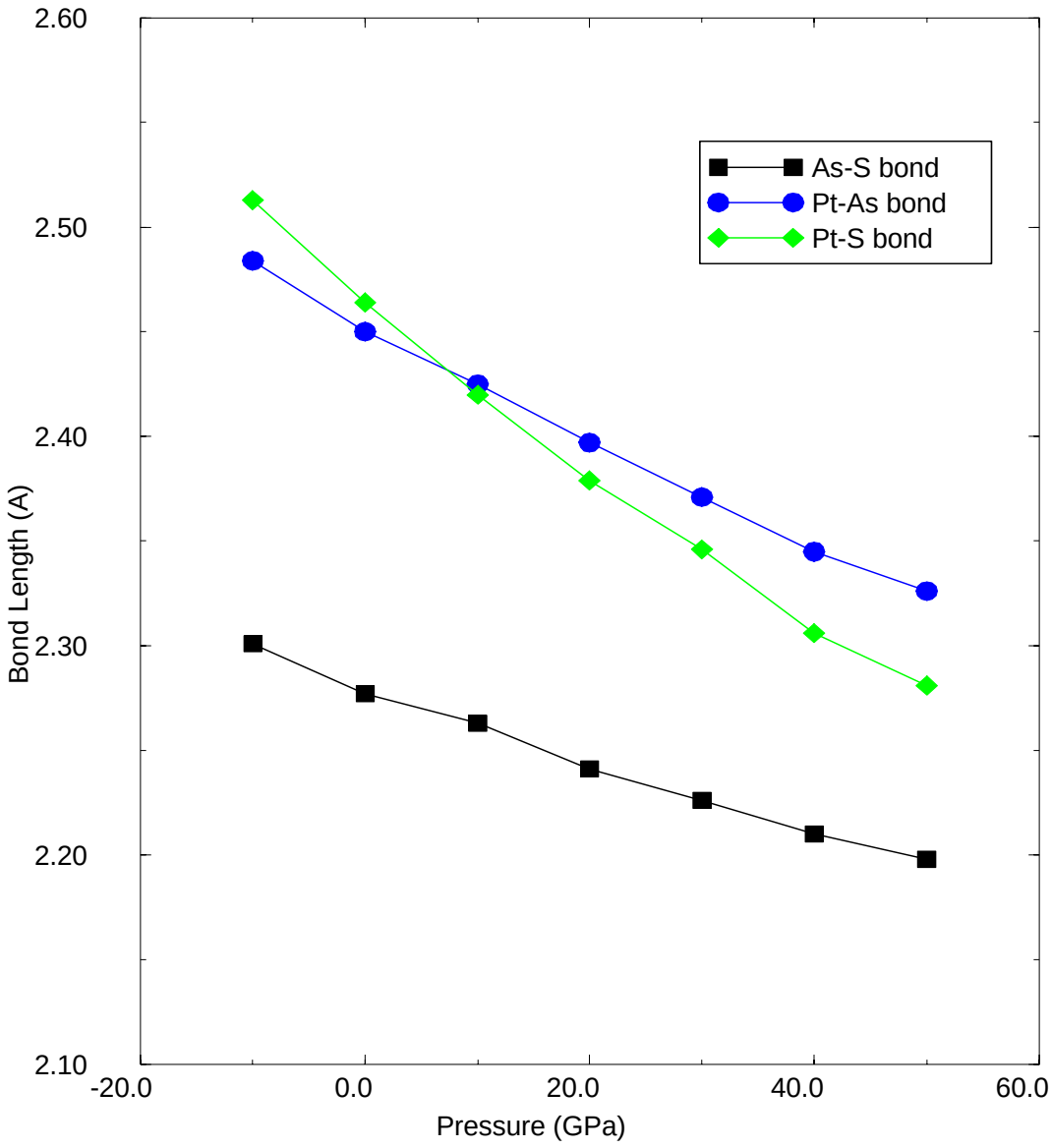


Figure 3.18: The calculated hydrostatic pressure response of the bond lengths for $Pt_4As_4S_4$.

parameter (u) for $PdPt_3S_4$, $PtAs_2$ and $Pt_4As_4S_4$ decreases with increase in pressure, while v and w (internal parameters) for $PdPt_3S_4$ increase with increase in pressure. We hope that these theoretical calculations will stimulate further experimental work on the equations of state and bulk moduli. It is only when these results are available, particularly bulk moduli that a comparison with our theoretical values could be able to asses the effects of LDA on the theoretical description of these quantities.

# Chapter 4

# ELECTRONIC AND OPTICAL PROPERTIES

## 4.1 Introduction

Most metal sulfides are not translucent and incident light is partly absorbed and partly reflected by them. A few sulfide minerals which are opaque in the visible range do not absorb radiation in the near-infrared region of the spectrum. Optical absorption spectra arise from the excitation of the valence electrons from the ground to higher excited energy states in the crystal. Thus, the peaks in the spectra can be assigned to particular excitations with the valence electronic structure. We have performed SCF calculations using both TB-LMTO and Castep planewave pseudopotential methods to predict electronic structures of these minerals. We shall, also present the response of the electronic energy band structures, densities of states, optical reflectivity and optical absorption at different pressures.

### 4.1.1 TB-LMTO-ASA

The method of TB-LMTO has been employed to calculate self-consistently the structure and electronic properties of cooperite, braggite, sperrylite and platarsite. The detailed procedure has already been discussed in chapter 2. Since this method uses the atomic sphere approximation (ASA), we had to insert empty spheres into open structures of PtS, $PdPt_3S_4$, $PtAs_2$ and $Pt_4As_4S_4$, which leads to 2 and 5 new empty sphere symmetry positions per unit cell in order to fill space between the atomic positions within the PtS

and $PdPt_3S_4$, respectively. For tetragonal PtS ( $P4_2/mmc$) the positions of atoms are generated by Pt:(2c) $(0.0, 0.5, 0.0)$ and S:(2e) $(0.00, 0.00, 0.25)$, and the additional two empty sphere symmetry centres E1:(2a) $(0.5, 0.0, 0.0)$ , E2:(2f) $(0.50, 0.50, 0.25)$. For also tetragonal $PdPt_3S_4$ ($P4_2/m$) Pd:(2d) $(0.0, 0.5, 0.5)$ , (Pt)1:(2e) $(0.00, 0.00, 0.25)$, (Pt)2:(4j) $(0.2572, 0.4667, 0.0000)$, S:(8k) $(0.3121, 0.1903, 0.2267)$, and the additional five empty spheres positions E1:(2f) $(0.50, 0.50, 0.25)$, E2: (4j) $(-0.0149, 0.2430, 0.0000)$, E3: (4j) $(0.1909, 0.0324, 0.0000)$, E4: (4j) $(0.4731, -0.3043, 0.000)$, E5:(8k)$(0.0939, 0.3897, 0.2516)$. Regarding sperrylite $PtAs_2$, its structure type is identical to that of pyrite with cubic space group symmetry Pa-3, and atoms are located at Pt : (4a) $(0.0, 0.0, 0.0)$ and As : (8c) $(u, u, u)$ with $u = 0.383$. Additional empty spheres are placed at E :(24d) $(x, y, z)$ , with x = 0.31681, y = 0.09448 and z = 0.21362. The cubic structure of platarsite, with space group of Pa-3, has metal atoms (Pt) at (4a) ( 0.0, 0.0, 0.0) and As : (8c) $(u, u, u)$ , S :(8c) $(u, u, u)$ with $u = 0.3858$. Additional empty spheres were placed at E :(24d) $(x, y, z)$ . The basis set of our calculations consisted of Pt 6s, 6p, 5d; Pd 5s, 5p, 4d; S 3s, 3p, 3d; As 4s, 4p, 4d with 1s, 2p states for the interestitial empty sphere. All k-space integrations were performed by the tetrahedron method [81] . The convergence to self-consistency was achieved with grid of 60, 18, 11 and 12 irreducible k points. Subsequently 315, 90, 119 and 384 k points were used to calculate the total energy and the densities of states (DOS) for PtS, $PdPt_3S_4$, $PtAs_2$ and $Pt_4As_4S_4$, respectively. In all calculations, convergence was deemed to have been achieved when tolerance in the total energy was $10^{-2} mRy$ per unit cell.

## 4.2 Electronic Properties

### 4.2.1 Cooperite (PtS)

The valence electronic configuration of Pt is $5d^6 6s^1$, and that of S is $3s^2 3p^4$. Since Pt is tetrahedrally cordinated by four S atoms, the d-orbital splits into two (e) and three ($t_2$) states, where the $e$ states are lower in energy than the $t_2$ states due to the tetrahedral field from the S atoms. In both low and high spin configurations, the electrons are located at $(e)^4(t_2)^5$.

The corresponding band structure and density of states at ambient pressure calculated using both TB-LMTO and Castep are presented in figs. 4.1 and 4.2, respectively. The TB-LMTO calculations indicate that PtS is a

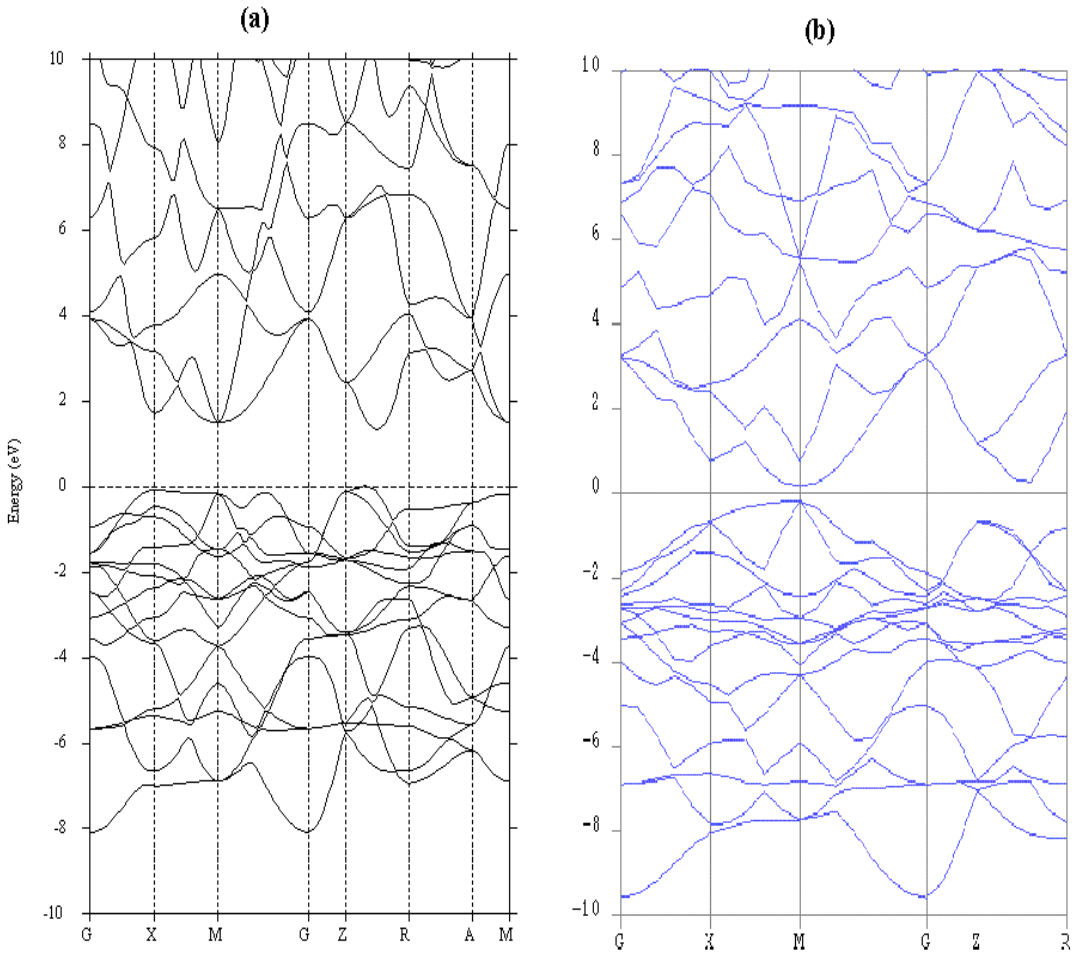


Figure 4.1: Self-consistent band structure of PtS at equilibrium volume along high symmetry lines between -10 eV and 10 eV. The zero of energy is at the top of the valence band. The calculations were done using both (a) TB-LMTO and (b) Castep.

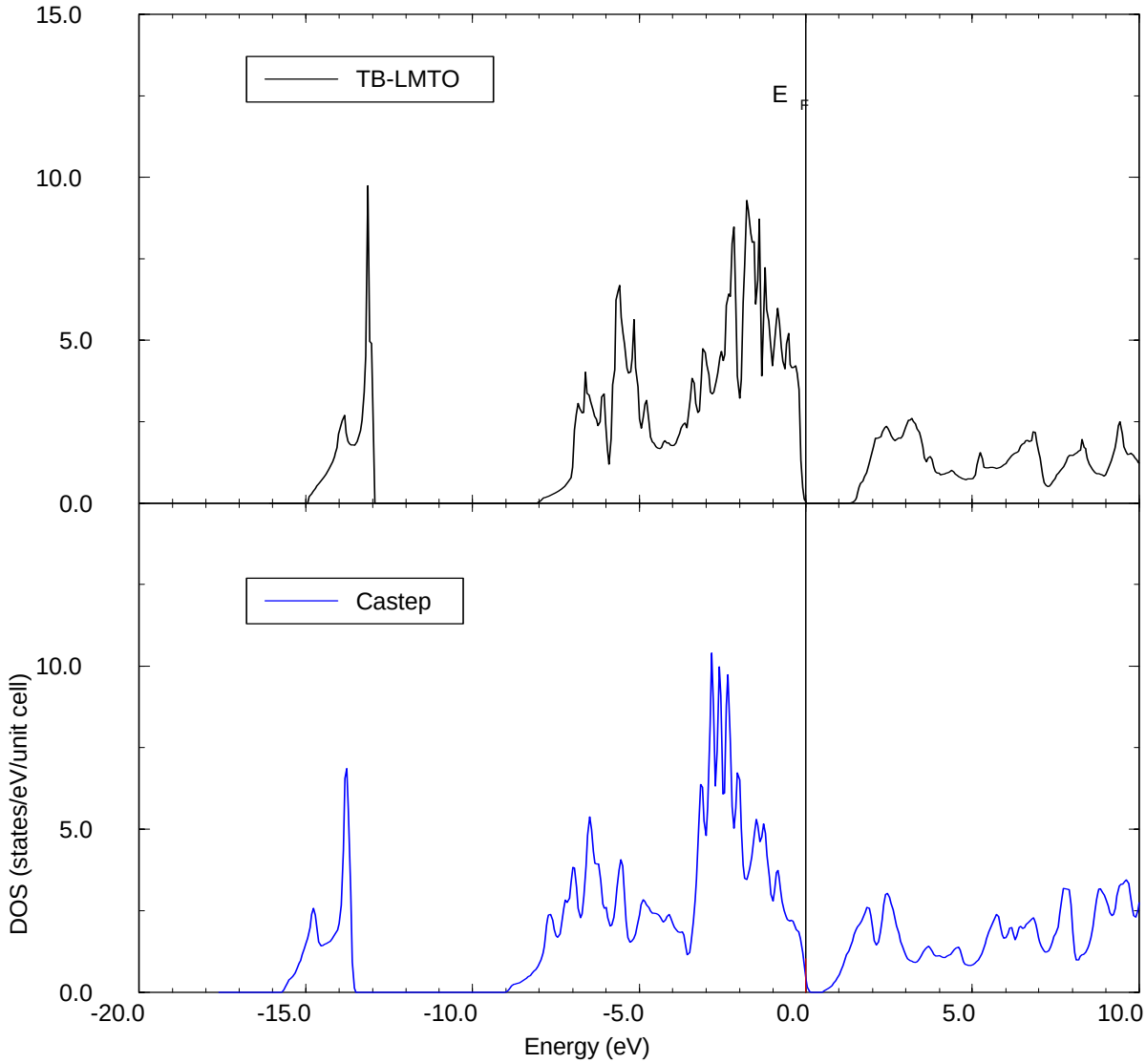


Figure 4.2: Total density of states for PtS at equilbrium volume as calculated using both TB-LMTO and Castep .

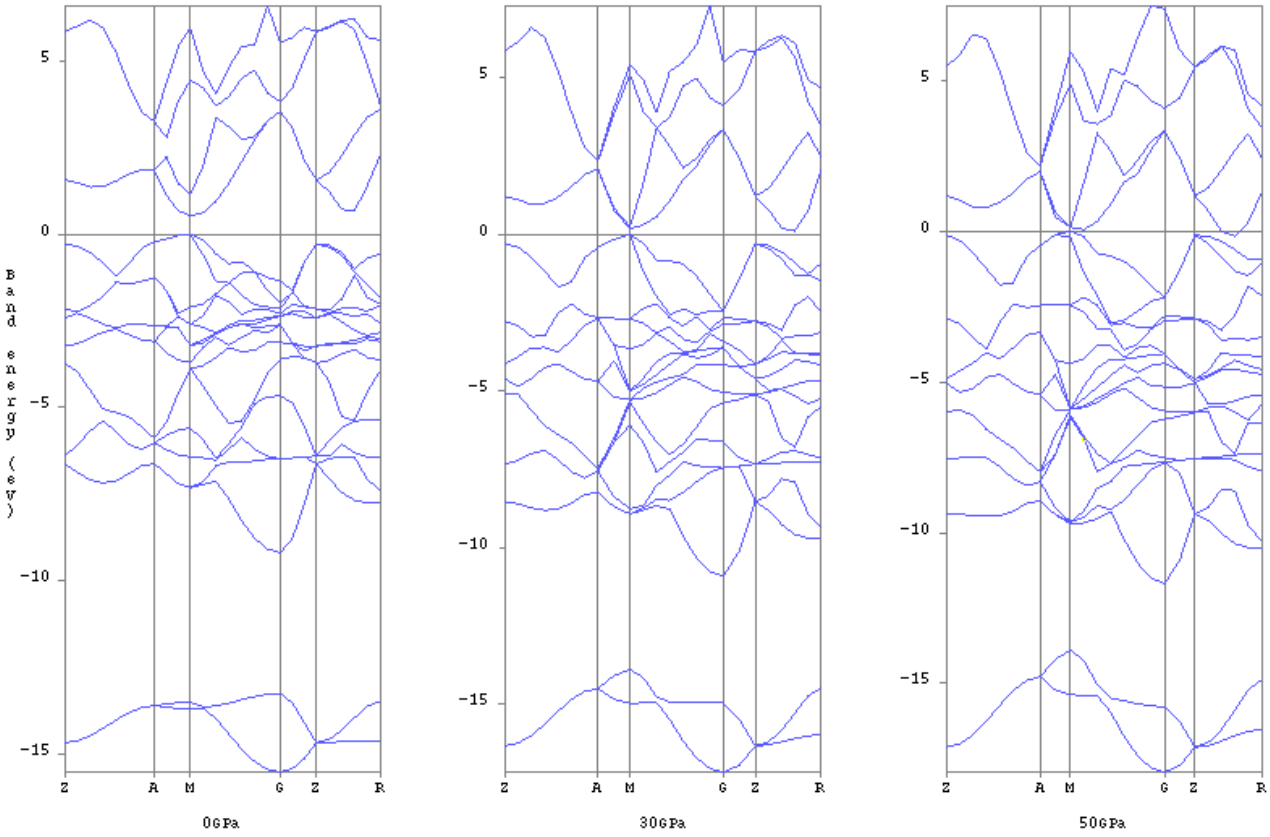


Figure 4.3: Evolution of the valence electron band structure of PtS as determined at 0, 30 and 50 GPa respectively. It is evident that a pressure-induced closure of the indirect band gap is predicted in these calculations (Castep).

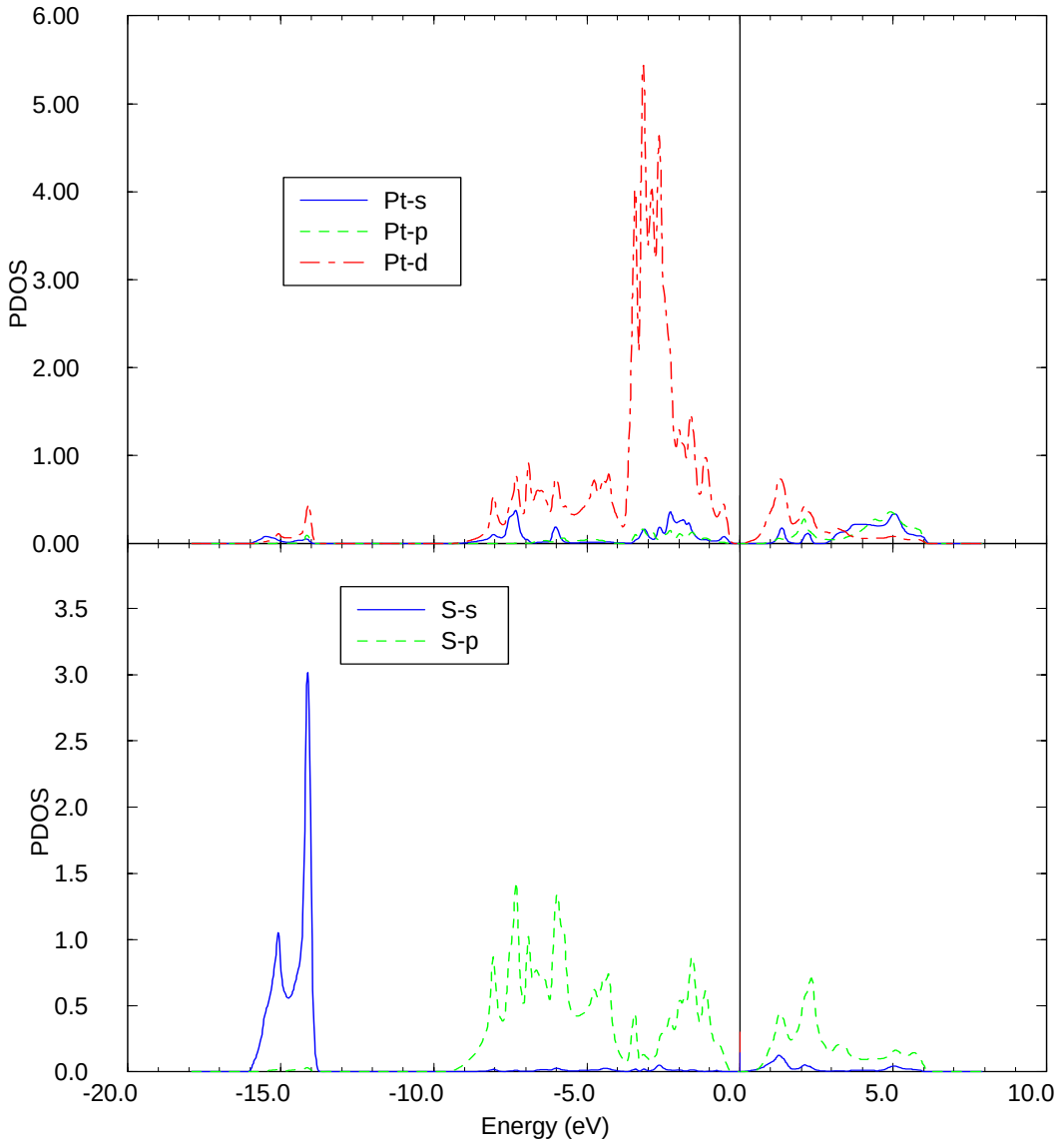


Figure 4.4: Calculated partial densities of states for PtS at 0GPa (Castep).

Figure 4.5: Calculated partial densities of states for PtS at 50GPa (Castep).

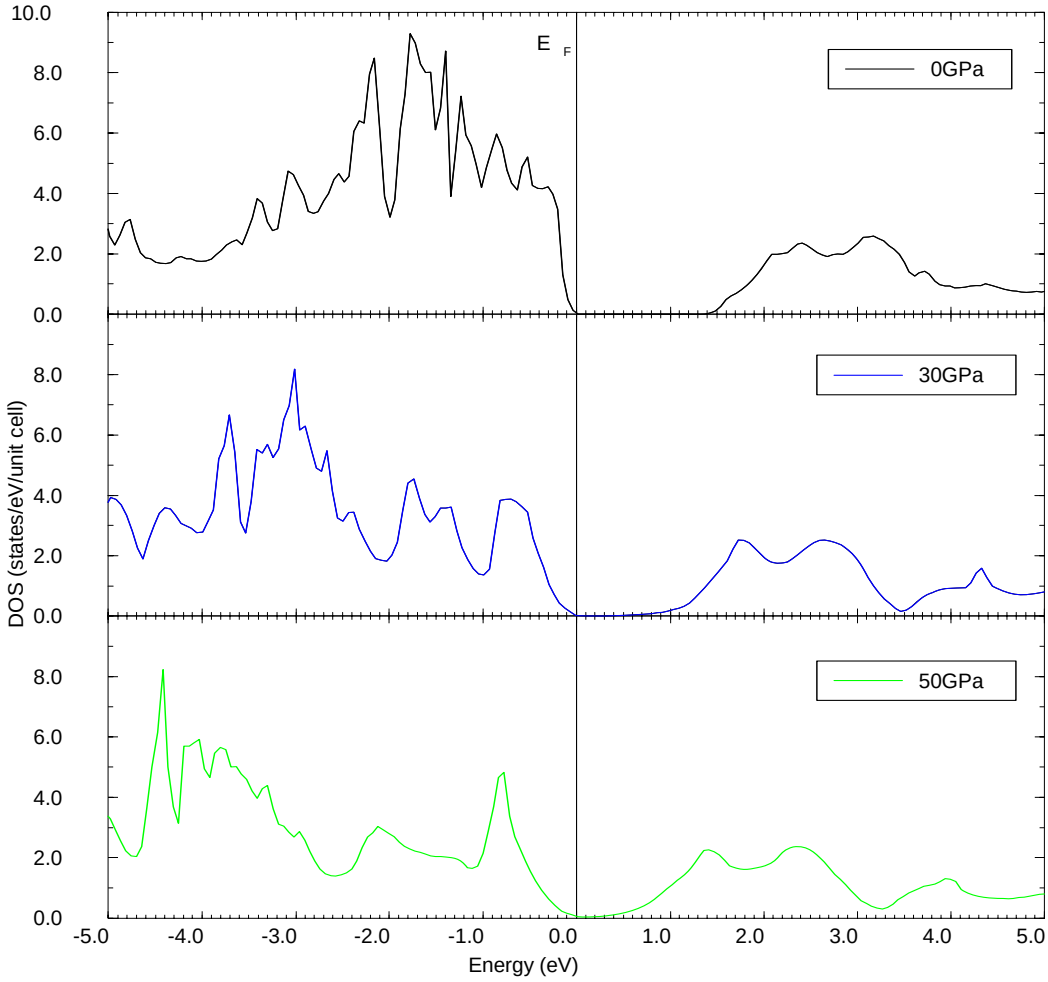


Figure 4.6: Total density of states for PtS projected around the Fermi level indicating the closure of the band gap induced by pressure variation calculated using TB-LMTO method.

semiconductor with an indirect band gap of 1.31 eV, with the band extrema located near between $ZR$ and $M$ point, respectively. The non metallic behaviour of PtS can be inferred from experiment where diffuse-reflectance measurements and absorption curves indicate a second possible energy gap of 1.4 eV [16].

The electronic band structure of PtS at several pressures were calculated using pseudopotential method and the response of the electronic structure to the pressure is shown in fig. 4.3. In all cases the band structures were calculated from fully relaxed atom positions and unit cell parameters. The zero pressure structure (in fig. 4.1) is clearly a semiconductor with direct band gap of 0.4 eV with both the valence maximum and the conduction minimum being located at the M point. The presence of a direct band gap has important consequences for optical applications of a semiconductor, because the probability of electronic transitions across the band gap is higher in materials with a direct band gap. This band gap is close to the optical band gap of 0.8 eV mentioned by Hulliger [16] and slightly different from the recent plane-wave basis calculation, using Vienna ab initio simulation program (VASP) [3] where essentially a zero band gap (0.06 eV) was predicted at the Fermi energy. We believe that this difference between the Castep and VASP calculations (results) is brought about by the linear interpolation used in these Castep calculations [82, 83]. The two plots of band structures and density of states from both Castep and TB-LMTO-ASA calculations do not differ by more than details, even though the two methods used are quite different. Both methods should in principle be able to produce results close to DFT-LDA limit, without any further important approximations than the description of the exchange- correlation potential. The large difference/discrepancy between Castep (pseudopotential) and TB-LMTO-ASA band gap calculations were not expected and is somehow difficult to explain. The reason for these discrepancy may be due to the spherical averaging in the ASA. As the pressure increases the minimum of the conduction band moves to the ZR line and the gap reduces. At a calculated pressure of 50 GPa the band is closed, showing a possibility of semiconductor-metal transition. The band structure for 50 GPa shows that the lowest point in the conduction is in the ZR line which has a slightly lower energy than the M point in the valence band. The conduction band at point L would now be more occupied than the valence band in the neighbourhood of the M point.

The partial density of states calculations are shown in figs. 4.4 and 4.5, and indicate that apart from the low-lying S(3s) band, a very strong bonding

-antibonding splitting in the Pt(5d)-S(3p) band complex is the main origin of the formation of the semiconductor band gap, as has already been well documented for the case of $RuAl_2$ and $RuGa_2$ [84]. The electronic states below the Fermi level around -15eV, are dominated by S(3s) states. Hence, we emphasize again here that just as in iron disulfide pyrite and marcasite polymorphs [23, 85] the energy gap in platinum sulfide depends critically on the covalent bonding properties rather than the conventional picture of the importance of ionic bonding within transition metal sulfides. This closure of band gap is reconfirmed by the calculation of DOS of the same relaxed structure using TB-LMTO method, and the result is displayed in fig. 4.6.

### 4.2.2 Braggite ($PdPt_3S_4$)

The valence electronic configuration of Pd is $4d^{10}$ , where all the orbitals are filled. As in PtS, the Pt atoms in $PdPt_3S_4$ are tetrahedally coordinated to four S atoms, and

the d-orbital of Pt is also split into two (e) and three ($t_2$) states, where the ($e$) states are lower in energy. The spin configuration is similar to that of PtS. The band structure and total of density (DOS) of $PdPt_3S_4$, shown in figs. 4.7 and 4.8, were calculated using TB-LMTO and Castep at ambient pressure. TB-LMTO calculations have predicted a direct band gap of 0.89 eV at the $\Gamma$ point. The electronic band structures of $PdPt_3S_4$ at several pressures were calculated self-consistently by means of Castep pseudopotential method and the response of the electronic structure to the pressure is shown in fig. 4.9. In all cases the band structures were calculated from fully relaxed atomic positions and unit cell parameters. At ambient pressure, we find that $PdPt_3S_4$ has an indirect band gap of 0.21 eV, with the valence maximum at point Z and the conduction minimum being located at the $\Gamma$ which is smaller than the one obtained with TB-LMTO and there is no experimental value available to compare with. As shown in figure 4-9, the energy band gap increases with increasing pressure and the energy gap calculated at 50GPa is found to be 0.39 eV using Castep. The energy gap of 0.99 eV at the pressure of 50GPa, was calculated using TB-LMTO. The shape of total density of states of $PdPt_3S_4$ on the whole resembles that of PtS discussed in 4.3.1. A closer inspection of the partial density of states, however, shows that the main contribution to the valence band comes essentially from Pt(5d) states whereas the Pd(4d) contribution here is relatively small. Hence, we empha-

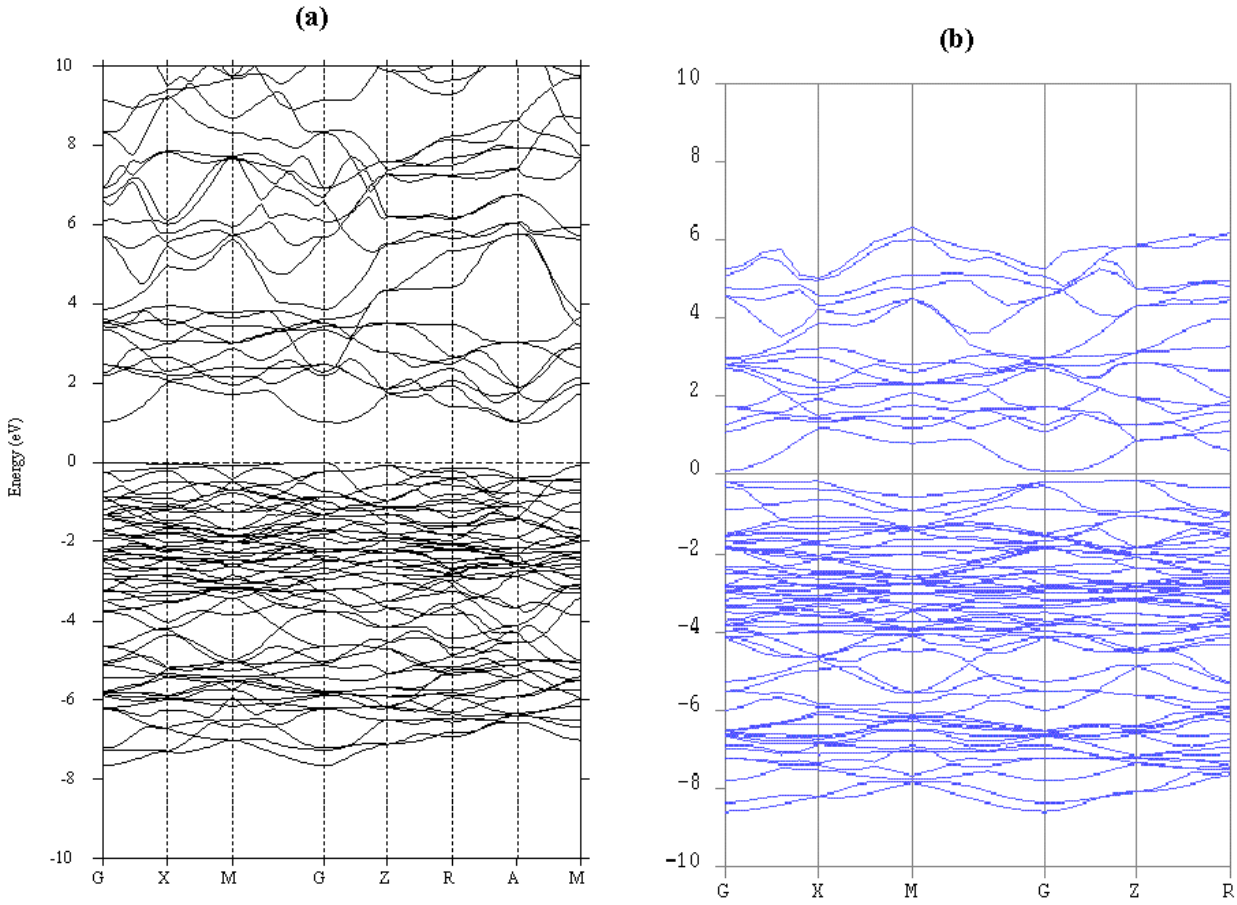


Figure 4.7: The calculated electronic band structure of $PdPt_3S_4$ crystal at the equilibrium volume along high symmetry lines plotted using (a) TB-LMTO and (b) Castep between -10 eV and 10 eV.

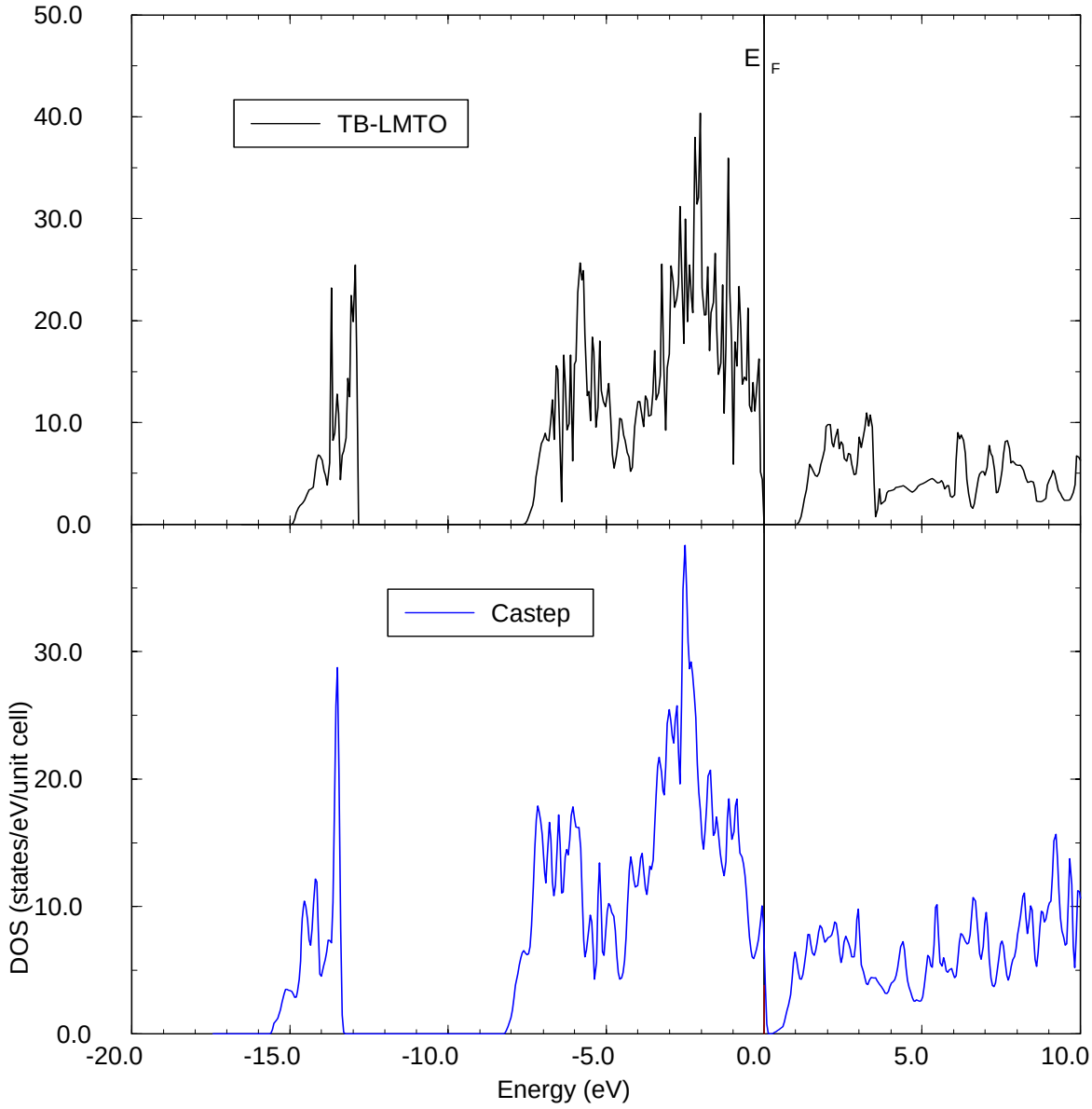


Figure 4.8: Total density of states for $PdPt_3S_4$ at equilibrium volume as calculated using both TB-LMTO and Castep methods.

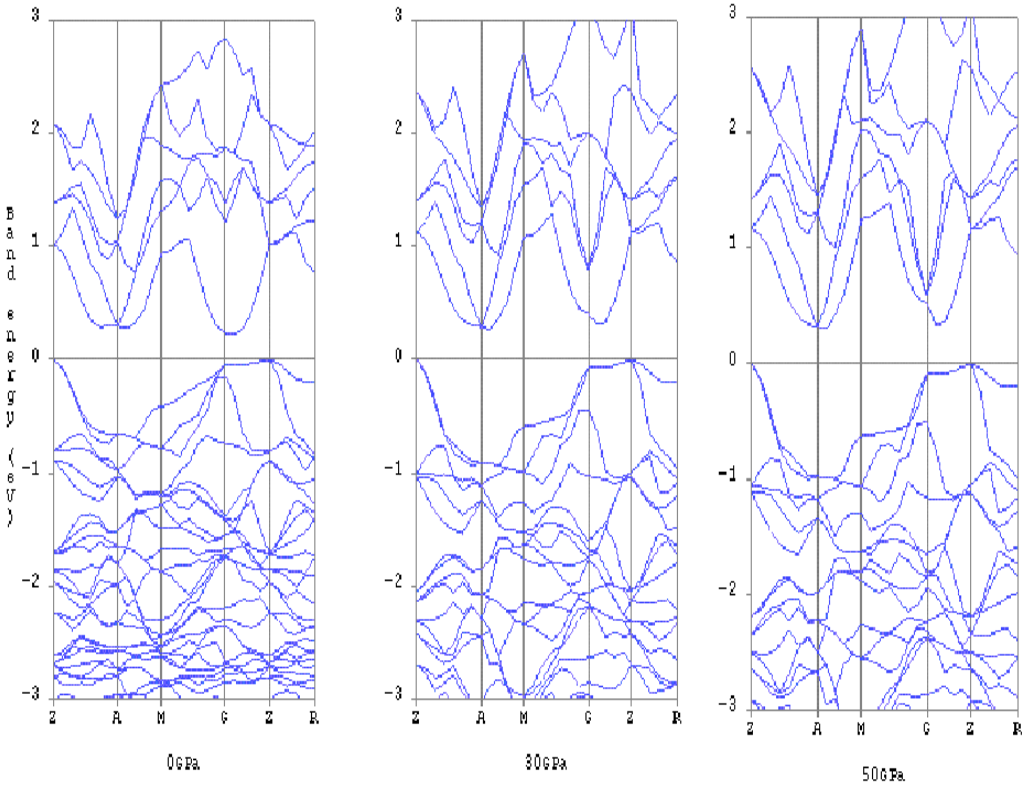


Figure 4.9: Evolution of the valence electron band structure of $PdPt_3S_4$ as determined at 0, 30 and 50 GPa respectively. This shows the widening of the band gap as the pressure increases (Castep).

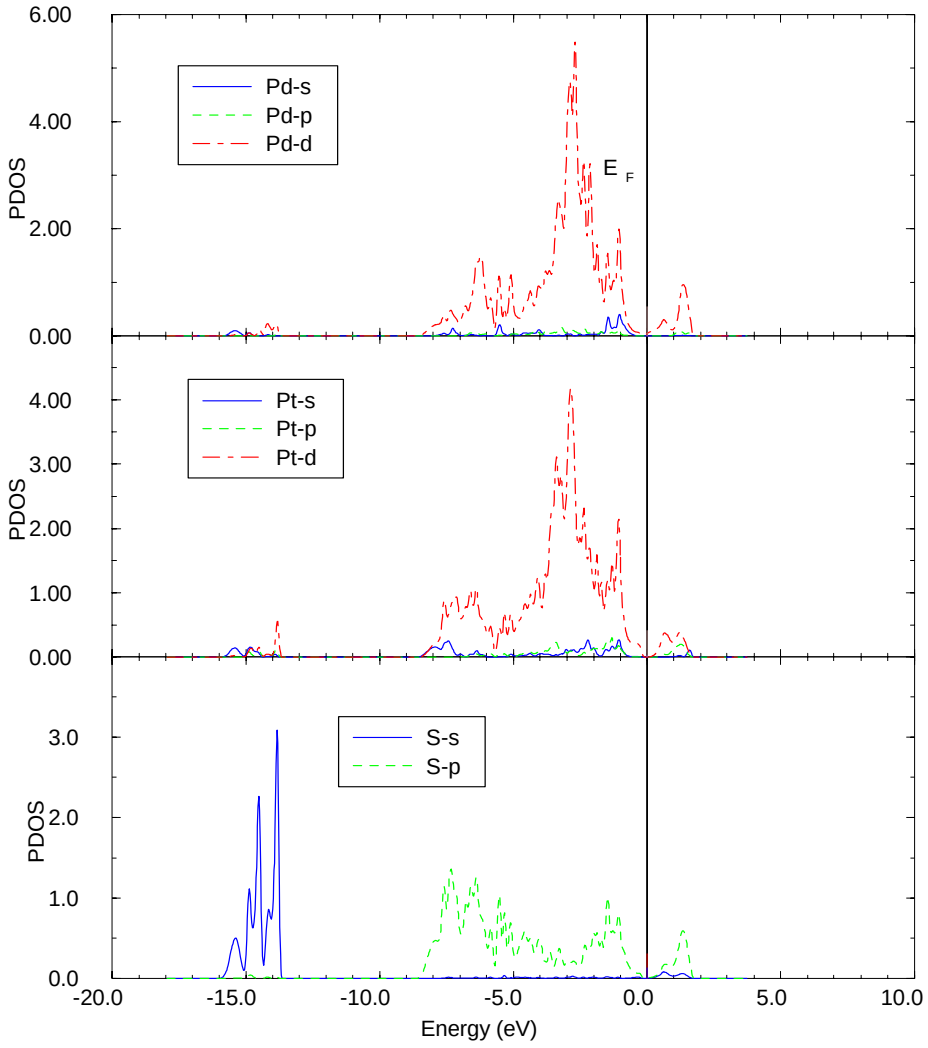


Figure 4.10: Calculated partial densities of states for $PdPt_3S_4$ at 0GPa (Castep).

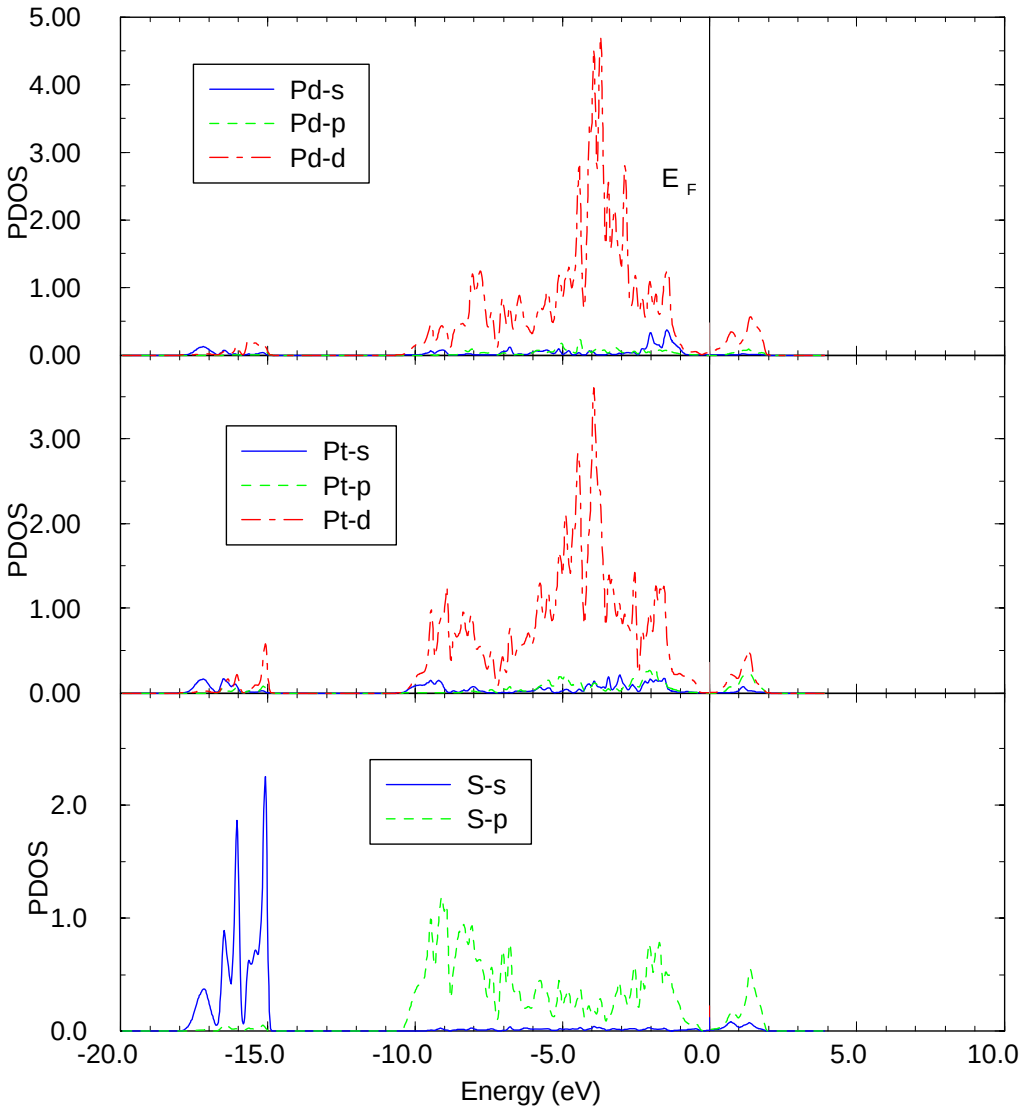


Figure 4.11: Calculated partial densities of states for $PdPt_3S_4$ at 50GPa (Castep).

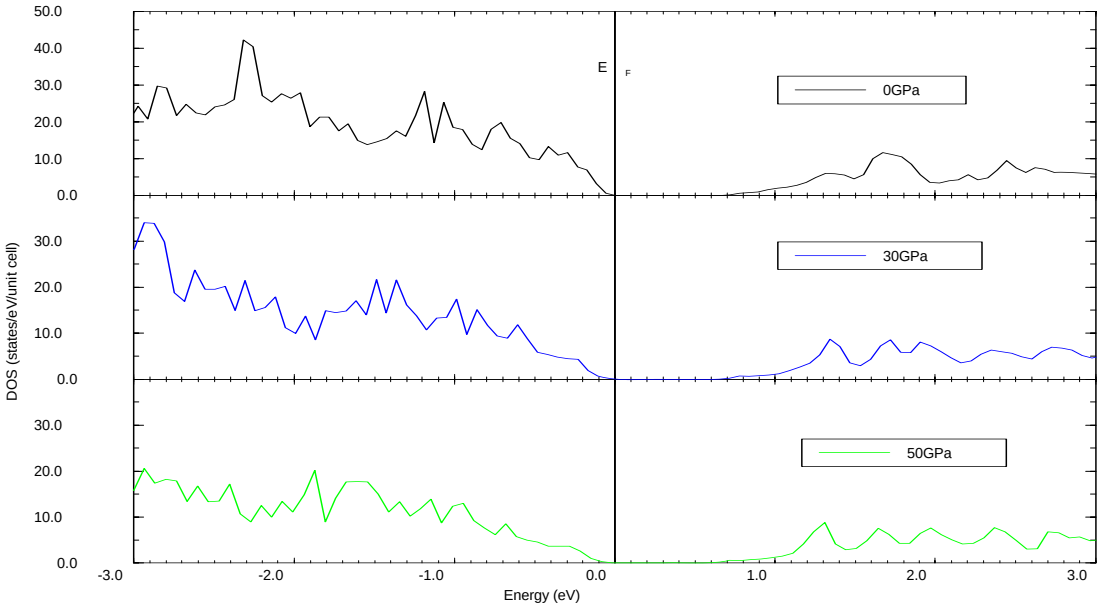


Figure 4.12: Total density of states for $PdPt_3S_4$ projected around the Fermi level to show the change in the band gap size under hydrostatic compression (TB-LMTO)

size again that as in case of PtS discussed in section 4.3.1 that the energy gap in $PdPt_3S_4$ depends critically on the bonding properties of Pt-S than the conventional picture of the crystal-field splitting within the transition metal d-band. It is evident from the bond lengths discussed in chapter 3, that Pt-S bond length in cooperite (PtS) is shorter than in braggite ($PdPt_3S_4$). Hence there is stronger Pt (5d)-S(3p) hybridization in cooperite (PtS) than in braggite ($PdPt_3S_4$). The electronic structure of PdS has been calculated in the braggite structure type in [3] where only a deep pseudogap at the Fermi energy has been found. Figs. 4.10 and 4.11 show the corresponding densities of states using Castep at pressures of 0GPa and 50 GPa, which also show band gap widening. Similar calculations were performed on the DOS using TB-LMTO to reconfirm the widening of the gap, and the results are displayed in fig. 4.12.

### 4.2.3 Sperrylite ($PtAs_2$)

The band structure and the density of states of $PtAs_2$ are shown in figs. 4.13 and 4.14, respectively and were calculated at ambient pressure using TB-LMTO and Castep. The TB-LMTO calculations yield an indirect semiconductor gap of 0.34 eV with the valence maximum between GM lines and the conduction minimum at the R point. No experimental band gap value is available, however this value is smaller than the predicted value of 0.71 eV for pyrite $FeS_2$ with a similar structure [23, 85]. As far as we know, experimental evidence for a semiconductor behaviour in $PtAs_2$ has been mentioned [1] and this calculation is the first theoretical prediction in literature. The electronic configuration of Pt is $5d^96s^1$, and that of As is $4s^24p^3$. Platinum is octahedrally coordinated to six

arsenic atoms, consequently the d-orbital is split into three ($t_{2g}$) and two ($e_g$) states, where the ($t_{2g}$)-states are low in energy than the ($e_g$) states and this is induced by the octahedral field from the S atoms. In both low and high spin configurations, the electron orbital occupation is : $(t_{2g})^6(e_g)^3$. $PtAs_2$ can be described in terms of states of $As_2^{2-}$ molecular ion ($4s\sigma, 4s\sigma^*, 4p\sigma, 4p\pi, 4p\pi^*$,and $4p\sigma^*$) and of crystal-field split 3d states of $Pt^{2+}$($e_g$ and $t_{2g}$). Two 4s-derived subbands are formed for $PtAs_2$. This splitting is due to the $\sigma - \sigma^*$ energy separation of As-4s derived molecular orbital in $As_2$ dimers in the $PtAs_2$

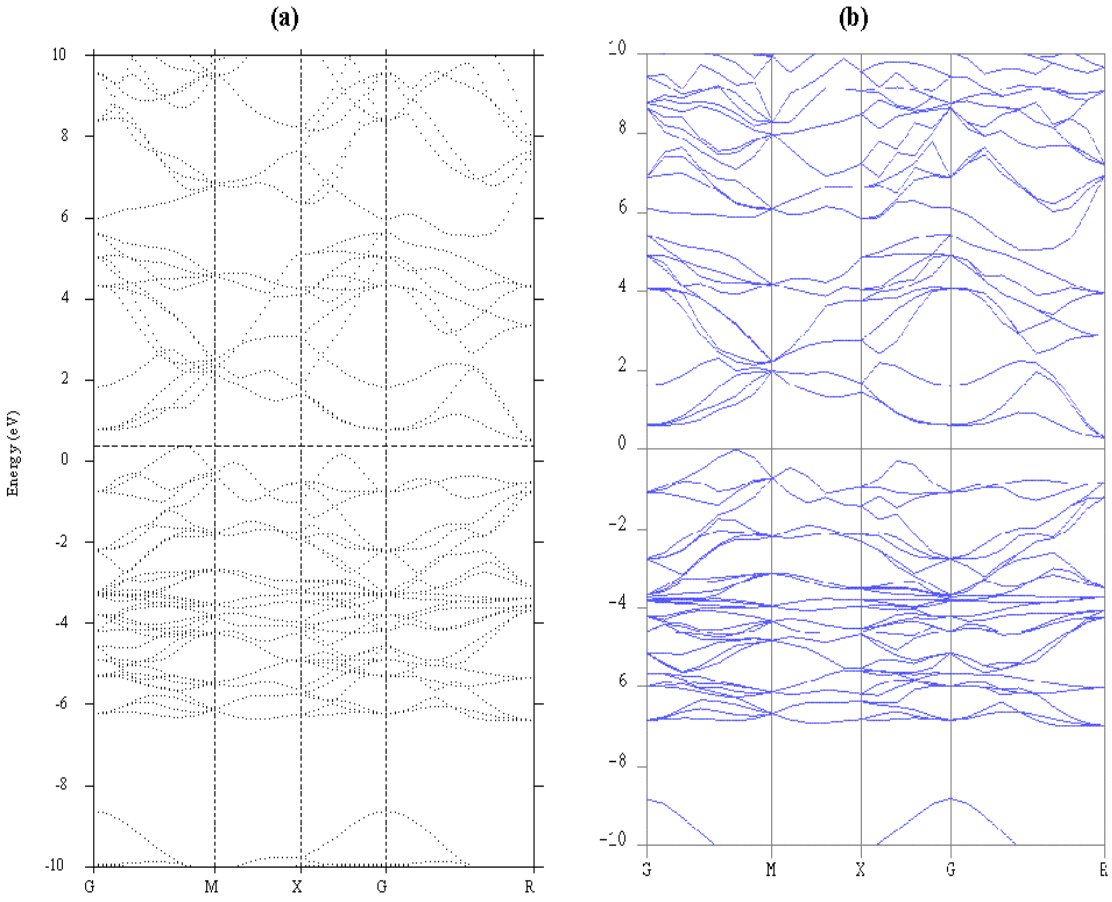


Figure 4.13: The calculated electronic band structure of $PtAs_2$ crystal at the equlibrium volume along high symmetry lines plotted using (a) TB-LMTO and (b) Castep between -10 eV and 10 eV.

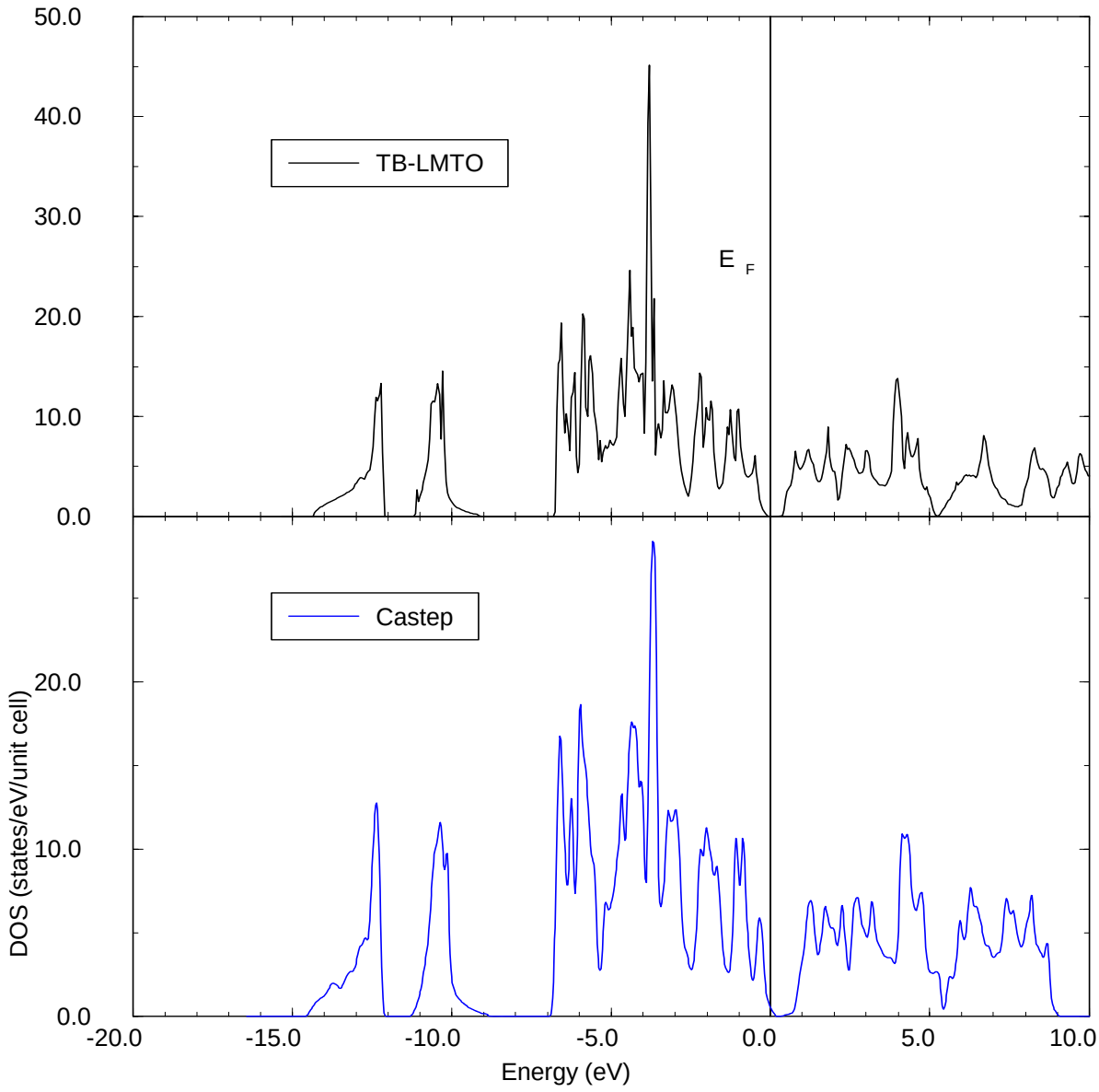


Figure 4.14: Total density of states for $PtAs_2$ at equilibrium volume as calculated using both TB-LMTO and Castep methods.

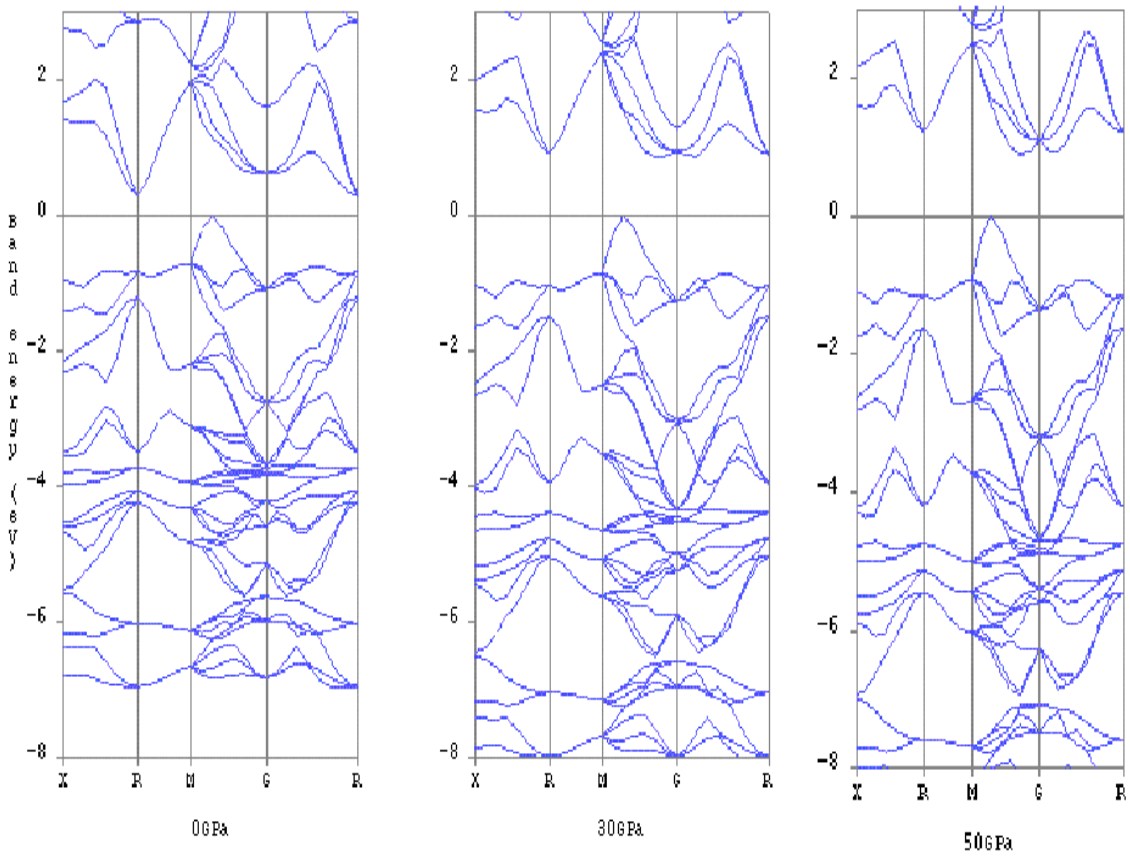


Figure 4.15: Evolution of the valence electron band structure of $PtAs_2$ as determined at 0, 30 and 50 GPa respectively. The band gap widen with an increase in pressure (Castep).

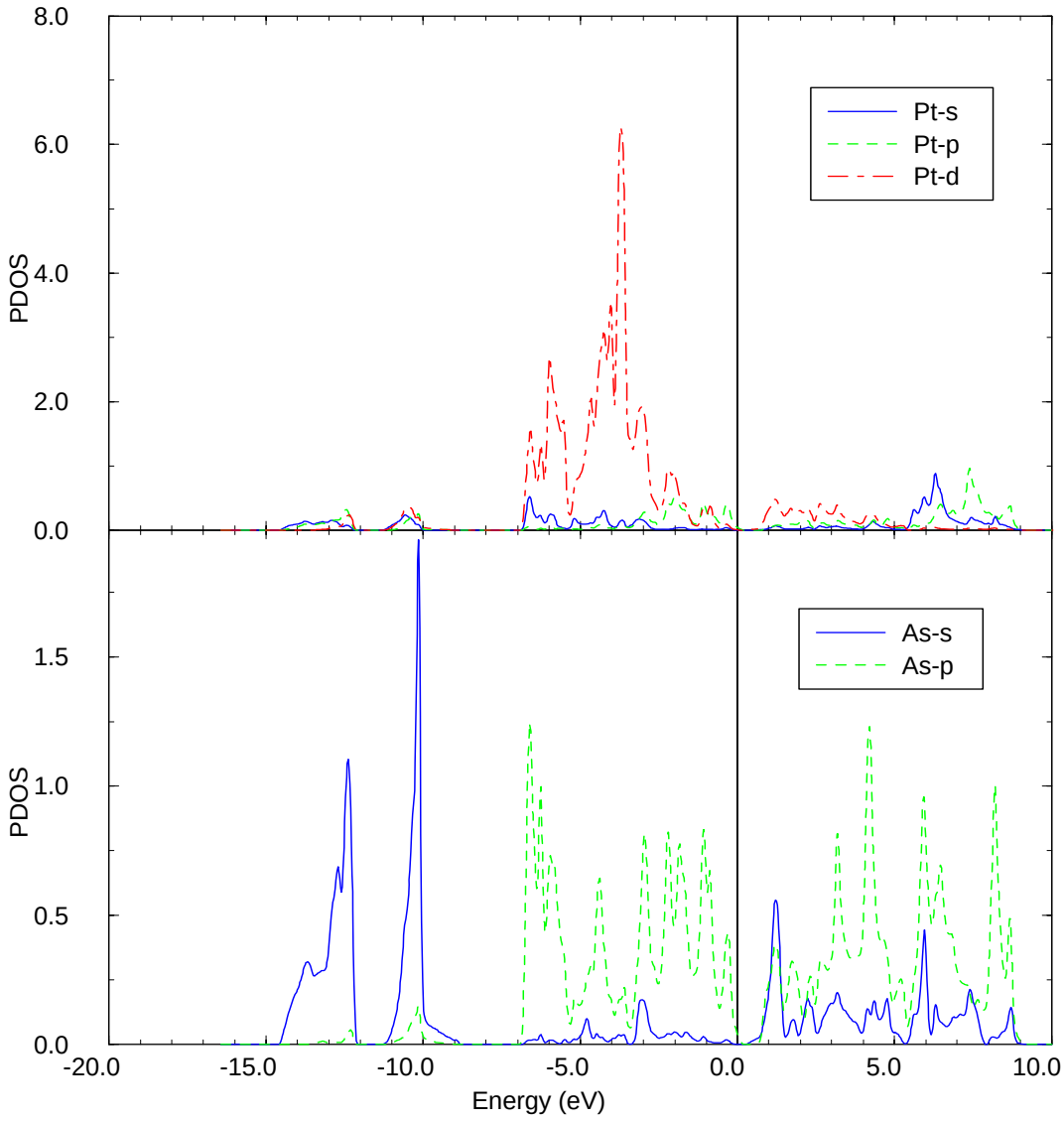


Figure 4.16: Calculated partial densities of states for $PtAs_2$ at 0GPa (Castep).

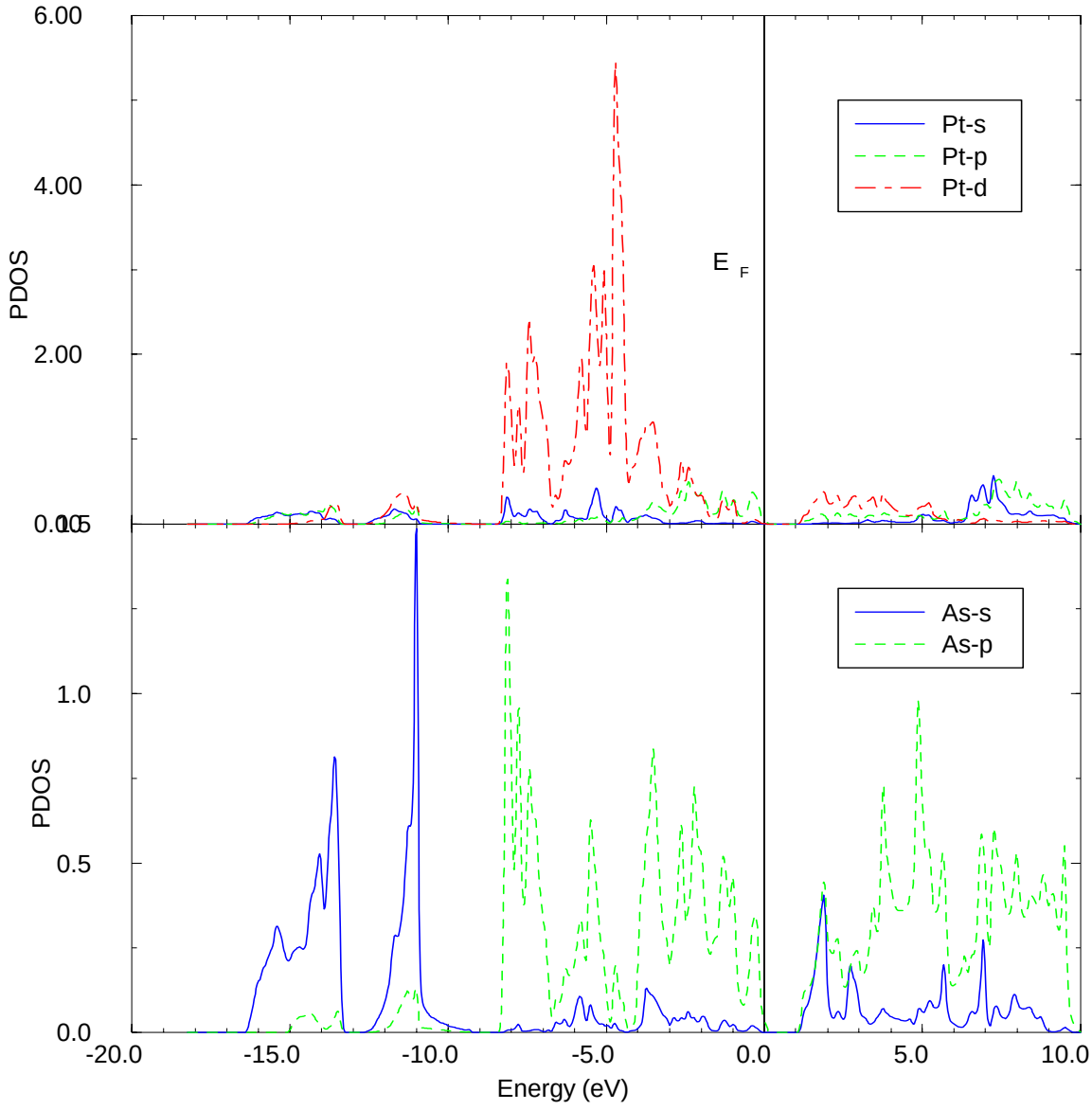


Figure 4.17: Calculated partial densities of states for $PtAs_2$ at 50GPa (Castep).

orbital. The lowest two bands near -14eV and -10eV in fig. 4.14 are well described by the bonding and antibonding pair of molecular states 4s$\sigma$ and 4s$\sigma^*$. The bands of states between -5eV and -1eV can be described as a mixture of states derived from molecular states 4p$\sigma$, $4p\pi$, and $4p\pi^*$ and a small bonding mixture of the Pt $e_g$ state. The narrow band just below the Fermi level is primarily the nonbonding Pt state $t_{2g}$. Finally, the unoccupied band

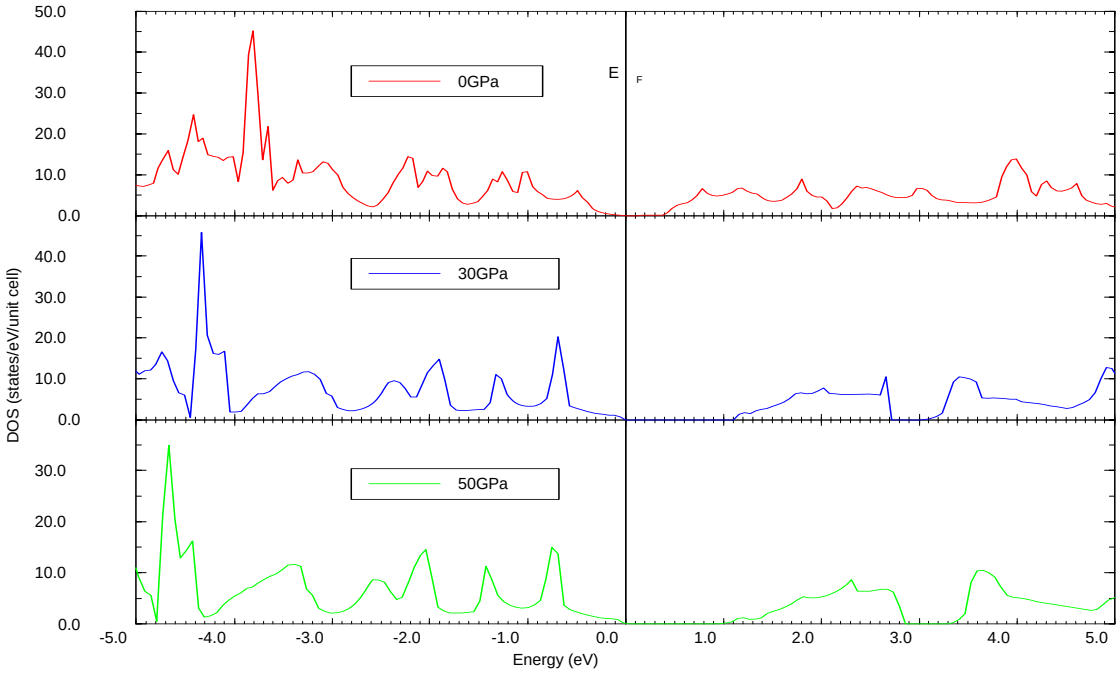


Figure 4.18: Total density of states for $PtAs_2$ projected around the Fermi level to show the change in the band gap size under hydrostatic compression (TB-LMTO).

above the Fermi level corresponds to the antibonding mixture of the antibonding molecular 4p$\sigma^*$ states and the Pt $e_g$. We see that the As(4s) states form a separate bonding-antibonding gap at high binding energy similar to the those of S(3s) states in pyrite $FeS_2$ [85]. The semiconductor gap again originates from the Pt(5d) and As(4p) hybridization effect.

We have also calculated the electronic energy band structure and density of states for $PtAs_2$ using castep at several pressures and the response of the

electronic structure to pressure are shown in fig. 4.15. The corresponding densities of states plotted at the pressure of 0GPa and 50GPa, respectively are shown in figs. 4.16 and 4.17. At ambient pressure , we find that $PtAs_2$ has an indirect band gap of 0.29 eV with both the valence maximum and the conduction mimimum located at the similar position as in TB-LMTO method ( GM lines and R point). At the pressure of 50GPa, a band gap of 0.99 eV was found. As is evident from the fig. 4.15, the electronic energy gap increases with increasing pressure. This was reconfirmed by repeating similar calculations on the DOS using TB-LMTO, and the results are shown in fig. 4.17. Energy gap of the same magnitude, 0.98 eV was produced at a pressure of 50 GPa using TB-LMTO. A similar trend is observed for $FeS_2$ under hydrostatic pressure [86].

### 4.2.4 Platarsite ($Pt_4As_4S_4$)

Platinum is octahedrally coordinated to three sulphur and three arsenic atoms, as a result the d-orbital is split into three ($t_{2g}$) and two ($e_g$) states, where the ($t_{2g}$)-states, are low in energy than the ($e_g$) states, induced by the octahedral field from the S atoms. In both the low and high spin configurations, the electron orbital occupation is: $(t_{2g})^6(e_g)^3$. The band structure and density of states computed for $Pt_4As_4S_4$ using TB-LMTO and Castep methods are depicted in figs. 4.19 and 4.20, respectively and show no gap at the Fermi level. The valence and conduction band hybridized Pt 5d - As 3p peaks are predominantly contributions of metal d states which define the shape of the upper part of the valence band as shown by the two methods. The density of states spectrum shows that the ground state of $Pt_4As_4S_4$ within DFT-LDA is metallic. The states below -10eV are 4As and 3s dominated states, which are associated with the formation of s-derived subbands from both As and S which is due to $\sigma - \sigma^*$ energy separation. In this case the crystal-splitting of the Pt d-levels into $t_{2g}$ and $e_g$ appears not large enough, to cause a band gap, as a result the metallic behaviour of $Pt_4As_4S_4$ is noted.

The electronic energy band structure of $Pt_4As_4S_4$ at several pressures were calculated and the response of electronic structure to pressure is shown in figs. 4.21, 4.22 and 4.23, respectively. In all cases the band structures were calculated from full relaxed atomic positions and unit cell parameters. The calculations still confirm the metallic behaviour of $Pt_4As_4S_4$ even at 50GPa.

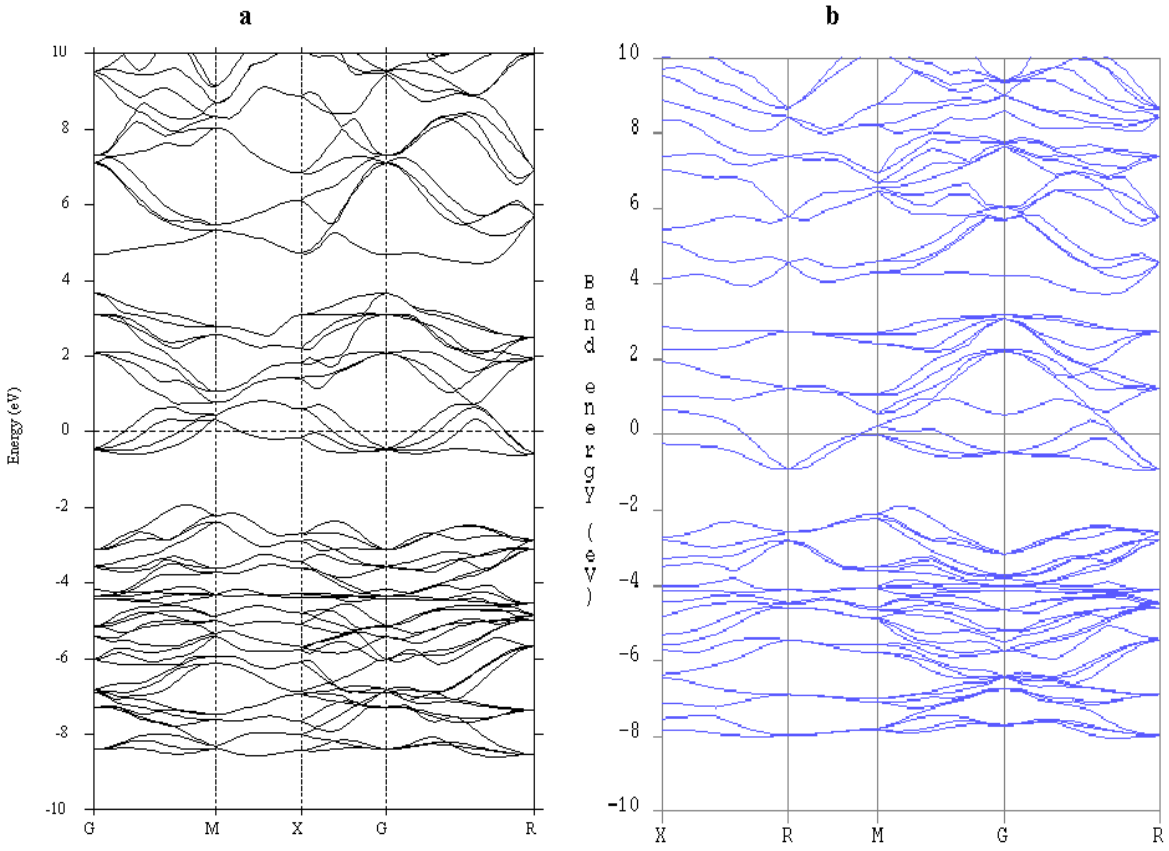


Figure 4.19: The calculated electronic band structure of $Pt_4As_4S_4$ crystal at the equilibrium volume along high symmetry lines plotted using (a) TB-LMTO and (b)Castep between -10eV and 10eV.

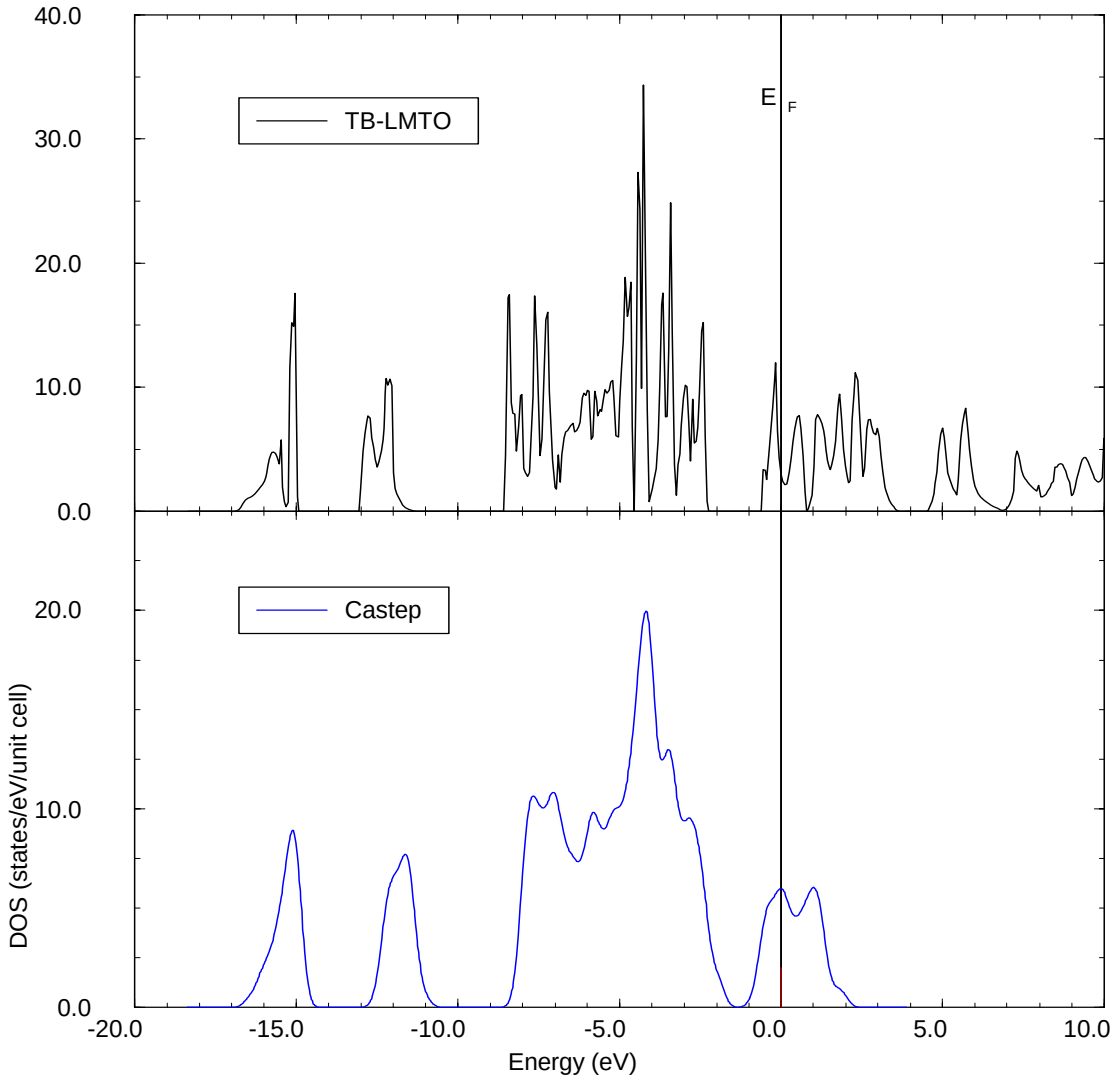


Figure 4.20: Total density of states for $Pt_4As_4S_4$ at the equilibrium volume calculated using TB-LMTO and Castep methods.

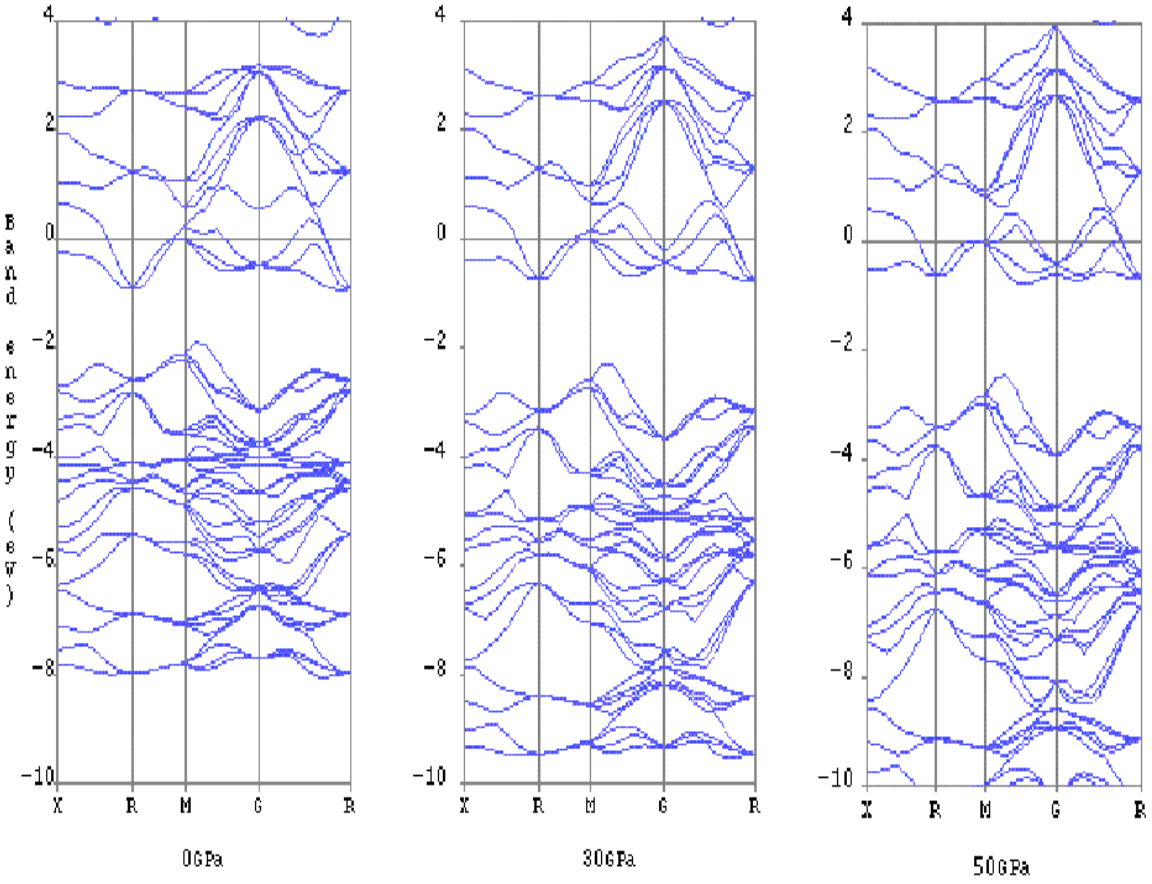


Figure 4.21: Evolution of the valence electron band structure of $Pt_4As_4S_4$ as determined at 0, 30, 50 GPa respectively (Castep).

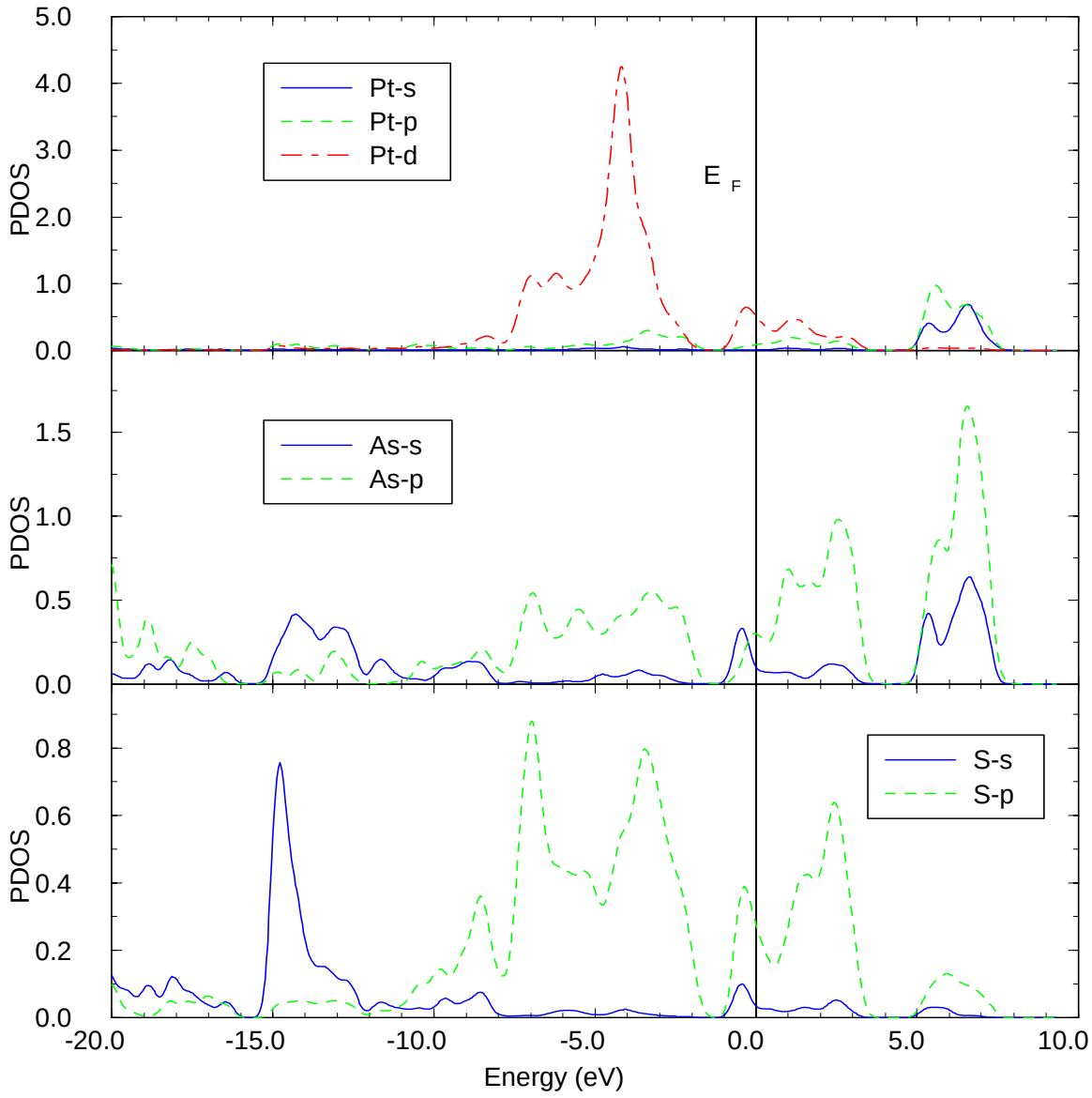


Figure 4.22: Calculated partial densities of states for $Pt_4As_4S_4$ at 0GPa (Castep).

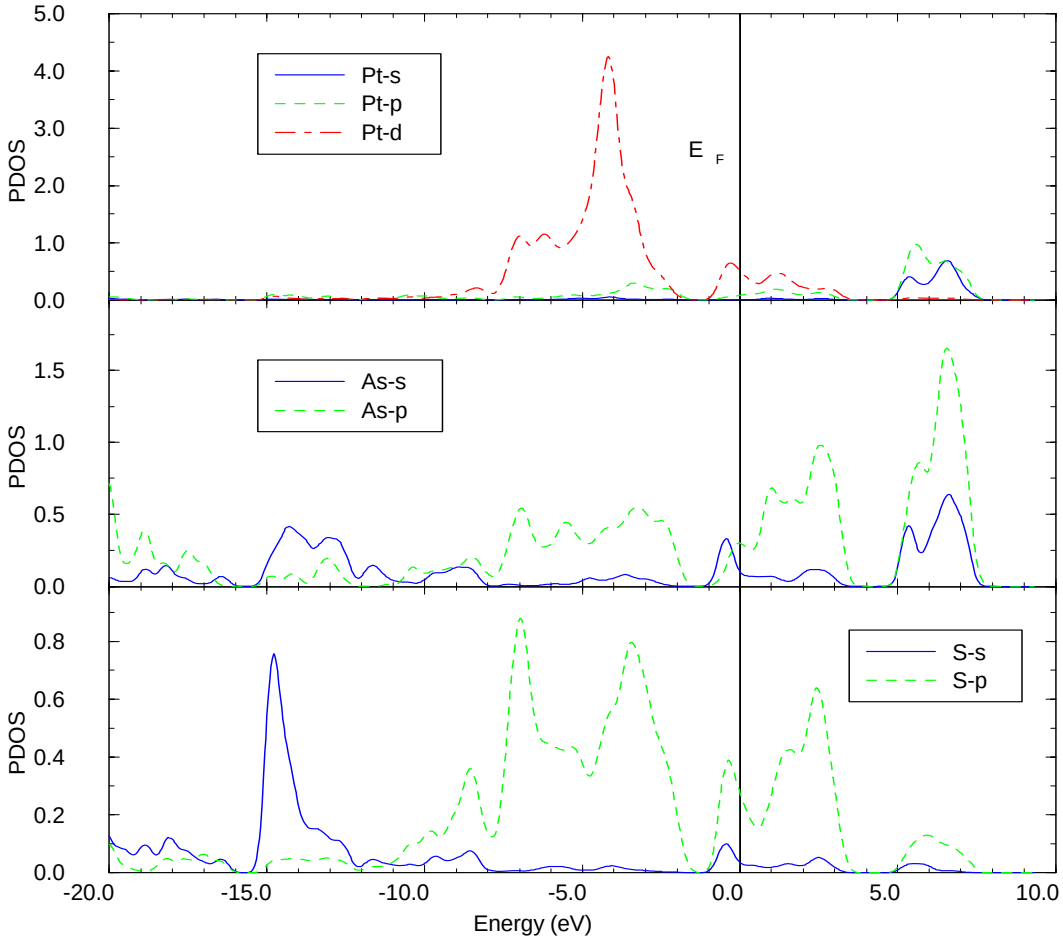


Figure 4.23: Calculated partial densities of states for $Pt_4As_4S_4$ at 50GPa (Castep).

## 4.3 Charge density

The valence electronic charge densities of platinum sulphide/arsenide have been calculated using the plane wave pseudopotential method. In order to analyze the densities in more detail, we have calculated the charge density differences by subtracting the pseudocharge distributions for the individual atoms from that of the compound.

In fig. 4.24, we show the charge density difference of PtS on the plane passing through the Pt and S sites along the direction [0 1 0]. Looking at the region between two Pt atoms, there is a large low-charge density channel, indicating no bond formation between the two Pt atoms. An interesting aspect is noticed in this figure, where the four lobes of highly concentrated charge difference around each Pt(platinum) atom pointing four neighbouring S(sulphur) atoms. Hence, it is clear that Pt-S bond is covalent in nature. At high pressure, slight(small) buildup of charges in the d-orbital of Pt is noticed.

Fig. 4.25 shows the high charge density at the midpoints of Pd-S and Pt-S bonds along [-0.84 -0.43 0.30] direction hence suggesting covalent bonding. No metallic bonding density appears between Pd and Pt atoms. We do not notice obvious changes as we increase the pressure on the system. Fig. 4.26 displays charge differences for $PtAs_2$ along [-0.71 0.00 0.70] direction. This plane is being chosen so as to pass both through arsenic (As) dimers and as well as platinum sites. Looking at the region between two adjacent Pt atoms, which appear both nearly symmetrical, there is positive charge density which suggests the formation of metallic bonding. A considerable similarity remains, however, in the charge density between the dimers arsenic(As-As) bond, and Pt-As bond, and it would be clearly correct to describe the bonds as covalent. At the high pressure as in fig. 4.26, we note the pronouncement of charge depletion around the Pt atoms, which may be strengthening the Pt-As bond. Finally, we display in fig. 4.27 the charge density difference on $Pt_4As_4S_4$ along [-0.71 0.00 0.70] direction, which is having similar patterns as that of $PtAs_2$. The region between two adjacent Pt atoms, where charge difference is spherical and positive suggests metallic type of bonding. However, deformated and positive charge density difference is noted on the Pt-As and Pt-S bonds, hence suggesting covalency. Also the S-As bond shows some symmetric pattern, which indicates covalency in the pair. At 50GPa (fig. 4.27) an increase in covalent and metallic bonding occurs between respective

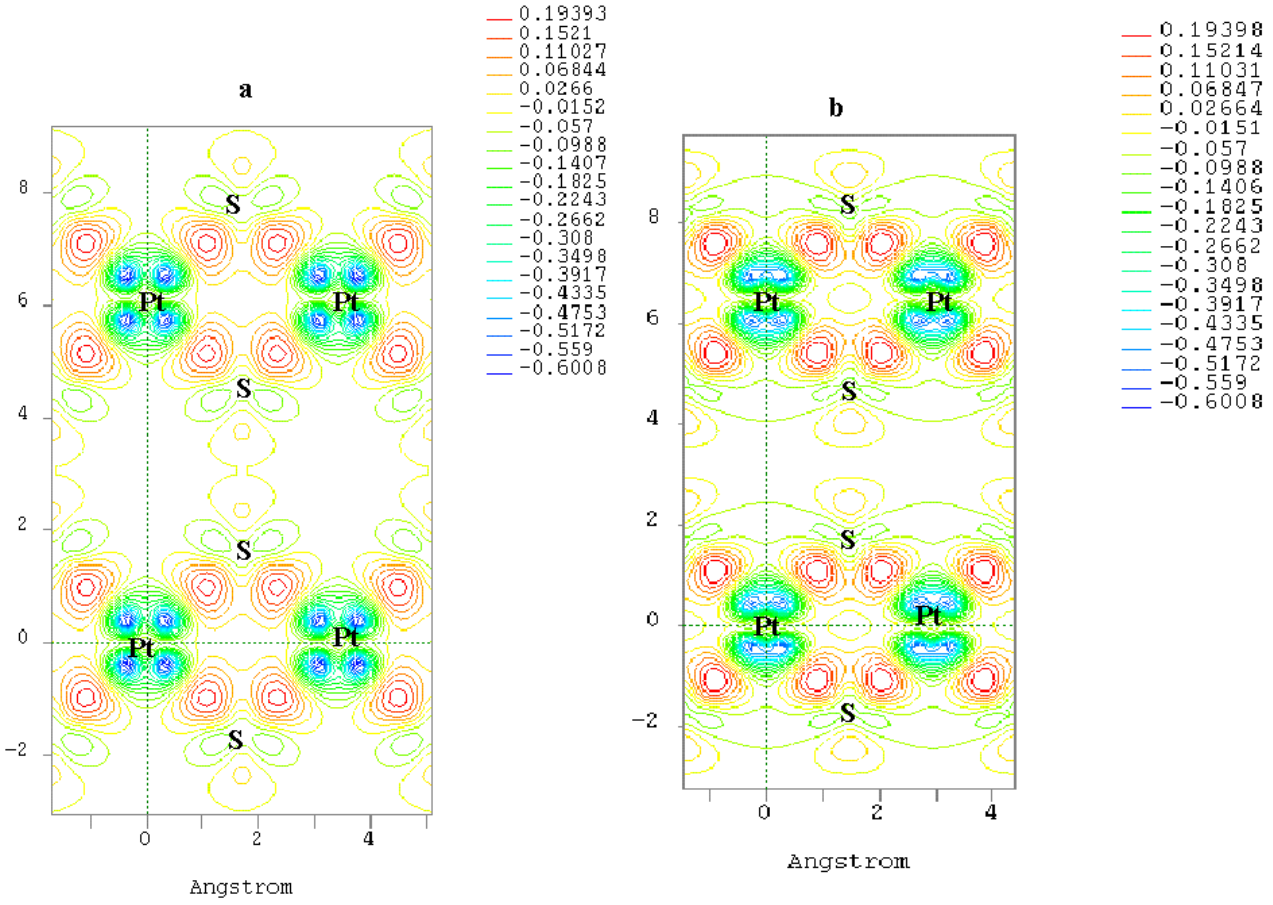


Figure 4.24: The self-consistent valence electronic charge difference of PtS determined at (a) 0GPa and (b) 50GPa.

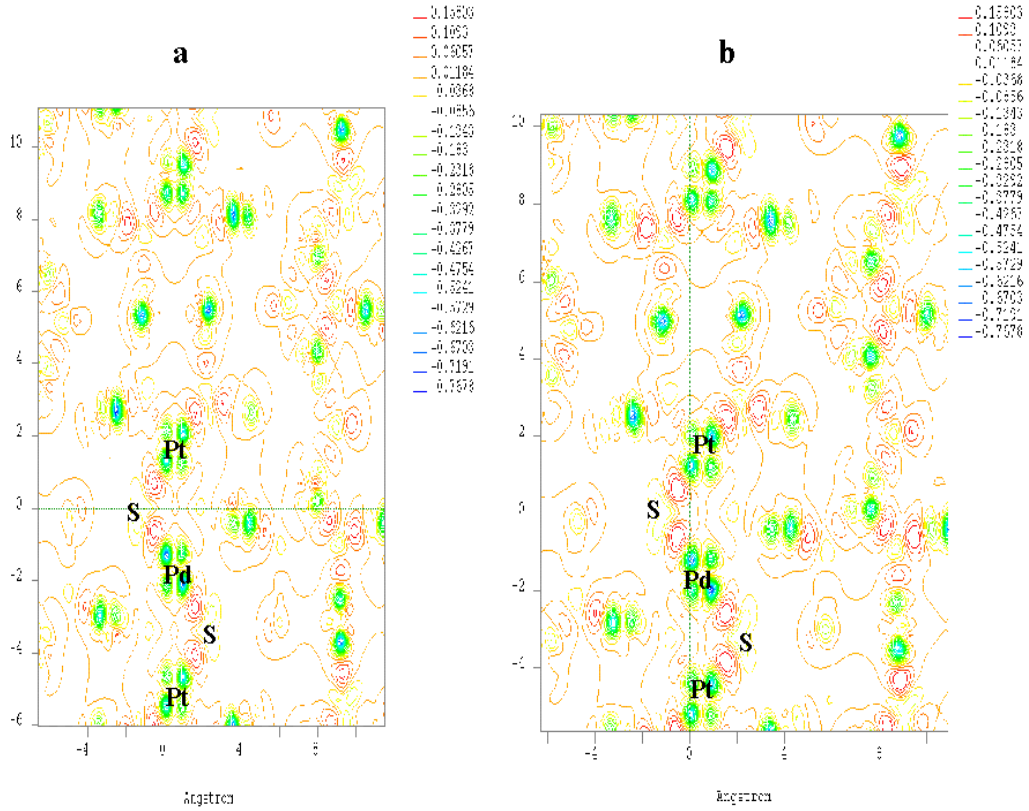


Figure 4.25: The self-consistent electronic valence charge difference of $PdPt_3S_4$ computed at (a) 0GPa and (b) 50GPa. (The red color indicates high density of electronic charge and the green color a depleted electronic charge).

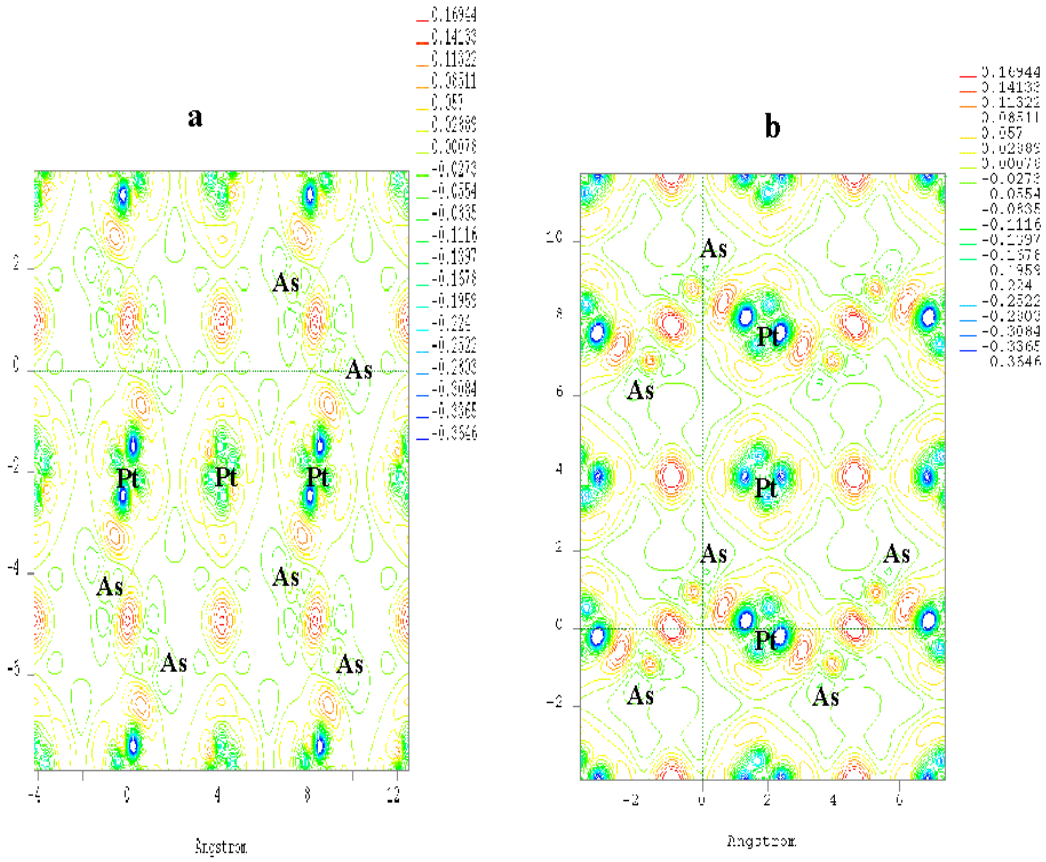


Figure 4.26: The self-consistent valence electronic charge difference of $PtAs_2$ determined at (a) 0 and (b) 50GPa.

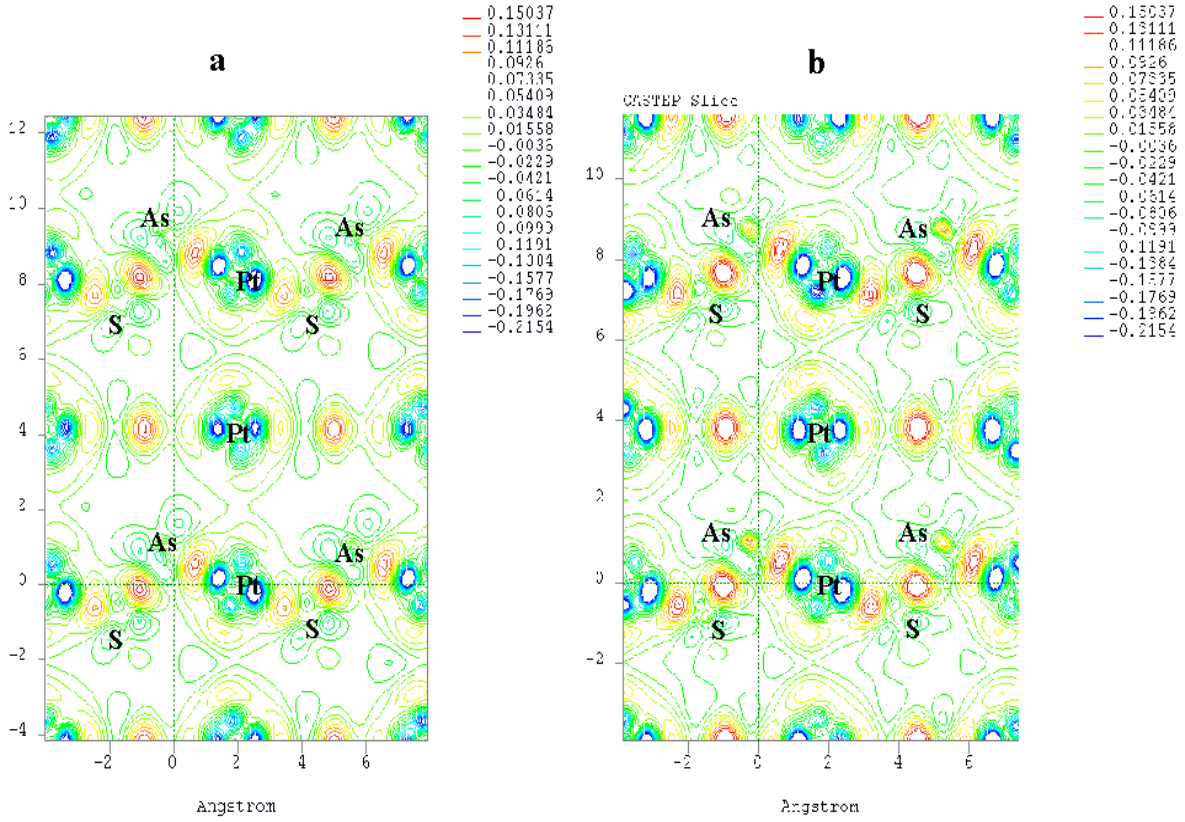


Figure 4.27: The self-consistent valence electronic charge difference of $Pt_4As_4S_4$ detemined at (a) 0 and (b) 50GPa.

atoms mentioned at 0GPa.

## 4.4 Optical Properties

The difference in the propagation of an electromagnetic wave through vacuum and some other material can be described generally by a complex refractive index

$$N = n + ik. \tag{4.1}$$

In vacuum it is real, and equal to unity. For transparent materials it is purely real, the imaginary part being related to the absorption coefficient by

$$\eta = \frac{2kw}{c}, \tag{4.2}$$

which gives the fraction of energy lost by the wave on passing through a unit thickness of the material concerned. This is derived by considering the rate of production of Joule heat in the sample.

The reflection coefficient can be obtained for the simple case of normal incidence by matching both the electric and magnetic fields at the surface,

$$R = \left|\frac{1-N}{1-N}\right|^2 = \frac{(n-1)^2 + k^2}{(n+1)^2 + k^2} \tag{4.3}$$

However, when performing calculations of optical properties it is common to evaluate the complex dielectric constant, and then express other properties in terms of it. The complex dielectric constant $\varepsilon(\omega)$ is given by

$$\varepsilon_1 + \iota\varepsilon_2 = N^2. \tag{4.4}$$

Hence the relation between the real and imaginary parts of the refractive index and dielectric constant is

$$\varepsilon^2 = n^2 - k^2\varepsilon_2 = 2nk. \tag{4.5}$$

A further useful form for the expression of optical properties is the optical conductivity,

$$\sigma = \sigma_1 + \sigma_2 = -\iota\frac{\omega}{4\pi}(\varepsilon - 1). \tag{4.6}$$

But, this is most useful for metals.

A further property we may calculate from the complex dielectric constant is the loss function. It describes the energy lost by a point electron passing through a homogeneous dielectric material, and is given by

$$\mathrm{Im}\left(\frac{-1}{\varepsilon(\omega)}\right) \tag{4.7}$$

Experimentally, the most accessible optical parameters are the absorption $\eta(\omega)$ and the reflction $\mathrm{R}(\omega)$ coefficients. In principle, given the knowledge of both these, the real and imaginary parts of N can be determined. However, in practice, the experiments are more complicated than the case of normal incidence. Polarization effects must be accounted for, and the geometry is quite involving. However, we only consider normal incidence, but polarization effects are taken into account.

Reflectance spectra of PtS, $PdPt_3S_4$, $PtAs_2$ and $Pt_4As_4S_4$, under high pressures are shown in figs. 4.28. Experimentally, reflectance is the easiest optical property to measure, but in most cases R (Reflectance) is a rather slowly varying function of wavelength and this makes it very difficult to locate the exact energies of interband transition. The reflectance spectra of PtS at ambient pressure shows a maximum reflectance peak of about 0.42 at 2eV. A notable change is observed on the size of the reflectance peaks as the pressure increases. Under high pressure, the reflectivity spectrum shows high reflectivity at lower energies with the reflectance peaks at 30GPa being higher than those observed at 50GPa. It also emerges that under high pressure, the first peaks are found to have shifted to lower energy level. $PdPt_3S_4$, shows a maximum reflectivity peak of about 0.45 at ambient pressure, corresponding to photon energy of 2.5 eV and increases to 0.88 at the pressure of 30GPa. It also evident that the reflectance peaks at 30GPa are higher than those at 50GPa, but both tend to shift to lower energy with pressure.The reflectance peaks at higher pressure have the same features as the one at ambient pressure.

In $PtAs_2$, we see a fair reflectance at low energy at ambient pressure. The main spectral features occur at 4eV, 8 eV and 9.5eV. The first peak at 4eV

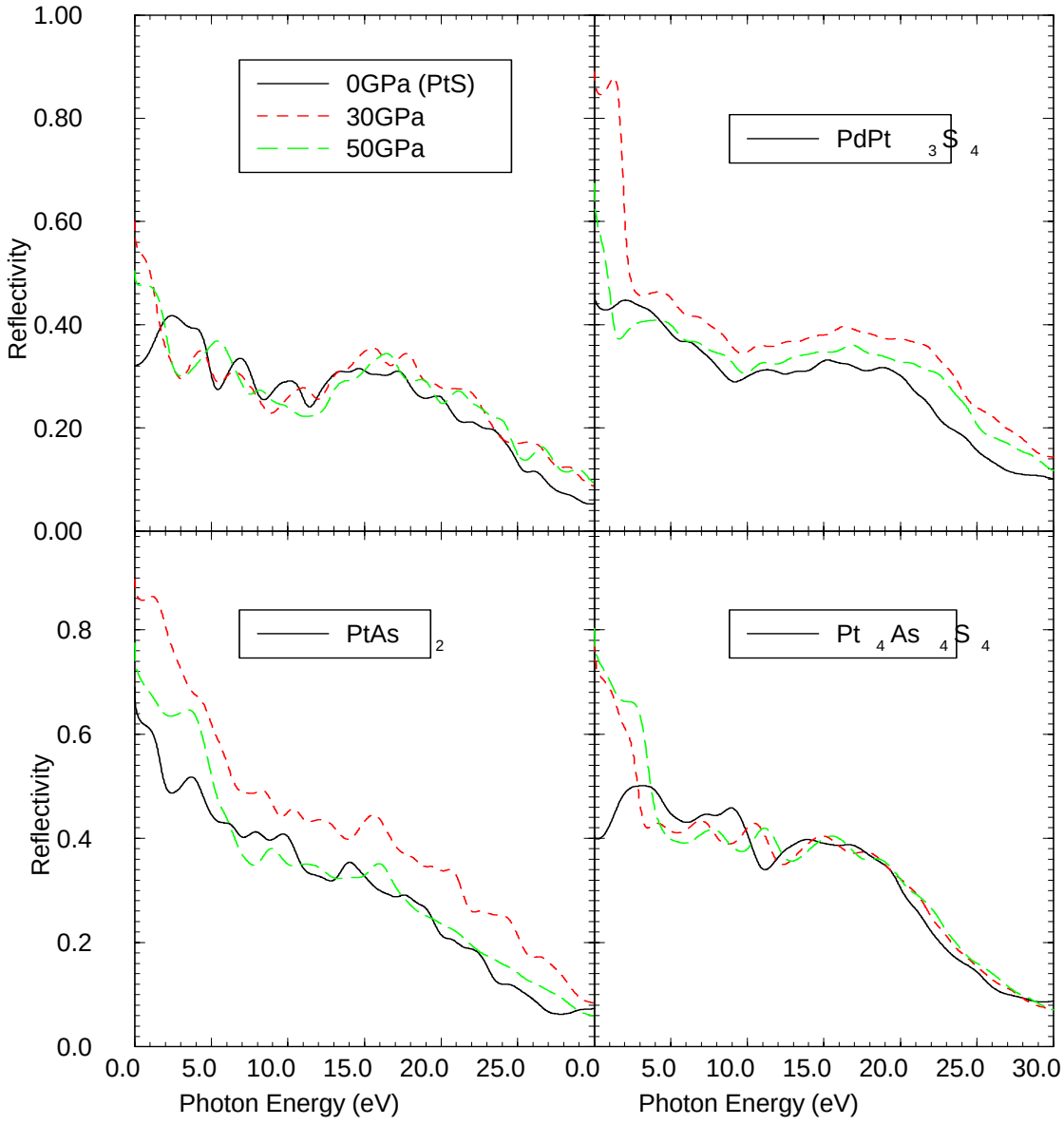


Figure 4.28: The calculated reflectivity spectra of PtS, $PdPt_3S_4$, $PtAs_2$ and $Pt_4As_4S_4$ at different pressures.

gives maximum reflectance of 0.52, the second and the third peak 0.42 and 0.40, respectively. Under high pressure the main spectral features are found to have shifted to high energy levels, as shown. A maximum reflectivity of 0.83 is reached at the pressure of 30GPa. The reflectance spectra of $Pt_4As_4S_4$ shows a maximum peak at about 3eV, and the other two minor peaks at 7and 10eV, giving reflectance of 0.52, 0.44 and 0,46 respectively. This shows that $Pt_4As_4S_4$ reflects about 0.50 of incident incident light at low energy (4 eV). The main spectral features shifted to high energy levels, under high pressure. A maximum reflectivity of 0.66 is noticed at 50GPa. In this case the reflectivity increases with increase in pressure. The reflectance peak at the pressure of 50GPa are higher than those of 30GPa.

The absorption spectra of PtS, $PdPt_3S_4$, $PtAs_2$ and $Pt_4As_4S_4$, under high pressure are shown in fig. 4.29. Due to the band gap energy , semiconductors are unable to absorb and reflect lower frequencies. Absorption and reflection start to occur at a frequency $w_0$ given by $\hbar^2 w_0 = E_g$ , and at this frequency we notice the so-called absorption edge. The absorption edge is responsible for the width of the energy gap. At higher frequencies absorption and reflection can be relatively high. Here, we must bring together the concepts of electron structure and the known optical properties (absorption) of materials. This is done by identifying the allowed energy levels. The major classification of electron transitions is between transitions within the same bands (intraband) and transitions between different bands (interband). The former are lower energy transitions which lead to the high reflectivity of the metals in the visible spectrum. The latter are higher energy transitions which can lead to specific colour in materials. The assigment of the peaks to the interband transitions is determined by transitions from the valence p-band of As (S) to the conduction d-band of the Pt. At ambient pressure (PtS), we observed the first two peaks at about 4 eV and 6.5 eV which are associated with the transitions at M and X points in the Brillouin zone as shown in fig. 4.1(b). It also has to be remembered that the probability of indirect, that is phonon-assisted, transitions is much lower than for direct transition. We further note that the intensity of the first peak is lower than the second , hence emphasizing that the first peak corresponds to transition to an $e_g$ bandlike state in Pt. We also observe, a decrease in the intensity of the peaks at a lower energy but rapid increament at higher energies as the pressure increases. The main peaks tend to shift to lower energy at energies less than 10eV. Absorption is enhenced under pressure, since the spectral features increases under pressure.

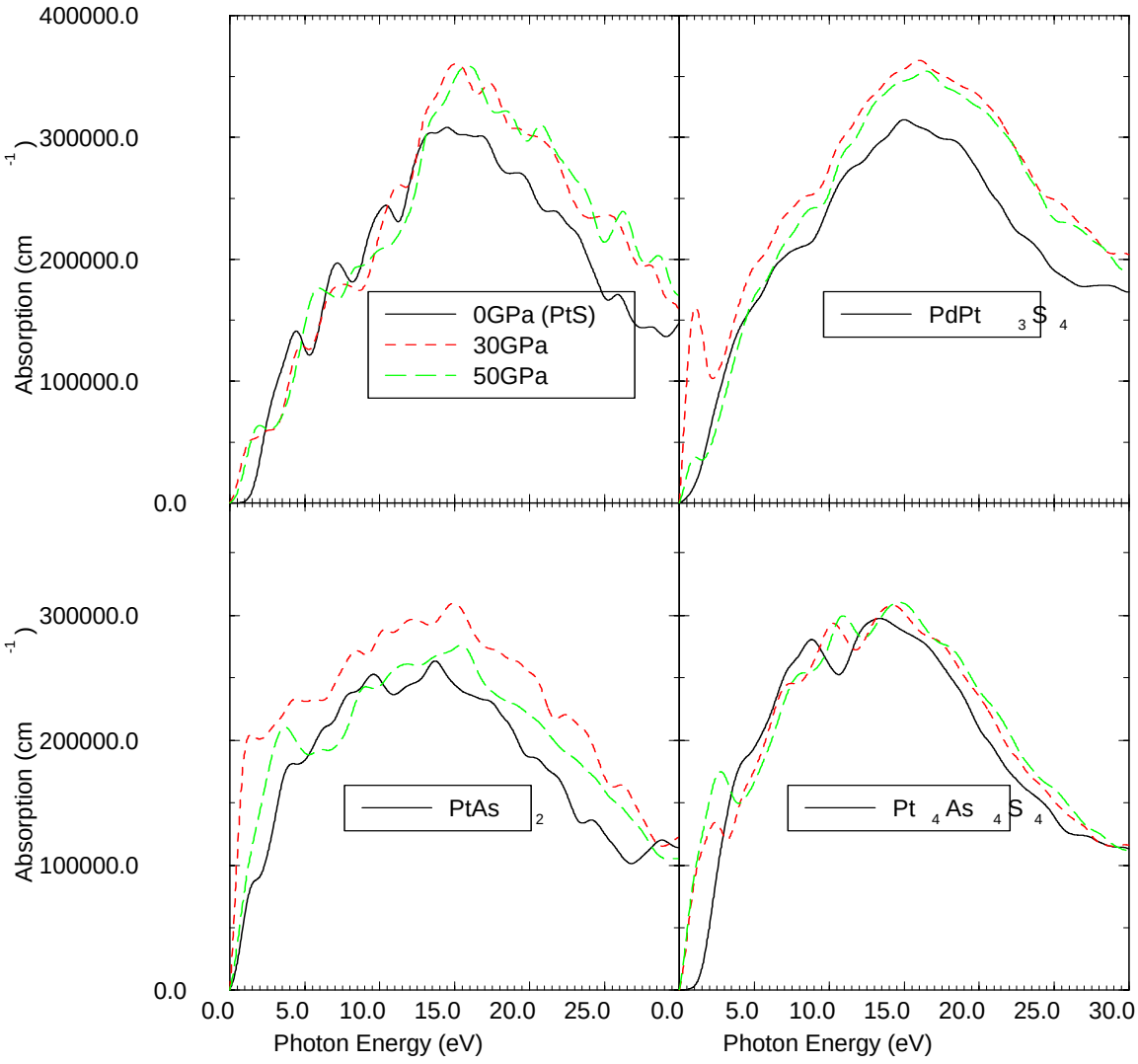


Figure 4.29: The calculated absorption spectra of PtS, $PdPt_3S_4$, $PtAs_2$ and $Pt_4As_4S_4$ at different pressures.

For $PdPt_3S_4$ , we observe the main spectral absorption at around 4.5eV and 7.6eV. It is these peaks that are associated with band to band transition along G and R points, as seen in fig. 4.7(b). Under high pressure the peak intensity increases, but the spectral features are the same as that of the ambient pressure, especially at higher pressure.

$PtAs_2$ shows the first two interesting peaks at 1.5 eV and 3.5eV , which correspond inter-band transtion along R and G point as shown in figure 4.13(b). The spectrum features at high pressure are similar to the one at ambient pressure but with the peaks under 30GPa higher than those of the pressure of 50GPa.

The absorption spectrum of $Pt_4As_4S_4$, indicates two jumps at around 4eV and 9.3eV. The first peak may be ascribed to intra-band transition along point R and the second one to G point (fig. 4.19(b)). The main peaks tend to shift to lower energy at energies less than 3eV, otherwise spectrum features at high pressure are similar to the one at ambient pressure.

### 4.4.1 Comparison with the experiment

Fig. 4.30 shows calculated reflectance spectra of cooperite along with the experimental results of Criddle et al. [18], for both Potgietersrus and Stillwater valley. The measurements were done within the visible region ranging from 400 to 700 nm. At the lower energy range, where the measurement of reflectivity is direct and band structures underlying the calculation is more accurate, the reflectance spectra of cooperite from Stillwater and Potgietersrus are similar, but are less dispersed, and both are different from the calculated results. The calculated reflectivity of cooperite shows a relatively lower reflectivity of less than 42 % at around 400 nm as compared to 45.5 % (400 nm) and 47.5 % (475 nm) for the Potgietersrus and Stillwater samples, respectively. Hence a deviation of 8 to 13% from experimental values is noted. The differences can be attributed to their compositional variations, since cooperite sample from both Pogietersrus and Stillwater contain palladium and nickel, whereas our model has neither trace of palladium nor nickel. However, the shape of the calculated reflectance curve resembles the experimental measurements, in particular those of Stillwater valley. The reflectance is near constant between 400 and 550 nm and a linear decrease commences beyond this range.

A comparison of the calculated and experimental reflectance spectra of

braggite ($PdPt_3S_4$) are given in fig. 4.31. A good agreement with the Stillwater sample is noted from 400 to 500 nm. Above this wavelength the calculated reflectance is near constant, whilst the experimental result decreases slightly followed by an abrupt reduction above 650 nm.

Calculated and experimental reflectance spectra of $PtAs_2$ are shown in fig. 4.32, from 400 to 750 nm. Our calculated curve and measurements of Criddle [87] and Tsintsov and Damyanov [88] generally exhibit similar features below 620 nm (at IR region).

However, our calculated reflectivity differs from the experimental results above 620 nm, where the latter depicts a sudden reduction, whilst the calculated curve remains near constant. Both curves show a gradual decrease in reflectivity deep into the visible region. The reflectivity curves of Picot and Johan [89] and Vyalsov [90] are different in the 400 - 600 nm range, both in shape and magnitude from our calculations. However, they reduce above 620 nm in agreement with other experimental results.

## 4.5 Conclusion

We have presented results for electronic and optical properties of the PtS, $PdPt_3S_4$, $PtAs_2$ and $Pt_4As_4S_4$ with two different electronic structure methods. Our results for electronic are predictions and complementary experiments are needed.

We are able to predict non-metallic behaviour of the three platinum group minerals; cooperite (PtS), braggite ($PdPt_3S_4$) and sperrylite ($PtAs_2$), and a metallic behaviour for $Pt_4As_4S_4$. A consistent account of the semiconductor band gaps and bonding properties for the three non-metallic structures is related to the crucial role of the hybridization between the Pt (5d) and S (3p) or As (4p) states. Our predicted values of the band gap for cooperite (PtS) is in good agreement with experiment. However, we find that our theoretical Castep calculations for the band gap is in substantial disagreement with the deduced optical absorption gap of 1.4 eV [16]. This theoretical Castep calculations showed a very good agreement with the value of 0.8 eV band gap [16], whereas TB-LMTO-ASA calculation is shown to be in poor agreement. In contrast, we find that the TB-LMTO-ASA calculation was in better agreement with the optical band gap measurement of 1.4 eV.

Interpretation of observed reflective spectra under ambient pressure is made through comparison with experimental data for the three materials.

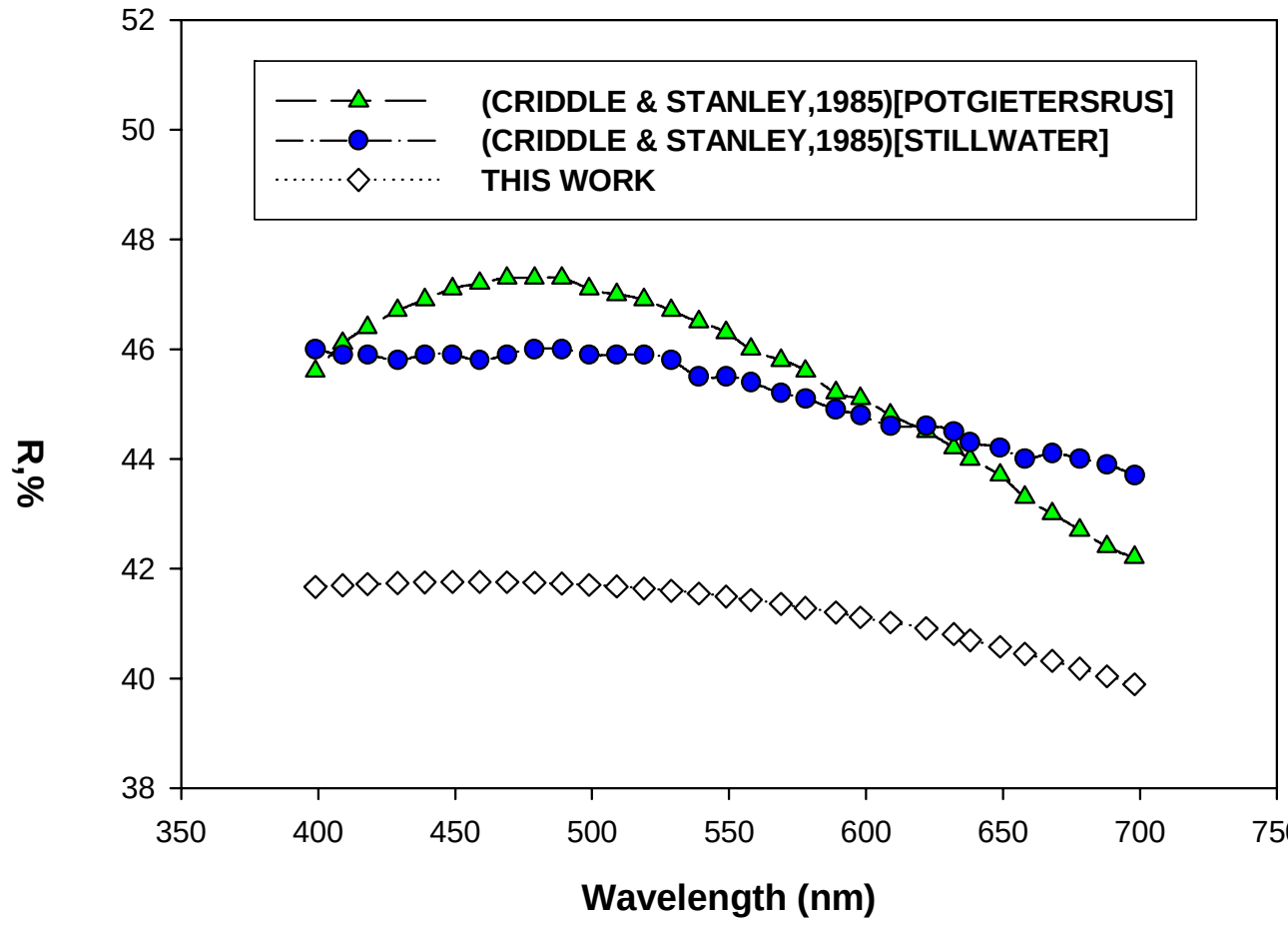


Figure 4.30: Reflectance spectra for Cooperite (PtS)

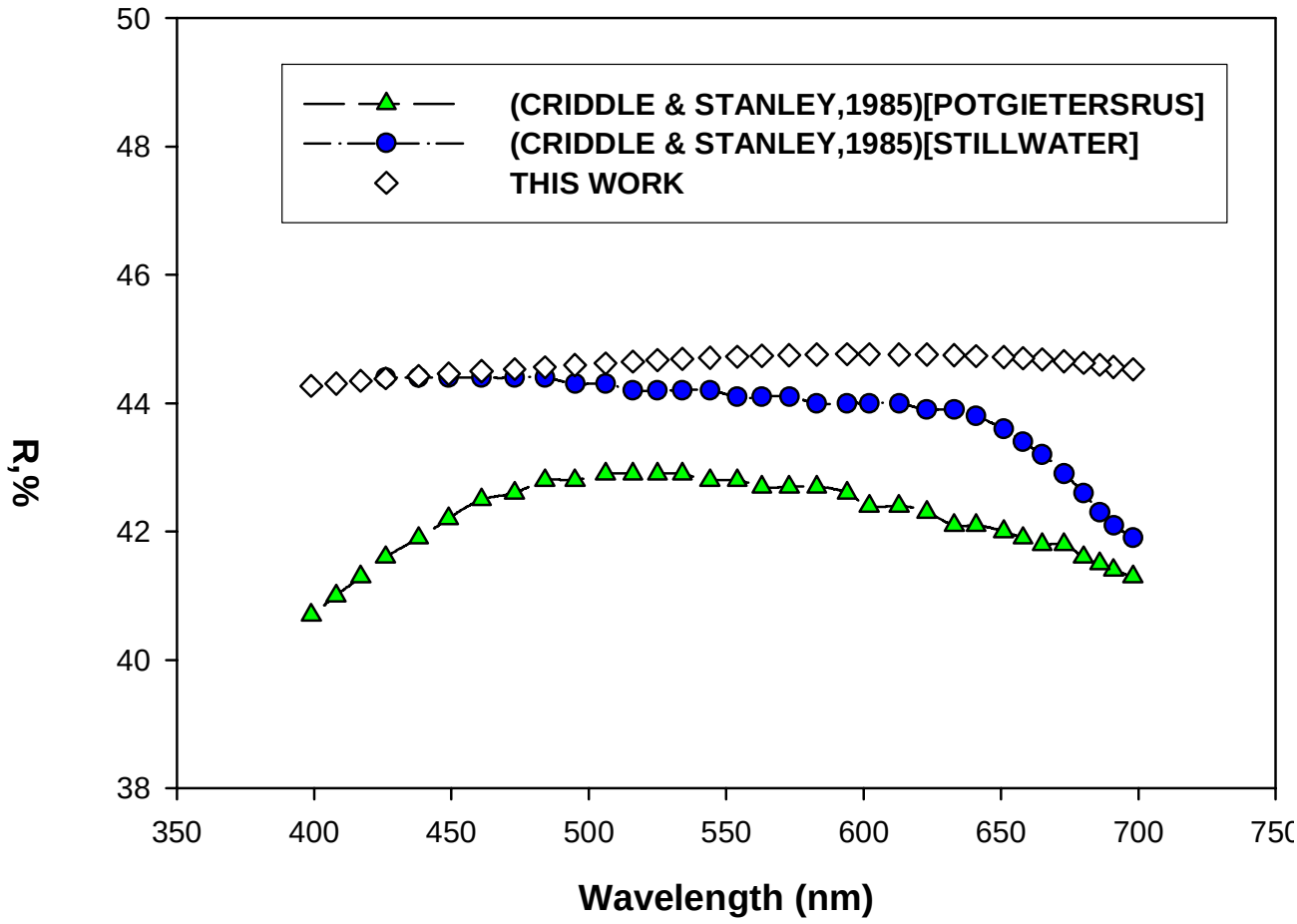


Figure 4.31: Reflectance spectra for Braggite ($PdPt_3S_4$)

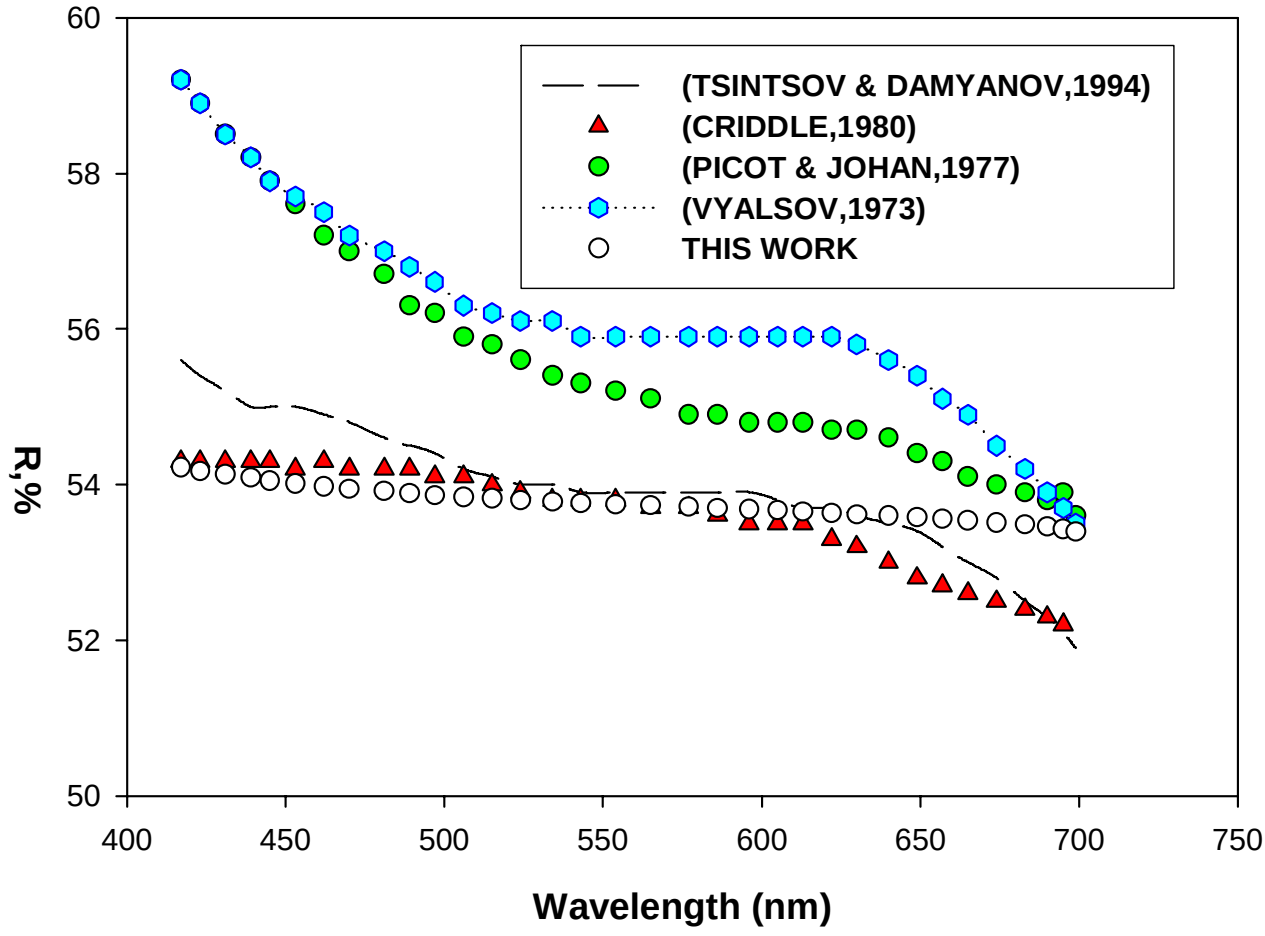


Figure 4.32: Reflectance spectra for Sperrylite ($PtAs_2$)

A comparison of the Stillwaters' copperite sample and our results indicates that the two have constant reflectivity at low wavelength of 400 to 550 nm. A similar behaviour is also observed with the Stillwater braggite, where a constant reflectivity from 400 to 500 nm is noted. Our calculations for sperrylite reflectivity differs from the experimental results above 620 nm, where the latter shows a sudden reduction, whilst the calculated curve remains near constant. We very much hope that this theoretical calculations will stimulate further experimental work.

# Chapter 5

# POTENTIAL MODELS

The starting point for any atomistic simulation is the identification of a suitable potential function which will enable the energy of a perfect crystal to be calculated. Indeed, the greater uncertainities in the numerical results are often due to the potential model, rather than problems with the simulations itself. The variable parameters required for the description of the short range potential energy terms can be obtained, either by empirically fitting to expand to experiment or by approximate quantum mechanical calculations (non-emperical), i.e calculating numerically the short range potential energy terms. The classical approach, namely atomistic simulation, was employed, in which the Born Model [91] of ionic solid is used to describe the interactions between ions. The basis of this approach is to calculate the total interaction energy, often called the lattice energy, of the system in question.

Atomistic simulation technique use simple, parameterised, analytic functions to describe the interaction between all species in the crystal. This enables the lattice energy of the system to be calculated. This is defined as the energy released when the component ions at infinity are brought together on the lattice sites. The interactions in a crystal are made up of the short range attractions and repulsions, which are modelled using adjustable parameters and long range electrostatic interactions, which contribute approximately 80% of the total interaction energy. In the next section, the potential models used will be discussed.

### 5.0.1 The Born Model of Solids

The Born Model of Solids [91], assumes that the sum of all pair wise interactions between atoms i and j gives the lattice energy of a crystal. The lattice energy can therefore be written as:

$$U(r_{ij}) = \sum_{i}^{N}\sum_{j}^{N}\frac{q_i q_j}{r_{ij}} + \sum_{i}^{N}\sum_{j}^{N}\phi_{ij}(r_{ij}) \tag{5.1}$$

The first term defines the long range electrostatic interactions and the second term the short range contribution, for $i \neq j$. It is considered adequate to calculate only the two body interactions for systems where the interactions are non-directional, such as ionic solids. Howevere, when studying systems containing a degree of covalent bonding, higher body terms must be added to the equation [63]. These would be of the form $\sum_j^N \sum_j^N \sum_J^N \phi_{i,j,k}(r_{i,j,k})$, for $i \neq j \neq k$

### 5.0.2 Coulombic Summation

When two atoms are brought from infinity, to their lattice site positions within the crystal, the lattice energy is released. This corresponds to the potential energy of the long range interactions and takes the form:

$$\Psi = \sum_{\mathbf{L},ij}\frac{q_i q_j}{4\pi\epsilon_0(rij + \mathbf{l})} \tag{5.2}$$

where $q_i$ and $q_j$ are the charges on the ions $i$ and $j$, $r_{i,j}$ is the displacement of ion $i$ from ion $j$ and $\mathbf{l}$ is the set of lattice vectors representing the periodicity of the crystal lattice. This long range interactions has a problem of slow convergence as a function of $r$. Hence, it is necessary to use mathematical models to deal with this summation. The two summation methods used for this potentials are, the Ewald summation for three-dimesional periodic systems and the Parry method for two-dimensional systems. The theory of the two methods will now be described.

### 5.0.3 Ewald Summation

The Ewald **[92]** approach for evaluating the Coulombic interaction assumes that the lattice is periodic in three dimensions. When describing the Coulom-

bic interaction, the charge density $\rho$ for a point charge is given by:

$$\rho_i = q_i \delta(r_i - r_{lattice}) \tag{5.3}$$

The function can thus take the value 0 or 1. The basis of the Ewald method is to replace the delta function by a Gaussian function.

$$\rho_i = q_i \exp\left(-\frac{(r_i - r_{lattice})^2}{\eta^2}\right) \tag{5.4}$$

where $\eta$ is the half width of the Gaussian. The original charge density is now given by:

$$\rho_i = q_i \left\{ \delta\left(r_i - r_1\right) - \exp\left(-\frac{(r_i - r_1)^2}{\eta^2}\right)\right\} + \exp\left(-\frac{(r_i - r_1)^2}{\eta^2}\right) \tag{5.5}$$

The equation is solved using Poisson'e equation, which relates the density $\rho$ to the second derivative of the potential $\phi$ [93]. The potential for the first part becomes:

$$\phi(r) = q_i \sum_j \left(q_j \frac{1}{r_{ij}} \operatorname{erf} c(\eta r_{ij})\right) \tag{5.6}$$

which sums all interactions of ion $i$ and $j$ over the whole lattice.

The second part is Fourier transformed to converge rapidly in reciprocal space, and is given by:

$$\rho(r) = q_i \sum_k \left(C_k \exp(iK \cdot R)\right) \tag{5.7}$$

where K are the reciprocal lattice vectors and R is $r_i$ - $r_1$ for all ions in a unit cell. The series converges because $C_k$ decreases as $k$ increases. Using Poisson's equation the potential of the second term of the equation becomes

$$\phi_i(r) = q_i \sum \left[q_i \frac{1}{V_k} \sum_k \left(\frac{1}{K^2} e^{-\pi^2 K^2 \eta^2} \cdot e^{ik \cdot r}\right)\right] + q_i \sum_j \left(q_j \frac{1}{r_{ij}} \operatorname{erf} c(\eta r_{ij})\right) - q_i^2 \frac{2\eta}{\sqrt{\pi}} \tag{5.8}$$

where the final term is the self-interaction.

### 5.0.4 Parry Methods

The Parry method [94, 95] is a special application of the Ewald method [92] for two dimensional crystal. The crystal is assumed to consist of a series of charged planes of infinite size rather than a finite lattice. When summing the electrostatic interactions the vectors are now divided into in-plane vectors, $\rho_{ij}$ and vectors perpendicular to the plane, $u_{ij}$. We can no longer assume the total charge of a plane of atoms to be zero as in the three dimensional cell and hence $K = 0$ term has to be evaluated. The part of the summation in reciprocal space then becomes:

$$\phi = \frac{\pi}{A} \left\{ \begin{array}{c} -2u_{ij}\,\mathrm{erf}(\eta u_{ij}) - \frac{2\exp(-\eta^2 u_{ij}^2)}{\sqrt{\pi}\eta} + \\ \sum\limits_{k\neq 0} \frac{\exp(-\eta^2 u_{ij}^2)}{k} \left[ \exp(ku_{ij})\,\mathrm{erf}\,c\left(\frac{k}{2\eta} - \eta u_{ij}\right) + \exp(-ku_{ij})\,\mathrm{erf}\,c\left(\frac{k}{2\eta} - \eta - \eta u_{ij}\right) \right] \end{array} \right\} \tag{5.9}$$

where $K$ is a two dimensional reciprocal lattice vector, $A$ is the surface area, erf and erfc are the standard and complementary error functions.

### 5.0.5 Short Range Two-Body Interactions

The short range attractive and repulsive interactions are described using simple parameterised models. It is essential that this model accurately describes the lattice properties if reliable, quantitative, results are to be obtained. This is particularly important for surfaces where it is necessary to describe the interaction at distances possibly far removed from those found in the bulk lattice [96].Here, follows a description of the most commonly used potential functions, including those used in this work.

### 5.0.6 The Harmonic Potential

One of the simplest potential functions is the harmonic function and is of form:

$$U(r_{ij}) = \frac{1}{2} k_{ij}(r_{ij} - r_0)^2 \tag{5.10}$$

where $k_{ij}$ represents the force constant associated with the deviation from the equilibrium bond separation and $r_0$ the equilibrium bond separation.

This potential is used for systems which have bonding interactions where atoms share electrons, i.e. covalently bonded species. A limitation of this potential function is however, that it cannot be used when the bond length $r_{ij}$ varies too much from equilbrium bond distance $r_0$ as this introduces the anharmonicity of real bonds which cannot be modelled using this potential. However, an alternative potential that can cope with a wider range of bond separations is the Morse potential, discussed in the next section.

### 5.0.7 Morse Potential

The Morse potential is used for covalent bonding when distances vary away from the equilbrium bond distance as it displays the correct anharmonic behaviour missing from the harmonic function. It is thus able to model systems away from their equilibrium bond distances such as point defects and surfaces or when temperature or pressure is applied. Morse potential is described mathematically by the expression:

$$U(r_{ij}) = A_{ij}\left\{1 - \exp\left[-B_{ij}\left(r_{ij} - r_0\right)\right]\right\}^2 - A_{ij} \tag{5.11}$$

where $A_{ij}$ is the bond dissociation energy, $r_o$ is the equilibrium bond distance and $B_{ij}$ is a function of the slope of the potential energy well and can be obtained from spectroscopic data. Due to its inclusion of the bond energy the Morse potential is often used with substraction of the Coulombic inteaction, allowing it to completely describe the bond for nearest neighbours. For second nearest neighbours a non-bonded potential, such as, Buckingham and Lennard-Jones, can be used are described below.

### 5.0.8 Lennard Jones Potential

The Lennard-Jones potential was originally developed to model intermolecular interactions of noble gases and is used widely to describe intermolecular interactions. It is an approximation which describes the complicated nuclear and electronic repulsions which dominate the attractive interactions at short separation. The potential takes the form:

$$U(r_{ij}) = \frac{A_{ij}}{r_{ij}^{12}} - \frac{B_{ij}}{r_{ij}^{6}} \tag{5.12}$$

The first term describes the repulsive forces, dependent on $r_{ij}^{-12}$ and is therefore dominant at very short displacements. The second term describes the attractive forces which accounts for the interactions at larger separations.

### 5.0.9 Buckingham Potential

The Buckingham Potential is similar to the Lennard-Jones potential and is widely used to model non-bonded interactions. It describes the potential energy as a function of distance, and has the following analytical form:

$$U(r_{ij}) = A_{ij} \exp\left(\frac{-r_{ij}}{\rho_{ij}}\right) - \frac{C_{ij}}{r_{ij}^6} \tag{5.13}$$

where the first term(the nearest neighbour interactions) describes the repulsive forces between the ions due to electron cloud overlap, and the second term( second-neighbour interactions) describing the attractive van der Waals interactions, with the usual $\frac{1}{r^6}$ dependence. The parameters $A_{ij}$ is associated to the hardness of the ions, $\rho_{ij}$ is related to the size of the ions and $C_{ij}$ is the term included to model dispersion. However, to assign any physical meaning to these parameters could be wrong, as the fitting methods cannot distinguish between individual parameters but consider the potential energy surface in its totality.

### 5.0.10 Three Body Potential

The three body potential is used for modelling the angular dependence of covalent materials. Changes in interaction energy caused by deviation from the equilibrium bond angle, $\theta$, which is described as the angle between a central ion, $i$, and two adjoining ions $j$ and $k$ is modelled by the three body potential. The potential is dependent on the square of the deviation from the equilibrium angle and is represented by:

$$U_{ijk} = \frac{1}{2} k_{ijk} \left(\theta - \theta_0\right)^2 \tag{5.14}$$

where $k_{ijk}$ is the force constant and $\theta_0$ is the equilbrium bond angle. Figure 5.1 shows a graphic representation of the angular bonding interactions which can be modelled using a three-body potential.

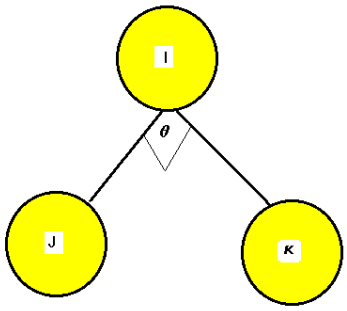


Figure 5.1: Schematic representation of the three body interaction.

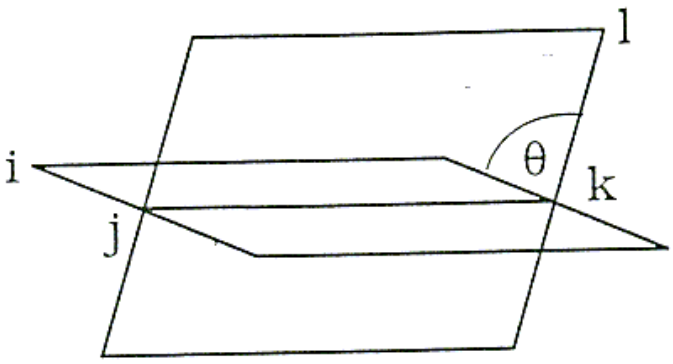


Figure 5.2: Schematic representation of the four body bonding.

### 5.0.11 Four Body Potential

The four body potential (often called torsional function) is used to model systems which have a planar nature due to $\pi$ bonding. In a plane of four atoms $i, j, k, l$ as in figure 5.2, the torsional or dihedral angle is the angle between $i, j$ and $k$. It has the form:

$$U = k_{ijkl}[1 - s\cos(n\theta_{ijkl})] \tag{5.15}$$

where $k_{ijkl}$ is the torsional force constant, $s = \pm 1$ depending on which conformation has the lowest energy. The planes are defined between the ions, $i, j$ and $k$ and between $i, k$ and $l$ where the potential energy is $n$ times the angle between these planes, depending on the number of identical rotations about the $j - k$ axis.

### 5.0.12 Ionic Polarisability

Ionic polarisabity is the distortation of the electron cloud surrounding an ion in an electric field. A dipole may affect short-range interactions between ions. In the rigid ion models, this interaction is completely overlooked, as this model treats the ion as point charges. The mean error introduced for not adding a polarisation term, is an underestimation of the dynamical properties of the lattice, as the lattice vibrations are strongly influenced by ionic polarisability.

A simple description of ionic polarisability can be obtained by using the point polarisability model. The point polarisable model has the following form:

$$\mu = \alpha E \tag{5.16}$$

where $\mu$ stands for the dipole moment, introduced by an electric field $E$ and ionic polarisability $\alpha$, fixed a parameter.

This simple approach has been used in the calculation of defect energies [64]. The methods does not however, account for coupling between short range repulsions and polarisability. Calculated values for defect energies using this method are consequently much lower than those results [97] .

Hence, due to these problem with the point polarisable ion model another model, which allows the polarisation of the ion to change with changing environment, was required. These requirement were found in the shell model.

### 5.0.13 Shell Model

The shell model is the oldest and most common method of incorporating environmental effects. In the shell model atomic interactions are represented by potentials between each pair of atoms in the system. Electronic polarization of the atoms is implemented via the Dick-Overhauser model [98], in which an atom is considered as a charged core X connected by a harmonic spring to a massless charged shell Y (see figure 5.3). The equilibrium distance between the core and shell is a representation of the electronic polarization of that atom. This is important, as there are no electrons in the shell model, all atoms are effectively represented by point charges and the shells approximate the effects of electron density flow on the atomic interactions.The core and the shell are coupled by harmonic spring with force constant $k_i$ giving rise to the interaction energy:

$$U = \frac{1}{2} k_i r_i^2 \tag{5.17}$$

where r is the distance between the core and the shell. The polarisability of a free ion is defined by:

$$\alpha_i = \frac{Y^2}{4\pi\varepsilon_0 k_i} \tag{5.18}$$

where $\varepsilon_0$ is the permittivity of free space and the numerical constant applies if Y is in electron charge units and $k$ is in units of $eV\mathring{A}^2$.

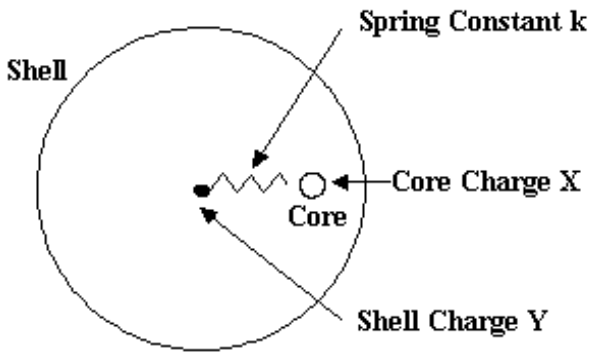


Figure 5.3: Schematic representation of the shell model.

The short range potentials are taken to act between shells, and associate polarizability to the short-range interactions. It should be noted that the

shell model doubles the species which are found in rigid ion model. The large number of species results in an increase in the number of degrees of freedom and thus lead to simulations which take a long time to minimize.

### 5.0.14 Derivation of Potential Models

For any meaningful calculations to take place, using atomistic simulation methods based on inter-atomic potentials, it is vital to obtain the appropriate potential models for the system under consideration. In some cases reliable potential models may already have been derived for the material, but in many cases however, this is simply not the case or the conditions under which the simulation are to run is far from those that the original model was fitted to. In these circumstances derivation of appropriate potential parameters will be required. Generally, there are two possible ways of deriving inter-atomic potential parameters. Firstly, the parameters can be determined by fitting to data calculated by ab-initio, electronic structure calculations, normally by attempting to produce an energy-surface (a function that describes how the energy of the system varies with atomic co-ordinate). Alternatively, it is possible to derive empirical potentials by trying to reproduce experimental data. The two possible ways of deriving potentials are now outlined.

#### Non-Empirical Derivation

The non-empirical approach is to calculate the total energy of the system from the first principles calculations as discussed in section 2.1.

This approach is valid over a wide range of inter-atomic separations making it a powerful modelling tool, since it does not depend of the availability of the experimental data. However, to date the empirical methods are generally most reliable, as the non-empirical techniques have, historically, difficulty predicting the long-range van der Waals dispersions correctly in bulk systems.

#### Empirical Derivation

Potential model parameters derived emperically requires good experimental data on crystal properties of relevent compounds. The cell dimensions, ion coordinates, elastic and dielectric properties for an example provide a reliable way of fitting the parameters as they are often well characterised, but the experimental error or disagreement between experimental sources may

be too great to derive a unique set of parameters in which case additional data is required. The procedure to derive an empirical set of parameters involves starting from a trial set of parameters which will give a set of calculated crystal properties, for an exampe, lattice energy, elastic constants,and dielectric constant, etc. The calculated crystal properties are compared with the known experimental crystal properties and the parameters are then adjusted iteratively using a least squares fitting procedure until the calculated values reproduce as closely as possible, the measured crystal data . The key quantity calculated in the fitting procedure is the "sum of squares", which is a measure of how good the fit is, with the aim of the fit being to minimise the sum of squares ($F$). It is calculated as follows:

$$F = \sum_{all observables} w \left[ f_{calc} - f_{obs} \right]^2 \tag{5.19}$$

where $f_{calc}$ and $f_{obs}$ are calculated and observable quantities that are being fitted, and $w$ is a weighting factor. There is no such thing as a unique fit since the fit will depend on the choice of weighting factor for each observable. The choice depends on several factors, such as the relative magnitude of the quantities and reliability of the data. This adjustment is continued until the difference in the previous equation is below a specified value. Usually the final disagreement is well within the experimental error. Advantages of this method include its relative simplicity as well as the ability to describe the full behaviour of a collection of atoms, including any partial covalency.

### 5.0.15 Potentials Used in this Work: Their Reliability and Transferability

The use of ab initio data to derive a reliable potential model is rather a new approach for mineral sulfides. This is the reason why an important part of this section is devoted to study of the fitting criteria. We also investigated the influence of both the potential parameter and the fitting quantities. The other aim of this study is to check if the derived model is suited for high pessure, temperature Molecular Dynamic simulations, and surface stabilities. This is important since it is generally possible for ionic materials to transfer potential parameters to surface calculations. The availability of accurate first-principle methods makes possible the derivation of reliable interatomic

potentials. However, obtaining a model which is able to describe the interactions of transition metal sulfides constitutes a challenging problem. This is partly due to the fact that the bonding in these materials is unlikely to be close to pure ionic and may involve a complex mixture of bond types ranging from ionic to covalent through to metallic [99]. These difficulties are further compounded by lack of experimental data with which to fit potential parameters. For this reason it is interesting to test the possibility of using a simple model that is exclusively fitted to ab initio data.

### 5.0.16 Importance of ab initio Data in the Development of Interatomic Potential

The first step was to perform full relaxation of both the volume and internal parameters using CASTEP (Cambridge Serial Total Energy Package) code, whose details have been documented in details elsewhere [25],within the local density approximation as discussed in chapter 2. Castep is a pseudopotential total energy code which employs special point integration over the Brillouin zone and a plane-wave basis for the expansion of the wavefunctions. Norm-conserving non-local pseudo-potentials of the form suggested by Kleinmann and Bylander [79] and ultrasoft pseudo-potentials [50] were used. Geometry optimization was performed using a Broyden-Fletcher-Goldfarb-Shanno (BFGS) based minimization technique. This optimization procedure incorporates symmetry constraints. The results for the lattice constant were in good agreement with the experimental data. As usual, DFT-LDA tends to underestimate the equilibrium lattice parameters of a crystal. The calculations also show that PtS, $PdPt_3S_4$ and $PtAs_2$ exhibit a semi-conductor behaviour whilst $Pt_4As_4S_4$ is metallic.

### 5.0.17 Fitting Procedure for $PtAs_2$ and $Pt_4As_4S_4$

The ab initio data which included equilibrium lattice parameters, internal relaxed coordinates, bulk modulli and elastic constants, were used for a relax fitting of potential parameters employing GULP-algorithm [100] in which the changes in the structural parameters on optimization are used to calculate the residual errors. The model recognises that different interaction potentials for $PtAs_2$ are required between $Pt^{2+}$ and $As^{2-}$. Therefore, an interaction between Pt - As, and $As_2$-$As_2$ were described by a combination of two body Buckingham potentials and the dimer, which is formed by As-As within a

bond length of 2.37Å, is described by two body intra-harmonic potential. Cation-cation(Pt-Pt) short-range interactions were neglected because they were weak. This type of model is known as Rigid Ion Model (RIM). Fitting of the potential parameter is performed as in the case of simultaneous equations, where the constants are observables and the unknown parameters being the potential parameters. For a number of observables,

Table 5.1: Optimised potential parameters derived and used for $PtAs_2$

| Buckingham | A (eV) | $\rho$ (Å) | C (eVÅ$^6$) | |
|---|---|---|---|---|
| As-As (non bonding) | 4063.116167 | 0.305 | 80.507 | |
| Pt-As | 42454788.78 | 0.13 | 0.00 | |
| | | | | |
| Harmonic(spring) | $k_s$ (eVÅ$^{-2}$) | $r_0$ (Å) | | |
| As-As (bonding) | 3.62 | 2.666 | | |
| | | | | |
| Three-body exponential | $k_b$ (eV.rad$^{-2}$) | $\theta_0$ (degrees) | $\rho_1$ ( Å) | $\rho_2$ (Å) |
| As-As-Pt | 7.0 | 109.65 | | |
| As-Pt-Pt | 2.0 | 109.65 | | |

one can vary one or two or all parameters describing the potential function at a time. As an for an example, A, C and $\rho$ could be varied simulatneously, or A can be changed while B and $\rho$ kept constant or vice-versa. The parameters A, C and $\rho$ for Buckingham potentials and the force constants $k$ for harmonic potentials were varied until the differences between the calculated and ab inito structure and properties were minimised.The relaxed fitting algorithm was used in all parameter determinations [100].

Here, an optimization of the crystal structure was performed at every stage of the least squares procedure. This algorithm had the benefit that the fitted quantities became the changes in structural parameters rather than the forces calculated at the experimental structure. It was a superior procedure, because minimising the forces did not guarantee to produce better results unless the second derivatives also improved. A minimum sum of squares does not always lead to accurate prediction of other properties which were not used as observables, for example phonon frequencies. Since this condition could be achieved when the structure is at a local minimum, rather than the global minimum, at which the structure will show instabilities, such as, distorted structure and/or imaginary phonon frequencies. It was necessary to validate

the model by performing calculations at the Brillouin zone center ($\Gamma-$ point), since any instabilities in the structure is easily detected by the first three phonon frequencies which correspond to the translation of the lattice. After initial fitting with two sets of two body Buckingham and harmonic potential, it was found that the calculated elastic potential, $C_{11}$, $C_{13}$ and $C_{33}$ were too soft when compared to the observable ones.

Previous studies of force field simulations of sulfides materials [99], included three-body interactions in order to account for the partial covaleny of the material. In order to allow for this, two sets of three-body potential terms As-As-Pt and As-Pt-Pt were included within the fitting procedure. These three-body potential terms also help to maintained tetrahedral environment between platinum and sulphurs in the $PtAs_2$ structure, which favours 109.65°. The shell model was also included in order to model the effects of polarization, paricularly for ionic species, but was found to have no significant contribution and therefore, was removed from the final refinement of $PtAs_2$ parameter set.

Table 5.2: Optimised potential parameters derived and used for $Pt_4As_4S_4$

| Buckingham | A (eV) | $\rho$ (Å) | C (eVÅ$^6$) |
|---|---|---|---|
| As-As (non bonding) | 4063.116167 | 0.305 | 80.507 |
| Pt-As | 42454788.78 | 0.13 | 0.00 |
| S-S | 4063.116167 | 0.305 | 80.507 |
| As-S | 4063.116167 | 0.305 | 80.507 |
| Pt-S | 42454788.78 | 0.13 | 0.00 |

| Harmonic(spring) | $k_s$ ((eVÅ$^{-2}$) | $r_0$ (Å) |
|---|---|---|
| As-As | 3.62 | 2.666 |

| Three-body exponential | $k_b$ (eV.rad$^{-2}$) | $\theta_0$ (degrees) | $\rho_1$ ( Å) | $\rho_2$ (Å) |
|---|---|---|---|---|
| As-S-Pt | 0.6 | 109.65 | | |
| S-Pt-Pt | 0.6 | 109.65 | | |
| As-Pt-Pt | 0.6 | 109.65 | | |

Once the best set of potential parameters for $PtAs_2$ had been obtained, a similar procedure was carried out for $Pt_4As_4S_4$, with the Pt-As, and As-As Buckingham potential parameters fixed and only harmonic and three-body terms were allowed to vary, in order to maintain compatibility of the force

field between atoms. The derived potential parameter sets for $PtAs_2$ and $Pt_4As_4S_4$ are given in Table 5.1 and 5.2.

### 5.0.18 Fitting Procedure for PtS and $PdPt_3S_4$

The potential form used to derive the interatomic potentials of PtS differs slightly from that of $PtAs_2$ and $Pt_4As_4S_4$ since the electronic polarization of ions in the lattice is accounted for by the addition of charged shells [98], as discussed in chapter 2. The core and shell are coupled by a harmonic spring of analytical form $U = \frac{1}{2}kX^2$, where $X$ represents the separation distance of the shell and core of an ion. During the energy minimization calculations, the shell positions are allowed to relax about the ion core resulting in a dipole that mimics the electron polarization. Shells are only included for describing the larger polarization associated with sulphur ions, and platinum atoms were represented by by a rigid ion. This type of model required a completely different interaction potentials between and within Pt-S, S-S as compared to Pt-As, and As-As in the previous model, because of a different environment. In the PtS structure, the Pt atoms are square planar coordinated with four S's, while the S's are tetrahedrally coordinated with four Pt's and Pt in $PtAs_2$ is tetrahedrally coordinated with six As's. Therefore, a new interaction Pt-S, and S-S Buckingham potentials have been defined. Two three-body Pt-S-S (90°) and S-Pt-Pt (109.5°) terms simulate additional interactions within the system. Here, parameters were determined by fitting to a fairly small ab initio database, like equilibrium lattice parameters, internal relaxed coordinates, bulk modulli and elastic constants. Furthermore, all Coulomb interactions are excluded in the system. Table 5.3 provides values for the optimized interatomic potential parameters. A similar procedure was also carried out on $PdPt_3S_4$. The structure of braggite $PdPt_3S_4$, is essentially a superlattice of cooperite as discussed in chapter 1. It is a tetragonal structure, with the combined coordination of square-planar coordinated metals and tetrahedrally coordinated sulphur and the PtS structure is embedded inside the $PdPt_3S_4$ structure. With the Pt-S, and S-S Buckingham potential parameters fixed, and a short-range Pd-S Buckingham potential was introduced into the environment. The harmonic term the Pd-S interactions terms and three-body terms were allowed to vary, until optimisation was achieved. The potential parameters for $PdPt_3S_4$ are depicted in table 5.4 .

Table 5.3: Optimised potential parameters derived and used for PtS.

| Buckingham | A (eV) | $\rho$ (Å) | C (eVÅ$^6$) | |
|---|---|---|---|---|
| Pt-$S_s$ | 11868.154988 | 0.249738 | 0.000 | |
| $S_s$-$S_s$ | 76338.001 | 0.001490 | 120.00 | |
| Core shell interaction(eVÅ$^{-2}$) | charge | Mass | | |
| S core | 1.0 | 195 | | |
| S shell | -3.0 | 32 | | |
| | | | | |
| Three-body exponential | $k_b$ (eV.rad$^{-2}$) | $\theta_0$ (degrees) | $\rho_1$ ( Å) | $\rho_2$ (Å) |
| | | | | |
| $S_s$-Pt-Pt | 4.9999 | 109.5 | 2.6 | 4.0 |

Table 5.4: Optimised potential parameters derived and used for PdPtS

| Buckingham | A (eV) | $\rho$ (Å) | C (eVÅ$^6$) | |
|---|---|---|---|---|
| Pt-$S_s$ | 16992.17930 | 0.23845 | 0.000 | |
| Pd-S | 9992.17930 | 0.238450 | 0.00 | |
| $S_s$-$S_s$ | 1200.00 | 0.0 | | |
| Core shell interaction(eVÅ$^{-2}$) | charge | Mass | | |
| S core | 1.0 | 195 | | |
| S shell | -3.0 | 32 | | |
| Three-body exponential | $k_b$ (eV.rad$^{-2}$) | $\theta_0$ (degrees) | $\rho_1$ ( Å) | $\rho_2$ (Å) |
| Pt-$S_s$-$S_s$ | 0.8901836270 | 90.00 | | |
| $S_s$-Pt-Pt | 10.61536270 | 109.5 | | |

**Water Potentials**

The potential parameters used for the intra- and intermolecular water interactions are those described in the study of MD simulations on MgO surfaces [102], where the intramolecular interactions between oxygen and hydrogen atoms are described by a Morse potential and intermolecularly by a Buckignham potential. The intermolecular interactions between oxygen and oxygen atoms were modelled with Lennard-Jones potential parameters, and intramolecular interactions between hydrogen and hydrogen atoms are described by Morse ptential parameters. A three-body harmonic potential was also included to reproduce the directionality of covalent bonds. Finally, to try and mimic the effect of the lone pairs of the oxygen atoms, the electrostatic interactions between the hydrogen atoms and between the hydrogen and oxygen atoms of a water molecule were partially removed, thus making the hydrogen atoms less repulsive. The potential parameters describing the interactions between water molecles and platinum surfaces were obtained, following the approach of Schroder et al. [103], by modifying the short-range Buckingham potentials which is necessary because of the fractional charges of the water molecule's oxygen and hydrogen atoms. The water potential parameters used in chapter 5 are listed in table 5.5 and 5.6.

We compare the derived interatomic potentials results with theoretical values obtained by means of the above-cited quantum mechanical methodology, and with the available experimental data.

### 5.0.19 Tests and Applications of the Potential

The purpose of this section is to test the quality of the derived interatomic potentials for all the systems. As a test for the validity, the present interatomic potentials should first correctly reproduce the structural properties, such as lattice parameters, bulk modulli and elastic constants. Then the results will be compared with ab initio calculations and experimental results whenever, available. Table 5.7, 5.8, 5.9 and 5.10, compare the properties of $PtAs_2$ , $Pt_4As_4S_4$, PtS and $PdPt_3S_4$, respectively used to develop interatomic potentials by the described procedure. By comparison, it is found that the present potentials reproduce the equilibrium lattice constant, bulk modulli and elastic constants well. The calculated lattice parameters for $PtAs_2$ differ from the ab initio values by 0.2%. The elastic constants calculated are reproduced with a relative error of approximately 16 %. In addition, whatever

Table 5.5: Optimised potential parameters derived and used for $PtAs_2$

| Ion | Charge(e) | | | |
|---|---|---|---|---|
| | core | | | |
| Pt | +2.0 | | | |
| As | -1.0 | | | |
| O | -8.0 | | | |
| H | +0.4 | | | |
| | | | | |
| Buckingham | A (eV) | $\rho$ (Å) | C (eVÅ$^6$) | cut -off -20 |
| As-As (non bonding) | 4063.116167 | 0.305 | 80.507 | |
| Pt-As | 42454788.78 | 0.13 | 0.00 | |
| Pt-O | 396.27 | 0.23 | 0.0 | |
| H-As | 555.4 | 0.208 | 30.0 | |
| As-O | 162222.6 | 0.2454 | 42.09 | |
| H-O | 396.27 | 0.23 | 0.0 | |
| | | | | |
| Harmonic(spring) | $k_s$ (eVÅ$^{-2}$) | $r_0$ (Å) | | |
| As-As (bonding) | 3.62 | 2.666 | | |
| | | | | |
| Lennard-Jones | | | | |
| O-O | 39344.9 | 42.15 | | |
| | | | | |
| Morse | | | | Coulombic subtraction(%) |
| H-H | 0.0 | 2.840499 | 1.5 | 50 |
| O-H | 6.203713 | 2.22003 | 0.92367 | 50 |
| | | | | |
| Three-body exponential | $k_b$ (eV.rad$^{-2}$) | $\theta_0$ (degrees) | $\rho_1$ ( Å) | $\rho_2$ (Å) |
| As-As-Pt | 0.6 | 109.65 | | |
| As-Pt-Pt | 0.6 | 109.65 | | |
| O-H-H | 4.19978 | 108.693195 | | |

Table 5.6: Optimised potential parameters derived and used for $Pt_4As_4S_4$

| Ion | Charge(e) | | | |
|---|---|---|---|---|
| | core | | | |
| Pt | +2.0 | | | |
| As | -1.0 | | | |
| O | -8.0 | | | |
| H core | +0.4 | | | |
| Buckingham | A (eV) | $\rho$ (Å) | C (eVÅ$^6$) | |
| As-As (non bonding) | 4063.116167 | 0.305 | 80.507 | |
| Pt-As(bonding) | 42454788.78 | 0.13 | 0.00 | |
| Pt-S | 42454788.78 | 0.13 | 0.00 | |
| S-S | 4063.116167 | 0.305 | 80.507 | |
| S-As (bonding) | 4063.116167 | 0.305 | 80.507 | |
| Pt-O | 396.27 | 0.23 | 0.0 | |
| H-As | 555.4 | 0.208 | 30.0 | |
| As-O | 162222.6 | 0.2454 | 42.09 | |
| H-S | 495.38 | 0.25 | 20.0 | |
| S-O | 162222.6 | 0.2454 | 42.09 | |
| H-O | 396.27 | 0.23 | 0.0 | |
| Harmonic | $k_s$ (eVÅ$^{-2}$) | $r_0$ (Å) | | |
| S-As (bonding) | 3.62 | 2.666 | | |
| Lennard-Jones | | | | |
| O-O | 39344.9 | 42.15 | | |
| Morse | | | | Coulombic subtraction (% |
| H-H | 0.0 | 2.840499 | 1.5 | 50 |
| O-H | 6.203713 | 2.22003 | 0.92367 | 50 |
| | | | | |
| Three-body exponential | $k_b$ (eV.rad$^{-2}$) | $\theta_0$ (degrees) | $\rho_1$ ( Å) | $\rho_2$ (Å) |
| S-As-Pt | 0.6 | 109.65 | | |
| As-S-Pt | 0.6 | 109.65 | | |
| S-Pt-Pt | 0.6 | 109.65 | | |
| As-Pt-Pt | 0.6 | 109.65 | | |
| O-H-H | 4.19978 | 108.693195 | | |

method was used to obtain the potentials, one of the important tests for the final validation is to use the potentials to calculate the properties of other structures that were not involved in the potential derivation. The lattice parameters were calculated as a function of pressure, and the results are shown in figures 5.4 to 5.7. Although there are obvious differences between the interatomic potential results and CASTEP calculations, the overall agreement is satisfactory, except for PtS where the new interatomic potentials could not reproduce the anomolous behavior of the c lattice constant as function of pressure as seen from the CASTEP calculations. However, we observed, from fig. 5.6, that the c-lattice constant of PtS from the newly derived interatomic potential tends to a constant value instead of reducing with pressure; which is an indication that it causes the anomaly noted in plane wave method (CASTEP). Hence, in general, these new interatomic pair potentials could be regarded as promising in predicting the structure.

Table 5.7: Ab initio and calculated properties of $PtAs_2$ at zero pressure and temperature.

| Properties | ab initio | Present work | Experiment |
|---|---|---|---|
| a (Å) | 5.90 | 5.91 | 5.97 |
| $\alpha$ (degrees) | 90 | 90.0 | 90 |
| Elastic Constants (GPa) | | | |
| $C_{11}$ | 355.5 | 305.98 | - |
| $C_{12}$ | 49.6 | 42.29 | - |
| $C_{44}$ | 151.6 | 95.31 | - |
| Bulk Modulus | 151.6 | 163.4 | |
| Vibrational frequencies at $\Gamma-$ point in $cm^{-1}$ | | | |
| Frequencies | | 0,0,0 | |
| | Mass(a.u) | Charge | |
| Pt | 195.9 | 2.00 | |
| As | 74.5 | -2.00 | |

### Thermodynamics Prediction

Our state-of-the-art Lattice Dynamics calculations based on the newly implemented analytical free energy derivatives were also performed using GULP.

Table 5.8: Ab initio and calculated properties of $Pt_4As_4S_4$ at zero pressure and temperature.

| Properties | ab initio | Present work | Experiment |
|---|---|---|---|
| a (Å) | 5.88 | 5.84 | 5.788 |
| $\alpha$ (degrees) | 90.0 | 90.0 | 90.0 |
| Elastic Constants (GPa) | | | |
| $C_{11}$ | 199.10 | 160.88 | - |
| $C_{12}$ | 98.9 | 132.61 | - |
| $C_{44}$ | 45.5 | 80.29 | - |
| Vibrational frequencies at $\Gamma-$ point in $cm^{-1}$ | | | |
| Frequencies | | 0,0,0 | |
| | Mass(a.u) | Charge | |
| Pt | 195.9 | 2.00 | |
| As | 74.5 | -2.00 | |

Table 5.9: Ab initio and calculated properties of PtS at zero pressure and temperature.

| Properties | ab initio | Present work | Experiment |
|---|---|---|---|
| a (Å) | 3.44 | 3.54 | 3.47 |
| c (Å) | 6.09 | 5.81 | 6.11 |
| $\alpha$ (degrees) | 90 | 90.0 | 90.0 |
| Elastic Constants (GPa) | | | |
| $C_{11}$ | 213.30 | 274.40 | - |
| $C_{12}$ | 69.70 | 39.94 | - |
| $C_{13}$ | 138.10 | 78.59 | - |
| $C_{33}$ | 314.20 | 373.27 | - |
| $C_{44}$ | 47.30 | 57.71 | - |
| $C_{66}$ | 18.70 | 13.24 | - |
| Bulk Modulus | 141.10 | 140.63 | - |

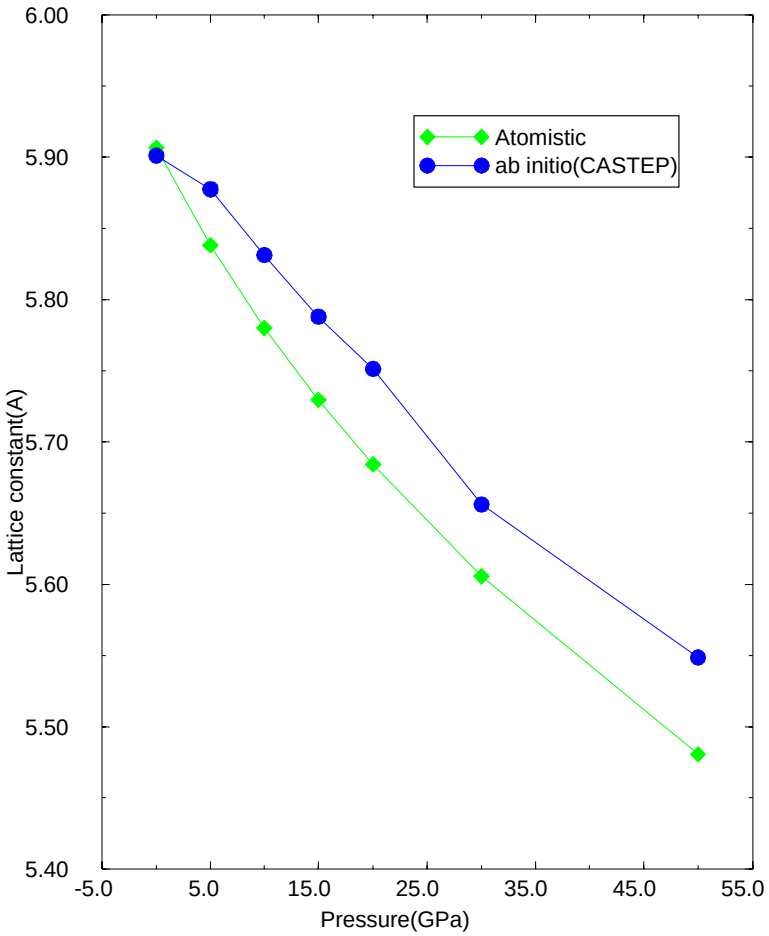


Figure 5.4: Plot of lattice constant as a function of pressure for $PtAs_2$ at zero temperature.

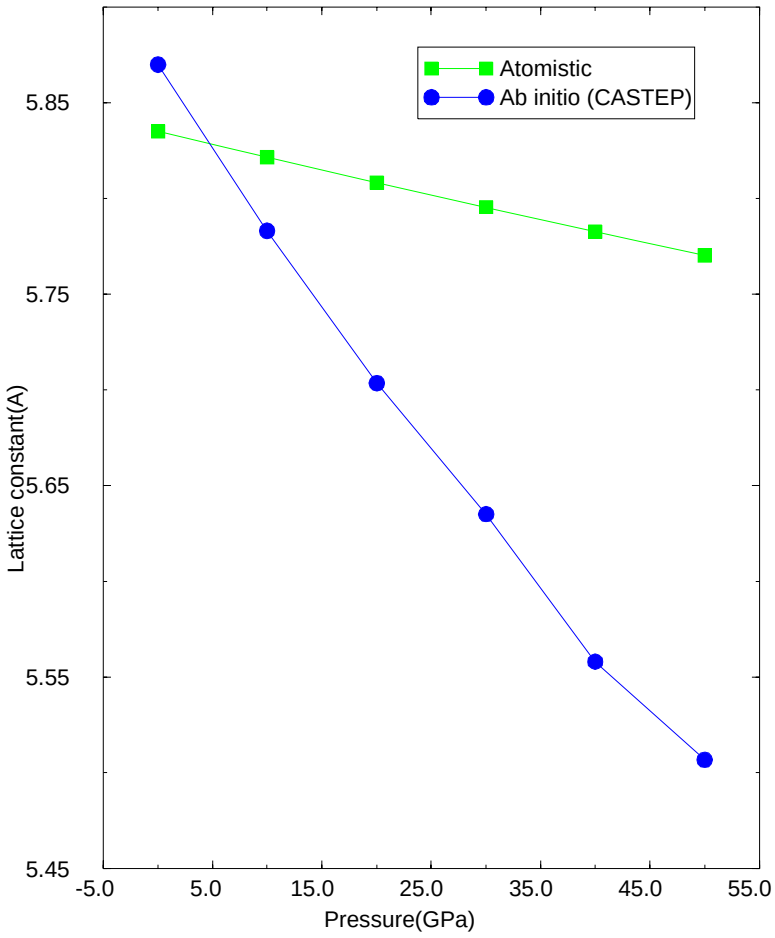


Figure 5.5: Plot of lattice constant as a function of pressure for $Pt_4As_4S_4$ at zero temperature.

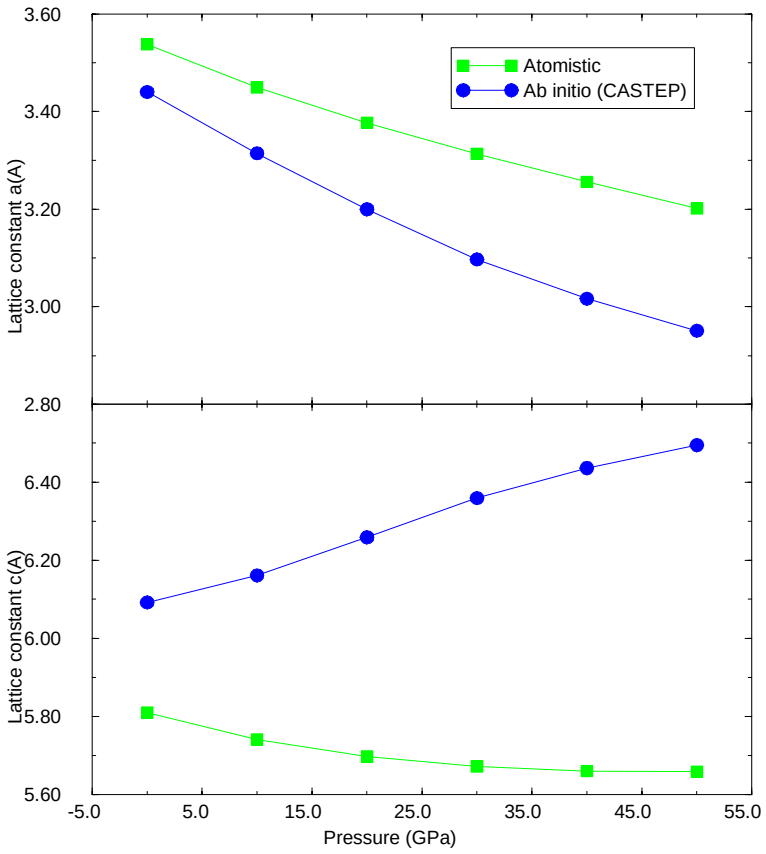


Figure 5.6: Plot of lattice constants a and c as a function of pressure for PtS at zero temperature.

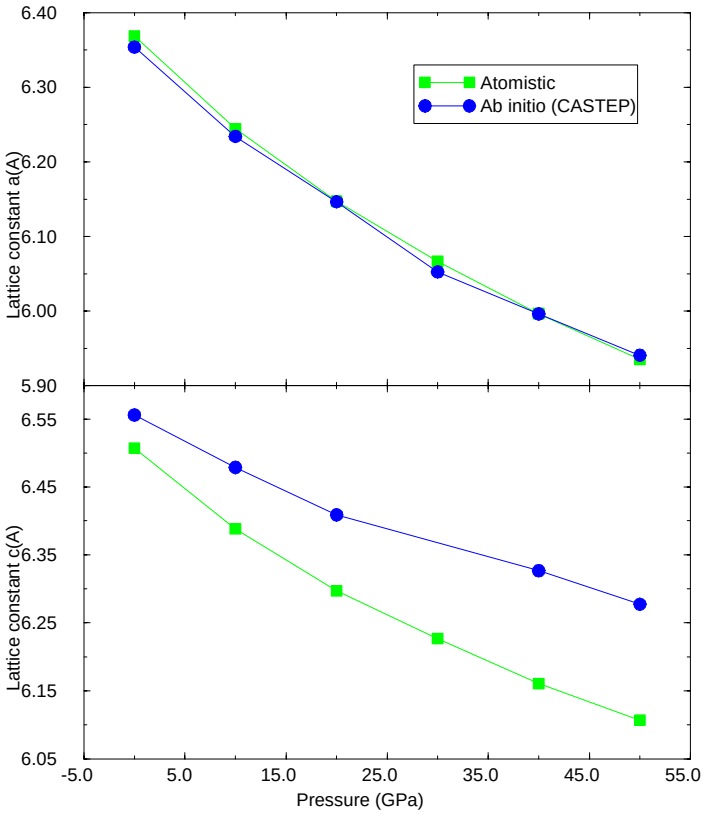


Figure 5.7: Plot of lattice constant as a function of pressure for $PdPt_3S_4$ at zero temperature.

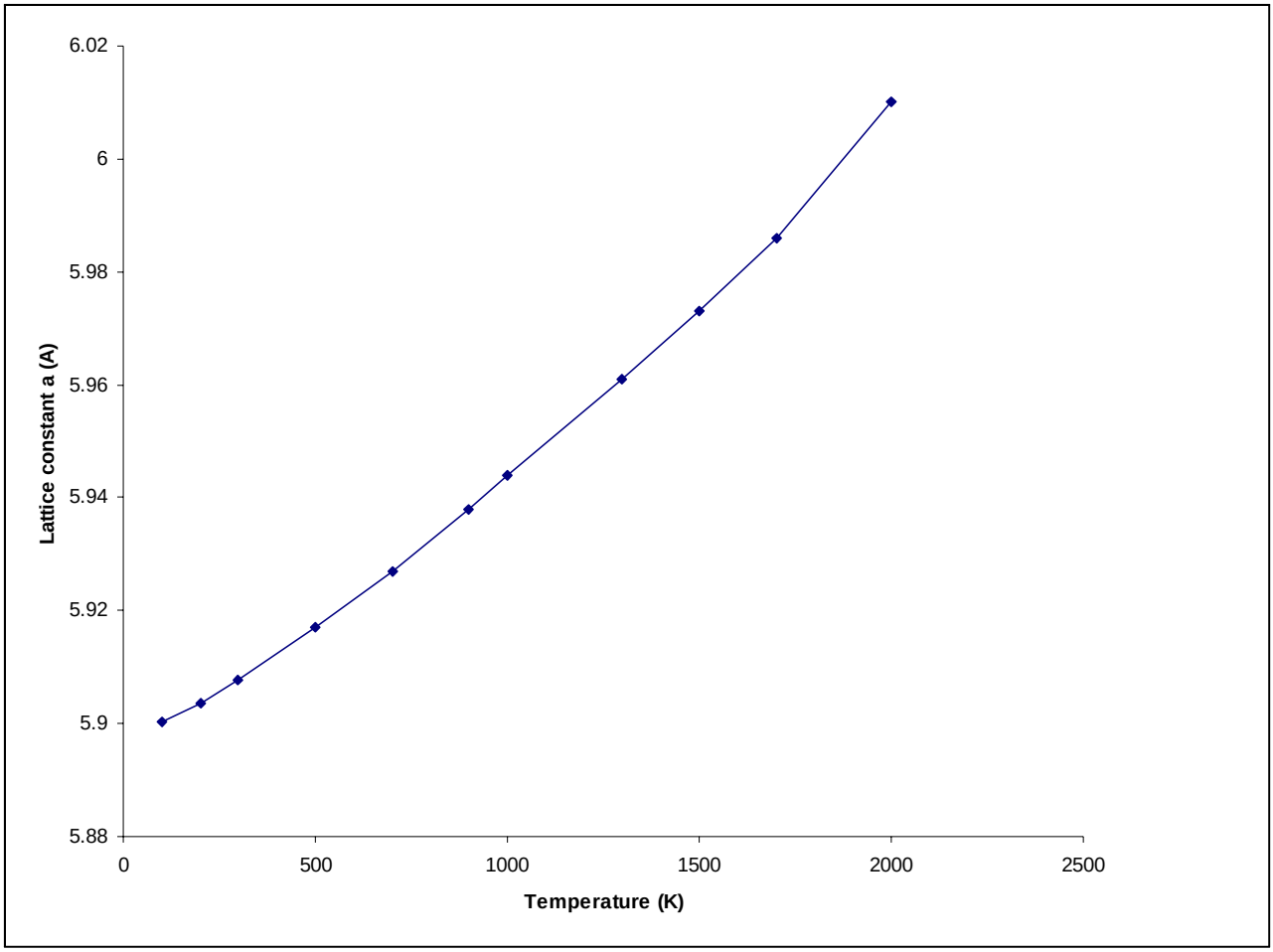


Figure 5.8: Lattice constant as a function of temperature for $PtAs_2$

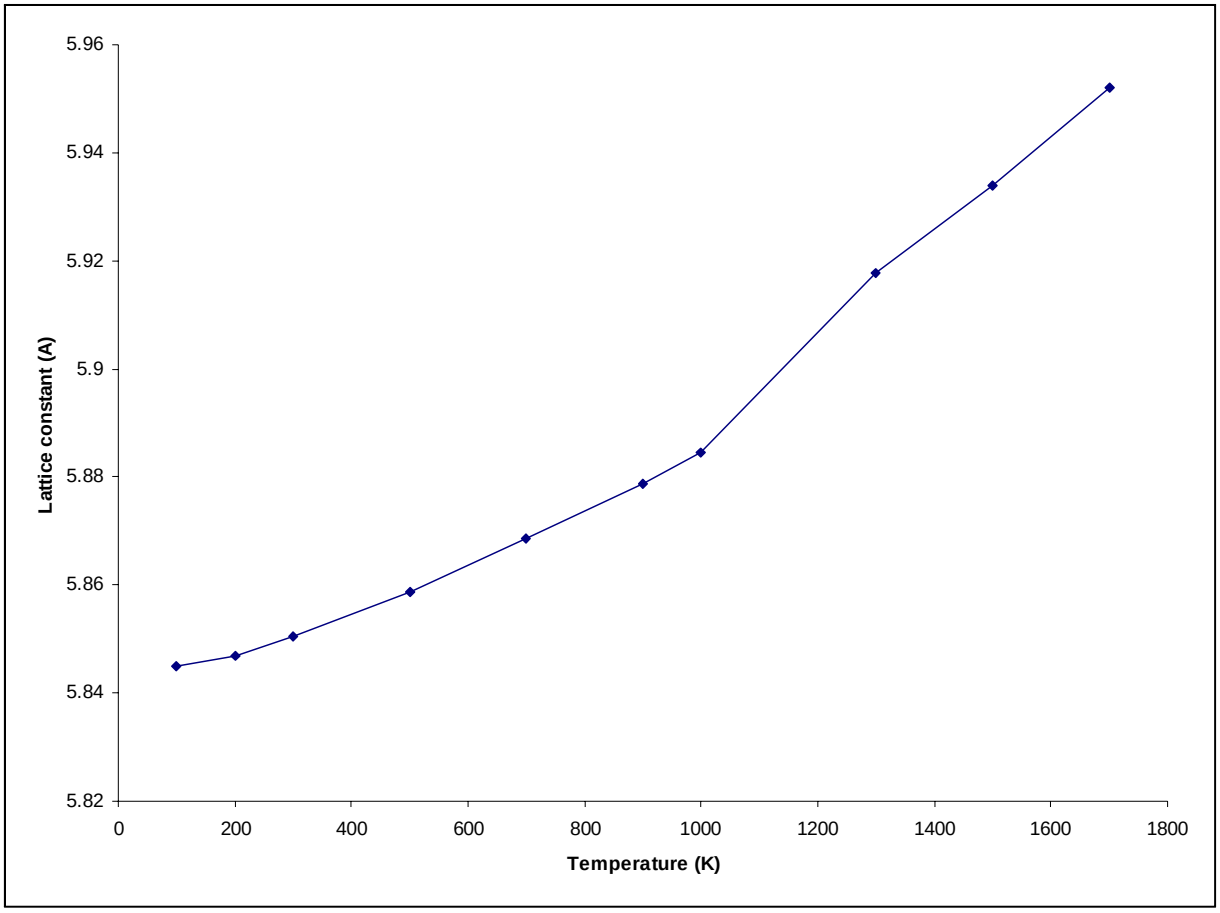


Figure 5.9: Lattice constant as a function of temperature for $Pt_4S_4As_4$

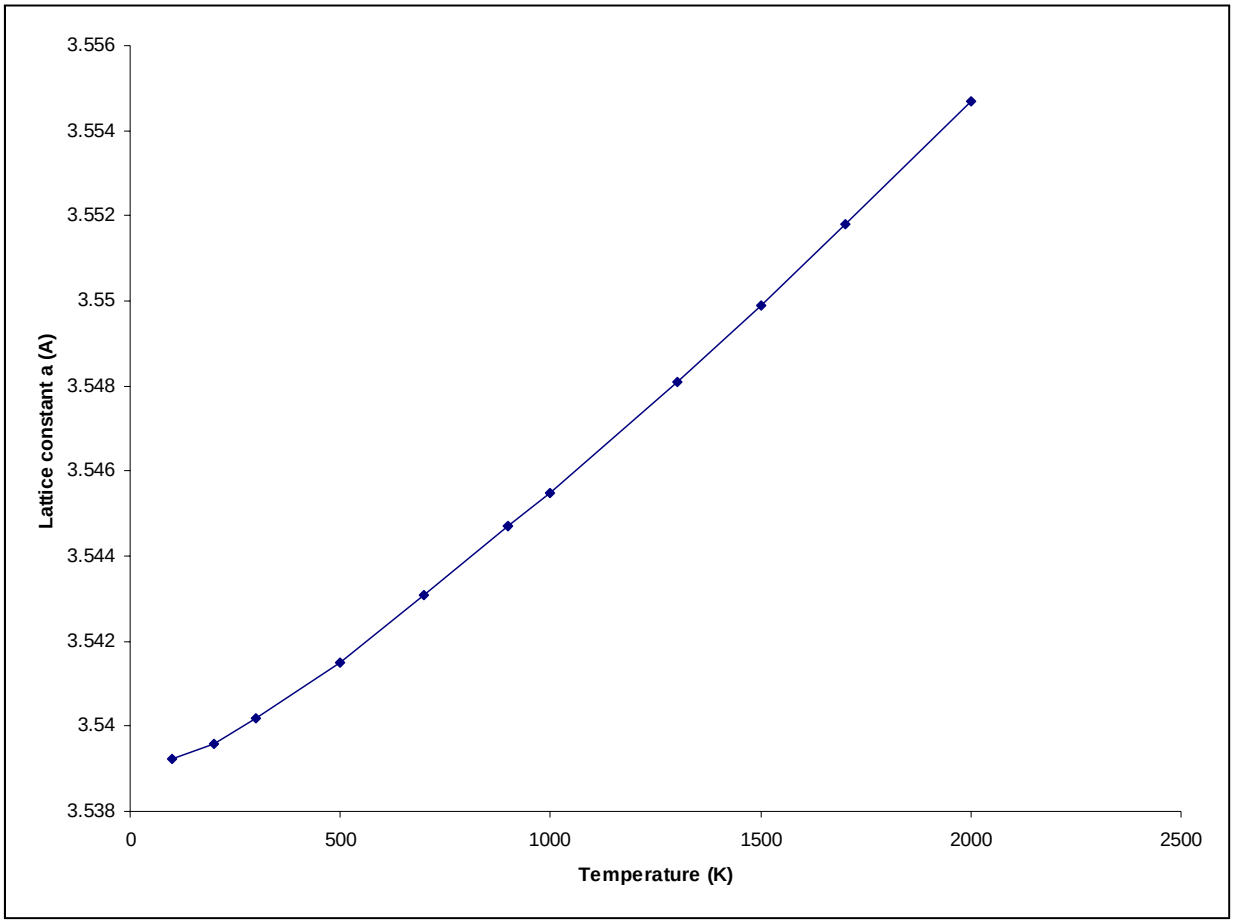


Figure 5.10: Lattice constant as a function of temperature for PtS

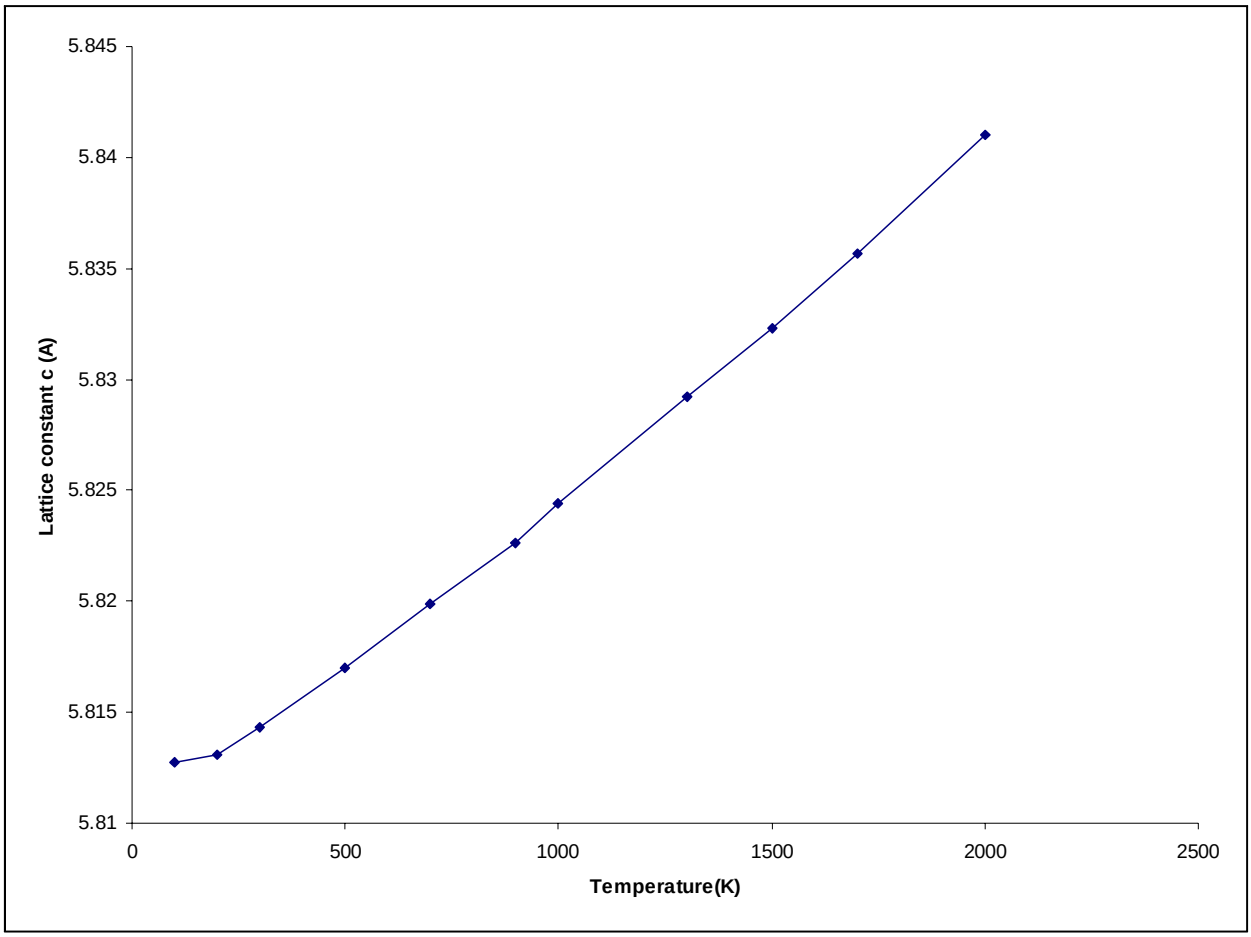


Figure 5.11: Lattice constant as a function of temperature for PtS

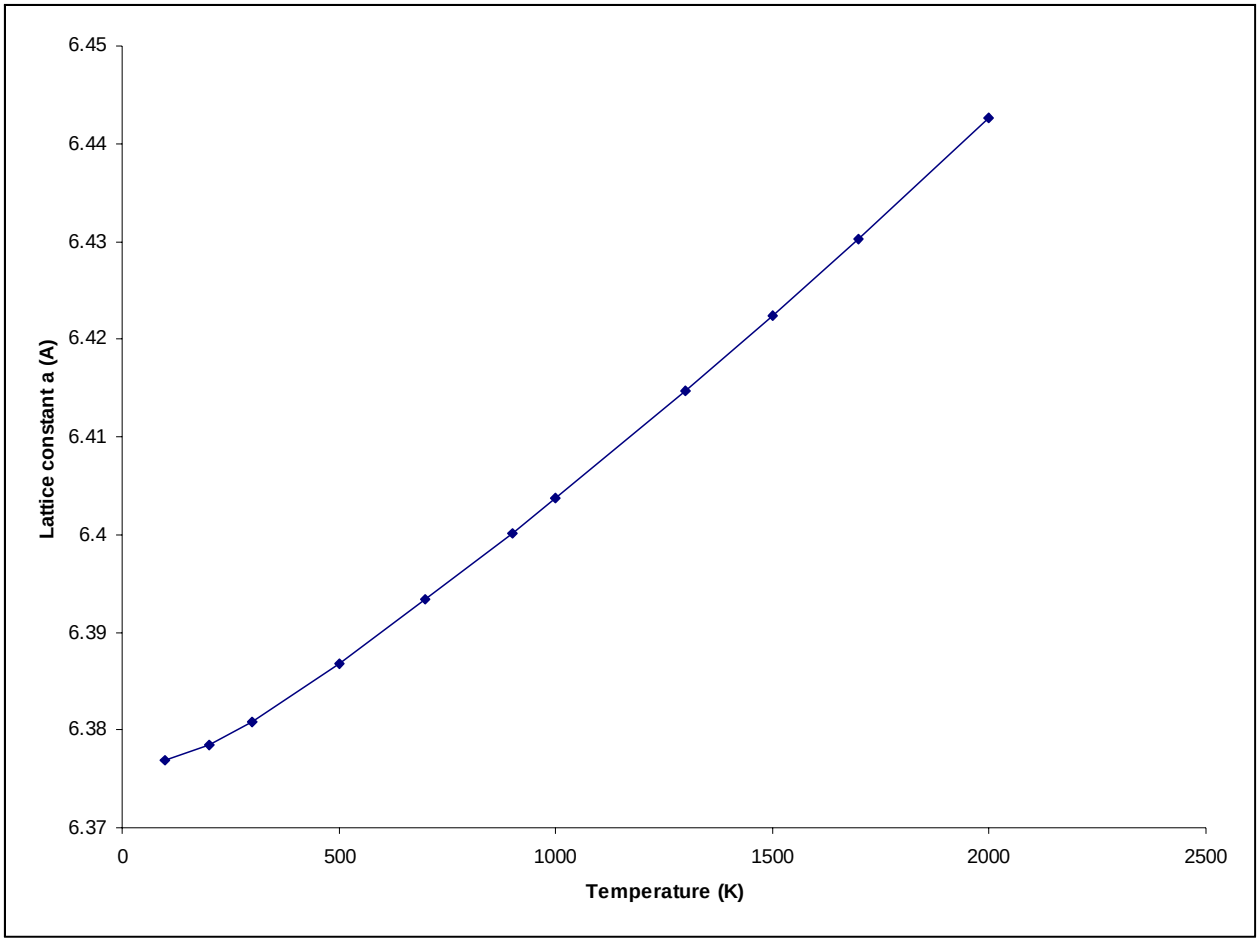


Figure 5.12: Lattice constant a as a function of temperature for $PdPt_3S_4$

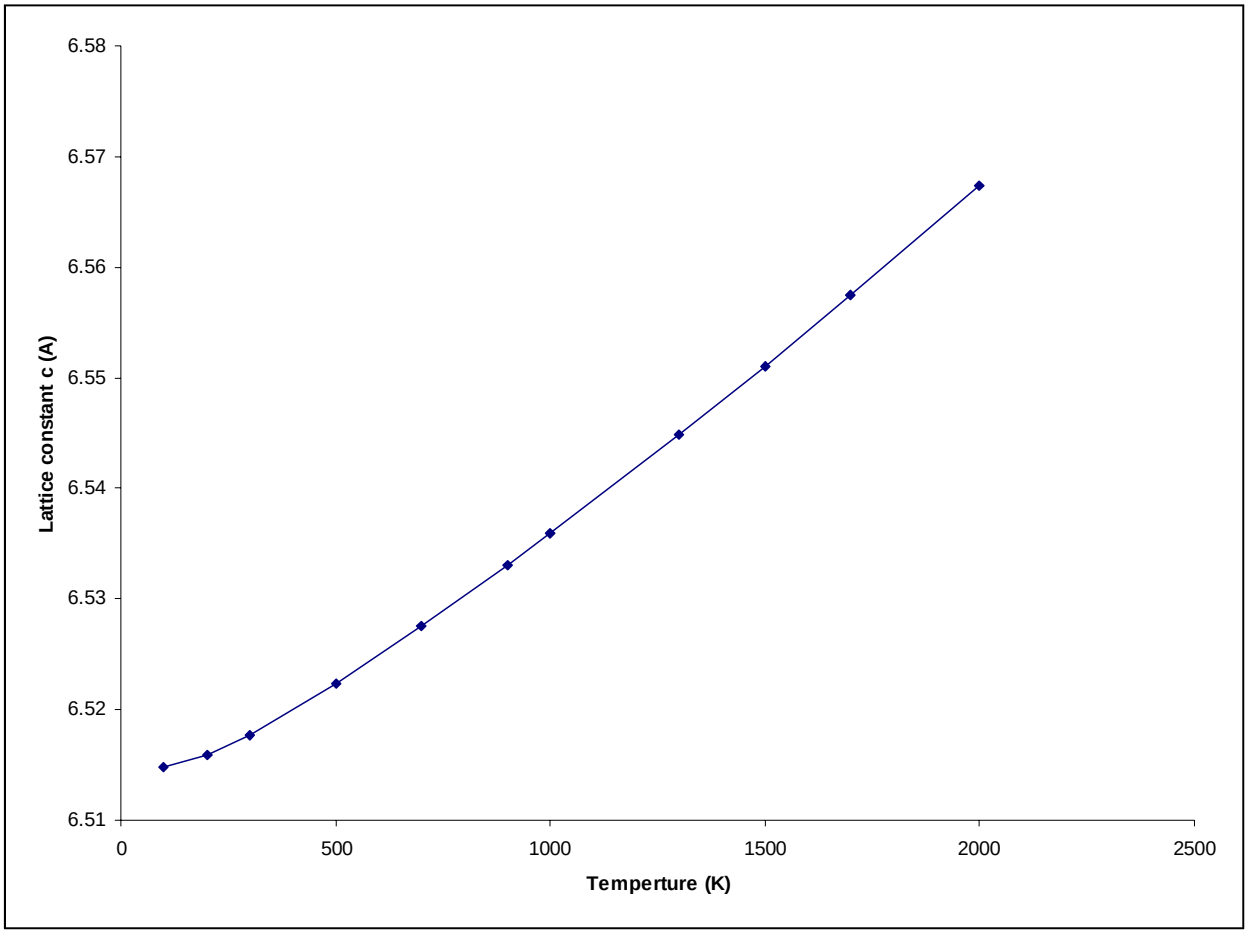


Figure 5.13: Lattice constant c as a function of temperature for $PdPt_3S_4$

Table 5.10: Ab initio and calculated properties of (Pd,Pt)S at zero pressure and temperature.

| Properties | ab initio | Present work | Experiment |
|---|---|---|---|
| a (Å) | 5.88 | 5.84 | 5.788 |
| $\alpha$ (degrees) | 90.0 | 90.0 | 90.0 |
| Elastic Constants (GPa) | | | |
| $C_{11}$ | 199.10 | 160.88 | - |
| $C_{12}$ | 98.9 | 132.61 | - |
| $C_{44}$ | 45.5 | 80.29 | - |
| Bulk Modulus | 174 | 151.3 | |
| Vibrational frequencies at $\Gamma-$ point in $cm^{-1}$ | | | |
| Frequencies | | 0,0,0 | |
| | Mass(a.u) | Charge | |
| Pt | 195.9 | 2.00 | |
| As | 74.5 | -2.00 | |

This new approach allows one to perform calculations of unprecedented precision with large Brillouin zone sampling grids, and without conventional "ZSISA"(Zero static interal stress approximation, in which only the unit cell parameters are determined by the free energy minimisation, while all atomic coordinates are calculated by minimisating the internal energy). Free energy minimisation was performed with $8X8X8$, $5X5X5$, $8X8X8$, $6X6X6$, grids for Brillouin zone integration for $PtAs_2$, $Pt_4As_4S_4$, PtS and $PdPt_3S_4$.These grids showed very good convergence for all properties.

The equilibrium values of the lattice parameters for $PtAs_2$, $Pt_4As_4S_4$, PtS and $PdPt_3S_4$, calculated at different temperatures with zero pressure are plotted in figure 5.7 - 5.10 and their expected increase with temperature is noted.

# 5.1 CONCLUSION

We have developed a new set of interatomic potentials for $PtAs_2$, $Pt_4As_4S_4$, PtS and $PdPt_3S_4$ by using the results of DFT_LDA calculations to fit to both the rigid-ion and shell models. In the absence of relevant experimental data, the potential parameters have been fitted to the structural parameters,

lattice constants and the bulk moduli. The predicted values of the lattice constants, elastic constants and bulk moduli, compare well with those of ab initio (CASTEP) method. The lattice parameters as a function hydrostatic pressure were performed and their response to hydrostatic pressure follow the general trend of the ab initio calculations, except for PtS which is showing some anomaly along c-lattice constant, for which there are no experimental results available. Also, the predicted elastic constants for $PdPt_3S_4$ by atomistic method are slightly high as compared to the ab intio ones.

# Chapter 6

# SURFACES AND CRYSTAL GROWTH

## 6.1 Introduction

The new force fields for modeling $PtAs_2$, $Pt_4As_4S_4$, PtS and $PdPt_3S_4$ have been derived as discussed in the previous chapter. These models of force fields reproduced the bulk structures and properties very well, as predicted from ab inito(CASTEP) calculations. The aim of the work in this chapter is to apply the atomistic techniques discussed in chapter 2 to investigate the surface structure, stability and reactivity of $PtAs_2$ and $Pt_4As_4S_4$, using potentials that have been validated against the bulk structural data. The interatomic potentials fitted to bulk properties are not guaranteed to be valid for lower coordination environments, such as those found at surfaces, hence, the present work considers the enduring problem of the transferability of effective potential models derived from bulk properties, to the study of surfaces. The surfaces for both PtS and $PdPt_3S_4$ will be left for future work, since the c lattice constant of PtS shows some anomalies at high pressure, where no experimental results are availabe for validation. Furthermore, PtS is the sub-structure of $PdPt_3S_4$. The low and high index surfaces of $PtAs_2$ and $Pt_4As_4S_4$ will be modeled. Different step surfaces were created in order to model more realistic surfaces with one dimensional defects. The equilibrium morphology is calculated, as a way to assess the change in surface energies.

In most technological applications of surface chemistry, for an example, in catalysis, the surfaces used to promote a reaction are highly nonideal.

They contain steps and other imperfections in large concentrations, which are thought to provide reactive sites. Also in thin-film growth, steps are crucial for producing smooth layers via the so-called step-flow mode of growth. Despite their importance, detailed information about the role of steps is scarce. On metals, it is generally argued that the reactivity at steps is increased due to a lower coordination number of atoms [101]. On semiconductors, the situation is less clear since step and terrace atoms often attain similar coordinations due to special reconstructions.

## 6.2 Surface Methodology

The energy minimisation code employed was METADISE [65], which is designed to model dislocations, interfaces and surfaces. Following the approach of Tasker (1979) [68], the crystal consists of a series of charged planes parallel to the surface and periodic in two dimensions as discussed in chapter 2.

The surface energy $\gamma$ is a measure of the thermodynamic stability of the surface with a low, positive value indicating a stable surface. It is given by

$$\gamma = \frac{E_s - E_b}{A} \tag{6.1}$$

where $E_s$ is the energy of the surface block of the crystal, $E_b$ is the energy of an equal number of atoms of the bulk crystal and $A$ is the surface area. The energy of the blocks are essentially the sum of the energies of the interactions and are calculated using Parry technique [95] whereas the short-range repulsions and van der Waals attractions are described by parametrized analytical expressions.

For hydrated surfaces the surface energies were calculated with respect to liquid water in order to assess the stability of the surface in an aqueous environmnent :

$$\gamma = \frac{E_d - (E_b + E_{H_20})}{A} \tag{6.2}$$

where $E_d$ is the energy of the surface block, suitably hydrated, while $E_b$ is the energy of the same number of bulk ions and $E_{H_2O}$ is the energy of the bulk water. The latter is the sum of the self-energy of water due to the intramolecular forces, and the energy of condensation due to the intermolecular forces.

In addition to calculating the surface energy we calculate the adsorption energy $E_{ads}$, i.e., the energy to adsorb water on the surface per water molecule, which is given by

$$E_{ads} = \frac{E_d - (E_s + nE_{H_2O})}{n} \tag{6.3}$$

where $n$ is the number of water molecules, $E_{H_20}$ is the self-energy of water and $E_d$ is the energy of the simulation cell including water. Energy minimisation of the various unrelaxed starting configurations provided a collection of minimum energy structures of surfaces with adsorbed molecules, from which we chose the lowest energy system as representing the global minimum. The low energy surfaces, and hence the most common surfaces of a crystal, are generally those of low Miller indices. These planes are the closest packed with large interplanar spacings.

### 6.2.1 Potential Models

The environment of the surface region of an ionic crystal will cause changes in the short-range interatomic interactions; namely, there is a change in the effective ion polarisability as one approaches a surface from the bulk of a crystal. Consequently some allowance for this should be made in the potential model used. We have identified the best potential model for use in the surface simulations and test their reliability. The simulations presented in this chapter are based on the potentials introduced in the previous chapter.

## 6.3 Results and Discussion

### 6.3.1 Dry Surfaces

#### $\mathbf{PtAs_2}$

The relaxed crystal was cut to obtain both the {100}, {110}, {111} low index as well as high index surfaces {210}, {310}, {410}, {510},{610} for $PtAs_2$. We shall only consider non-dipolar terminations. The results on unhydrated surfaces will be presented first, followed by hydrated surfaces of $PtAs_2$. For $PtAs_2$, arsenic dimer pairs were maintained at a distance of 2.3Å or less apart, so as to have a surface which closely resemble the bulk. In this

case, we can cut through the arsenics of different dimers, not within a dimer. The surfaces were then energy minimsed to allow for surface relaxation and the resulting surface energies, are given in table 6.1. It is clear that the {100} surface is, by virtue of the lowest surface energy ($\gamma = 1.06$ Jm$^{-2}$) the most stable under the dry conditions. The order of the relative stability of the surfaces changes with surface relaxation and is {100} > {110} >{111}, which is similar to that of rock salt structured materials, and AsAs-anions terminations are most stable for each surfaces of low index.

No experimental evidence results for $PtAs_2$ are available to validate our calculations.

Table 6.1: Unrelax and relax surfaces energies of unhydrated $PtAs_2$.

| Surface (hkl) | Unrelax Surface (Jm$^{-2}$) | Relax surface (Jm$^{-2}$) | Termination |
|---|---|---|---|
| {100} | 1.098 | 1.011 | As-As |
| {110} | 2.09 | 1.899 | As-As |
| {111} | 2.931 | 2.497 | As-As |
| {210} | 1.803 | 1.613 | As |
| {310} | 1.610 | 1.438 | As-As |
| {410} | 1.500 | 1.348 | As-As |
| {510} | 2.475 | 1.936 | Pt |
| {610} | 1.378 | 1.244 | As-As |

**{100} surface**

Cutting the {100} plane gives two possible surface terminations, the one terminated by platinum ions, the other by arsenic ions. The {100} arsenic terminated surface (fig. **6.1**) is the most stable dry surface, with a surface energy of 1.01 Jm$^{-2}$. The {100} surface is a type II surface which has a small surface area with non-dipolar termination from arsenic(As) atoms. The surface has two platinum (Pt) atoms situated slightly beneath four arsenic atoms. One platinum at the center of the unit cell is coordinated to five arsenic atoms and the one at the corner of the cell is also coordinated to the extra three arsenic atoms in the neighbouring unit cell. These two platinums are accessible to the adsorbing molecules.

**{110} surface**

The {110} surface is a type II surface. The top of the edges of the model show how the layer is truncated, which is characterised by As atom in a

zigzag arrangement, with only every second As atom attached directly to a terminal As atom at the surface to form a dimer. The {110} surface is

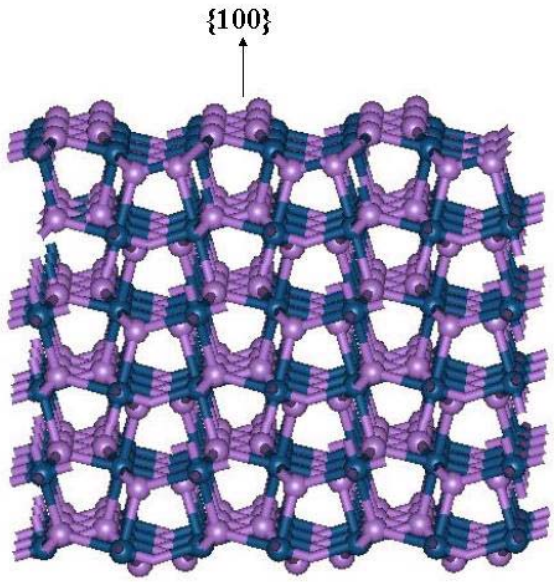


Figure 6.1: Sideview of the geometry optimised {100} most dry stable surface ( As = Purple, Pt = blue ).

terminated by arsenic atoms, with two platinums on two different edges of the cell accessible to the adsorbing molecules and the one immediately below the surface not accessible to the adsorbing species. This surface has a much larger surface energy than the {100} surface (Table 6.1). Fig. 6.2 shows the {110} As-terminated surface, which is the second most stable dry surface.

**{111} surface**

Cutting {111} plane gives also two possible surface terminations, which can be labelled acording to the terminating species, {111} Pt for platinum terminated plane, and {111} As for the arsenic terminated plane. The {111} As terminated surface (fig. 6.3) is a third most stable dry surface of the low indices. It has a large unit surface area as compared to other platinum low index surfaces and has three sulphur atoms and four platinum atoms at the surface. This surface has two platinum atoms fully accessible, and another

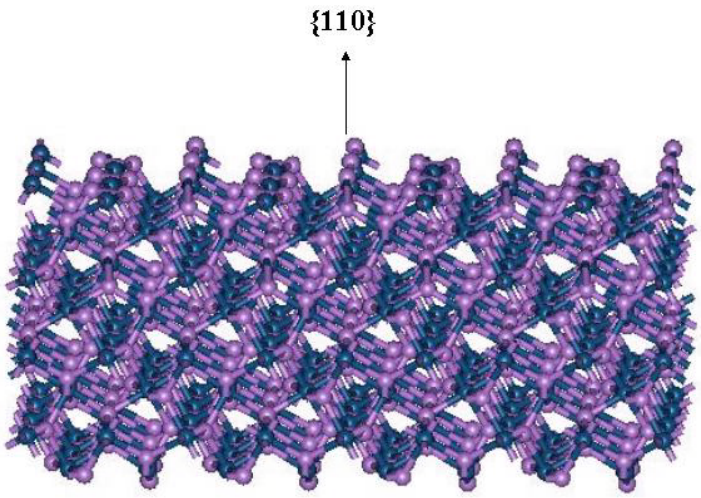


Figure 6.2: Sideview of the geometry optimised {110} most dry stable surface ( As = Purple, Pt = blue ).

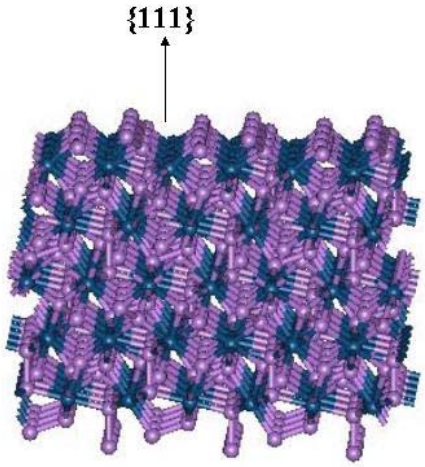


Figure 6.3: Sideview of the geometry optimised {111} most dry stable surface ( As = Purple, Pt = blue ).

two platinums below the arsenic group inaccessible to the adsorbing species.

**{210} surface**

The {210} surface has the smallest unit cell area of all the high indices surface considered in the current study, with a surface energy of 1.6 $Jm^{-2}$. Owing to the small surface area there are only two platinum atoms per unit cell accessible to adsorbing species, with the other two platinums on the surface inaccessible since they are six fold coordinated. It is observed from fig. 6.4 that this surface microfacets into steps of {100} plane, with surface energy of 1.60 $Jm^{-2}$, and it is a type II surface.

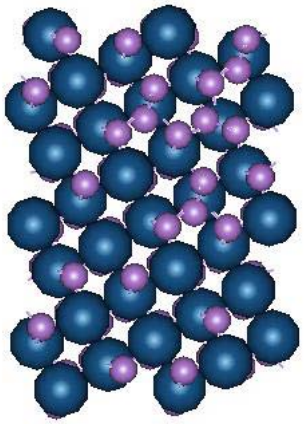

Figure 6.4: Sideview of the geometry optimised {210} most dry stable surface ( As = Purple, Pt = blue ).

**{310} surface**

The {310} surface is a type II surface. It is mainly terminated by arsenic atoms, with six of seven platinum atoms on the surface accessible to the adsorbing species. The surface (fig. 6.5) also microfacets into steps of {100} planes, and it has a surface energy of 1.44 $Jm^{-2}$.

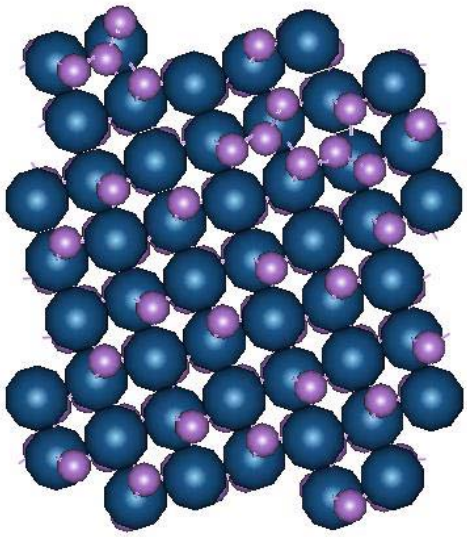

Figure 6.5: Sideview of the geometry optimised {310} most dry stable surface ( As = Purple, Pt = blue ).

**{410} surface**

Fig. 6.6, shows the {410} surface which depicts some steps found on the {100} surface. The {410} surface has two possible surface terminations, of type I and type II. The most stable surface is of type II with surface energy of 1.28 $Jm^{-2}$. It has five platium atoms available to adsorbing species, and two inaccessible platinum atoms.

**{510} surface**

Cutting the {510} surface gives two possible surface terminations, which are, the arsenic and platinum terminated planes. The platinum terminated planes (fig. 6.7) (type II surface) are the most stable with surface energy of 1.24 $Jm^{-2}$. The seven platinum atoms out of ten platinums are accessible to the adsorbing species.

**{610} surface**

The {610} surface has two possible surface terminations, and has the largest unit cell area of all the surfaces considered. The arsenic terminated surface is the most stable

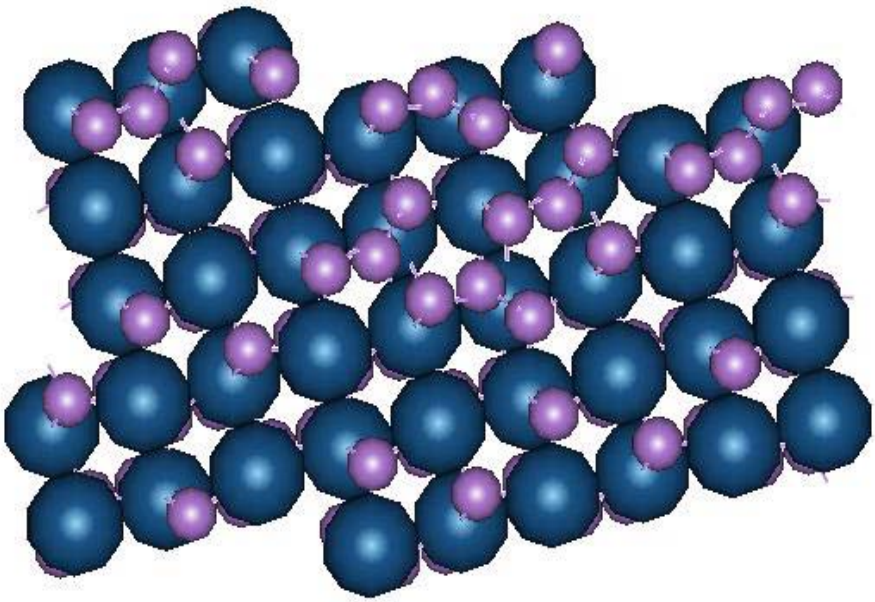

Figure 6.6: Sideview of the geometry optimised {410} most dry stable surface ( As = Purple, Pt = blue ).

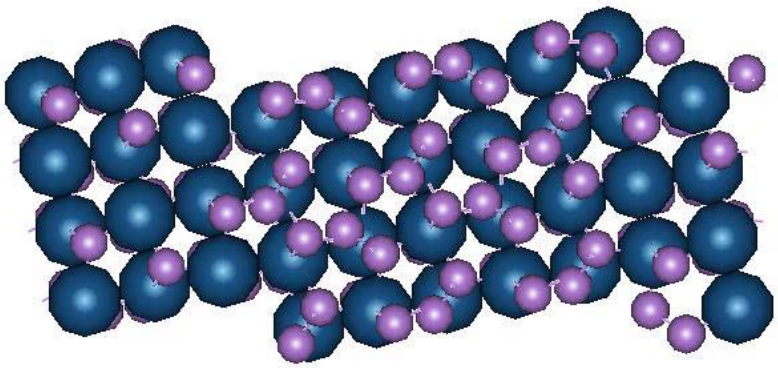

Figure 6.7: Sideview of the geometry optimised {510} most dry stable surface ( As = Purple, Pt = blue ).

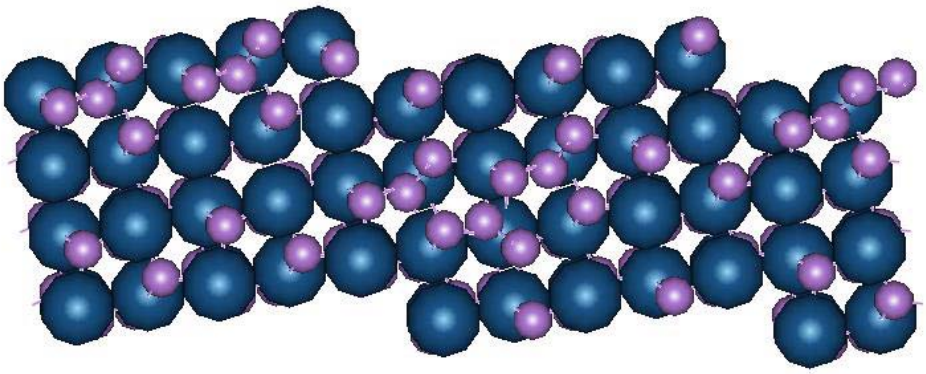

Figure 6.8: Sideview of the geometry optimised {610} most dry stable surface ( As = Purple, Pt = blue ).

among the high index surfaces with a relatively small surface energy (1.22 $Jm^{-2}$). It has twelve platinum atoms (fig. 6.8) available to adsorbing species, and is a type II surface.

**Stepped Surface** The experimental data suggests that the peculiar geometric and electronic structure of the stepped surface give rise to reaction channels that are much more effective than those on ideal surfaces.

**Dissolution and growth** The aim is to investigate the energies of surface growth via a new modelling technique which uses a high index surface as an approximation for a stepped version of a low index surface. Properties of solid materials, in particular their reactivity, depend heavily on the nature of the crystal surfaces. Crystal growth is known to occur at stepped sites on the crystal surface, and it has been shown that nucleation occurs preferentially at these sites. This has led to an idea that higher index surfaces could be used to model stepped low index surfaces. By modelling a selection of high index surfaces, we can identify suitable high index surfaces which can be used as models for stepped surfaces. Consider a crystal face of a crystal containing one monatomic step. The main aim is to incorporate $Pt^{2+}$ in a growing $PtAs_2$ crystal and this process occurs in a form of steps. Each step in the growth process, namely the incorporation of a new $PtAs_2$ unit at the growing steps, was modeled by a full energy minimisation technique (METADISE). Figs. 6.9 and 6.10 show a schematic representation of modeled dissolution and growth process, where the green shaded box is a removed or newly incorporated $PtAs_2$ unit. We will study two types of steps, which are obtuse and acute, as these are seen experimentally to form the dissolving edges of etch pits, especially with mineral oxides [102]. Although the crystal size decreases during dissolution, when the reaction is controlled by polypitting (formation and growth of pits), the edge free energy increases at the very first stage of reaction owing to the creation of pits and dissolution steps. The constant composition experimental results demonstrate the development of surface roughness as the dissolution steps are formed, implying an increase of the total edge length during the reaction. This is an exactly analogous mechanism to that of crystal growth, in which the formation of embryos of critical size plays a key role in the overall mechanism. In contrast to crystal growth, dissolution is a processs of size reduction, and when the particle size

is sufficiently reduced, critical phenomena become important hence the influence of size must be taken into consideration. It is interesting to note that these critical phenomena are readily apparent for sparingly soluble minerals for which the critical conditions are attained much more readily.

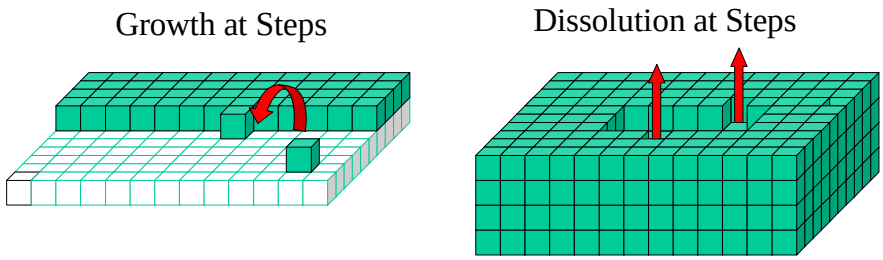


Figure 6.9: Schematic representation of both crystal growth and dissolutions

The results point to the importane of understanding the detailed mechanism of dissolution when attempts are made to measure, experimentally, the solubilities of sparingly soluble minerals. Fig. 6.12 shows graphs of the energetics of these steps for the addition of $PtAs_2$. It is observed from these graphs that addition of an $PtAs_2$ unit is thermodynamical favourable for both acute and obtuse steps and the acute steps are found to be the most stable of the two. It is only when two steps for both the acute and obtuse for {510} neighbouring Pt units are already present and that the addition of a further Pt unit is an exothermic process.

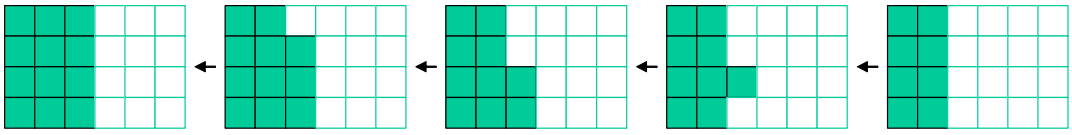

Figure 6.10: Schematic representation of the modeled growth process at the step edges, where green shaded box is the removed $PtAs_2$ cation units.

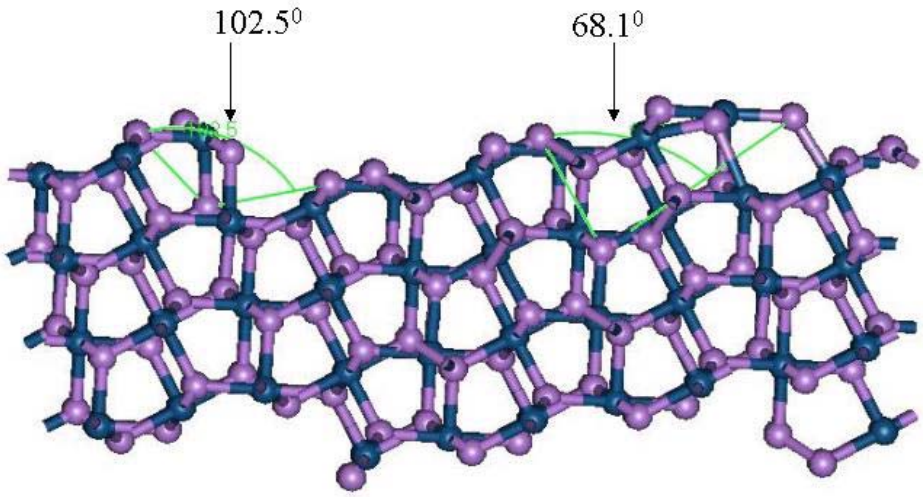


Figure 6.11: Schematic representation of stepped {510} and {610} surfaces for $PtAs_2$.

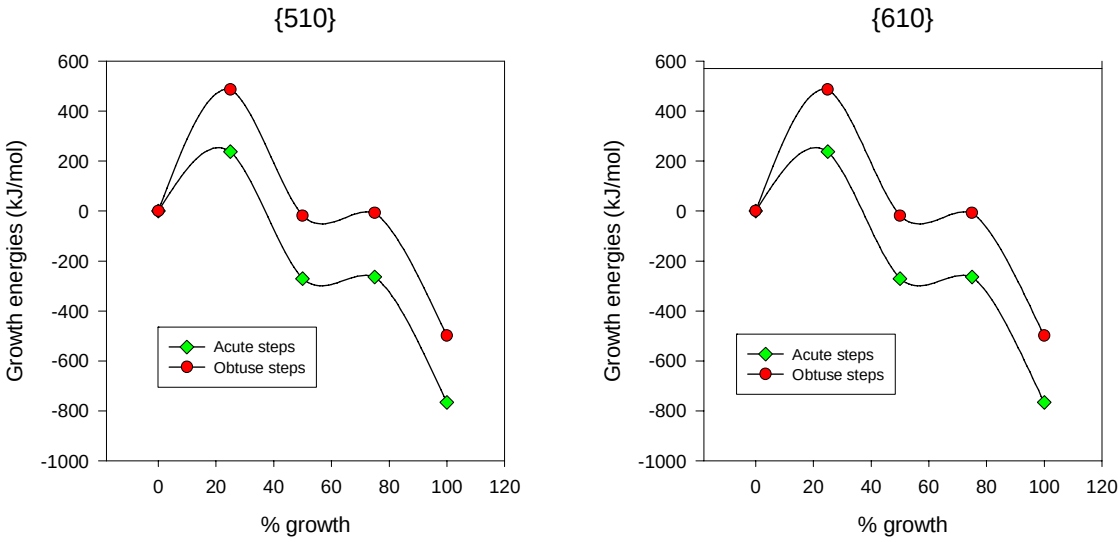


Figure 6.12: Energies of sequential growth of $PtAs_2$ units at acute and obtuse steps on both {510} and {610} surfaces.

### $Pt_4As_4S_4$

We created a range of surfaces with low Miller indices as these surfaces have the largest inter-planar spacing and consequently generally the most stable. The surfaces studied were the low index surfaces {110}, {110},{111}, including {210}, {310}, {410}, {510} and {610} planes and their symmetry-related surfaces. Most were non-dipolar type I and II surfaces, which tend to give multiple terminations, possibly by either platinum ions or arsenic-sulphur ions. The calculated surface energies of all planes are shown in table 6.2.

**{100} surface**

The {100} surface has the smallest unit cell area of all the surfaces considered, and is the most stable of all the dry surfaces with surface energy of 1.08 $Jm^{-2}$. The {100} surface is a type II surface and is terminated by AsS( arsenic-slphurs) ions, with two platinums, one located at the center and the other on the edge unit cell. Both platinums are accessible to the adsorbing molecules and are also coordinated to two arsenic and three sulphur ions. Fig. 6.13, shows the most stable surface termination where upon geometry optimisation, the surface energy of 1.08 $Jm^{-2}$ is obtained.

**{110} surface**

Table 6.2: Unrelax and relax surfaces energies of unhydrated $Pt_4As_4S_4$

| Surface (hkl) | Unrelax Surface ($Jm^{-2}$) | Relax surface ($Jm^{-2}$) | Termination |
|---|---|---|---|
| {100} | 1.10 | 1.08 | SAs |
| {110} | 2.87 | 1.82 | SAs |
| {111} | 2.931 | 1.96 | SAs |
| {210} | 1.83 | 1.42 | Pt |
| {310} | 1.64 | 1.32 | SAs |
| {410} | 1.52 | 1.28 | SAs |
| {510} | 1.44 | 1.24 | SAs |
| {610} | 1.39 | 1.21 | SAs |

Cutting the {110} planes gives two possible surface terminations, which are; the platinum-terminated planes and AsS(Arsenic-sulphur) terminated planes. The AsS terminated surfaces are the most stable with the surfaces energy of 1.82 $Jm^{-2}$ and there are three platinum atoms accessible to adsorbing species. The {110} surface (fig. 6.14 ) is a type II surface and the second most stable surface of the $Pt_4As_4S_4$ low indices.

**{111} surface**

Cutting the {111} plane also gives two possible surface terminations, which can be labelled according to the terminating species, {111} Pt for platinum terminated plane, and {111} AsS for the arsenic-sulphur terminated plane. The {111} AsS terminated surface (fig. 6.15) is the third most stable dry surface of the low indices. It also has the larger unit surface area as compared to {100} surface and has three platinum ions on the surface, of the three only two platinum ions are fully accessible to the adsorbing species.

**{210} surface**

The {210} surface has one of the smallest unit cell areas and it has a relatively large surface energy of all high index surfaces considered. The most stable surface is terminated by platinum atoms with the dry surface energy of 1.42 $Jm^{-2}$ and is of type II. In view of the small surface area there are only two platinum atoms per unit cell accessible to adsorbing species. Fig. 6.16 shows that this surface microfacets into steps of the {100} plane.

**{310} surface**

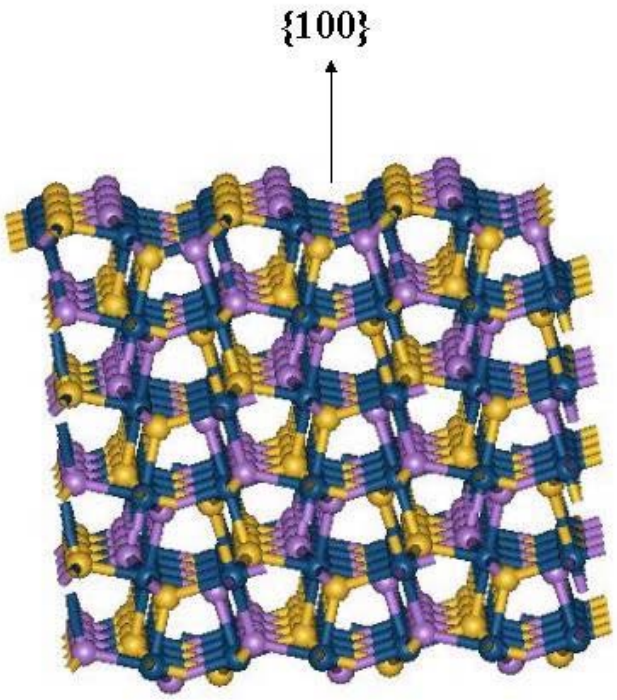


Figure 6.13: Sideview of the geometry optimised {110} most dry stable surface of Pt4As4S4 ( As = Purple, Pt = Blue, S= Orange ).

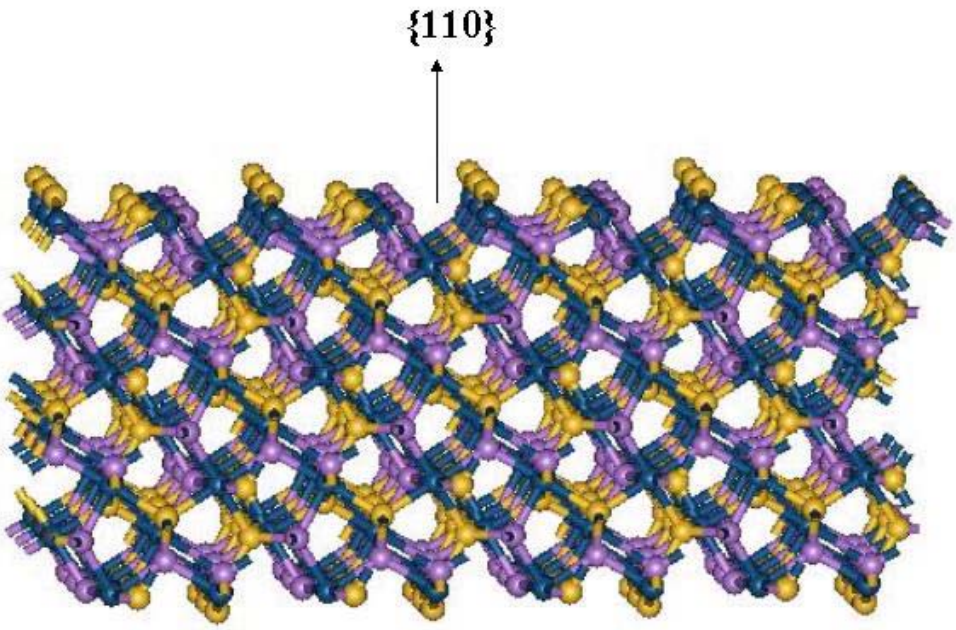


Figure 6.14: Sideview of the geometry optimised {110} most dry stable surface of $Pt_4As_4S_4$ ( As = Purple, Pt = Blue, S= Orange ).

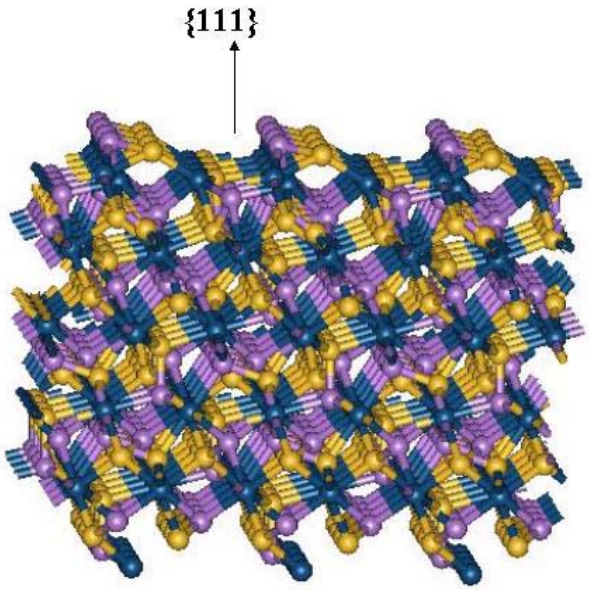


Figure 6.15: Sideview of the geometry optimised {111} most dry stable surface of $Pt_4As_4S_4$ ( As = Purple, Pt = Blue, S= Orange ).

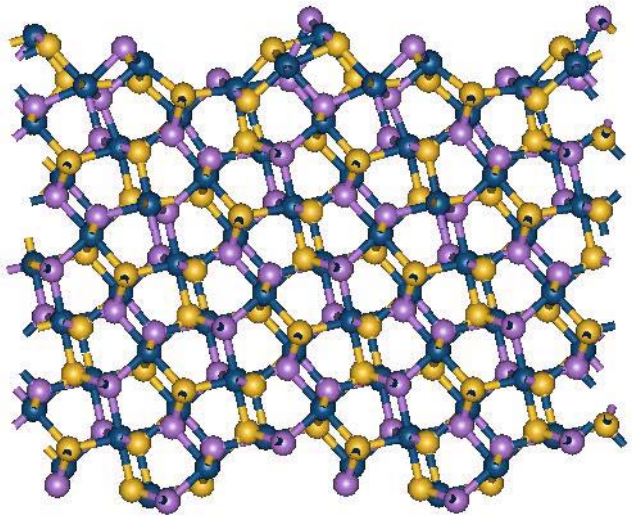

Figure 6.16: Sideview of the geometry optimised {210} most dry stable surface of $Pt_4As_4S_4$ ( As = Purple, Pt = Blue, S= Orange ).

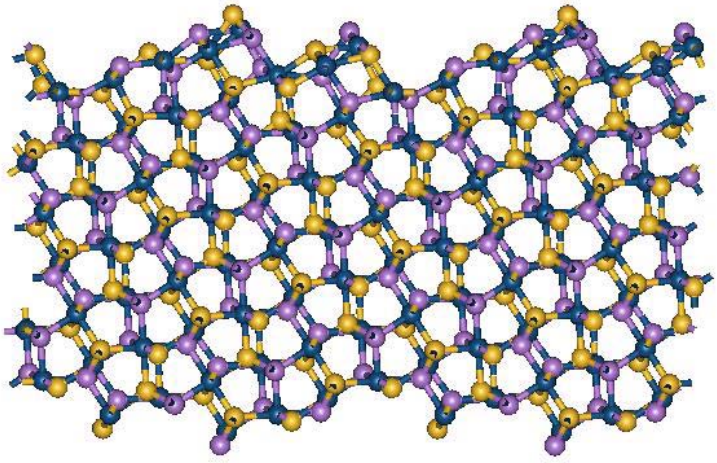

Figure 6.17: Sideview of the geometry optimised {310} most dry stable surface of $Pt_4As_4S_4$ ( As = Purple, Pt = Blue, S= Orange ).

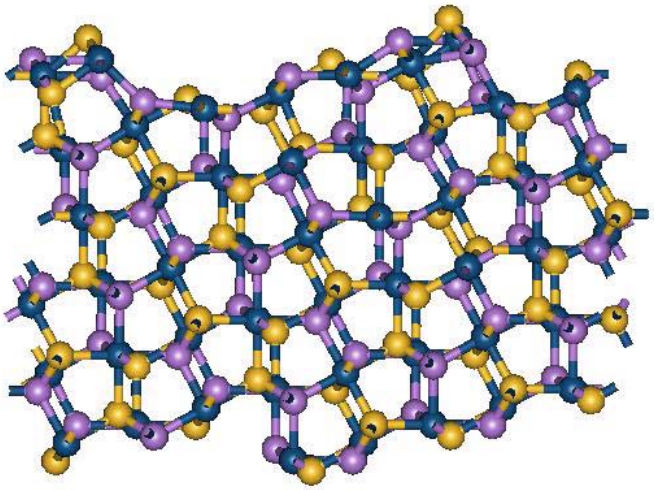

Figure 6.18: Sideview of the geometry optimised {410} most dry stable surface of $Pt_4As_4S_4$ ( As = Purple, Pt = Blue, S= Orange ).

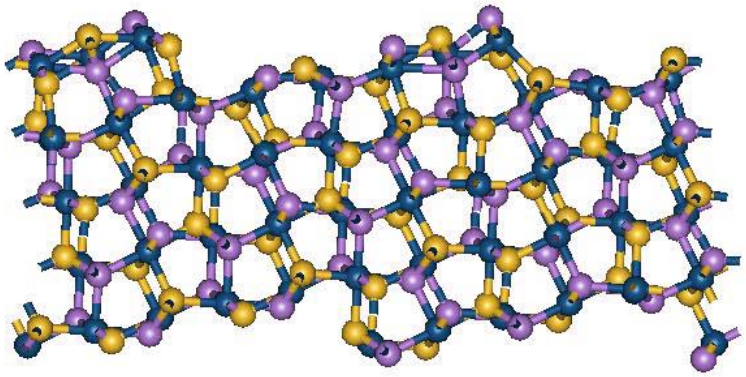

Figure 6.19: Sideview of the geometry optimised {510} most dry stable surface of $Pt_4As_4S_4$ ( As = Purple, Pt = Blue, S= Orange ).

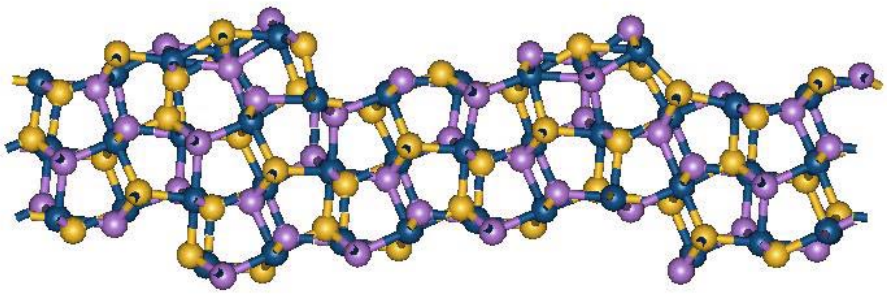

Figure 6.20: Sideview of the geometry optimised {610} most dry stable surface of $Pt_4As_4S_4$ ( As = Purple, Pt = Blue, S= Orange ).

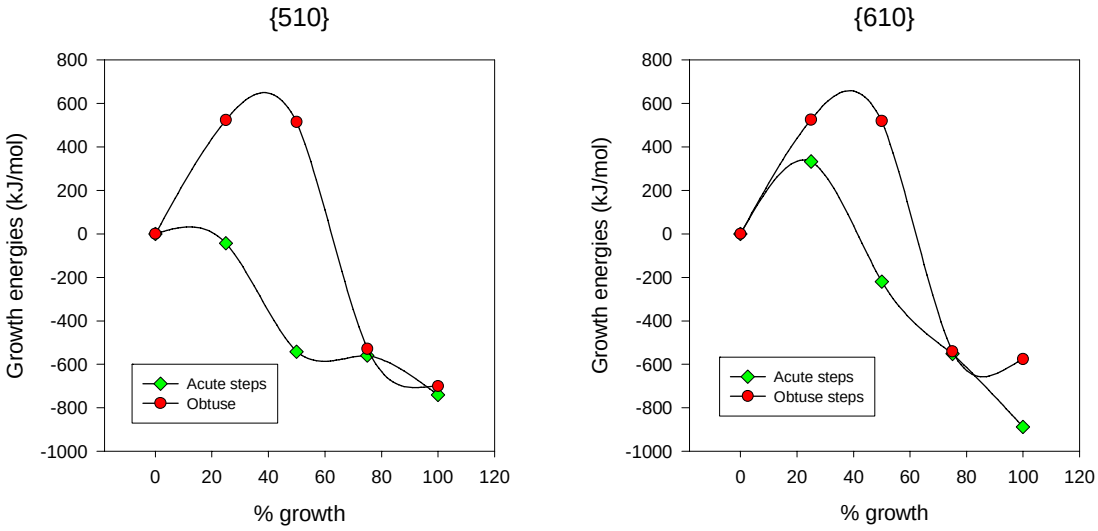


Figure 6.21: Energies of sequential growth of $Pt_4As_4S_4$ units at acute and obtuse steps on both {510} and {610} surfaces.

Cutting in the {310} direction gives two different terminated surfaces. The AsS (Arsenic-sulphur) terminated surface (fig. 6.17) of type II surface being the most stable one with surface energy of 1.32 $Jm^{-2}$. This surface also microfacets into steps of the {100} plane. There are only three platinum atoms accessible to the adsorbing species.

### {410} surface

The {410} surface is type II surface and terminated by AsS( arsenic-slphurs) atoms. It has all its five surface platinum atoms accessible to the adsorbing molecules. Fig. 6.18, shows the most stable surface termination where, after geometry optimisation of the surface, the surface energy is 1.28 $Jm^{-2}$.

### {510} surface

The {510} surface is type II surface, and its most stable surface (fig. 6.19) is terminated by platinum atoms, with the surface energy of 1.24 $Jm^{-2}$. There are three platinum atoms accessible to the adsorbing species.

**{610} surface**

The most stable surface of {610} cleavage plane, which is a type II surface, is terminated by arsenic-sulphur ions. The surface (fig. 6.20) has six platinum atoms accessible to the adsorbing species and it has dry surface energy of 1.21 $Jm^{-2}$. Furthermore, the surface is relatively stable as compared to other high index ones.

**Stepped surface**

We will consider steps obtained by cutting the {510} and {610} surfaces. Fig. 6.21 shows graphs of the energetics of these steps for the addition of $Pt_4As_4S_4$. It is observed from these graphs that addition of an PtAsS unit is thermodynamical favourable for both acute and obtuse steps and the acute steps are found to be the most stable.

### 6.3.2 Hydrated Surfaces

We next investigated the adsorption of water on the most stable dry surfaces studied in the previous section to evaluate the energies of adsorption and the relaxed hydrated surface structure. We will concentrate on those surface terminations that are the most stable under aqueous conditions. These planes will therefore be expressed in the crystal morphology, in a growth/dissolution environment and will have terminations most commonly observed under conditions of mineral separation processes. We will adsorb water-molecules one after the other onto the surface, especially on the metal platinum ion. Subsequently both the surface and the adsorbing water molecules were allowed to fully relax using a Newton Raphson energy minimisation technique [65]. The most stable configuration is then used as an input for the adsorption of the next water molecules. This process is continued until full monolayer coverage is achieved, which is defined as the maximum number of water molecules which can be adsorbed at the surface in a single layer, before formation of a second layer, or when the adsorption becomes endothermic. The water molecule itself can be adsorbed onto the surface in several ways e.g., it can be coordinated by one hydrogen to a surface platinum, or bonded by its oxygen to a surface platinum. The calculated surface energies before and after adsorption together with hydration energies for the various surfaces are given

in Table 6.3. It is observed that hydration has a stabilising effect on all the surfaces under consideration.

Table 6.3: Surface and hydration energies for $PtAs_2$ surfaces. Hydration energies are the energies for the full monolayer of adsorbed water.

| Surface (hkl) | $\gamma_{rel}(\mathrm{Jm}^{-2})$ | $\gamma_W(\mathrm{Jm}^{-2})$ | Hydration Energy(kJ/mol) |
|---|---|---|---|
| {100} | 1.01 | 0.26 | -27.10 |
| {110} | 1.89 | 0.90 | -132.10 |
| {111} | 2.50 | 0.79 | -144.70 |
| {210} | 1.60 | 0.55 | -128.45 |
| {310} | 1.44 | 0.57 | -63.00 |
| {410} | 1.35 | 0.46 | -78.95 |
| {510} | 1.94 | 0.42 | -64.32 |
| {610} | 1.24 | 0.36 | -38.15 |

**$PtAs_2$**

**{100} surface**

Amongst all $PtAs_2$ surfaces the As-terminated {100} surface is stabilised the most by the adsorption of water, from a relatively stable dry surface with energy of 1.01 $\mathrm{Jm}^{-2}$ to a very stable hydrated surface with energy of 0.26 $\mathrm{Jm}^{-2}$. There are two platinum atoms per unit cell accessible to adsorbing water molecules and the surface accommodates exactly two water molecules. Fig. 6.22 shows {100} surface covered with a monolayer of water. Each of these platinum atoms strongly coordinates one water molecule, with Pt-O distance of 2.3 Å. Table 6.3 shows the average adsorption energies per water molecule for a full monolayer of water on each surface. We note that hydration of the {100} surface releases the least energy, only 27.1 $\mathrm{kJmol}^{-1}$, which emanates from the dry {100} surface being already a stable plane with a low surface energy. When creating the {100} surface, the platinum ions, which had six-fold coordination in the bulk material, are lowered to five-fold coordination when the material is cut to expose the {100} surface. Consequently, the loss of this one bond by platinum does not seem to enhance reactivity of the surface platinum ions. The increase from five-fold coordination of platinum at the dry surface to six-fold coordination by the adsorption of two water molecules at the hydrated surface does not, therefore, release a large amount of energy.

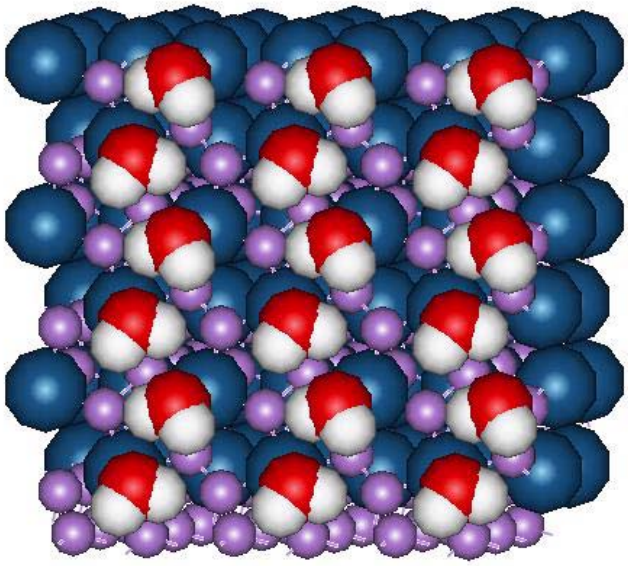

Figure 6.22: Plane view of the {100} $PtAs_2$ hydrated surface, with the water molecules coordinated to surface platinum atoms. Pt = dark blue, As = purple, O(oxygen) = red, H = white

**{110} surface**

The $PtAs_2$ {110} surface is a type II surface and fig. 6.23 gives its hydrated plane view. It is terminated by arsenic atoms, with two platinum atoms, each on the opposite edge of the cell accessible to the adsorbing species, with each of these surface platinum atoms able to accommodate one water molecules at Pt-O distance of 2.3 Å. Two molecules of water were placed on top of the surface to form a monolayer of water, and the surface was stabilised from 1.9 $Jm^{-2}$ to 0.9 $Jm^{-2}$. The {110} surface is one of the

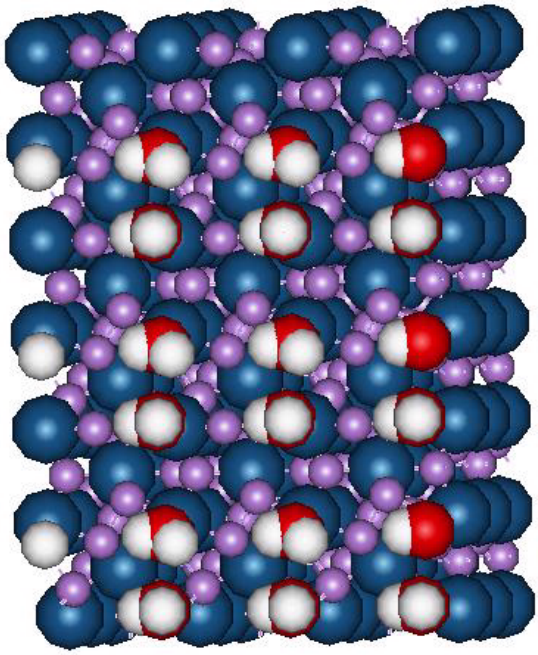

Figure 6.23: Plane view of the {110} $PtAs_2$ hydrated surface, with the water molecules coordinated to surface platinum atoms. Pt = dark blue, As = purple, O(oxygen) = red, H = white

surfaces stabilised least by the adsorption of water. Even though it is able to adsorb two water molecules per unit cell as in both {100} and {111} , it is still only marginally less stable than the {111} which has a larger surface area, and was the least stable of all the dry surfaces considered. This surface has released 132.1 $kJmol^{-1}$ which is a considerable amount of energy. When

creating the {110} surface, the platinum ions, are lowered to four-fold coordination. This surface is highly reactive and upon hydration each platinum ion coordinates to one water molecules, hence increasing their coordination number to six.

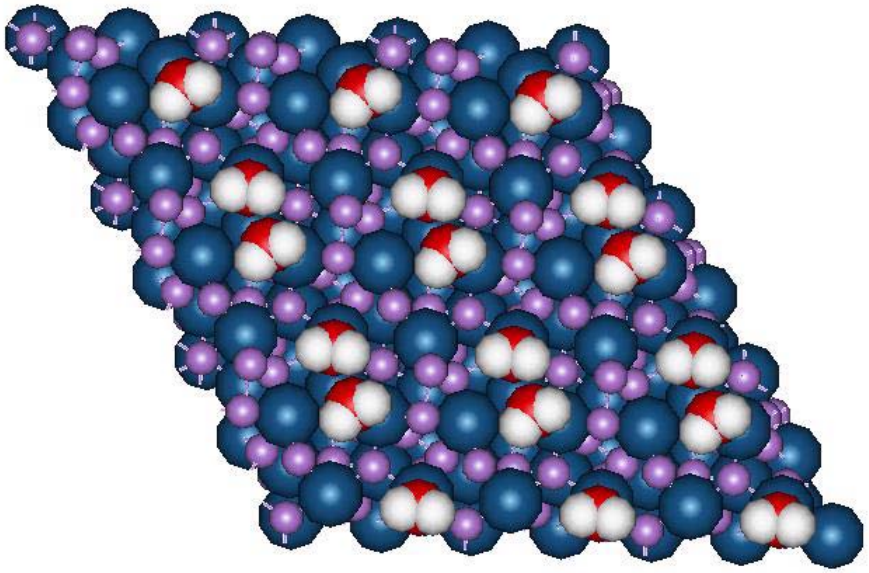

Figure 6.24: Plane view of the {111} $PtAs_2$ hydrated surface, with the water molecules coordinated to surface platinum atoms. Pt = dark blue, As = purple, O(oxygen) = red, H = white

**{111} surface**

It has one of the largest unit surface area amongst the $PtAs_2$ low index surfaces considered thus far. In addition it has four platinum atoms at the surface but only two are accessible to adsorbing species. Fig. 6.23 gives the plane view of the {111} $PtAs_2$ hydrated surface. The {111} surface is also stabilised considerably by the adsorption of water, from 2.5 $Jm^{-2}$ for the dry surface to 0.8 $Jm^{-2}$ for the hydrated surface, and is now the second most stable hydrated surface. Each of these platinum atoms strongly coordinates one water molecule, with Pt-O distance of 2.3 Å. The {111} surface, releases the largest amount of energy upon hydration, an average of 144.7 $kJmol^{-1}$.

The platinum ions lose two bonds when this surface is created, leaving four-fold coordinated platinum ions in the plane. This surface is consequently highly reactive and upon hydration each platinum ion coordinates to one water molecules, hence increasing their coordination number to six.

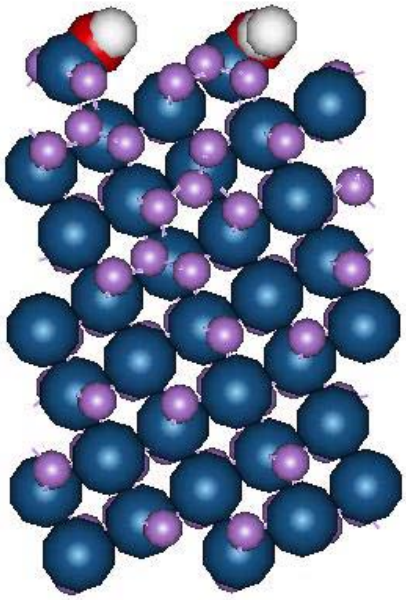

Figure 6.25: Plane view of the {210} $PtAs_2$ hydrated surface, with the water molecules coordinated to surface platinum atoms. Pt = dark blue, As = purple, O(oxygen) = red, H = white

**{210} surface**

The {210} surface is less stable than the dominant {100} surface, and it can be described as steps of {100} planes, in effect resembling edges consisting of low-coordinated atoms in a {100} surface. The surface shown in fig. 6.25 is stabilised considerably by the adsorption of a monolayer of water. Its surface energy is reduced from 1.6 $Jm^{-2}$ for the dry surface to 0.55 $Jm^{-2}$ by the adsorption of a complete monolayer of water. Its unit cell has the smallest surface area of all the high index surfaces considered, with only five surface

platinum atoms per unit cell. These platinum atoms are able to coordinate only two water molecules, with Pt-O distances of 2.3 Å for both, on the edges of a steps defect of the unit cell.

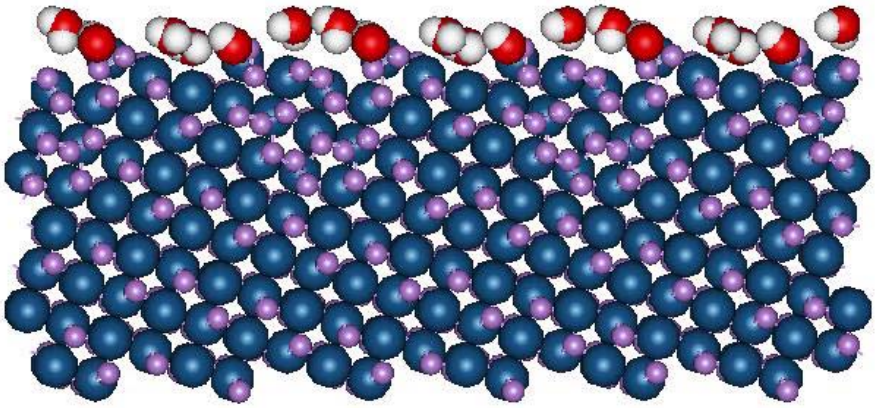

Figure 6.26: Plane view of the {310} $PtAs_2$ hydrated surface, with the water molecules coordinated to surface platinum atoms. Pt = dark blue, As = purple, O(oxygen) = red, H = white

**{310} surface**

The adsorption of water to the {310} surface also has a considerable stabilising effect from 1.44 $Jm^{-2}$ for the dry surface to 0.57 $Jm^{-2}$ for a full monolayer of water, and the process releases 63 $kJmol^{-1}$. Fig. 6.26 shows the hydrated surface, where some of the water molecules adsorb in the gaps on the surface, hence rendering it smooth.

**{410} surface**

On the hydrated {410} surface, the water molecules tend to cluster around the top of the edge (fig. 6.27), and they are coordinated to the same platinum

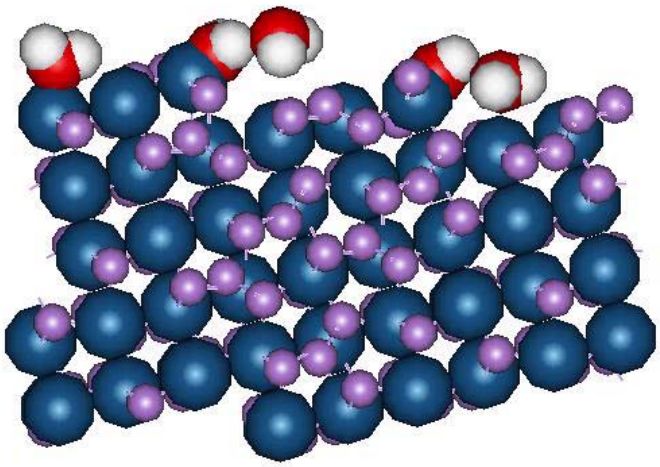

Figure 6.27: Plane view of the {410} $PtAs_2$ hydrated surface, with the water molecules coordinated to surface platinum atoms. Pt = dark blue, As = purple, O(oxygen) = red, H = white

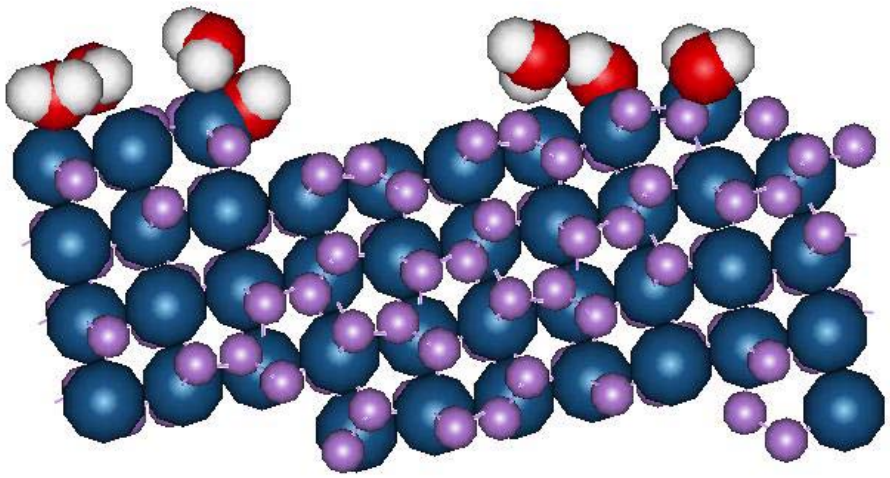

Figure 6.28: Plane view of the {510} $PtAs_2$ hydrated surface, with the water molecules coordinated to surface platinum atoms. Pt = dark blue, As = purple, O(oxygen) = red, H = white

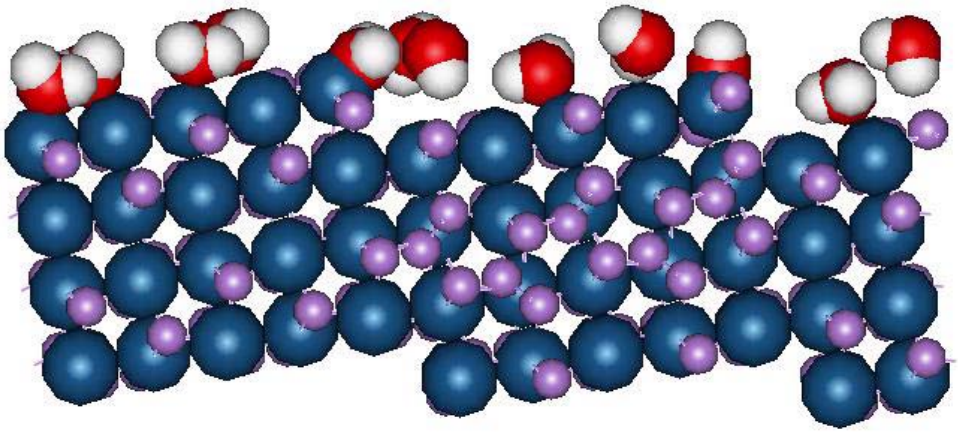

Figure 6.29: Plane view of the {610} $PtAs_2$ hydrated surface, with the water molecules coordinated to surface platinum atoms. Pt = dark blue, As = purple, O(oxygen) = red, H = white

atom. There are either two or three water molecules clustering around the top edges and are hydrogen bonded to oxygen atoms of the neighbouring water molecules and others are attached to surface of the platinum atom on the terrace. These water molecules release an average energy of 78.95 $kJmol^{-1}$ when they adsorb on the surface.

**{510} surface**

Water adsorbs to the platinum terminated surface in a very regular pattern (fig. 6.28 ), with the surface stabilised considerably by hydration, from 1.94 $Jm^{-2}$ for the dry surface to 0.42 $Jm^{-2}$ for the hydrated surface. The structure of the {510} surface allows for two water molecules to be adsorbed per surface on some selected platinum atoms, with the hydration energy of –64.32 $kJmol^{-1}$. The water molecules coordinate to surface platinum atoms via their oxygen atoms at a distance of 2.39 Å, and are hydrogen bonded via both their hydrogen atoms to oxygen atoms of different water molecules.

**{610} surface**

The adsorption of water molecules stabilises the {610} surface (fig. 6.29) from 1.24 to 0.36 $Jm^{-2}$ and the surface has adsorbed ten water molecules per unit cell, which results in the surface having the largest coverage of the $PtAs_2$ surfaces. One water molecule is adsorbed on each of the platinum atoms on the terrace, with the step terminating platinum atom coordinating either one or two water molecules. The adsoprtion around the step is slightly more disordered, although there is little interaction between water molecules themselves, with virtually all the stability arising from interaction between the water molecules and the surface atoms. Adsorption of water has very little effect on the surface energy and the hydration energy 38.15 $kJmol^{-1}$ is the second lowest energy of the surfaces studied.

**$Pt_4As_4S_4$**

**{100} surface**

The {100} surface is still the most stable surface upon hydration, with the surface energy lowered considerably from 1.08 $Jm^{-2}$ to 0.30 $Jm^{-2}$, as shown in table 6.4. The {100} surface, contains surface platinum atoms which are five -fold coordinated. We note that upon hydration the {100} surface releases the least energy, which is only 31.2 $kJmol^{-1}$, showing that, the loss of this one bond by platinum does not seem to have lead to enhance reactivity of the surface platinum ions significantly. The water molecules are adsorbed

Table 6.4: Surface and hydration energy for $Pt_4As_4S_4$ surfaces. The hydration energies are the energies for the full monolayer of adsorbed water.

| Surface (hkl) | $\gamma_{rel}(\mathrm{Jm}^{-2})$ | $\gamma_W(\mathrm{Jm}^{-2})$ | Hydration Energy(kJ/mol) |
|---|---|---|---|
| {100} | 1.08 | 0.30 | -31.16 |
| {110} | 1.82 | 1.56 | -226.74 |
| {111} | 1.96 | 0.55 | -195.40 |
| {210} | 1.43 | 0.81 | -184.94 |
| {310} | 1.32 | 0.66 | -141.95 |
| {410} | 1.28 | 0.55 | -93.03 |
| {510} | 1.24 | 0.30 | -106.02 |
| {610} | 1.22 | 0.28 | -59.05 |

flat onto the surface, bounded by their oxygen atoms to a five coordinated surface platinum atom with a bond length 2.6 Å, one at the center and another at the corner of the unit cell, and the two hydrogens of the same water molecules bridging the neighbouring sulphurs. Water adsorbs to the platinum surface in a very regular zig-zag pattern. Fig. 6.30 , shows the most stable surface termination upon geometry optimisation. The stabilisation of the surface is thus due to two factors; firstly the presence of the water layer increases the coordination of the surface platinum and oxygen atoms, which in the dry surface are lower coordinated than in the bulk material. Secondly, the energetical advantage of close interaction of the water molecules with the surface together with the intermolecular interactions within the water layer outweighs the loss of hydrogen-bonded interactions the water molecules would otherwise experience in the liquid, which lowers the energy of the surface compared to the bulk material and liquid water.

**{110} surface**

The surface and hydration energies of the hydrated surfaces are presented in table 6.4, and it is noted that hydration has slightly enhanced stability of {110} surface, however, it is the least stable surface of the three low index surfaces. Fig. 6.22 shows {110} surface covered with a monolayer of water. We observe that hydration of the {110} surface releases the highest energy of 226.7 $\mathrm{kJmol}^{-1}$. When {110} surface was created, the platinum ions, which had six-fold coordination in the bulk material, were lowered to

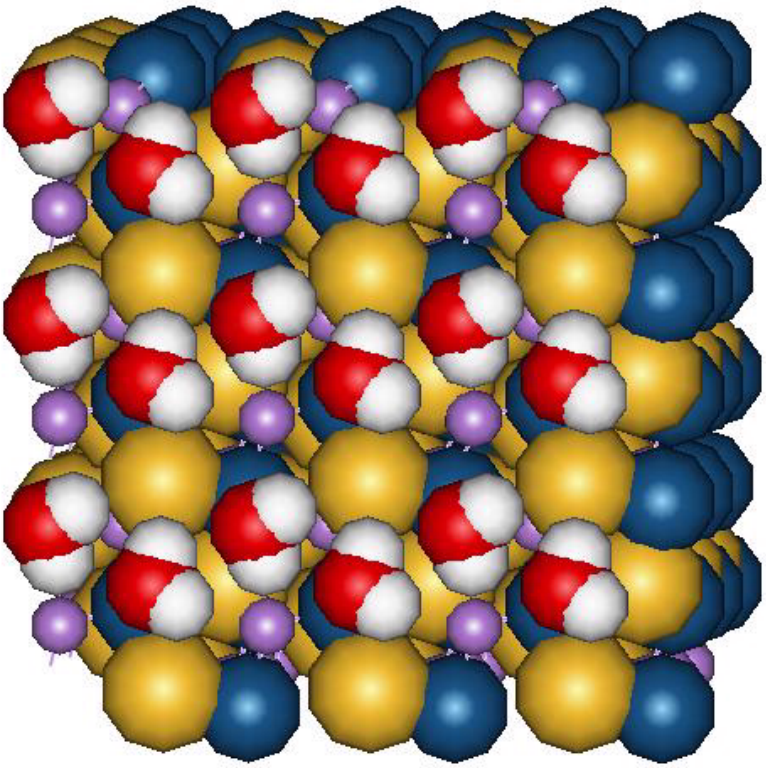

Figure 6.30: Plane view of the {100} $Pt_4As_4S_4$ hydrated surface, with the water molecules coordinated to surface platinum atoms. Pt = dark blue, O(oxygen) = red, As = purple, S = yellow, H = white.

five-fold coordination. The loss of one bond by platinum appears to have enhanced reactivity of the surface platinum ions. The increase from five-fold coordination of platinum on the dry surface to six-fold coordination by the adsorption of two water molecule at the hydrated surface therefore enhanced the release of such energy.

**{111} surface**

As in the case of the {100} surface, the {111} surface is stabilised considerably by the adsorption of a monolayer of water. Its surface energy is reduced from 1.96 $Jm^{-2}$ of the dry surface to 0.6 $Jm^{-2}$ after hydration. Amongst the three surface platinum atoms only one is, accessible to adsorbing water molecules, and the surface manages to adsorb only one water molecules per unit cell. This adsorbed water molecule coordinates strongly to the most accessible platinum atom and weakly to the two inaccessible platinum atoms. The water molecule is situated between two surface sulphur atoms, hence there is little bonding between the water molecules on the surface. In this, case the adsorption of the one water molecule to the five-fold coordinated platinum atom releases substantial energy amounting to 195.4 $kJmol^{-1}$.

**{210} surface**

The adsorption of water onto the platinum-terminated {210} surface is different from observations on the $PtAs_2$ high index surfaces which depicts some stepped surfaces, but with water adsorbing in a very regular pattern on the flat (planar) surface. Adsorption of a full monolayer of water has stabilising effect on the surface from 1.43 $Jm^{-2}$ to 0.81 $Jm^{-2}$. Each surface platinum atom coordinates one water molecule and all the water molecules coordinate via their oxygen atoms to the surface platinum atoms at Pt-O distances of 2.5 Å. These water molecules have adsorption energies of 184.94 $kJmol^{-1}$.

**{310} surface**

The {310} surface, is stabilised considerably by the adsorption of a monolayer of water and its surface energy is reduced from 1.32 $Jm^{-2}$ for the dry surface to 0.66 $Jm^{-2}$ by the adsorption of a complete monolayer of water. On this surface (fig. 6.34) there are three surface platinum atoms per unit cell

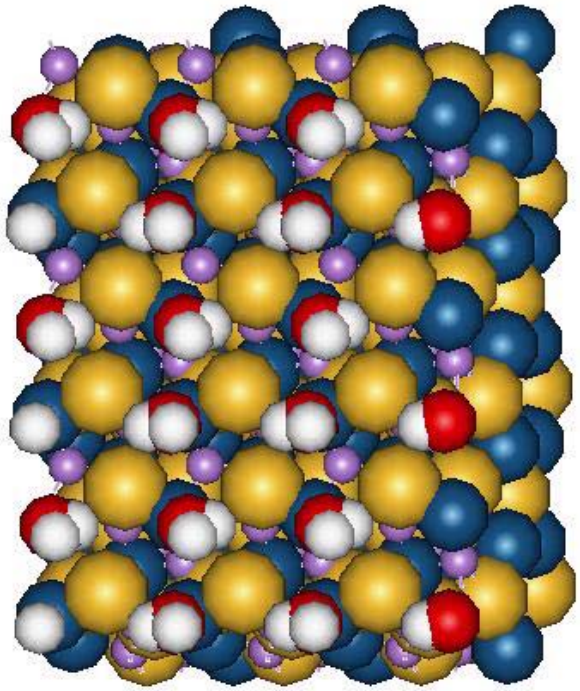

Figure 6.31: Plane view of the {110} $Pt_4As_4S_4$ hydrated surface, with the water molecules coordinated to surface platinum atoms. Pt = dark blue, O(oxygen) = red, As = purple, S = yellow, H = white.

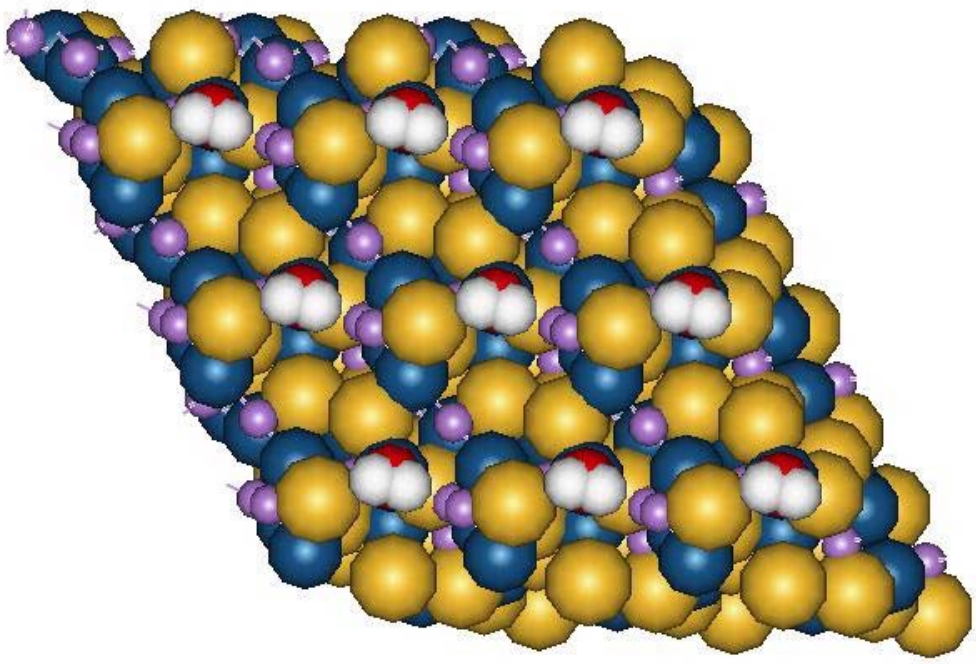

Figure 6.32: Plane view of the {111} $Pt_4As_4S_4$ hydrated surface, with the water molecules coordinated to surface platinum atoms. Pt = dark blue, O(oxygen) = red, As = purple, S = yellow, H = white.

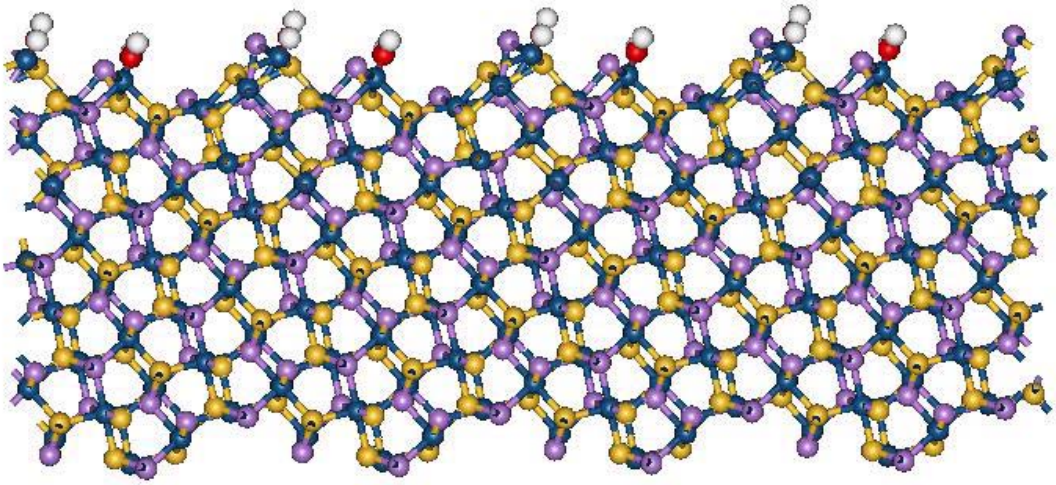

Figure 6.33: Side view of the {210} $Pt_4As_4S_4$ hydrated surface, with the water molecules coordinated to surface platinum atoms. Pt = dark blue, O(oxygen) = red, As = purple, S = yellow, H = white.

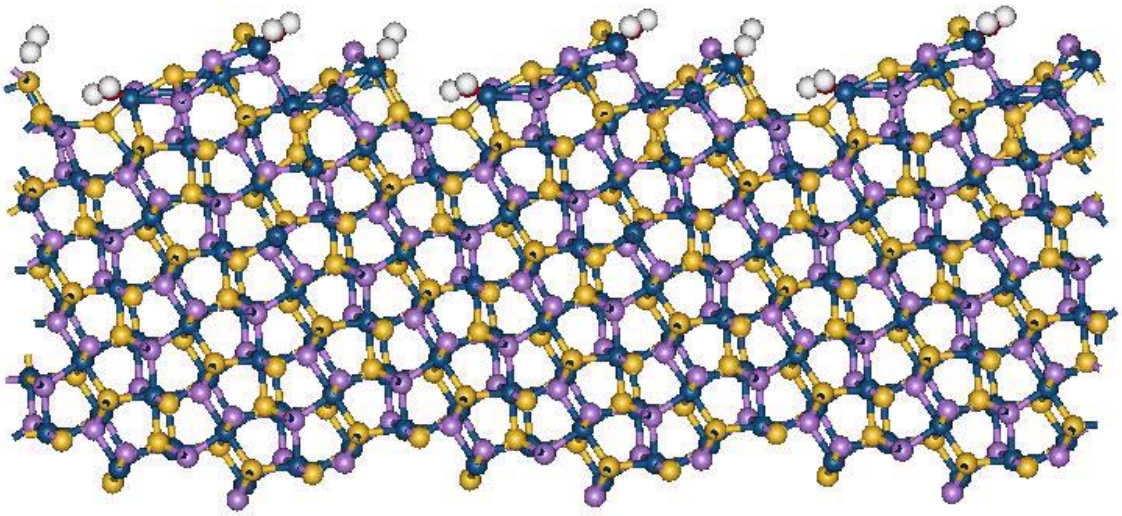

Figure 6.34: Side view of the {310} $Pt_4As_4S_4$ hydrated surface, with the water molecules coordinated to surface platinum atoms. Pt = dark blue, O(oxygen) = red, As = purple, S = yellow, H = white.

accessible to adsorbing species. Two of the adsorbed water molecules are situated at the top edges of the steps and the third water molecules is adsorbed to the platinum atoms situated along side of the step edge. The structure of the {310} surface allows for one water molecule to be adsorbed per surface platinum atom, giving an average hydration energy of 141.95 kJmol$^{-1}$. The water molecules coordinate to surface platinum atoms via their oxygen atoms at distances of 2.3, 2.5 and 3.8 Å.

**{410} surface**

There are four platinum atoms per unit cell accessible to adsorbing water molecules and the surface accommodates five water molecules (fig. 6.35). Some of the water molecules tend to cluster around one platinum atom, and are bond coordinated to the same platinum atom, with the distances of 3.2 and 3.3 Å. The very stable surface energy for the hydrated surface is mainly due to the formation of this stable hydrogen-bonded network of water molecules around the surface platinum atoms. Each of the other three platinum atoms strongly coordinate one water molecule, with Pt-O distances of 2.36, 2.37 and 2.44 Å. The stable hydrated surface is a result of the energetically very favourable adsorption energies of the five water molecules, with these water molecules releasing an average energy of 93.03 kJmol$^{-1}$ when they adsorb to the surface. Then the adsorption of water stabilises the surface to a much greater extent, giving a surface a energy of 0.55 Jm$^{-2}$.

**{510} surface**

The {510} surface (fig. 6.36 ) was among the most stable dry surfaces, with a surface energy of 1.24 Jm$^{-2}$, but it is still stabilised further by the adsorption of a monolayer of water to 0.30 Jm$^{-2}$. The surface has three surface platinum atoms per unit cell accessible to adsorbing species, and the surface is able to accommodate three water molecules at Pt-O distances of between 2.42 and 2.74 Å. The {510} surface, releases on average the adsorption energy upon hydration, of 106.02 kJmol$^{-1}$.

**{610} surface**

The {610} surface is stabilised the most of all the high index surfaces by the adsorption of water, from a relatively unstable dry surface with a surface energy of 1.22 Jm$^{-2}$ to a very stable hydrated surface with a surface energy of 0.22 Jm$^{-2}$. There are six platinum atoms per unit cell accessible to adsorbing water molecules and the surface accommodates exactly six water

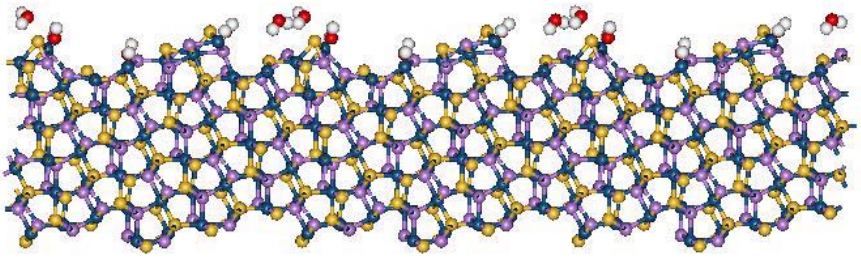

Figure 6.35: Side view of the {410} $Pt_4As_4S_4$ hydrated surface, with the water molecules coordinated to surface platinum atoms. Pt = dark blue, O(oxygen) = red, As = purple, S = yellow, H = white.

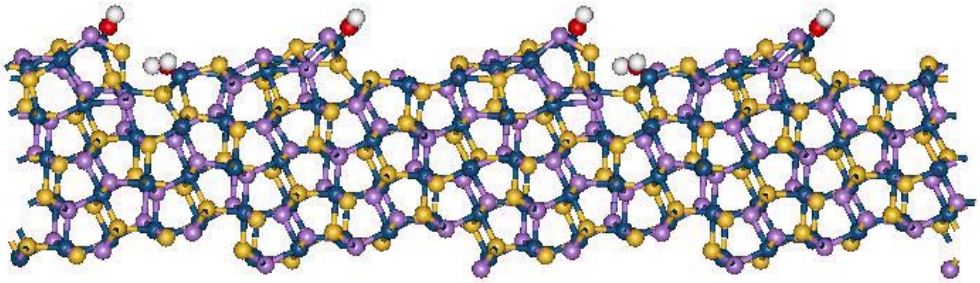

Figure 6.36: Side view of the {510} $Pt_4As_4S_4$ hydrated surface, with the water molecules coordinated to surface platinum atoms. Pt = dark blue, O(oxygen) = red, As = purple, S = yellow, H = white.

molecules (fig. 6.37). The average adsorption energy of water molecules onto the {610} surface is 59.05 kJmol$^{-1}$ and is relatively small among the high index surfaces.

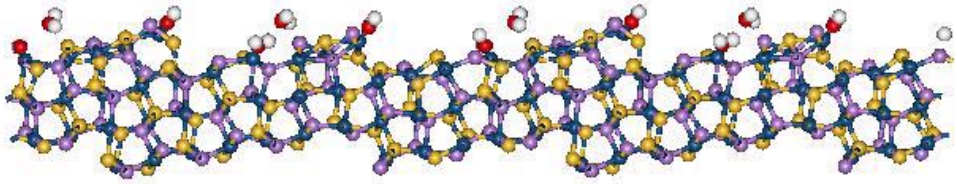

Figure 6.37: Side view of the {610} $Pt_4As_4S_4$ hydrated surface, with the water molecules coordinated to surface platinum atoms. Pt = dark blue, O(oxygen) = red, As = purple, S = yellow, H = white.

### 6.3.3 Morphology

The equilibrium morphology of a crystal is determined by the surface energy and related growth rate of the various surfaces and provides a measure of the relative stabilities of the surfaces. Wulff's Theorem [69] showed that a polar plot of surface energy versus orientation of normal vectors would give the crystal morphology based on the approach of Gibbs [104], who proposed

that under thermodynamic control the equilibrium form of a crystal should possess minimal total surface free energy for a given volume. Moreover, a surface with a high surface free energy is expected to have a large growth rate and this fast growing surface will not be expressed in the morphology of the resulting crystal. Only surface with low surface free energies, and hence slow growing, will be expressed. However, crystal growth is a complex kinetic process and will be affected by many factors and hence the equillibirum morphologies should be treated more as a repesentation of the effect of the addition of water to the different surfaces rather than the definitive growth morphology. The equilibrium morphology of a crystal in this case, is obtained from the surface energies, by assuming a crystal adopts a shape to lower its surface energy hence provides a measure of the relative stabilities of the surface.

Fig. 6.38 shows an experimental morphology of $PtAs_2$ expressing surfaces [webmineral.com/data/Sperrylite.shtml]. The {100} surface is too dominant. The equilibrium morphology from the value of the unhydrated $PtAs_2$ crystal are shown in fig. 6.39 and 6.40 for both the unrelaxed and relaxed morphology. The comparison of these morphologies with the experimental morphology clearly shows that the equilibrium morphology of the unrelaxed morphology closely resembles the experimental morphology, with the {100} surface dominating. The same surfaces are expressed in the calculated unrelaxed equilibrium morphology as are found in the experimental morphology excluding the {111} surface which is seen experimentally, and {100}surface is somewhat too stable with respect to both {111}, {102} and {201}. The calculated unrelaxed morphology expresses {100}and {102} surfaces, which agree with the fact that these are experimental cleavage planes and we should therefore expect these surfaces to be stable relative to the other dry surfaces. The relaxed equilibrium morphologies (fig. 6.40) show the {100} surface being the only represented surface, which is different from the experimental one in fig. 6.38.

The morphology of the hydrated surface (fig. 6.41) is similar to the relaxed unhydrated morphology showing only the {100} surface.

Fig. 6.42 and 6.43 show the morphologies of the dry $Pt_4As_4S_4$ calculated respectively from the unrelaxed and relaxed surface energies in table 6.2, where the dominant {100} surface is expressed in both cases. When the surface relaxation is taken into account, the main feature of the new crystal shape (fig. 6.43) is the appearance of the {310} and {610} surfaces, although the {100} surface is still too stable/dominant. When the surfaces

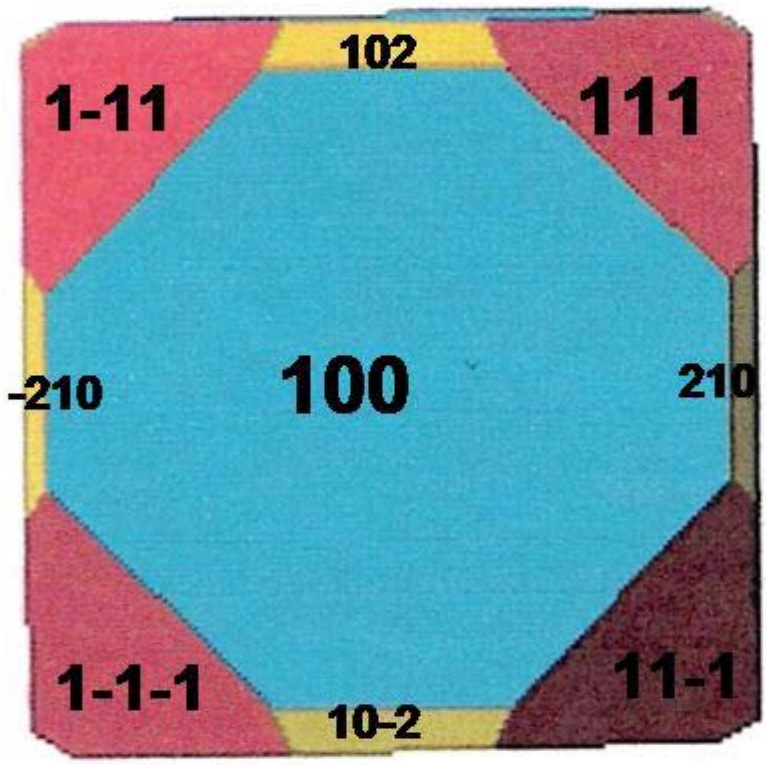


Figure 6.38: Experimental morpholgy of $PtAs_2$.

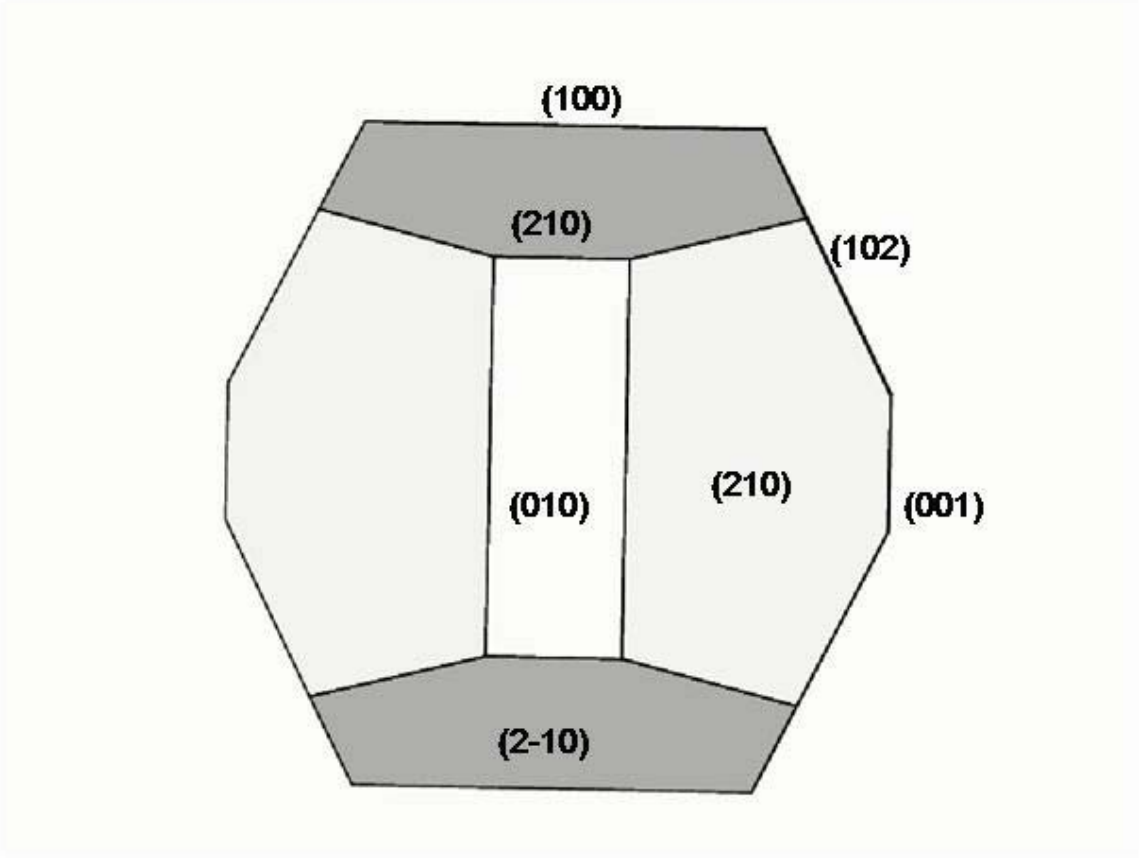


Figure 6.39: The calculated thermodynamical equilibrium morpholgy of the unrelax-dry $PtAs_2$ crystal.

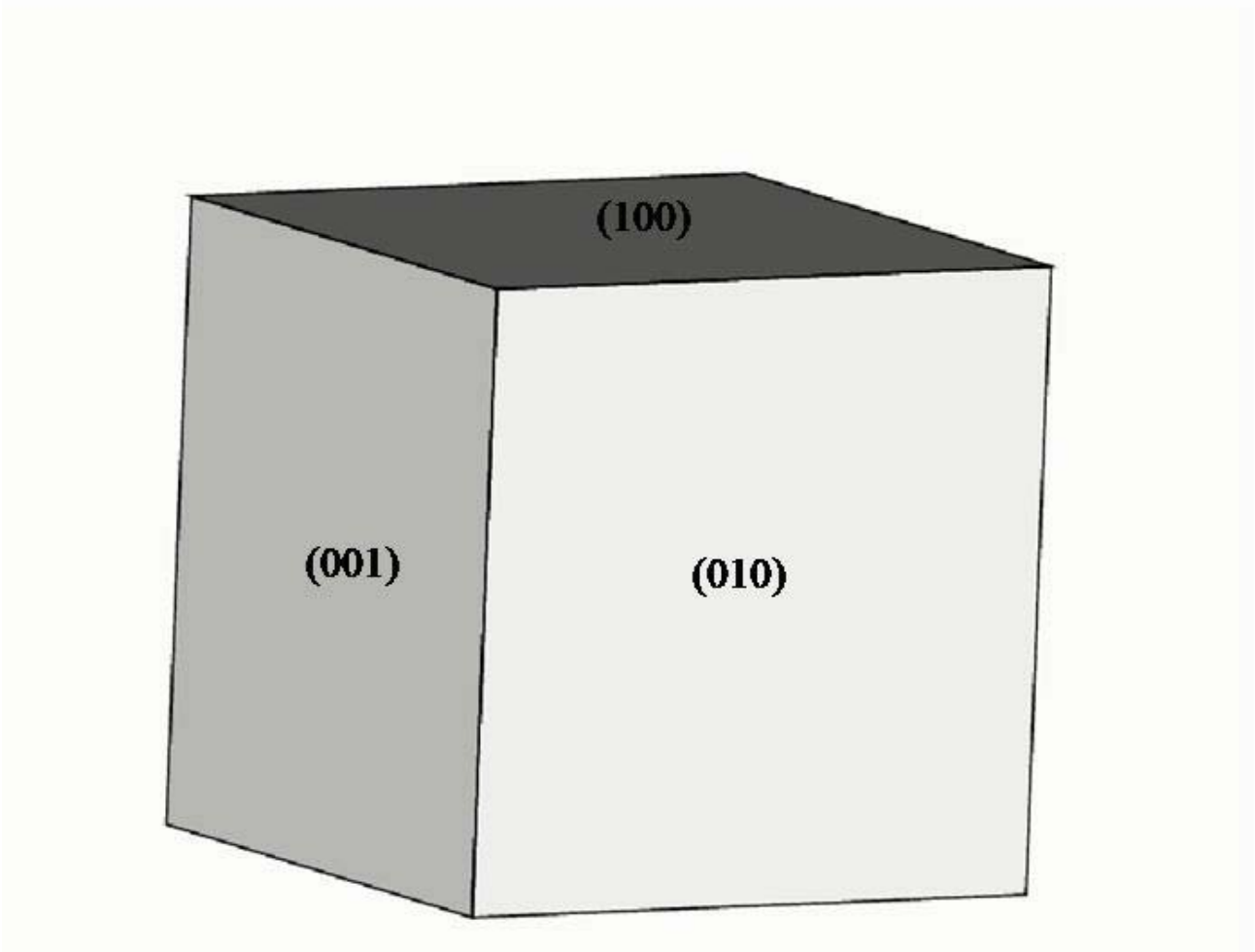


Figure 6.40: The calculated thermodynamical equilibrium morpholgy of the relax-dry $PtAs_2$ crystal.

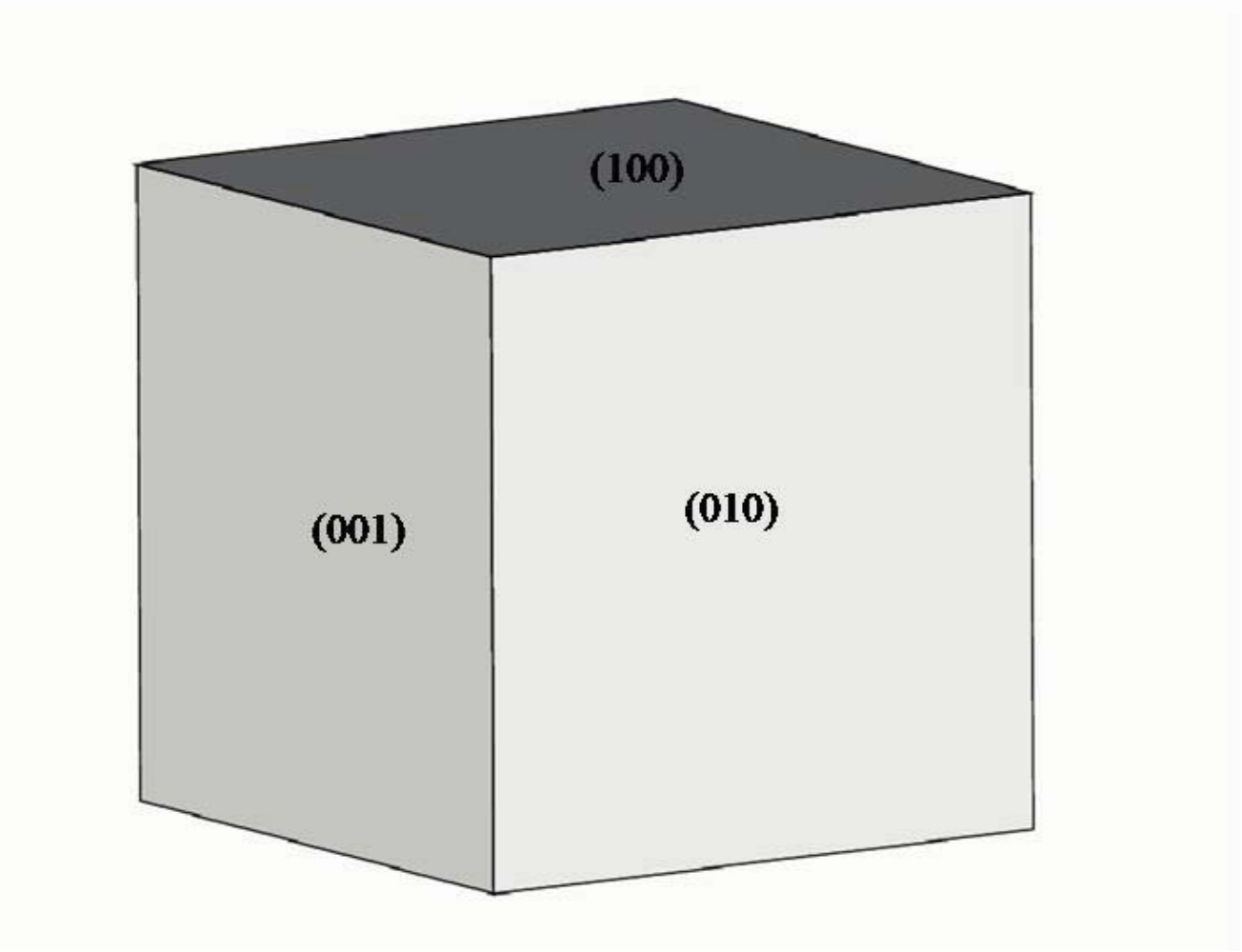


Figure 6.41: The calculated thermodynamical equilibrium morpholgy of the hydrated $PtAs_2$ crystal.

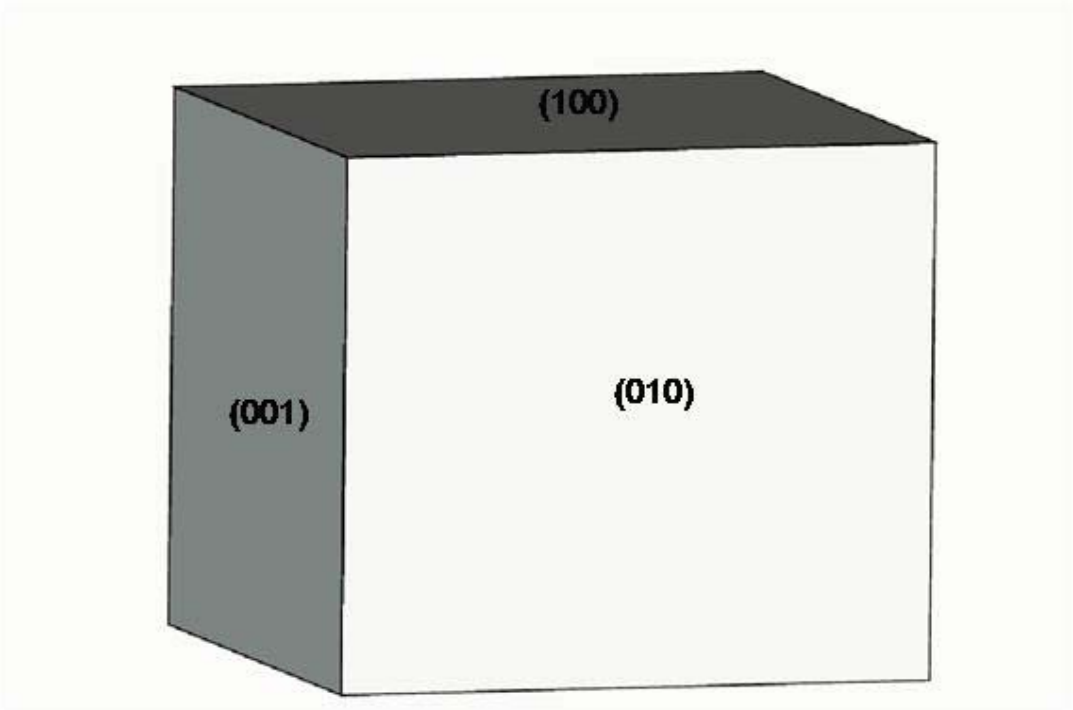


Figure 6.42: The calculated thermodynamical equilibrium morpholgy of the unrelax-dry $Pt_4As_4S_4$ crystal.

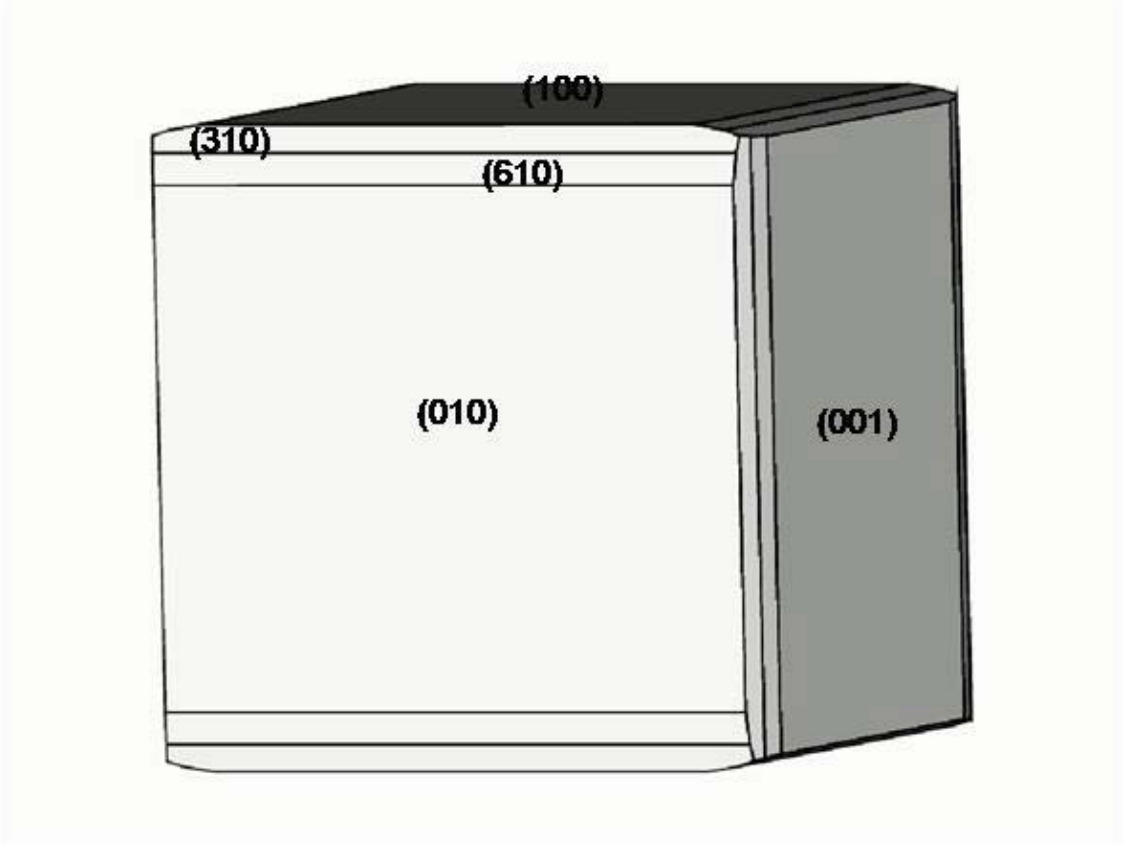


Figure 6.43: The calculated thermodynamical equilibrium morpholgy of the relax-dry $Pt_4As_4S_4$ crystal.

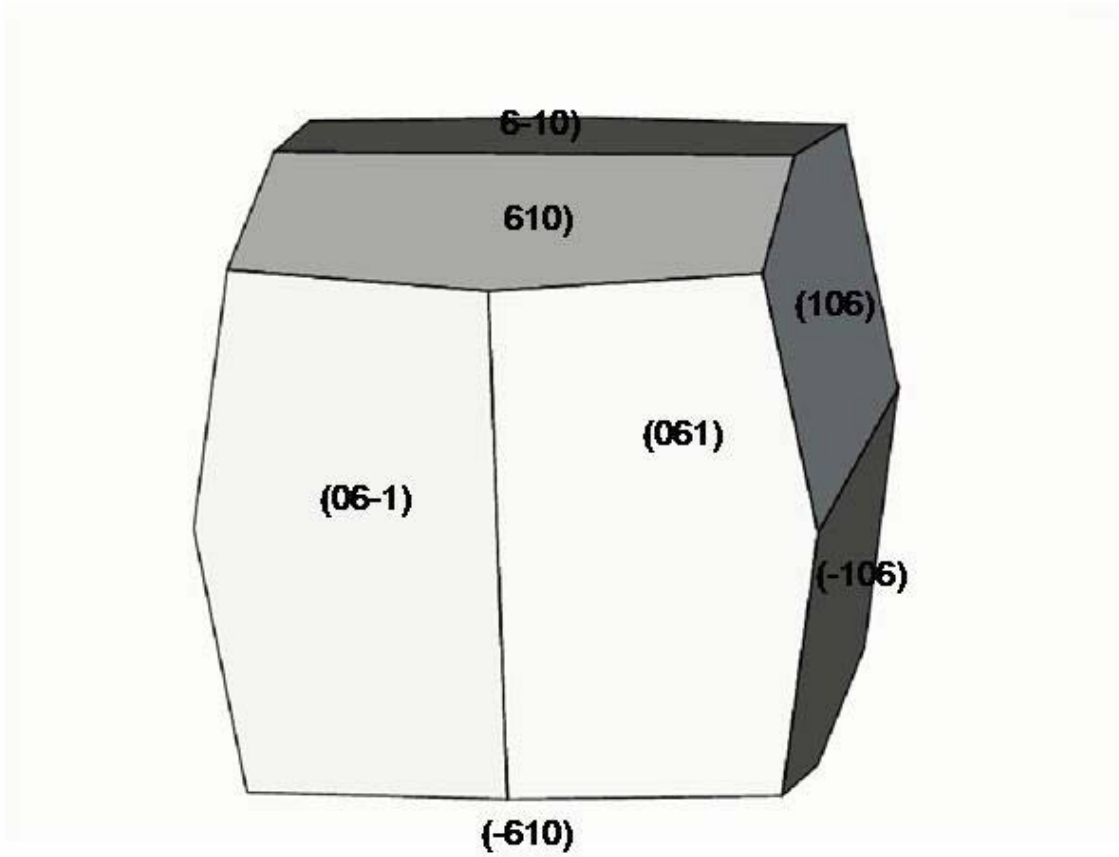


Figure 6.44: The calculated thermodynamical equilibrium morpholgy of the hydrated $Pt_4As_4S_4$ crystal.

are hydrated, the morphology changes due to the dissimilar stabilisation of the different surfaces by adsorption of water. Fig. 6.44 shows the calculated morphology based on the hydrated surfaces which is different from the morphology of dry surfaces. Not surprisingly, taking into account the low surface energy of the {610} surface in table 6.4, the {610} surface is now expressed in the hydrated morphology at the expense of both the {100} and {310} surfaces, neither of which is observed in the hydrated morphology.

## 6.4 Conclusion

This study has advanced considerably our understanding of the surface stability and structure of $PtAs_2$ and $Pt_4As_4S_4$. The surface energies, stabilities and reactivities of both $PtAs_2$ and $Pt_4As_4S_4$ were calculated using the energy minimisation technique and {100} surface were found to be the most stable surface in vacuo for both $PtAs_2$ and $Pt_4As_4S_4$, respectively. We have modelled the adsorption of water onto the surfaces of $PtAs_2$ and $Pt_4As_4S_4$. Consequently, we find that both the low and high index surfaces of $PtAs_2$ and $Pt_4As_4S_4$ respectively, were considerably stabilised by the adsorption of water molecules.

We have also investigated the initial stages of both dissolution and growth of both $PtAs_2$ and $Pt_4As_4S_4$ respectively, on two dry stepped platinum surfaces. The surfaces throughout were charge neutral and neutral $PtAs_2$ and PtAsS units were removed from the surfaces, of both $PtAs_2$ and $Pt_4As_4S_4$ respectively. The platinum surface {410} and {510} surfaces consisting of obtuse (105 degrees) steps were less stable than the acute (86 degrees) steps, in vacuo. Thus, dissolution process modelled at the unhydrated stepped surfaces shows initial and subsequent removal of both the $PtAs_2$ and PtAsS units to occur preferentially at the acute step edges.

We also found that the equilibrium morphology of $PtAs_2$ obtained using the surface energies of the various unrelaxed dry surfaces agree well with the experimentally found morphology, indicating that the relative stabilities of the surfaces were modelled correctly. The three surfaces expressed in the relaxed equilibrium morphology of $PtAs_2$, {100}, {210} and {102}, are in good agreement with experiment.

It is observed that the crystal morphology of $Pt_4As_4S_4$ does show significant changes when the environment is altered, and the {610} surfaces is the

most stable surface and therefore, the only one expressed in the final crystal morphology upon hydration. Unfortunately, as yet there are no experiments as well as ab initio calculations with which to make comparisons.

# Chapter 7

# CONCLUSIONS AND FUTURE WORK

## 7.1 CONCLUSIONS

In this study, we have shown that an efficient and accurate description of the ground state properties of PGM can be obtained with first principles pseudopotential planewave and TB-LMTO techniques.

We have made self-consistent, first principle calculations of both relaxed and unrelaxed structures, electron densities and optical spectra, of PGM. A satisfactory agreement with experimental results has been obtained for the equilibrum lattice parameters of PtS, $PdPt_3S_4$, $PtAs_2$ and $Pt_4As_4S_4$ [1]. We have reported on an extensive theoretical study of high-pressure effects in the PGM using pseudopotential calculations. Our general observations are that density functional techniques are capable of adequately describing not only the equilibrium structural properties, but are also very effective in predicting detailed pressure-induced changes in the unit cell and atomic positions. It also gives relatively accurate predictions of total energy and bulk moduli that are derived from the P-V equation of state. The variation of PtS bond lengths with respect to the applied pressure were computed. Both Pt-Pt and Pt-S bond lengths decrease with increase in pressure, while S-S bond length increases with the increase in the pressure. This gives an account of the unusual behaviour of relative lattice constant c and $c/c_0$ which increases as the pressure increases. The negative sign shows that the structure has a highly anisotropic response to the increase in pressure and the material expands

along the c axis while contracting along a axis. The a-axis compression is essentially linear in pressure for PtS, $PdPt_3S_4$, $PtAs_2$ and $Pt_4As_4S_4$. It is also observed that the bond lengths in tetragonal $PdPt_3S_4$ and in cubic $PtAs_2$ and $Pt_4As_4S_4$ decrease with an increase in pressure. However, the bond lengths in $Pt_4As_4S_4$ decrease faster than those in $PtAs_2$. We have also shown the pressure response of the internal parameters for $PdPt_3S_4$, $PtAs_2$ and $Pt_4As_4S_4$. It is clear that the internal parameter (u) for $PdPt_3S_4$, $PtAs_2$ and $Pt_4As_4S_4$ decrease with increase in pressure, while v and w (internal parameters) for $PdPt_3S_4$ increase with increase in pressure. A similar trend where the internal parameter u decreases with hydrostatic pressure is observed in the pyrite structure of $FeS_2$ [85].

The main result is that the energy band structures obtained with the two techniques, exhibit the semiconductor behavior of PtS, $PdPt_3S_4$ and $PtAs_2$, with the energy gap decreasing from PtS$\rightarrow$ PdPtS$\rightarrow$ $PtAs_2$. $Pt_4As_4S_4$ is predicted metallic. We have predicted semiconductor band gaps of 1.3 , 0.89 and 0.34 eV, respectively for PtS, $PdPt_3S_4$ and $PtAs_2$ using the TB-LMTO method, and band gaps of 0.41, 0.21 and 0.29 eV, respectively using the pseudopotential method. Interestingly, TB-LMTO band gap for PtS is about thrice (1.3 eV) as large as Castep planewave pseudopotential calculations (0.41 eV). As far as we know, the experimental data on optical band gap in PtS is 0.8 eV with second possible energy gap (1.4 eV) [16]. From the chemical formulae, these compounds, in going from PtS$\rightarrow$ $PdPt_3S_4$ $\rightarrow$ $PtAs_2$, differ from each other only by either sequential addition or substitution of one palladium or sulfur atom. There are no experimental band gaps for $PdPt_3S_4$ and $PtAs_2$, as far as we know, but their semiconductor behaviour is only mentioned by Vaughan [1]. Our investigations extend and confirm studies that had suggested that the electronic structure of the transitional metal sulphides determined largely by short-range interactions in the S 3p, As 4p - transition metal - d band complex and in particular by covalent bonding of the transition metal d and the ligand p states in the eventually distorted octahedral or tetrahedral environment of S or As atoms.

Strong covalent bonding and the formation of structure induced gap or pseudogap, at the Fermi level are also important for understanding the stability of the late 4d and 5d (PtS, $PdPt_3S_4$, $PtAs_2$ and $Pt_4As_4S_4$).

Our analysis of the valence charge distribution is consistent with a strongly covalent model in PtS, $PdPt_3S_4$, $PtAs_2$ and $Pt_4As_4S_4$. Charge density differences show strong covalent bonding between Pt-S bond of PtS, Pd-S, Pt-S bond of $PdPt_3S_4$, Pt-As, As-As bonds of $PtAs_2$ and Pt-As, Pt-S and S-As

bonds of $Pt_4As_4S_4$. Metallic bonding between adjacent Pt atoms is observed in $PtAs_2$.

The optical properties of these minerals have been studied theoretically. The origin of the main absorption peaks has been determined. It is shown that large interior parts of the BZ are responsible for the formation of those peaks.

We observe that the reflectivity spectra of PtS, $PdPt_3S_4$, $PtAs_2$ and $Pt_4As_4S_4$ are very close to each other, with $PtAs_2$ having higher reflectivity at low pressure, and $Pt_4As_4S_4$ higher reflectivity at higher pressure. Pressure dependence of the reflectance spectra of these PGM can be interpreted on the basis of a band model. The reflectance peak corresponding to the inter band transition between $t_2$ and $e_g$ (for tetragonal), $e_g$ and $t_{2g}$ (for cubic) shifts to the higher energy side as the pressure increases. This observation may indicate that the binding energy increases under high pressure for these systems.

Despite their apparently covalent nature, it has been possible to derive new set of ionic interatomic potential models to describe PtS, $PdPt_3S_4$, $PtAs_2$ and $Pt_4As_4S_4$. These potential models were derived by using the results of DFT-LDA calculations to fit the rigid-ion, shell-model and three-body interactions. The quality of these potentials is good, as shown by the agreement between the experiment and our ab initio plane wave method at ambient pressure structure, lattice constants, elastic constants and bulk modulli. The pressure dependence of the lattice constants were performed and the results are in good agreement with the plane wave method, especially for $PdPt_3S_4$, $PtAs_2$ and $Pt_4As_4S_4$. The c-lattice constant of PtS on interatomic potential tends to a constant value instead of reducing pressure, which is an indication that is sensitive to the anomaly noted in our plane wave results.

The model of potential parameters for $PtAs_2$ and $Pt_4As_4S_4$ were transfered from the bulk to study the surfaces. We have futher derived suitable potentials that enabled us to study the effect of water on the mineral surfaces. We studied the surface energies, stabilities and reactivities of both $PtAs_2$ and $Pt_4As_4S_4$ respectively, using the energy minimisation technique, and $\{100\}$ surfaces were found to be the most stable surface under dry conditions in both cases. The effect of water or hydration on the different surfaces were modelled, and consequently, find that all surfaces are considerably more stabilised by the adsorption of water molecules.

We have also investigated the initial stages of both dissolution and growth of both $PtAs_2$ and $Pt_4As_4S_4$ respectively, on both dry acute and obtuse

stepped platinum surfaces. The surfaces throughout were charge neutral and neutral $PtAs_2$ and $Pt_4As_4S_4$ units were removed from the surfaces, of both $PtAs_2$ and $Pt_4As_4S_4$ respectively. The aim is to investigate the energies of surface growth via a new modelling technique which uses a high index surface as approximation for a stepped version of a low index surface. Crystal growth is known to occur at stepped sites on the crystal surface, it has been shown that nucleation occurs preferentially at these sites. This has led to the idea that higher index surfaces could be used to model stepped low index surfaces. The platinum surface {410} and {510} surfaces consisting of obtuse (105 degrees) steps were less stable than the acute (86 degrees) steps, in vacuo. Thus, dissolution process modelled at the unhydrated stepped surfaces shows initial and subsequent removal of both the $PtAs_2$ and PtAsS units to occur preferentially at the acute step edges.

We also found that the equilibrium morphology of $PtAs_2$ obtained using the surface energies of the various unrelaxed dry surfaces agree well with the experimentally found morphology, indicating that the relative stabilities of the surfaces were modelled correctly. The three surfaces expressed in the unrelaxed equilibrium morphology of $PtAs_2$, {100}, {210} and {102}, are in good agreement with experiment. Upon hydration the morphology changes completely, with {100} surface being the only face expreesed in the equilibrium morphology.

It is observed that the crystal morphology of $Pt_4As_4S_4$ does show significant changes when the environment is altered, and the {610} surfaces is the most stable surface and therefore, the only one expressed in the final crystal morphology upon hydration. There are no currently experiments as well as ab initio calculations with which to compare the interatomic potential results.

## 7.2 FUTURE WORK

The results presented in this dissertation indicate that the future for ab initio computational simulations of PGM is extremely promising. Several avenues of further investigations of PGM are immediately suggested. We hope that our theoretical calculations will stimulate more experimental work on the equations of state, bulk moduli and band gaps in PGMs. It is only when these results are available, particularly bulk moduli that a comparison with our theoretical values could be able to asses the effects of LDA on the

theoretical description of these quantities.

It is also important that the elastic properties for these systems could be studied both theoretically and experimentally since this will help significantly in the development and improvement of their interatomic potential models. After the success in modelling the hydrated surfaces, the next step could be to study the physisorption of water molecules at the different crystal surfaces and hence model the surface under aqueous conditions. Another area for further research includes modelling adsorption of water at surface defects and steps, using both atomistic simulation techniques and molecular dynamics simulations of crystal growth and dissolution in aqueous solution.

# Bibliography


[1] Vaughan, D.J. and Graig, J.R. (1978). Cambridge University Press, Cambridge, London-New York-Melbourne

[2] Carbi, L.J. (1972). Minerals Sci. Eng., **4**, 3.

[3] Raybaud, P., Kresse, G., Hafner, J. and Toulhoat, H. (1997). J. Phys.: Condens. Matter **9**, 11085.

[4] Tsai, M.H.and Hass, K.C. (1995). Phys. Rev B, **51**, 14616.

[5] Hurly, J. and Wedepohl, P.T. (1993). Journal of Material Science, **28**,5648.

[6] Kumar, G.S., Raja, M. and Parthasarathy, S. (1995). Electrochimca Acta, **40**, 285.

[7] De Villiers, J.P.R. (1998). Molecular Simulation, **00**, 81.

[8] Hurly, J. and Wedepohl, P.T. (1993). Journal of Materials Science, **28**, 5648.

[9] Nickel, H.E., (1995). Internal Mineralogical Association, Commission on New Minerals and Minerals Names: Definition of a Mineral, Mineralogy and Petrology, **55**, 323.

[10] Evstigneeva, T., Moh, G.H. and Tarkian M. (1995). N. Jb. Miner. Abh. 169, **3**, 273.

[11] Evstigneeva, T. and Tarkian M. (1996). Eur. J. Mineral, **8**, 549.

[12] Goghill, B.M., and Wilson A.H.(1993). Mineralogical Magazine, **57**, 613.

[13] Cabri, L.J., Stewart, J.M., Turner, K. and Skinner, B.J.(1978). Am. Mineral. **63**, 832.

[14] Childs, J.D. and Hall, S.R. (1973). Acta Cryst. B, **29**, 1446.

[15] Vaughan, D.J. and Lennie, A.R. (1991). Sci. Progress Edinburg, **75**, 371.

[16] Hulliger, F. (1965). J. Phys. Chem. Solids, **26**, 639.

[17] Collins, R., Kaner, R., Russo, A. and Avignant. (1979). Inorganic Chemistry, **3**, 727.

[18] Criddle, A.J. and Stanley, C.J. (1985). Can. Mineral., **23**, 149.

[19] Mernagh, T.P. and Hoatson, D.M.(1995). Can. Mineral., **33**, 409.

[20] Dunn, P.J., Cabri, L.J., Chao, G.Y., Fleischer, M., Francis, C.A., Grice, J.D., Lambor, J.L. and Pabst, A.(1984). Am. Mineral., **64**, 406.

[21] Cabri, L.J., Campbell, J.L., Lamflamme, J.H.G., Leigh, R.G., Maxwell, J.A. and Scott, J.D. (1985). Can. Mineral., **23**, 133.

[22] Chryssoulis, S.L., Cabri, L.J. and Lennard, W. (1989). Economic Geolo, **84**, 1684.

[23] Nguyen-Manh, D., Pettifor, D.G., Sithole, H.M., P.E., Arcangeli, C., Tank, R. and Jespen, O. (1998). Mta. Res. Soc. Symp. Proc., **491**, 401.

[24] de Leeuw, N.H., Parker, S.C., Sithole, H.M. and Ngoepe, P.E. (2000). J. Phys. Chem. B, **104**, 7969.

[25] Cerius 3.0. Quantum Mechanics-Physics. (1997). CASTEP, ESOCS, Fast Structure, MSI, San Diego, CA.

[26] Jepsen, O., Andersen, O.K., Krier, G. (1994). Lectures on Methods of Electronic Structure Calculations, edited by Kumar, V., Andersen, O.K. and Mookerjee, A., (Worth Scientific).

[27] Krier, G., Jepsen, O., Burkhart, A., and Andersen, O.K. (April 1995). TB-LMTO-ASA program, Stuttgart.

[28] von Barth, U. and Hedin, L. (1972). J. Phys.: Condens. Matter **5**, 1629.

[29] Born, M. and Oppenheimer, R. (1927). Ann. Physik, **84**, 457.

[30] Fahy, S., Wang, X.W. and Louie, S.G. (1990). Phys. Rev. B, **42**, 3503.

[31] Umrigar, C.J., Wilson, K.G. and Wilkins, J.W. (1988). Phy. Rev. Lett., **60**, 1719.

[32] Wei, D. and Osseo-Asare, K. (1996). J. Electrochem. Soc., **143**, 1996, 3192.

[33] Ceperly, D.and Kalos, M. (1979). In K. Binder, editor Monte Carlo Methods in Statistical Physics. Springer, Berlin.

[34] Thomas, L.H.(1926). Proc. Camb. Phil. Soc., **23**, 542.

[35] Fermi, E. (1928). Phys., **48**, 73.

[36] Hohenberg, P. and Kohn, W. (1964). Phys. Rev.B, **136**, 864.

[37] Kohn, W. and Sham, L.J. (1964). Phys. Rev.A, **140**, 1133.

[38] Slater, J.C.(1951). Phys. Rev. **81**, 385.

[39] Slater, J.C. (1974). Quantum Theory of Molecules and Solids, **4**, McGraw-Hill, New York.

[40] Chadi, D.J.and Cohen, M.L. (1973). Phys. Rev. B, **8**, 5757.

[41] Joannopoulos, J.D. and Cohen, M.L. (1973). J. Phys.: Condens. Matter **6**, 1572.

[42] Evarestov, R.A.and Smirnov, V.P. (1983). Phys. Status. Solid., **119**, 9.

[43] Monkhorst, H.J. and Pack, J.D. (1976). Phys. Rev., **13**, 5188.

[44] Cohen, M.L. and Heine, V. (1970). Solid State Physics, **24**, 37.

[45] Phillips, J.C. (1958). Phys. Rev. **112**, 685.

[46] Yin, M.T. and Cohen, M.L. (1982). Phys. Rev. B, **25**, 7403.

[47] Joannopoulos, J.D., Starkloff, T.H., Kastner, M. (1977). Phys. Rev. Lett., **38**, 660.

[48] Joannopoulos, J.D., Starkloff, T.H.(1977). Phys. Rev. B, **16**, 5212.

[49] Shirley, E.L., Allan, D.C., Martin, R.M. and Joannopoulos, J.D. (1989). Phys. Rev. B, **40**, 3652.

[50] Vanderbilt, D. (1990). Rev. B, **41**, 7892.

[51] Andersen, O.K., Postnikov, A.V. and Yu Savrasov, S. (1992). Mat. Res. Soc. Symp. Proc., **253**, 37.

[52] Andersen, O.K., Jepsen, O. and Sob (1987). In Electron Band Structure and its Applications, edited by M. Yussouff, Lecture Notes in Physics, **283**, Springer-Verlag, Berlin, 1.

[53] Skriver, H.L. (1984). The LMTO method (Springer-Verlag, Berlin).

[54] Andersen, O.K., Arcangeli, C. and Tank, R.W. (1998). Mat. Res. Soc. Symp. Proc., **491**, 3.

[55] Jepsen, O and Andersen, O.K. (1995). J. Phys. Rev. B, **97**, 35

[56] Ferreira, L.G., Ozolins, V. and Zunger, A. (1999). Phys. Rev. B **60**, 1687;

[57] Mishin, Y. Farkas, D. Mehl, M.J. and Papaconstantopolos, D.A. (1999). Phys. Rev. B **59**, 3393

[58] A.B. Belonoshko, R. Ahuja, O. Eriksson, and B. Johansson (2000). Phys. Rev. B **61**, 3838

[59] Y. Mishin, M.J. Mehl, D.A. Papaconstantopolos, A.F. Voter, and J.D. Kresse (2001). Phys.Rev. B **63**, 224106

[60] Y. Mishin, M.J. Mehl, and D.A. Papaconstantopolos (2002). Phys.Rev. B 65, 224114

[61] Baskes,M.I. , Asta, M. and Srinivasan, S.C. (2000). Philos. Mag. A **81**, 991

[62] Press,W.H., Teukolsky, S.A., Vetterling, W.T., and B.P. Flannery, B.P., Numerical Recipes. Cambridge University Press, Cambridge, 2nd edn (1992)

[63] Catlow, C.R.W., Computer Modelling in Inorganic Crystallography, ed. C.R.W. Catlow, Academic Press, London (1997)

[64] Catlow, C.R.W, Norgett, M.J., UKAEA report AERE-M2936 (1976)

[65] Watson, G.W., Kesley, E.T., de Leeuw, N.H., Harris, D.J., Parker, S.C. J. (1996) Chem. Soc., Faraday. Trans., 92, 433.

[66] Tasker,P.W.(1978). Technical report, AERE(R9130).

[67] Bertaut,F.(1958). Compt Rend, 246:3447.

[68] Tasker, P.W. (1979). The stability of ionic crystal surfaces., 12,4977.

[69] Zur Frage der Geschwindigheit des Wachstums und der Aufloesung der Krystallflachen. Z. Kristallogr Kristallgeom 34: 949.

[70] Kantorovich, LN. Phys. Rev. B (1995) 51, 3520

[71] Kantorovich, L.N. Phys. Rev. (1995), 51, 3535.

[72] Taylor, M.B, Berrera, G.D., Allan, N.L., Barron, T. H. K., Mackrodt, W.C., Phys. Rev. B (1997), 56, 14380.

[73] Allan, N.L., Barron, T.H.K., Bruno, J.A.O. (1996), J. Chem. Phys., 105, 8300

[74] Allen, M.P. and Tildesley, D.J. (1989). Computer simulation of liquid. Oxford: Clarendon Press.

[75] Jacobs, P.W.M. and Rycerz, Z.A. (1997). Computer modelling in organic crystallography. Academic Press, London.

[76] Forester, T.R. and Smith, W.(1995). DL_Poly user manual (CCLRC, Daresbury Laboratory, Daresbury, Warrington, UK.

[77] Hoover, W.G. (1985). Phys. Rev. A, **31**, 1695

[78] Sob, M., Turek, I. and Vitek, V. (1998). Mat. Res. Soc. Symp. Proc., **491**, 79.

[79] Kleinmann, L. and Bylander, D.M. (1982). Phys. Rev. B, **48**, 1425.

[80] Murnaghan, F.D. (1944). Proc. Natl. Acad. Sci., 30, 244.

[81] Blochl, P., Andersen, O.K. and Jespen, O. (1994). Phys. Rev. B, **49**, 16223.

[82] Auckland, G.J. (1998). Phys. Rev. Lett., **80**, 2233.

[83] Auckland, G.J. (1998). Phys. Rev. Lett., **81**, 3301.

[84] Nguyen-Mahn, D., de Lassardiere, G.T., Julien, J.P., Mayou, D. and Cyrot-Lackmann, F. (1992). Sol. State. Commun., **82**, 329.

[85] Sithole, H.M., Nguyen-Manh, D., Pettifor, D.G. and Ngoepe, P.E. (1999). J. Molecular Simulation, **22**, 31.

[86] Sithole, H.M. (2000). Electronic and Atomistic Simulation of FeS2. Ph.D.Thesis, Univ. of the North, SA.

[87] Criddle, A.J. (1980). Can. Mineral., **18**, 533.

[88] Tsintsov, Z.L. and Damyanov, Z.K. (1994). N. Jb. Miner. Mh., **11**, 518.

[89] Picot, P. and Johan, Z. (1977). Atlas de mineraux metalliques. Mem. B.R.G.M. N90.

[90] Vyalsov, L.N. (1973). Acad. Sci. U.S.S.R., IGEM, Moscow, 67.

[91] Born, M.M.; Huang, K. Dynamical Theory of Crystal Lattices, Oxford University Press, Oxford 1954

[92] Ewald, P.P. (1921). Die Berechnung optischer und elektrostatischer Gitterpotentiale. Annalen der Physik, **64**, 253.

[93] Kittel, C. (1971). Introduction to Solid State, John Wiley, New York.

[94] Parry, D.E. (1976). Surface Science, **64**, 253.

[95] Parry, D.E. (1976). Surface Science, **54**,195.

[96] Allan, N.L., Rohl, A.L., Gay, D.H., Catlow, C.R.A., Davy, R.T., and Mackrodt, W.C. (1993). Faraday Discussions, **95**, 273.

[97] Faux, I.D. (1971). J. Phys. C, **4**, L211.

[98] Dick, B.G., JR., and Overhauser, A.W., (1958). Phys. Rev. **112**, 90.

[99] Wright, K and Jackson, R.A. (1995). J. Mater. Chem., **5**, 2037.

[100] Gale, J.D. (1996). Philos. Mag.B., 7**3**, 3.

[101] Somorjai, G.A. (1994). Introduction to Surface Chemistry and Catalysis, Wiley, New York.

[102] de Leeuw, N.H. and Parker, S.C. (1998). Phys. Rev. B, **58**, 13901.

[103] Schroder, K.P., Sauer, J., Leslie, M., Catlow, C.R.A., Thomas, J.M. (1992). J. Chem. Phys. Lett., **188**, 320.

[104] Gibbs, J.W. (1928). Collected works, Longman, New York.

[105] Fleet, M.E., Stone, W.E. and Crocket, J.H. (1991). Geochimica et Cosmochimica Acta, **55**, 2545.

[106] Williamson, A.J., Kenny, S.D., Rajagopal, G., Needs, R.J., Fraser, L.M., Foulkes, W.M.C. and MacCallum, P. (1996). Phys. Rev. B, **53**, 9640.

[107] Merkle, R.K.W., Pikl, R., Verryn, S.M.C. and De Waal, D. (1997). N. Jb. Miner. Mh., **11**, 518.

[108] Helmy, H.M., Stumpfl, E.F and Kamel, O. (1995). Economic Geology, **90**, 2350.

[109] Tropkovic, M., Todorivic, M. and Holclajtner-Antunovic, I. (1994). Analytica Chimica Acta **296**, 315.

[110] Diella, V., Ferrario, A. and Girardi, V.A.V. (1995). Ore Geology Review **9**, 445.

[111] St-Onge, M.R. and Lucas, S.B. (1993). Can. J. Earth Sci., **31**, 206.

[112] Yang, S.H., Drabold, D.A., Adams, J.B., Ordejon, P and Glassford, K. (1997). J. Phys.: Condens. Matter **9**, 39.

[113] Wimmer, E.(1996). NATO Series: Electronic Structure Methods.

[114] Wimmer, E., Freeman, A.J., Weinert, M., Krakauer, H., Hiskes, J.R. and Karo, A.M. (1982). Phys. Rev. **48**, 1128.

[115] Slater, J.C. and Koster, G.F. (1954). Phys. Rev., **94**, 1498.

[116] Teter, M. (1993). Phys. Rev. B, **48**, 5031.

[117] Rappe, A.M., Rabe, K.M., Kaxiras, E. and Joannopoulos, J.D.(1990). Phys. Rev. B, **41**, 1227.

[118] Troullier, N. and Martins, J.L. (1991). Phys. Rev. B, **43,** 1993**.**

[119] Payne, M.C., Teter, M.P., Allan, D.C., Arias, T.A. and Joannopoulos, J.D. (1992). Rev. Mod. Phys., **64**, 1045.

[120] Becke, A.D. (1988). Phys. Rev. A, **38**, 3098.

[121] Methfessel, M., Rodriguez, C.O. and Andersen, O.K. (1989). Phys. Rev. B, **40**, 2009.

[122] Methfessel, M. and Scheffler, M.(1991). Physica B, **172**, 175.

[123] Bose, S.K. (1998). Mat. Res. Soc. Symp. Proc., **491**, 105.

[124] Bose, S.K., Jespen, O. and Andersen, O.K. (1994). J. Phys.: Condens. Matter **6,** 2145**.**

[125] Kobayashi, S. and Fujiwara, T. (1997). Phys. Rev. B, **55**, 7445.

[126] Andersen, O.K. and Jespen, O. (1984). Phys. Rev. Lett. **53**, 2571.

[127] Reinaldo-Falagan, M. Tarazona, P., Chacon, E. and Hernandez, J.P. (1997). J. Phys. Condens. Matter **9**, 9799.

[128] Harrison, W.A. (1992). Surface Science, **299**, 298.

[129] Agrawal, B.K., Srivastava, P. and Agrawal, S. (1998). J. Phys. Condens. Matter **10**, 67.

[130] Heid, R. and Bohnen, K.P. (1999). Phys. Rev. B, **60**, 3709.

[131] Haydock, R. (1998). Mat. Res. Soc. Proc. **491**, 35.

[132] Sutton, A.P. (1993). Electronic Strcuture of Materials ( Claredon Press, Oxford).

[133] Temmerman, W.M., Durham, P.J. and Vaughan, D.J.(1993). Phys. Chem. Minerals, **20**, 248.

[134] Zeng, Y. and Holzwarth, N.A.W. (1994). Phys. Rev. B, **50**, 8214.

[135] Bannister, F.A. (1932). Miner. Mag., **23**, 188.

[136] Eyert, V., Hock, K.H., and Tributsch, S.F. (1998). Phys. Rev. B, **57**, 6350.

[137] Huang, Y.S., Huang, J.K. and Tsay, M.Y. (1993). J. Phys. Condens. Matter **5**, 7827.

[138] Vocadlo, L., Patel, A. and Price, G.D. (1995). Min. Mag. **59**, 597.

[139] Kurmaev, E.Z., van Ek, J., Ederer, D.L., Zhou, L., Callcott, T.A., Perera, R.C.C., Cherkashenko, M.V.and Moloshag (1998). J. Phys. Condens. Matter **10**, 1687.

[140] Xie, J., Zi, J and Zhang, K.(1995). Phys. Stat. Sol.(b), **192**, 95.

[141] Takele, S. and Hearne, G.R. (1999). Phys. Rev. B, **60**, 4401.

[142] Yang, Z.R. and Yu, J.T. (1995). J. Appl. Phys. **77,** 1710.

[143] Mori, N. and Takahashi, H. (1987). High-Pressure Research in Mineral Physics, edited by H.M. Manghanani and Y. Syono, 341.

[144] Manning, B.A. and Goldberg, S. (1996). Soil. Soc. Am. J., **60**, 121.

[145] Ashby, M.F. (1992). Material Science and Technology, **8**, 102.

[146] Ogut, S.and Rabe, K.M. (1994). Phys. Rev.B, **4**, 2075.

[147] Horsfield, A and Kenny, S.D. (1998). Mat. Res. Soc. Proc. , **491**, 57.

[148] Jones, E.D., Modine, N.A., Allerman, A.A, Kurtz, S.R. and Wright, A.F. (1999). Phys. Rev. B, **60**, 4430.

[149] Lucovsky, G., White, R.M., Benda, J.A. and Revelli, J.F. (1973). Phys. Rev. B, **7**, 3859.

[150] Emtage, P.R. (1964). Phys. Rev., **138**, A246.

[151] Clark, S.J., Ackland, G.J. and Akbarzadeh, H.(1995). Phys. Chem. Solids, **56**, 329.

[152] Chall, M., Winkler, B. and Milman, V. (1996). J. Phys. Condens. Matter **3**, 9049.

[153] Vernes, A., Ebert, H., Bensch, W., Heid, W. and Nather, C. (1998). J. Phys. Condens. Matter **10**, 761.

[154] Catti, M. and Valerio, G. and Dovesi, R. (1995). Phys. Rev. B, **51**, 7441.

[155] Eyert, V. and Hock, K.H. (1998). Phys. Rev. B, **57**, 12727.

[156] Damon. D.H., Miller, R.C. and Sugar, A. (1965). Phys. Rev., **138**, A636.

[157] Mankai, C. and Rondhani, H. (2000). J. Phys. Condens. Matter **12**, 907.

[158] Park, K.T., Novikov, D.L. Gubanov, V.A. and Freeman, A.J. (1994). Phys. Rev. B, **49**, 4425.

[159] Manassidis, I and Gillan, M.J. (1994). J. Am. Ceram. Soc., **77**, 335.

[160] Kruse, C., Finnis, M.W., Millman, V.Y., Payne, M.C., De Vita, A. and Gillan, M.J. (1994). J. Am. Ceram. Soc., **77**, 431.

[161] Kirchhoff, F., Holender, J.M. and Gillan, M.J. (1994). Phys. Rev. B, **49**, 17420.

[162] Hsueh, H.C., Vass, H., Clark, S.J., Ackland, G.J. and Crain, J. (1995). Phys. Rev. B, **51**, 23.

[163] Hanfland, M., Beister, H. and Syassen, K.(1989). Phys. Rev. B, **39**, 12598.

[164] Kresse, G. and Hafner, J.(1997). Phys. Rev. B, **55**, 7539.

[165] Allan, D.R., Kelsey, A.A., Clark, S.J., Angel, R.J. and Ackland, G.J. (1998). Phys. Rev. B, **57**, 5106.

[166] Karki, B.B., Warren, M.C., Stixrude, L., Ackland, G.J. and Crain, J. (1997). Phys. Rev. B, **55**, 3465.

[167] Lemoigno, Z.Y. Wu, F., Gressier, P., Ouvard, G., Moreau, P. and Rouxel, J. (1996). Phys. Rev. B, 54, R11009.

[168] Zhou, P. and Fischer, J.E. (1996). Phys. Rev. B, **53**, 12643.

[169] Jansen, H.J.F. and Freeman, A.J. (1987). Phys. Rev. B, **35**, 8207.

[170] Cohen, M.L. (1998). Solid State Communications, **107**, 589.

[171] Andersen, O.K.(1975). Phys. Rev. B, **8**, 3060.

[172] Hamann, D.R., Schluter, M. and Chiang, C. (1979). Phys., C, 12, 1494.

[173] Mostert, J.C. and Roberts, P.N.(1973). Journal of the South African Mining and Metallurgy, 290.

[174] D' Arco, P., Silvi, B., Roetti, C. and Orlando, R. (1991). Journal of Geophysics Research, **96**, 6107.

[175] Smith, W., Greaves, G.N. and Gillan, M.J. (1995). J. Phys. **103**, 3091.

[176] Liu, F.L., Mostoller, M., Milman, V., Chisholm, M.F. and Kaplan, T.(1995). Phys. Rev. B, **51**, 17192.

[177] Glotzel, D., Segall, B. and Andersen ,O.K. (1980). Solid State Communications, **36**, 403.

[178] Alouani, M and Khan, M.A. (1987). J. Phys. F: Met. Phys. **17**, 519.

[179] Gillan, M.J., Manassidis, I. and DE Vita, A. (1994). Philosophical Magazine B, **69**, 879.

[180] Tang, S. and Freeman, A.J. (1994). Phys. Rev. B, **50**, 1.

[181] Coyotecatl, H.A. and Cocoletzi, G.H. (1998). J. Phys. Condens. Matter **10**, 79.

[182] Yang, J., Cui, B., Mao, W., Yang, Y., Chen, D., Yang, J. and Cou, C. (1998). Journal of Physical Society of Japan, **67**, 576.

[183] Liu, H.J. and Ye, Y.Y. (1998). Solid State Communications, **106**, 197.

[184] Alemany, M.M.G., Rey, C. and Gallego, L.J. (1998). Phys. Rev. B, **58**, 685.

[185] Miwa, R.H. and Ferraz, A.C. (1998). J. Phys. Condens. Matter **10**, 5739.

[186] Saito, T., Schulman, J.N. and Arakawa, Y. (1998). Phys. Rev. **B**, 57, 13016.

[187] Rohl, A.L. and Gay, D.H. (1995). Mineralogical Magazine, **59**, 607.

[188] Holender, J.M. and Gillan, M.J. (1996). Phys. Rev. B, **53**, 4399.

[189] Hudson-Edward, K.A., Macklin, M.G., Curtis, C.D. and Vaughan, D.J. (1996). Environ. Sci. Technol., **30**, 72.

[190] Filonov, A.B., Migas, D.B., Shaposhnikov, V.L. and Borisenko, V.E., Henrion, W., Rebien, M., Stauss, P. and Lange, H. (1998). Journal of Applied Physics, **83**, 4410.

[191] Antonov, V.N., Krasovka, O.V., Krasovskii, E.E., Kudryavtsev, Y.V, Nemoshkalenko, V.V, Yavorsky, B.Y, Lee, Y.P. and Kim, K.W. (1997). J. Phys. Condens. Matter. **9**, 11227.

[192] Villars, P. and Calvert, L.D. (1985). Person's Handbook of Crystalographic Data for Intermetallic Phases, American Society of Metals, Metal Parks.

[193] Chamber of mines of South Africa (1996). "South African Mining Industry Statical Tables".

[194] Crawson, P. (1996). "Minerals Handbook 1996-97", MacMillan Press Ltd.

[195] Nguyen-Mahn, D., Pettifor, D.G., Shao, G.S. Miodownik, A.P. and Pastural, A. (1996). Phil. Mag. A, **74**, 248.

[196] Benbattouche, N, Saunders, G.A., Lambson, E.F. and Honle, W.(1989). J.Phys. D:Appl. Phys., **22**, 670.

[197] Nguyen-Mahn, D., Ntoahae, P.S., Pettifor, D.G. and Ngoepe, P.E. (1999). Molecular Simulation, **22**, 23.

[198] Jeong, J., Lee, I., Oh, J.H. and Chang, K.J. (1998). J. Phys. Condens. Matter **10**, 5851.

[199] Nguyen-Mahn, D., Paxton, A.T. and Pettifor, D.G. (1995). Intermetallics, **3**, 9.

[200] Nguyen-Manh, D, Bratkovsky and Pettifor, D.G. (1995). Phil. Trans. Soc. Lond. A, **351**, 529.

[201] King-Smith, R.D., Payne, M.C. and Lin, J.S. (1991). Phys., Rev., B, **23**, 13063.

[202] Jones, H. (1975). "The Theory of Brillouin Zones and Electronic States in Crystals" second, revised edition, North-Holland Publishing Company, Inc, New-York.

[203] Jiles, D. (1994). Electronic Properties of Materials, Chapman & Hall, London, Glasgow, Weinheim, New York, Tokyo, Melbourne, Madras.

[204] Ashcroft, N,W. and Mermin, N.D. (1976). Solid State Physics, Saunders College Publishing.

[205] Fantucci, P., Polezzo, S., Sironi, M. and Bencini, A.(1995). J. Chem. Soc. Dalton Trans., 4121.

[206] Yang, T.R., Yu, J.T., Huang, J.K., Chen, S.H., Tsay, M.Y. and Huang, Y.S. (1994). J. Appl. Phys., **77**, 1710.

[207] Seeliger, W., Troughton, G.L., Alonso-Vante, N. and Tributsch, H. (1995). J. Electrochem. Soc., **142**, L166.

[208] Folkers, W., Sawatzky, G.A., Hass, C., de Groot, R.A. and Hillebrecht, F.U. (1987). J. Phys. C, Solid State Phys. **20**, 4135.

[209] Goniakowski, J., Holender, J.M., Kantorovich, L.N., and Gillan, M.J. (1996). Phys. Rev. B, **53**, 957.

[210] Neumann, A., Nguyen-Mahn, D., Kjekshus, A. and Sutton, A.P. (1998). Phys.Rev.B, **57**, 11149.

[211] Srinivasachar, S., Helble, J.J. and Boni, A.A. (1990). Prog. Energy Combust. Sci., **16**, 281.

[212] Senior, G.D., Polling, G.W. and Frost, D.C. (1989). International Journal of Mineral Processing, **27**, 221.

[213] Popov, S.R., Vucinic, D.R. and Kacanik, J.V. (1989). International Journal of Mineral Processing, **27**, 205.

[214] Smestad, G., Ennaoui, A., Fiechter, S., Tributsch, H., Hofmann, W.K. and Birkholz, M. (1990). Solar Energy Materials, **20**, 149.

[215] Kumarapeli, P.S., Kheang, L., Hoy, L. and Pintson, H. (1990). Can. J. Earth Sci., **27**, 27.

[216] Ferrer, I.J., de la Heras, C. and Sanchez, C. (1995). J. Phys. Condens. Matter **7**, 2115.

[217] Tauson, V.L. and Akimov, V.V. (1993). Chemical Geology, **109**, 113.

[218] Bertini, I., Ciurli, S. and Luchinat, C. (1995). Structure and Bonding, **83**, 1.

[219] Abass, A.K., Ahmed, Z.A and Tahir, R.E. (1986). Phys. Stat. Sol., **97**, 243.

[220] Sudo, S.and Miyadai, T. (1985). Journal of the Physics Societal of Japan, **54**, 3934.

[221] Ferrer, I.J., De las Heras, C., Menendez, N., Tornero, J. and Sanchez, C. (1993). Journal of Materials Science, **28**, 389.

[222] Nakat, J.E., Fisher, K.J., Dance, I.G. and Willett, G.D. (1993). Inorg. Chem. **32**, 1931.

[223] Womes, M, Karnatak, R.C., Esteva, J.M., Lefebvre, I., Allan, G., Olivier-Fourcades, J. and Jumas, J.C. (1996). J. Phys. Chem Solids, **58**, 345.

[224] Bullett, D.W.(1982). J. Phys. C: Solid State Phys., **15**, 6163.

[225] Schoonen, M.A.A. and Barnes, H.L. (1991). Geochimica et Cosmochimica Acta, **55**, 1495.

[226] Gupta. V.P., Chandra, K. and Srivastava, V.K. (1992). Journal of Materials Science Letters, **5**, 165.

[227] Pauling, L. (1978). Canadian Mineralogist, **16**, 447.

[228] Ferrer, I.J. and Sanchez, C. (1992). Solid State Communications, **81**, 371.

[229] Lopez-Cruz, E. (1990). Phys. Stat. Sol., **162**, K131.

[230] Lalvani, S.B., Weston, A. and Masden, J.T. (1990). Journal of Materials Science, **25**, 107.

[231] Karguppikar, A.M. and Vendeshwar, A.G. (1988). Phys. Stat. Sol., 109, 549.

[232] Harada, T. (1998). Journal of the Physical Society of Japan, **67**, 1352.

[233] Schmid-Beurmann, P. and Lottermoser, W. (1993). Phys. Chem. Minerals, **19**, 571.

[234] Sutton, A.P., Finnis, M.W., Pettifor, D.G. and Ohta, Y. (1988). J. Phys. C, **21**, 35.

[235] Johnson, C.K. (1965). ORTEP. Report. ORNL-7394, Oak Ridge National Laboratory, Oak Ridge, Tennesse.

[236] Pulay, P. (1969). Mol.Phys., **17**, 197.

[237] Pettifor, D.G. (1995). Bonding and Structure of Molecules and Solids, Clarendon Press, Oxford.

[238] Ziman, Principles of the Theory of Solids ( Cambridge at the University Press, 1965).

# Appendix A

# Choices available in DFT and HFT.

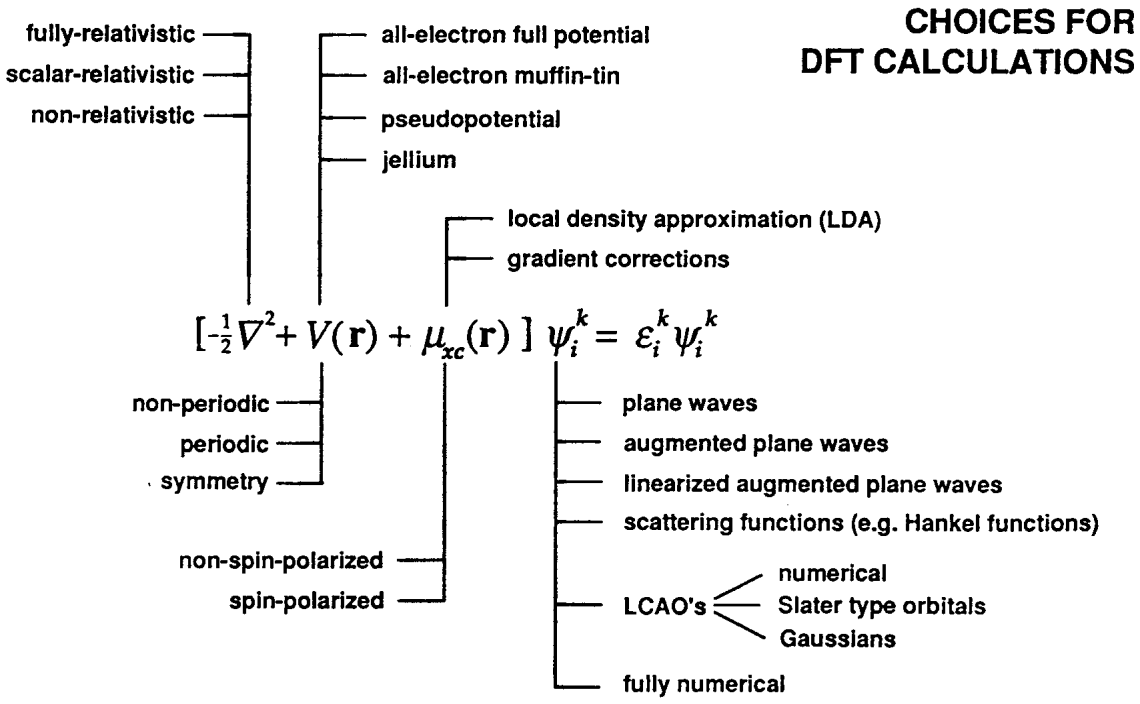


Figure A.1: Overview of electronic structure methods od solving DFT and HFT equations.

# Appendix B

# The Hellmann-Feynman Theorem

Suppose that a certain system has a hamiltonian H ($\varrho$) that depends continously on the parameter $\varrho$; suppose the the eigenstate $|\varphi(\varrho)\rangle$ is known

$$H(\varrho)|\varphi(\varrho)\rangle = \epsilon(\varrho)|\varphi(\varrho)\rangle. \tag{B.1}$$

The Hellmann-Feynman theorem states that

$$\frac{\partial\epsilon(\varrho)}{\partial\varrho} = \frac{\langle\varphi(\varrho)|\frac{\partial H}{\partial\varrho}\varphi(\varrho)\rangle}{\langle\varphi(\varrho)|\varphi(\varrho)\rangle}. \tag{B.2}$$

When applied to one-electron Hamiltonian equation

$$H\varphi_i(r) = \varepsilon_i\,\varphi_i(r), \tag{B.3}$$

assuming the wave function $\varphi$ to be normalized, the theorem gives

$$\nabla\varepsilon_i = \langle\varphi_i|\nabla H|\varphi_i\rangle. \tag{B.4}$$

Equation B.4 states that inorder to calculated the forces acting on the nuclei, it is neccesary to solve one-electron Hamiltonian ($H\varphi_i(r) = \varepsilon_i\,\varphi_i(r)$ ) and then evaluate the expectation value of the Hamiltonian gradient.

## B.1 The Pulay Forces

Within the Born-Oppenheimer [29] approximation atomic nuclei move in an effective potential which is the sum of the total nuclear Coulom repulsion energy and the energy of the electronic system in the ground state. in order words, the total energy of the systems acts as an effective potential for the nuclei. As a consequence of this, in any total energy method, the internuclear forces are opposite of the gradients of the total energy

$$F = -\nabla E^{tot.} \tag{B.5}$$

Suppose we have the same conditions as those used for the derivation of the Hellman-Feyman, but we do not impose $|\varphi(\varrho)\rangle$ to be an eigenstate of $H(\varrho)$. Stated differently, we have a hamiltonian $H(\varrho)$ and a state $|\varphi(\varrho)\rangle$ both depending continuously on the parameter $\varrho$. For simplicity we assume $|\varphi(\varrho)\rangle$ real and normalized.

When the expected value $\epsilon(\varrho)$

$$\epsilon(\varrho) = \langle\varphi(\varrho)|H(\varrho)|\varphi(\varrho)\rangle \tag{B.6}$$

is differentiatde with respect to $\varrho$ we have

$$\frac{\partial\epsilon(\varrho)}{\partial\varrho} = \langle\varphi(\varrho)|\frac{\partial H(\varrho)}{\partial\varrho}|\varphi(\varrho)\rangle + 2\left(\frac{\partial}{\partial\varrho}\langle\varphi(\varrho)|\right)H(\varrho)|\varphi(\varrho)\rangle. \tag{B.7}$$

The first term in B.7 is the Hellmann-Feynman force. The second one is a consequence of $|\varphi(\varrho)\rangle$ not being an eigenstate of $H(\varrho)$.

# Appendix C

# Generation of Pseudopotentials

The typical method for generating an ionic pseudopotential for a atom of species $\alpha, \upsilon_\alpha$ is illustrated in Figure C.1 and proceeds as follows: All-electron calculations are performed for an isolated atom in its ground state and some excited states, using a given form for the exchange-correlation density functional. This provides valence electron eigenvalues and valence electron wave functions for the atom. A parameterized form for the ionic pseudopotential is chosen. The parameters are then adjusted, so that a pseudoatom calculation using the same form for exchange-correlation as in the all-electron atom gives both pseodowave functions that match the valence wave functions outside some cutoff radius $r_c$ and pseudoeigenvalues that are equal to the valence eigenvalues. The ionic pseudopotential obtained in this fashion is then used, without further modification, for any environment of the atom. The electronic density in any new environment of potential obtained in this way and the same form of exchange-correlation functional as employed in the construction of the ionic pseudopotential. A generalization of this pseudopotential construction procedure for solutions of the atom that are not normalizable has been introduced by Hamann [172].

Finally it should be noted that ionic pseudopotentials are constructed with $r_c$ ranging typically from one to two times the value of the core radius. It should also be noted that, in general, the smaller the value of $r_c$, the more "transferable" the potential. (The entire procedure for solving the problem of a solid, given an ionic pseudopotential, is outlined in the review by Payne et. al.[119])

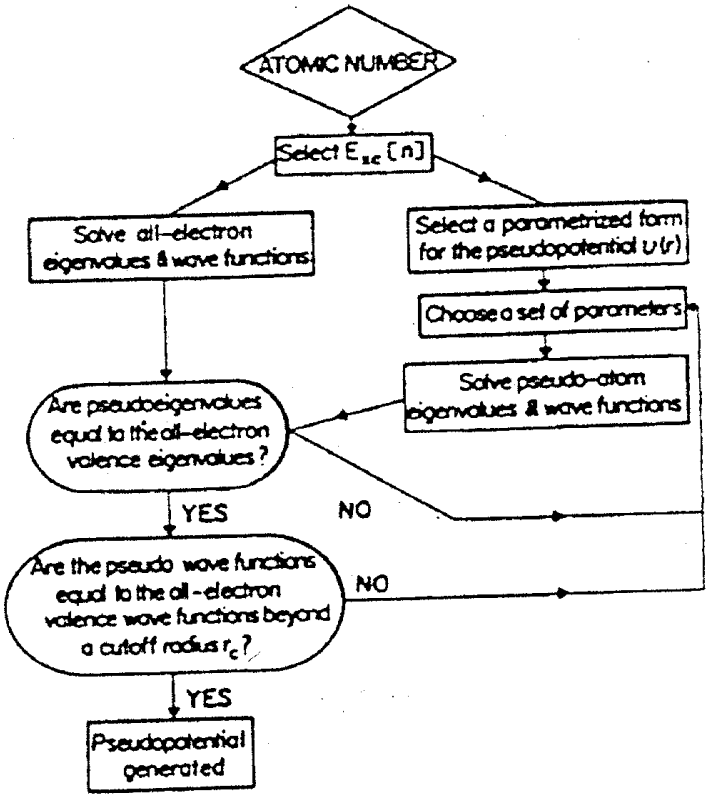


Figure C.1: Flow chart describing the construction of an ionic pseudopotential for an atom

# Appendix D

# BFGS Minimization Method

The BFGS (Broyden-Flecther-Goldfarb-Shanno) algorithm is a method for finding the minimum of a function of several variables. It seeks to take account of the different second derivatives of the function with respect to these variables, but using information only about the function and its first derivatives at each point.

Expanding the function $f(x)$ about the current position $x_0$ to second order in the displacement gives:

$$f = f(x_0) + \nabla f \cdot (x - x_0)^T \cdot \mathbf{A} \cdot (x - x_0) \tag{D.1}$$

where $\mathbf{A}$ is the second order derivative matrix. The optimal choice of $x$ to minimize the energy would therefore be

$$(x - x_0) = \mathbf{A}^{-1} \cdot \nabla f \tag{D.2}$$

The problem is then to obtain a reasonable estimate of $\mathbf{A}^{-1}$ . We start off with some approximation to the Hessian, which is then iteratively improved after each step. In fact, when far from the minimum our use of an approximate Hessian may be a better choice than the true Hessian, as we force the former to always be positive definite, ensuring the step direction chosen should always cause the energy to decrease. However, this does not guarantee that the full step length suggested in Eq. D.2 will decrease the energy, just that the energy initially decreases along this direction. Therefore if the energy does increase we can adopt a backtracking strategy to choose a smaller step.

If the $i+1^{-th}$ step involves moving from $x_i$ to $x_{i+1}$**,** and the gradients at each point are $\nabla f_i$ and $\nabla f_{i+1}$ respectively, then the next approximation for the Hessian $\mathbf{A}_{i+1}$ is obtained by updating the previous approximation $\mathbf{A}_i$, according to the formula below:

$$\mathbf{A}_{i+1} = \mathbf{A}_i + \left(1 + \frac{(\nabla f_{i+1} - \nabla f_i) \cdot \mathbf{A}_i \cdot (\nabla f_{i+1} - \nabla f_i)}{(x_{i+1} - x_i) \cdot (\nabla f_{i+1} - \nabla f_i)}\right) \frac{(x_{i+1} - x_i) \otimes (x_{i+1} - x_i)}{(x_{i+1} - x_i) \cdot (\nabla f_{i+1} - \nabla f_i)}$$

$$- \frac{\mathbf{A}_i \cdot (\nabla f_{i+1} - \nabla f_i) \otimes (x_{i+1} - x_i)}{(x_{i+1} - x_i) \cdot (\nabla f_{i+1} - \nabla f_i)} - \frac{(x_{i+1} - x_i) \otimes \mathbf{A} \cdot (\nabla f_{i+1} - \nabla f_i)}{(x_{i+1} - x_i) \cdot (\nabla f_{i+1} - \nabla f_i)} \quad \text{(D.3)}$$

The rigorous derivation of this formula shows that for an exactly quadratic N-dimensional energy surface, it will converge to the exact Hessian in N steps or less.

# Appendix E

# Bulk Modulus Calculations

For the lattice constants at zero pressure $a_0$ and $c_0$, the ambient pressure volume is

$$V_0 = \frac{\sqrt{3}}{2} a_0^2 c_0$$

The one dimensional analog of the Murnaghan equation [80] provides an approximation for describing the nonlinear relation between normalized lattice parameters and pressure $P$,

$$r/r_0 = \left[ \left( \frac{B'}{B_0} \right) P + 1 \right]^{-\frac{1}{B'}} \tag{E.1}$$

Here, $r$ is the lattice constant along one of the crystal axes, $B_0^{-1} = -\left(\frac{\partial \ln r}{\partial P}\right)_{P=0}$ is the linear compressibility, and $B^{'}$ is the pressure derivative of $B$ (i.e. $\frac{\partial B}{\partial P}$).

$$B' = \frac{\partial B}{\partial P}$$

$$\kappa = B_0^{-1} = -\left( \frac{\partial \ln r}{\partial P} \right)_{P=0}$$

$$c/c_0 = \left[ \left( \frac{B'}{B_0} \right) P + 1 \right]^{-\frac{1}{B'}} \tag{E.2}$$

$$a/a_0 = \left[ \left( \frac{B'}{B_0} \right) P + 1 \right]^{-\frac{1}{B'}} \tag{E.3}$$

and

$$V/V_0 = \left[\left(\frac{B'}{B_0}\right) P + 1\right]^{-\frac{1}{B'}} \tag{E.4}$$

# Appendix F

# Publications and Papers Presented at International Conferences

## F.1 Publications

- Nguyen-Mahn, D., Ntoahae, P.S., Pettifor, D.G. and Ngoepe, P.E. (1999). "Electronic Structure of Platinum Group Mineral : Prediction of Semiconductor Band Gaps." Molecular Simulation, **22**, 23.

- Arnaud Marmier, Petros S. Ntoahae, Phuti E. Ngoepe, David G. Pettifor and Stephen C. Parker, " Platinum Sulfide: Negative compressibillity and new structure." (in progress)

- Ntoahae, P.S.,Ngoepe, P.E.,Nguyen-Mahn, D. and Pettifor, D.G. "Internal Relaxations, Presure Dependence and Optical Properties of Platinum-Group Minerals." ( in progress )

## F.2 Papers Presented at International Conferences

- Ntoahae, P.S. and Ngoepe, P.E. "First Principle Study of Structural, Electronic and Optical Properties of Platinum-Group Minerals.", September 1997, IUCr Structural Chemistry Indaba II, Kruger National

Park, SA.

- Ntoahae, P.S. and Ngoepe, P.E. " Applications of Computer Simulation Methods to the Study of Platinum Group Minerals.", December 1997, Polar Solids Meeting, Liverpool, UK.

- Ntoahae, P.S. and Ngoepe, P.E. " Applications of Computer Simulation Methods to the Study of Platinum Group Minerals.", December 1997, University of Exeter, Exeter, UK.

- Ntoahae, P.S., Ngoepe, P.E., and S.C. Parker. " Atomistic Simulation of Platinum Sulfide minerals", December 2002, University of Reading, UK.

- Ntoahae, P.S., Ngoepe, P.E., and S.C. Parker. " Atomistic Simulation of Sulfide Surfaces and their reacivity with water.", December 2003, University of Loughborough, UK

### F.2.1 Local presentations

Presented **20** papers at the following local conferences: Annual South African Institute of Physics (9), Annual FRD/Royal Society - Materials Modelling Meeting (8), Bi-Annual University of the North Interscience (3)